Compressive Instabilities in Metal-coated Polymer Microtrusses

by

Bharat Vinod Bhaga

A thesis submitted in conformity with the requirements
for the degree of Doctor of Philosophy
Graduate Department of Aerospace Science and Engineering
University of Toronto

Abstract

Compressive Instabilities in Metal-coated Polymer Microtrusses

Bharat Vinod Bhaga

Doctor of Philosophy

Graduate Department of Aerospace Science and Engineering

University of Toronto

2019

Lightweight structures directly contribute to the sustainability of aviation, as their use reduces the structural weight of aircraft which in turn reduces fuel burned during flight. One family of lightweight structures are metal-coated polymers. Hybrid polymer-nanometal microtrusses are a member of this family. These structures are fabricated by 3D printing complex truss-like structures out of polymer material, and electrodepositing nanocrystalline metal onto the polymer. Recent work has shown that buckling instabilities govern the strength of these systems. Hence this study focuses on modelling local shell buckling, one of the critical buckling mechanisms.

In studying filled-shell buckling, hollow-shell buckling theory provides the framework for the behaviour of the shell as it undergoes buckling in a filled cylindrical shell. However, a model for the core must be realized. The Southwell stress model is used to develop an energy model of the core as it is subject to radial displacements, and the Timoshenko energy method is then utilized to determine the axial buckling load for a filled cylindrical shell. The models developed in this thesis include a fundamental model where the shell and core are fully adhered, a non-adhesion model where the shell and core are not adhered, a hollow-core model where the core is partially hollowed out along its axis, and an inelastic model where the shell behaviour is inelastic. These models are later verified through finite element analysis. Experiments on dogbone specimens also revealed some practical implications that must be considered when attempting to validate these theories. In addition, optimization for minimum mass design was carried out using the newly-developed models.

The results of these studies indicate that while the new models are theoretically sound, there are still aspects of metal-coated polymer structures which bear investigating. Fine-tuning of the present models is warranted, which may include more complex curve fitting procedures for determining the model constants or the use of numerical techniques other than finite differences. In addition, the manufacturing processes for these structures must be improved prior to their use as primary structural elements in aerospace applications.

Acknowledgements

It is very difficult to name all the people who contributed to this thesis (either directly or indirectly). As such, the people named below are in no particular order.

First to my mother, father and brother...the constants in my life. Without your continuous support, I would not be where I am today.

To my supervisor, Dr. Craig A. Steeves for his guidance and mentorship these many years. This being said, our friendship is such that we often get carried away talking about interesting topics whether or not they were thesis related.

To my aunt and uncle in Ottawa: Masi and Masa. Thank you for taking care of me during the four years in Ottawa during my time at Carleton University and for your always-present support up till today.

To my sisters and my brother (once again), who each insisted that have one sentence in this thesis to illustrate their contributions:

– my brother Arjun, who constantly reminded me to stay cool, have fun, and to not get too stressed out;
– my sister Saakshi, who "silently motivated me to do my best" and may be "[one of] the only reason[s] I completed this thesis;" and
– my sister Divya, who provided "continuous motivation which helped me fix my grammar on a regular basis."

To my aunt and uncle in Toronto – Foi and Foa. Your continued insistence in having me stay a couple nights each week and the amazing meals I got each time won't be forgotten. Thanks also to my sisters Renu Bhen and Deeshana Bhen.

To my grandparents, Nani and Nana, who not only helped me clarify many parts of my thesis, but also motivated me to always consider the next steps in whatever paths I follow both during and after my thesis.

To the many friends who have come and gone at UTIAS (this list is not exhaustive): Martin Juhas, Qian Zhang, Sandipan Chatterjee, Jaehoon Won, Vishal Singh, Adam O'Brien, Nick Ewaschuck, David Platt, Katie Daley, Samuel Cheung, Daniel Pepler and Ron Heichman. Those who did not attend UTIAS but whose names bear mentioning: Sampurna Rout and Sheetal Makhanjee. These and many more people would all take a thesis-size document just to thank properly.

And last but most certainly not least, to the awesome four-legged companions that have come and gone during my time at UTIAS: my dog Dora, my cat Trooper and our present dog Khushi.

"To understand anything is to find something in it which is our own"

– H.H. Swami Chinmayananda

Table of Contents

List of Figures

List of Tables

List of Symbols

$a_1, b_1, c_1, ...$	fitting constants for the non-adhesion core model
$a_\mathrm{s}, b_\mathrm{s}$	node spacing in the radial and axial directions for discretized Southwell model equations
A	buckle wavelength amplitude
A'	buckle wavelength amplitude or penetration distance for non-adhesion model
$A_\mathrm{v}, B_\mathrm{v}, C_\mathrm{v}$	fitting constants for Voce material model
b	penetration length for the non-adhesion model
b/λ	non-dimensional penetration length for the non-adhesion model
D	flexural stiffness of a flat plate
D^*	flexural stiffness of a curved plate, modified for hollow shell buckling
D_sb	flexural stiffness of a curved plate, modified for hollow simultaneous buckling
E	Young's modulus of shell material
$\overline{E}$	non-dimensional Young's modulus, E_c/E
E_c	Young's modulus of core material
E_T	tangent modulus for inelastic model
f	load target for minimum mass optimization
$\overline{f}$	non-dimensional load target
F, F_FL	local shell buckling load for a filled shell under an axial compressive load
$\overline{F}$	non-dimensional buckling load, $F/(El^2)$
F_b	local shell buckling load as determined from Abaqus simulations
F_FG	global buckling load for a filled shell under an axial compressive load
F_hi	inelastic local shell buckling load for a hollow shell under an axial compressive load
F_HCG	global buckling load for a filled shell with a hollow core under an axial compressive load
F_HCL	local shell buckling load for a filled shell with a hollow core under an axial compressive load
F_HCS	simultaneous buckling load for a filled shell with a hollow core under an axial compressive load
F_HG	global buckling load for a hollow shell under an axial compressive load
F_HS	local shell buckling load for a hollow shell under an axial compressive load
F_TG	global buckling load for a thick hollow shell under an axial compressive load
F_TL	local shell buckling load for a thick filed shell under an axial compressive load
F_s	inelastic local shell buckling load for the shell in a filled cylinder
g	shear layer constant for a beam on an elastic foundation
$\overline{h}$	hollowness factor for a filled shell with a hollow core, r_i/r
I	second moment of area

k	foundation spring constant for a beam on an elastic foundation
K	core model constant for filled shell
$\hat{K}$	contracted form of polynomial for hollow core model
K_f	core model constant for filled shell with a solid elastic core
$K_\mathrm{i}, K_\mathrm{s}$	core model constants for filled shell with a non-adhered core
l	length of cylinder
m	number of half buckle waves
M	mass of a cylinder
$\overline{M}$	non-dimensional mass of cylinder
M_FS	mass of a filled shell
M_HC	mass of a filled shell with a hollow core
M_HS	mass of a hollow-shell cylinder
M_TS	mass of a thick shell cylinder
p, q	distributed and axial loads applied to a beam on an elastic foundation
P_cr	local shell buckling load of a filled shell for Karam and Gibson model
$p_{00}, p_{10}, p_{01}, ...$	fitting constants for hollow-core model
r	inner radius of shell and outer radius of core
r, z, θ	Polar coordinate directions (radial, axial, circumferential)
$\overline{r}$	non-dimensional radius, r/l
r'	separation distance between shell and core for non-adhesion model
r_e	effective radius of shell for simultaneous buckling
r_i	inner radius of core (hollow core only)
t	thickness of shell
$\overline{t}$	non-dimensional shell thickness, t/r
t_e	effective thickness of shell for simultaneous buckling
U_b	internal energy arising from bending of the shell longitudinal sections due to buckling deformations
U_c	internal energy arising from stretching of the shell hoop sections due to buckling deformations
U_c2	internal energy arising from stretching of the shell hoop sections due to separation between the shell and the core
U_e	external energy due to an applied axial load
U_i	internal energy due to deformations caused by buckling
U_ic	internal energy under continued axial compression
U_p	internal energy contained in the polymer core
w	radial deformations due to buckling
x, y, z	Cartesian coordinate directions
y_0	centroid location for simultaneous buckling of a filled shell with a hollow core
$\overline{y}_0$	non-dimensional centroid location
γ	empirical correction factor for hollow shell buckling
δl	axial deformation applied to axisymmetric section of cylinder for Abaqus simulations
δl_b	eigenvalue solution from Abaqus simulations representing axial deformation to cause buckling
Δ	axial deformation applied to the end of a cylinder
ε	axial strain applied to a cylinder
ε_rc	radial strain arising from circumferential stretching of shell
ε_T	true strain
κ	curvature of a shell surface undergoing buckling deformations
$\lambda, \lambda_\mathrm{CR}$	critical buckling wavelength for a filled shell under an axial compressive load
$\overline{\lambda}$	non-dimensional critical buckle wavelength, λ/t
λ_HC	critical buckling wavelength for a filled shell with a hollow core under an axial compressive load
λ_HS	critical buckling wavelength for a hollow shell under an axial compressive load
λ_TS	critical buckling wavelength for a thick hollow shell under an axial compressive load
μ	Lagrange multiplier
ν	Poisson's ratio of shell material
ν_c	Poisson's ratio of core material

ρ	density of shell material
$\overline{\rho}$	non-dimensional density, ratio of shell-to-core densities ρ_c/ρ
ρ_{c}	density of core material
σ_0	stress amplitude for radial stress boundary condition in Southwell stress model
σ_{CR}	buckling stress for a filled shell under an axial compressive load, Karam and Gibson model
σ_{M}	buckling stress for a filled shell under an axial compressive load, Myint-U model
σ_{HS}	buckling stress for a hollow shell under an axial compressive load
$\sigma_r, \sigma_z, \sigma_\theta$	stress in radial, axial and circumferential directions
σ_{rB}	stress boundary condition for Southwell model
σ_{rc}	radial stress arising from circumferential stretching of shell
σ_{SB}	buckling stress for simultaneous buckling of the shell and core
σ_x, σ_y	stress in x- and y-directions
σ_{T}	true stress
σ_{TY}	yield stress or material strength
τ_{xy}, τ_{rz}	shear stresses in xy and rz planes
ϕ, ψ, ζ	stress functions used for the Southwell model
$\phi_0, \psi_0, \phi_1, ...$	values from discretized forms of the governing equations of the Southwell model

Chapter 1

Introduction

With the world's industries moving to become greener to reduce their environmental impact, aviation is examining environmentally-friendly technologies that will not only reduce the aviation industry's impact on the environment, but will also help airline operators save money in the process. The sustainable aviation initiative aims to "reduce the footprint of next-generation aircraft, engines and avionics systems" [8]. A multitude of technologies are being researched or developed to meet the challenges of sustainable aviation for the commercial sector, focusing on all aspects of aircraft or their everyday operations. For instance, novel configurations for aircraft propose to overhaul the airframe design through the use of unconventional configurations, such as the blended-wing body [9] or the truss-braced wing [10]. Alternative sources of fuel are being considered, and in some cases have already been tested on existing engine architectures [11, 12]. Electric taxiing operations aim to reduce or eliminate fuel consumption during ground operations [13].

A key part of any aircraft design is its structure, whether the aircraft has a novel blended wing body design or a legacy tube-and-wing configuration. For civil aircraft, the empty weight of an aircraft is defined as the weight before fuel, passengers and cargo are present [14]. As the structure can contribute half of the empty weight of an aircraft, light-weight structural designs are utilized. Lighter structures lead to reduced fuel consumption, translating into reduced aircraft emissions and directly contributing towards the goals of sustainable aviation. In legacy aircraft such as the Boeing 737 family and its derivatives, metals dominate the aircraft empty weight [15]. However in more recent aircraft such as the Boeing 787 or the Airbus A350, composite materials are predominantly utilized for the structure [16, 17]. While composite materials are preferred for their higher strength-to-weight ratios than metals [18, 19], their use is coupled with several drawbacks. Composites materials are more expensive to produce than metals, and require specialized tooling and worker training. Compared to metal structures, it is not always clear when a composite structure is damaged, necessitating the use of exotic inspection methods. For these reasons, they are often passed over in favour of all-metal structures.

For aerospace applications, it is of interest to create structures which have high strength-to-weight ratios while also being economical to produce. Composite materials are light-weight, strong, and expensive; metals are heavy, strong and low-cost [18, 19]. Conversely, polymer materials are light-weight and not very strong, but they have low manufacturing costs [20]. Due to these characteristics, polymer materials in aerospace applications are typically relegated to roles which do not require high strength. The most common applications for polymer materials in aircraft are as matrix materials for fibre-polymer composites, and for the passenger seating [19]. In order to create structural components that satisfy the three criteria for weight,

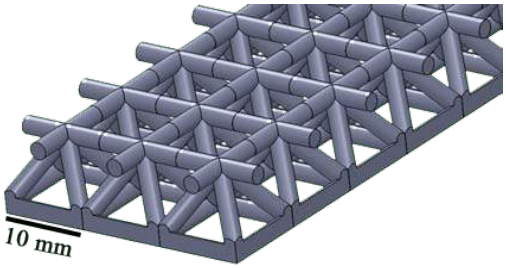

Figure 1.1: A typical microtruss topology with cylindrical struts. One unit cell of this microtruss has an edge length of 10 mm. [image modified from Lausic et al. [1].]

cost, and strength, a proposed idea is to harness the advantages of both metal and polymer materials [1, 21]. Metal-coated polymer parts have traditionally been used in non-structural applications [22], but specifically-tailored parts can be used to replace their heavier all-metal counterparts. This requires careful design of metal-coated polymer structures to produce components which have minimum weight, superior strength, and economical production costs. Used in conjunction, organized cellular polymer materials and nanocrystaline metals provide the solution for this criteria.

Foamed polymer materials – an application of cellular solids – have previously been utilized in sandwich panel construction, where their low densities make them ideal for sandwich cores [23, 24]. Due to the random orientation of the foam cells, foamed materials suffer from bending-dominated behaviour. It has been shown by Deshpande [25] that structures with more stretching-dominated behaviour have higher strength-to-weight ratios than those with bending-dominated behaviour. A microtruss, as shown in Figure 1.1, is an example of an organized cellular architecture whose deformations are stretch-dominated. This contribues to their higher strength-to-weight and stiffness-to-weight performance metrics compared to less-organized cellular solids. 3D printing is the most attractive manufacturing method for these geometries, as the complex microtruss topologies can be manufactured with ease and with less material waste compared to more traditional methods of manufacture [26, 27]. The reduced amount of waste produced by 3D printing methods also furthers the goals of sustainable aviation.

Looking at metals, there are now economical ways to produce high-strength metals known as nanocrystalline metals. As their name implies, nanocrystalline metals have grain sizes on the nanometer scale, providing them with increased strength via the Hall-Petch effect [4, 28–31]. For instance, nanocrystalline nickel may have up to seven times the strength of its conventional counterpart. The increased strength of nanocrystalline metals allows for structures with higher strength-to-weight ratios compared to the same application if using conventional metals. At present, the most repeatable process for producing nanocrystalline metals is electrodeposition [28, 32], an application for which capital investments are very low compared to more exotic methods of manufacture.

A metal-coated polymer microtruss is produced by first 3D printing a polymer preform followed by electrodeposition of a nanocrystalline metal coating [1, 4, 21, 33]. These structures harness the mass-efficient topology of a microtruss structure along with the high-strength properties of nanocrystalline metal. In

addition, the metal coating on the outside of the microtruss struts positions the metal away from the neutral axes of bending [21], further increasing the bending and buckling resistance of these structures. Though there have been advances in producing these hybrid structures, their use in practical applications requires a thorough understanding of their behaviour. Previous studies involving three-point bending tests of hybrid microtrusses have found that their failure is governed by compressive instabilities of the struts [1, 4], while the nanocrystalline metal coating provides the strength of these structures. As the struts have cylindrical goemetries as seen in Figure 1.1, the compressive failure mechanisms of metal-coated polymer cylinders are of interest. Through understanding the failure mechanisms of metal-coated polymer cylinders, knowledge of the failure mechanisms of hybrid microtrusses will be developed.

1.1 Thesis Objectives and Outline

The primary goals of this thesis are as follows:

- model failure mechanisms relevant to metal-coated polymer cylinders under axial loads,
- examine the behaviour of metal-coated polymer cylinders through experiments, and
- optimize strut geometries for minimum mass design of microtrusses.

As the struts in metal-coated polymer microtrusses are metal-coated polymer cylinders, the modelled failure mechanisms can be applied to study the behaviour of hybrid metal-polymer structures. A variety of cylinder configurations and conditions are examined, including those where the metal coating is not fully adhered to the polymer substrate or where polymer core is partially hollowed out.

A summary of the existing research on metal-coated polymer cylinders is presented in Chapter 2, which also provides a thorough background to the related topics of hollow metal shells and foam-filled cylinders subject to axial loads. Compresssive instabilities are the dominant failure modes of metal-coated polymer microtrusses [1, 4, 21]. For metal-coated polymer cylinders, the compressive failure mechanisms are Euler buckling and local shell buckling. Of these two mechanisms, local shell buckling is less explored. When considering metal-coated polymer cylinders, hollow-shell theory [34–37] governs the behaviour of the metal shell while the core requires separate treatment. The Southwell model [6, 38, 39] is employed to develop a model for the polymer core of the metal-coated polymer cylinder. This model is presented in Chapter 3.

The derivation of local shell buckling loads is explored for the following cases:

1. A metal-coated polymer cylinder with a fully-adhered metal shell and polymer core undergoing elastic local shell buckling (Chapter 4);
2. A metal-coated polymer cylinder where the metal shell and polymer core are not adhered (Chapter 5);
3. A metal-coated polymer cylinder where the core is partially hollowed out along its axis (Chapter 6); and
4. A metal-coated polymer cylinder where the metal shell exhibits inelastic behaviour (Chapter 7).

These four models utilize the core model development of Chapter 3, and finite element studies are utilized to verify all of the models. The results of experimental investigations into the behaviour of metal-coated polymer cylinders are presented in Chapter 8. For minimum-mass design in aerospace applications, optimization can be utilized to achieve designs with the highest strength-to-weight ratios [14]. The methods and results of optimization studies, which optimize cylinder geometries relevant to the models developed in Chapters 4 through 6, are presented in Chapter 9. Finally, Chapter 10 provides a summary of the findings and concluding comments.

List of Publications

To date, the work contained in this thesis has been published in four conference proceedings (two of which are peer-reviewed) and will be published in one peer-reviewed journal.

Bhaga B. and Steeves, C.A.; "Compressive Instabilities in Metal-Coated Polymer Microtrusses," *Student Research Symposium 2014*, University of Toronto Institute of Aerospace Studies, December 2014, Toronto

Bhaga B. and Steeves, C.A.; "Compressive Instabilities in Metal-Coated Polymer Microtrusses," *CASI AERO 2015*, May 19-22. Montreal

Bhaga B. and Steeves, C.A.; "Compressive Instabilities in Metal-Coated Polymer Microtrusses," *Proceedings of The Canadian Society for Mechanical Engineering International Congress 2018*, May 27-30. Toronto

Bhaga B. and Steeves, C.A.; "Modelling Hybrid Polymer-Nanometal Lightweight Structures," *ICASSE 2018*, Aug 2018. Moscow

Bhaga B. and Steeves, C.A.; "Modelling Hybrid Polymer-Nanometal Lightweight Structures," *Aerospace Systems*, 2018 (to be published)

Chapter 2

Literature Review

2.1 Introduction

The continued move towards more fuel-efficient designs for aircraft is taking place on all fronts, from aerodynamic shape optimization to new combustion technology for aircraft engines. From a structural standpoint, the empty weight of aircraft can be reduced by utilizing materials with higher ratios of strength-to-weight and stiffness-to-weight. Polymer microtruss structures coated with nanocrystalline metal (or simply hybrid microtrusses) offer the lightweight benefits of polymers while potentially providing the same or better strength than metal structures. Like any new technology, the behaviour of this new structure must be better understood before it is used to replace current structural components in aircraft.

This literature review covers the topics dealing with the failure mechanisms in metal-coated microtrusses as outlined in the flowchart of Figure 2.1. The strength and stiffness of nanocoated microtrusses are derived from the metal coating; the 3D-printed polymer contributes little to the structure [4, 21]. Hence, the failure mechanisms of the metal coating on metal-coated polymer cylinders are of more importance.

Although other failure modes for metal-coated microtrusses exist, such as failure of nodal connections, previous studies on nanocoated microtrusses have shown that their strength is governed by compressive instabilities [21]. As the truss elements of nanocoated microtrusses can be modelled as metal-coated polymer cylinders, the present topic explores the compressive instabilities associated with metal-coated polymer cylinders. The goal is to understand the compressive failure modes associated with metal-coated cylinders, and by extension the failure modes of metal-coated polymer microtrusses.

The literature on the properties and manufacturing methods of nanocrytstalline metals is discussed first, followed by the rationale for the microtruss design. Next, an overview of the failure modes of interest is given, with a strong focus on local shell buckling. An in-depth review of hollow-shell buckling will be done, followed by a review of the existing body of knowledge on filled-shell buckling. There are a limited number of studies on filled shells with hollow cores, inelastic buckling of filled shells, and optimization of filled shell geometries; an overview of these will be provided.

2.2 Nanocrystalline Metals

Nanocrystalline metals, or simply nanometals, are those which have average grain sizes less than 100 nm [29]. Conventional metals, by comparison, are composed of grains which are typically larger than 10 µm.

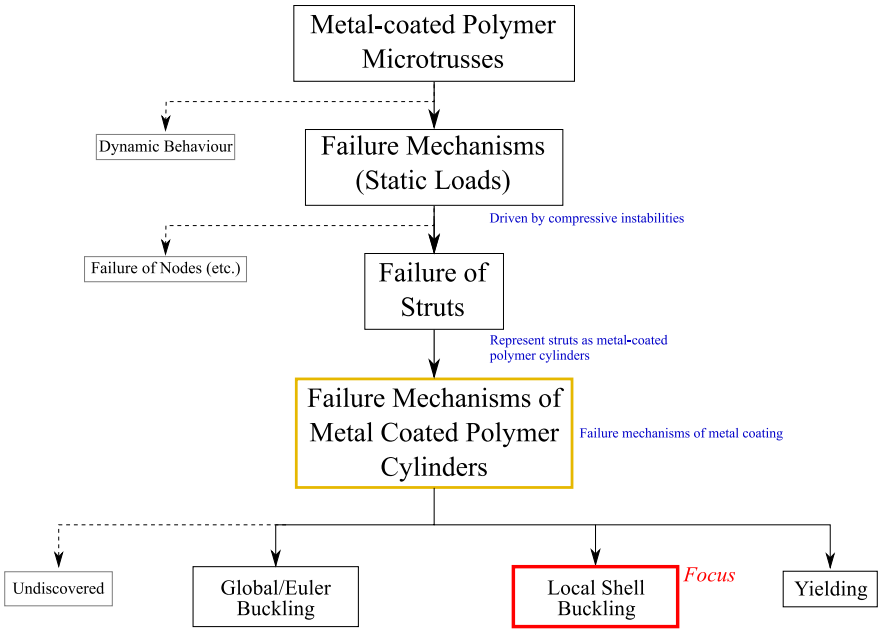

Figure 2.1: A flowchart of topics relevant to metal-coated polymer microtruss structures and their failure mechanisms.

The reduced grain size of nanocrystalline metals improves material strength, wear resistance [28, 29], and superplastic formability [40]. The increased material strength is a consequence of Hall-Petch strengthening, whereby smaller grain sizes offer higher material strength [18]. The strength of nanocrystalline metals can be up to seven times greater than their conventional counterparts [28, 29]. However, the advantages of these metals also come with decreases in ductility and Young's modulus. In particular, the decrease in Young's modulus of nanocrystalline metals is due to the increased grain boundary volume fraction [41]. The higher yield strength can often result in more brittle behaviour, similar to when materials are cold-worked [18]. It is of note that the density of metals changes little as their grain sizes are reduced [28, 30].

Metals which are most readily produced in nanocrystalline forms include iron, nickel, lead, cobalt, and copper as well as alloys of these metals [28, 29]. The strength of these metals has been shown to increase as grains are reduced to sizes between 10 and 20 nm. Below this threshold, further grain size reduction leads to the reverse Hall-Petch effect, causing a decrease in material strength [18, 29].

Through the use of nanometals, a substantial decrease in weight required for a given application can be realized. For designs dominated by strength, less material is required for a given application if a nanocrystalline metal is used compared to its conventional counterpart [4].

2.2.1 Processing Techniques and Manufacturability

Several manufacturing methods for nanocrystalline metals exist, however only a few have potential for future development into larger-scale processes which can be readily used for industrial-level production of nanocrystalline metals. Current methods to produce nanometals include mechanical alloying, gas phase condensation, severe plastic deformation, and electrodeposition [29, 40, 42].

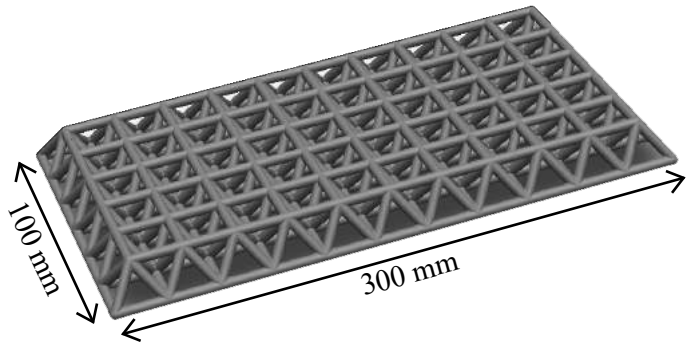

Figure 2.2: An example of a microtruss geometry with major dimensions given for scale.

A primary manufacturing issue for nanometals is the variation of material properties across manufacturing processes [29, 30], and between different material batches produced by the same process. Furthermore, the grain size reduction capabilities of various processes vary: while mechanical alloying can yield grain sizes on the order of 5 to 10 nm [42], severe plastic deformation of metals cannot yield grain sizes below 150 nm. Some processes cannot produce very large amounts of material owing to the apparatus required for nanometal production. Consolidation of small quantities can lead to specimen purity issues, such as the introduction of voids during consolidation operations or the appearance of hydrogen pockets [29, 32]. These purity issues can lead to sample densities below the theoretical values of the parent materials.

The aforementioned issues currently prevent large scale industrialised manufacturing of nanometals. However, of the existing methods, electrodeposition has proven to be the most reliable. The electrodeposition process can be tailored to produce repeatable material properties, with results that are consistent across different material batches [28]. This is done by carefully controlling vital parameters of the electrodeposition process, including current density, supplied voltage, deposition material choices and constituents of the electrodeposition bath [1, 4, 28]. The electrodeposition of nanometals has been shown to increase their purity, specifically by reducing the presence of voids in the produced materials [28]. In addition, the grain size variation of electrodeposited nanometals is very narrow [28, 29].

Electrodeposition methods are well-developed, and the investment required to procure the equipment for the process is not prohibitive [28, 29]. This is especially advantageous considering the reliability of the electrodeposition method for nanometal production. While electrodeposition methods are typically used for thin metal coatings [18], it is possible to create very thick depositions of nanometal (i.e. thickness of 2 mm or greater) with purities comparable to thin coatings by utilizing the aforementioned process controls.

2.3 Microtruss Structures

Truss structures are extremely efficient for load bearing applications. A truss is an example of a cellular solid, whereby voids are deliberately introduced in order to improve the strength-to-weight and stiffness-to-weight ratios of the structure [23]. A more typical example of a cellular solid is a stochastic foam, which can be

made of polymers (for instance, Styrofoam^{TM}), metals, or even edible solids [23]. Typical stochastic foams are comprised of an interconnected network of solid struts.

A main disadvantage of stochastic cellular solids, however, is that their mechanical behaviour is bending dominated [1, 4, 21]. It is desirable to have a structure that is stretch-dominated, as this allows for higher values of strength-to-weight and stiffness-to-weight ratios relative to those which are bending dominated [25]. The use of a microtruss allows for stretch-dominated truss members while at the same time exploiting the advantages of cellular architectures [43]. The term "microtruss" is used since these trusses are significantly smaller than large-scale trusses used in current major structural assemblies. A typical microtruss is shown in Figure 2.2 with major dimensions labelled for scale.

Efficient design of the microtruss geometry requires consideration of both the strut design and the number of connections at each truss node [21]. The Maxwell criterion provides an algebraic rule that stipulates the nodal connectivity of a truss to ensure rigidity [25, 44]. For three-dimensional trusses, 6 connections per node are necessary but not sufficient in order to ensure completely stretch dominated behaviour for a truss structure. Fewer connections at each node than this will result in increased bending-dominated behaviour. The best strut cross-section for maximizing axial compression loading at minimum strut mass is found to be a hollow cylindrical strut with a sandwich-type wall [45]. However these are hard to manufacture, especially at the scales of microtruss structures. The next best strut design is a thin hollow cylindrical strut, however these would also be difficult to fabricate. For metal-coated polymer struts, a cylindrical cross-section is ideal with the polymer preform positioning the stiffer metal coating away from the strut neutral axes [1, 4, 31, 33].

As can be inferred from the microtruss geometry in Figure 2.2, the use of more traditional manufacturing methods to make these complex structures will result in high costs and large amounts of material waste. For this reason, 3-dimensional (3D) printing is the most cost- and time-effective way to manufacture these structures, while also saving on material usage.

2.4 3D Printing Methods and their Limitations

3D printing, or additive manufacturing, is a method to produce materials by depositing and/or curing a material in layers, while also hardening these layers through some secondary procedure to produce a finished part [4, 21, 26, 27, 46]. 3D printing methods require some feedstock material which is deposited or fused to shape the part being manufactured. Support material is often required while parts are being printed, which must be discarded upon completion of the part or removed through finishing processes.

Several 3D printing technologies exist, each intended for different end uses. Three of the main processes in common use include fused deposition modelling, selective laser sintering, and stereolithography [26, 47, 48]. All of these processes require a flat plate upon which to build parts, one layer at a time. Figure 2.3 provides diagrams of how these three processes produce a part. Fused deposition modelling heats a thin plastic "filament" feedstock and deposits it in layers on a plate, with the heat from the hot deposited plastic

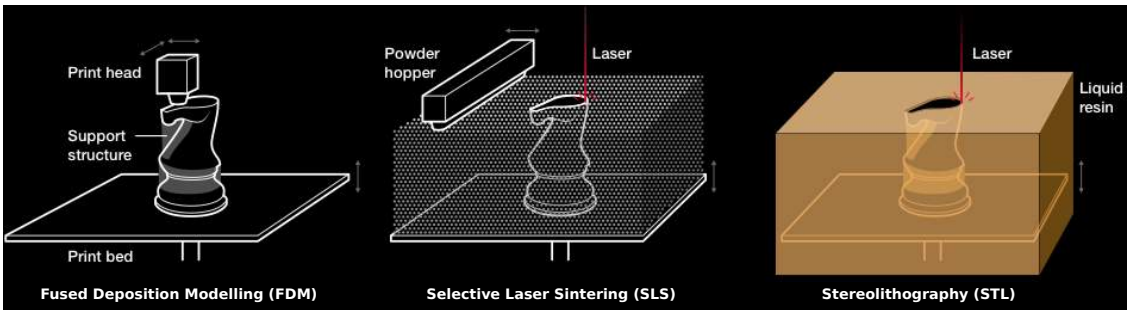

Figure 2.3: Illustration showing some common processes of 3D printing. From left to right: fused deposition modelling, selective laser sintering and stereolithography. [image modified National Geographic [2]]

melting the layers together [26, 47]. These printers are intended for desktop use at offices, and produce parts at lower costs and reduced qualities compared to other methods. Selective laser sintering involves heating fine powders with lasers, which cause the powder particles to coalesce and harden together. This is done in layers to produce the final part, and this technology can also be used to produce parts made of a wide variety of materials, including metals [49].

Finally, stereolithography produces parts either by selectively curing a photo-sensitive polymer using ultraviolet lasers (as shown in Figure 2.3), or by depositing an ultraviolet-sensitive liquid in layers [26, 50, 51]. These layers are cured upon sufficient exposure to ultraviolet light, causing them to harden. Stereolithography printers can produce very high resolution parts with fewer voids compared to other 3D printing technologies. It is among the most promising processes for producing 3D-printed polymer parts for end-use applications [52]. However, stereolithography places stricter limitations on materials that can be used due its reliance on photopolymerization. The cured material properties are also harder to control [26].

While 3D printing allows for the manufacture of complex designs with relative ease compared to traditional manufacturing methods, there are still some drawbacks which must be overcome. The inherent voids introduced in many methods of 3D printing lead to failure inevitably occurring through brittle fracture with little ductility, especially when compared to similar polymer materials produced through more conventional means [26, 48]. In addition, lower-quality printing methods such as fused deposition modelling [47] can lead to unreliable material properties. As with early manufacturing issues of nanocrystalline metals, this currently limits their viability for use in major structural applications. However, these issues are being overcome with advances in 3D printing technology.

2.5 Metal-coated Polymer Microtrusses

With the deposition of nanocrystalline metal onto a microtruss structure, the high-strength capabilities of nanocrystalline materials can be utilized, while at the same time realizing the structural efficiency of the cellular architectures of microtrusses [1, 4, 21, 33, 53]. Two photographs of coated microtruss structures are shown in Figure 2.4, while a representation of the scales relevant to a coated microtruss are seen in Figure

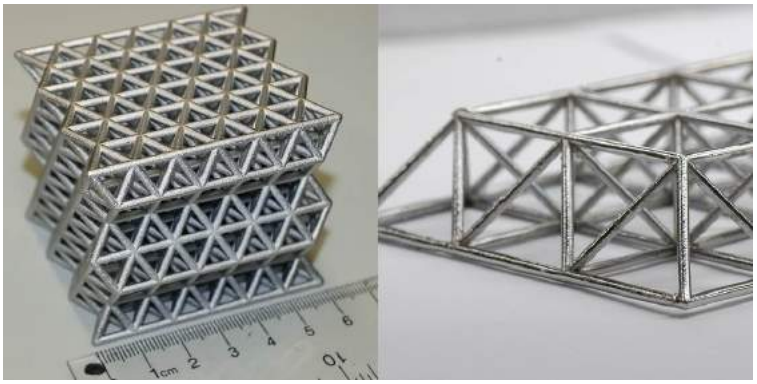

Figure 2.4: Two photographs of metal-coated polymer microtruss structures [3]

2.5. The geometry of the microtruss struts is controlled by changing the dimensions t, r and l, as shown in Figure 2.5. The use of a nanometal for the coating allows for further tailoring of the structure by controlling the grain size of the electrodeposited nanometal. If desired, the polymer preform can be made only for the purpose of providing a geometry for deposited nanometal to conform to, and can later be removed [1, 4]. However, a thin hollow shell structure presents other problems which lead to drastically reduced strength; these will be discussed in later sections.

2.5.1 Electroless Coating of Polymer Materials

Electrodeposition requires electrically conductive surfaces in order to deposit metal [54], regardless of whether the metal to be deposited is conventional or nanocrystalline. 3D printed microtrusses are made of polymer materials, and surface preparation must be performed so that nanocrystalline metals can be readily electrodeposited [55–57]. Due to the low conductivity of polymer materials, surfaces to be coated with nanocrystalline metal must be prepared through a series of processes, as depicted in Figure 2.6. These surface preparation steps are, briefly [1, 22, 56, 58]:

1. Cleaning with standard industrial-grade solvents,
2. Etching to roughen the polymer surface (an optional step),
3. Pre-activation using one of various solutions,
4. Activation or "seeding" using catatylic solutions, and
5. Metallization through electroless coating.

Surface cleanliness is paramount to starting the process as any residue or contaminants will negatively affect adhesion quality [22, 58]. The etching step, while not performed on all polymers, allows for mechanical roughness to be created on the polymer surface [52] . This allows for better adhesion, but the process must be time-limited as over-etching will negatively affect coating quality.

The surface preparation step (or pre-activation step) is of highest importance while also being the most difficult to accomplish chemically. For this reason, the solutions used in this step are proprietary [22, 56, 57]. The polymer being coated guides the chemistry of this step and will determine the selection of appropriate

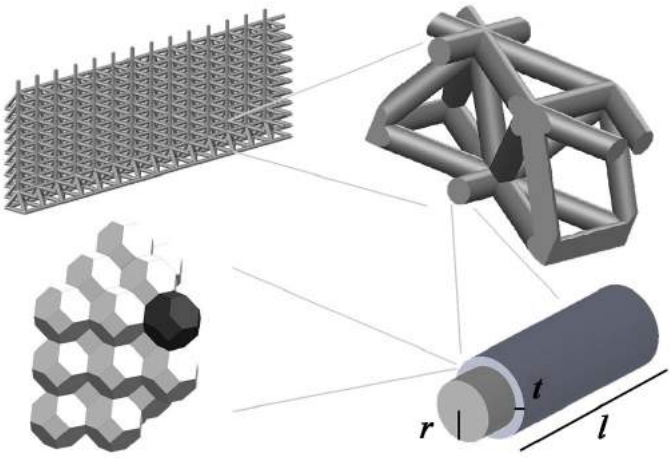

Figure 2.5: Diagram showing the different scales associated with a nanocoated microtruss structure. From top left clockwise: coated microtruss structure, one unit cell of the coated microtruss, one cylindrical strut showing dimensions t, r and l; and the individual polymer and nanometal atoms [image modified from Lausic et al. [4]]

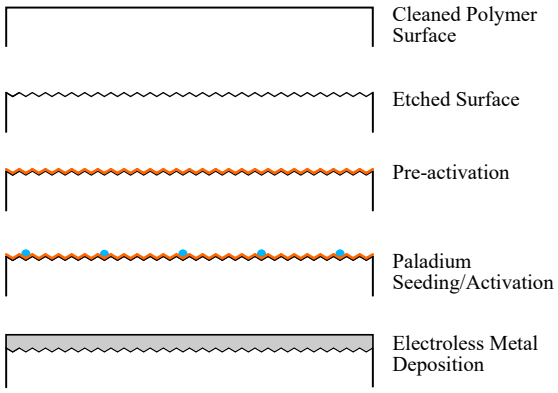

Figure 2.6: Diagrams of the steps required to coat a polymer surface with electroless metal.

compounds to use [59]. If chosen correctly, certain pre-activation solutions will allow for better adhesion between the electroless metal layer and the polymer surface. The activation step uses a readily-available chemical solution containing catalytic metal ions, typically chromium and/or palladium [22, 60, 61].

The final step is an electroless process used to "metalize" the now-activated polymer surface with a thin layer of metal. Nickel or copper are most commonly used for the metallization, with nickel being preferred as it involves a less complicated process [22, 58]. As the name implies, electroless plating does not require a voltage source: the coating process proceeds through a redox reaction occurring between the activated polymer surface and a metal ion-filled solution [54], resulting in deposition of a thin layer of metal.

The quality of the metallized polymer surface is affected not only by handling of specimens, but also on other factors which are not controlled in these steps. For instance, some polymers will be harder to metallize with nickel or copper due to the inherent chemistry between the base polymer material and the metal, which may prevent good adhesion [59]. Because some of these steps are performed above room temperature, the ambient temperature can also play a factor, especially in the final metallization step [22, 57].

In many cases, the adhesion between the metallization layer and the polymer will be less than that between the electrodeposited nanometal and the metallization layer. The poor adhesion between the electroless metal coating and polymer substrate can lead to premature failure of the coating through buckling, even if a load is applied only to the polymer substrate [62]. The larger the difference in Young's modulus between the polymer substrate and the thin metal film, the more pronounced this buckling delamination of the metal coating [63]. The known adhesion issues between the metal and polymer surfaces can hinder the strength of metal-coated polymer structures, and warrants inclusion in models for compressive instabilities of the metal-coated polymer structures.

2.5.2 Failure Mechanisms in Metal-Coated Microtrusses

Previous studies on nanocoated microtrusses in bending have shown that their failure mechanisms are driven by compressive instabilities [1, 4, 64]. As the truss elements of nanocoated microtrusses are metal-coated polymer cylinders (as seen in Figure 2.5), the present research topic seeks to explore the compressive instabilities associated with metal-coated polymer cylinders. The goal of the project is to understand the compressive failure modes associated with these metal-coated cylinders, and by extension the failure modes associated with nanocoated microtrusses.

The behaviour of metal-coated polymer microtruses must be understood in order to develop accurate models for these structures. While this behaviour also includes other aspects (such as responses to dynamic loading, as seen in Figure 2.1), the focus of this research is on the failure mechanisms in static or quasi-static loading conditions. More specifically, this refers to the failure mechanisms of the struts themselves. As the struts used for metal-coated microtruss structures have cylindrical cross sections, the failure mechanisms of metal-coated polymer cylinders will be investigated in detail. Henceforth, the focus will be on the failure mechanisms of metal-coated polymer cylinders in axial compression, or metal shells filled with polymer cores.

The two compressive instabilities of interest for metal-coated polymer cylinders are local shell buckling and global (or Euler) buckling, as seen in Figure 2.7. Local shell buckling is characterized by the appearance of waves on the surface of the cylindrical shell [34, 65, 66], while global buckling results in the lateral deflection of a column relative to its original undeformed axis. Both of these failure modes arise from buckling instabilities under the action of compressive loads.

The Euler buckling load for a strut of uniform material is given as [34, 65, 67]:

$$F = \frac{\pi EI}{(kl)^2}, \tag{2.1}$$

where F is the Euler buckling load, E is the Young's modulus of the strut material, I is the second moment of area of the strut cross-section, k is the effective column length factor and l is the length of the strut. The value of of k is dependant upon the end conditions of the strut [65, 67]. For metal-coated polymer microtrusses, the nodal connections of the microtruss geometry cause the struts to have a behaviour in between those of pin ends ($k = 1$) and fixed ends ($k = 0.5$) [21].

As the metal coatings of microtruss structures are responsible for the majority of the load-bearing capacity, past investigations of the metal-coated microtrusses assumed that the failure mechanisms of the struts only depended on the geometry and material properties of the metal shell [1, 4], and that the polymer core contributed only parasitic weight. However, for thinly-coated microtruss structures, where the cross-sectional area of the polymer is much greater than that of the shell, the polymer contributes markedly towards the load-bearing capabilities of the struts, and also increases their resistance to buckling. With respect to Euler buckling, the method of transformed sections [67] can be used to adapt the Euler buckling load to a strut made of multiple materials, such as a metal-coated polymer cylinder. However, local shell buckling

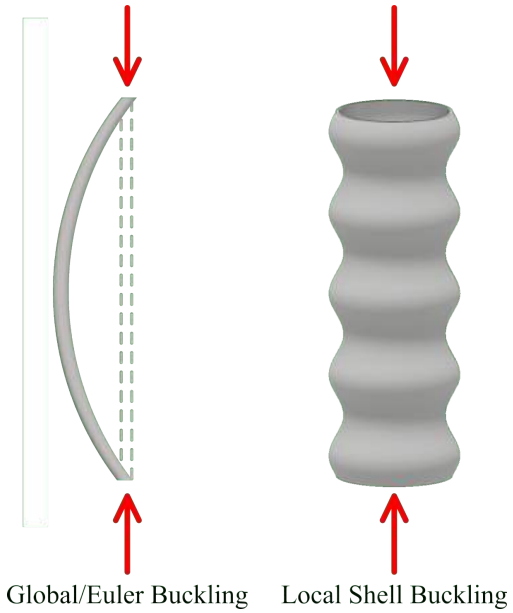

Figure 2.7: A thin slender strut undergoing global buckling (left), and a thin cylindrical shell undergoing local shell buckling (right)

of filled cylindrical shells – or simply filled-shell buckling – is an ongoing research topic. The theories of filled-shell buckling make use of the concepts of hollow-shell buckling. A discussion of hollow-shell buckling is undertaken prior to discussing the existing literature on filled-shell buckling.

2.6 Hollow-Shell Local Shell Buckling

Hollow-shell buckling is an instability that occurs when a thin cylindrical shell is subject to axial compression loads, as shown in Figure 2.7. It is characterized by sinusoidal waves along the length of an axially-loaded shell. The appearance of local shell buckling on a cylinder has two basic forms, as seen in in Figure 2.8. The concertina or accordion folds appear as axisymmetric rings [66, 68–70], while diamond indents are not axisymmetric about the cylinder's circumference. Combinations of one or more concertina folds and diamond indents can be observed after a cylinder has failed. For hollow-shell structures, the shell's geometry dictates which of these buckling modes is more prevalent [66, 68]. The appearance of buckling folds is immediate upon the reaching the critical load of a thin hollow shell. However for metallic shells, further compression of the shell beyond its critical load will result in the coalescence of many folds into one or two folds [68].

The local shell buckling load for a thin cylindrical shell in axial compression was found independently by several authors [71]: Lorenz in 1908 [37], Timoshenko in 1910 [34], and Southwell in 1914 [36]. At the inception of buckling, the energy of a thin shell undergoing buckling deformations includes its bending energy and its circumferential stretching energy. The shell bending energy refers to the energy contained under the bending action of longitudinal sections of the shell as they undergo sinusoidal buckling deformations, while the circumferential stretching energy results from the tension or compression of the shell hoop sections. The critical – or buckling – load occurs when the total shell energy no longer increases as the axial load is

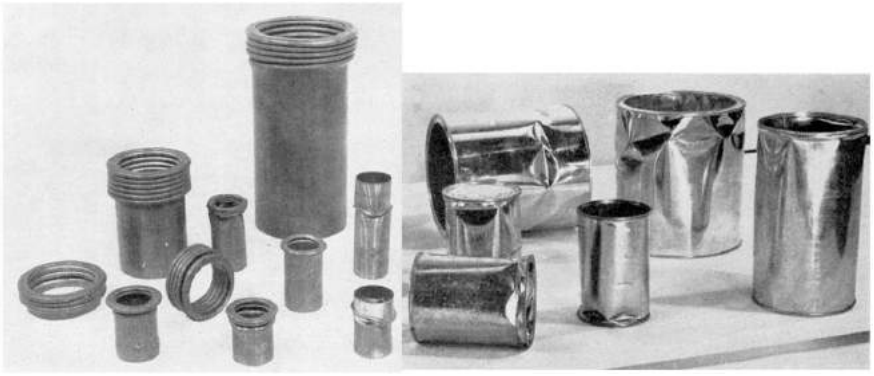

Figure 2.8: Photographs of various hollow shells after local shell buckling failure. The images depict concertina buckling (left) and diamond buckling (right) [images modified from Allan [68]].

increased further. For a thin cylindrical shell in axial compression, the stress in the shell at which this occurs is found to be [34, 36, 37, 68, 71–76]:

$$\sigma_{\text{HS}} = \frac{E}{\sqrt{3(1-\nu^2)}}\frac{t}{r}, \tag{2.2}$$

where σ_{HS} is the axial buckling stress of the shell, E is the Young's modulus of the shell's material, ν is its Poisson's ratio, and t and r are the thickness and inner radius of the shell, respectively.

A later derivation of Equation 2.2 by von Karman and Tsien in 1914 [35], along with the derivation by Timoshenko [34], proved that the buckled shape of the shell – be it axisymmetric or non-axisymmetric – is not a factor in determining its buckling load. The end conditions also do not affect the buckling load provided that the cylinder is sufficiently long [34–36, 72, 73, 75, 77]. However, the buckling load of the shell is dependant directly on its critical buckling wavelength, and a value for this wavelength must be found before the buckling load can be determined.

One outcome of the various investigations into hollow-shell buckling was a partial differential equation expressing the radial deflection of the shell as a function of the coordinate axes. This equation, known as Donnell's equation, takes the form [74, 75, 78]:

$$\frac{Et^3}{12(1-\nu^2)}\nabla^8 w + \frac{Et}{r^2}\frac{\partial^4 w}{\partial x^4} + t\nabla^4\left(\sigma_x\frac{\partial^2 w}{\partial x^2} + 2\tau_{xy}\frac{\partial^2 w}{\partial x \partial y} + \sigma_y\frac{\partial^2 w}{\partial y^2}\right), \tag{2.3}$$

where ∇ is the gradient operator, w is the radial deformation of the shell, x and y are the axial and circumferential coordinates of the cylinder, respectively; σ_x, σ_y and τ_{xy} are the axial, circumferential and shear stresses, respectively; and E, ν, t and r are as in Equation 2.2.

Donnell's equation became prominent because the only unknown is the radial buckling deformation w, a variable that previous theorists up till this time had not been able to isolate. This equation became indispensable at finding buckling loads for various loading conditions in thin cylindrical shells, including combined loading configurations [72, 74, 75]. By setting r to zero, the Kirchoff-Love plate bending equations can be recovered from Equation 2.3 [35, 74, 75]. The local shell buckling equation for hollow cylinders (Equation 2.2) is obtained upon simplification of Equation 2.3 to account for axial loading only.

Experimental investigations were carried out in an attempt to validate the theoretical buckling load (Equation 2.2). The majority of these attempts, however, attained less than 80% of the theoretical load [72, 73, 76–81]. This is because local-shell buckling loads of thin shells are extremely sensitive to material or geometric imperfections, or loading asymmetry around the shell circumference. The effects of imperfections become more pronounced as shells become thinner (i.e. the shell thickness-to-radius ratio, t/r becomes smaller), as the magnitude of the imperfections is nearly equivalent to that of the shell thickness [73, 78, 79, 81]. The imperfection sensitivity of hollow shells has forced designers to create less optimal designs by using stringer-stiffened shells or other fortifying elements [73, 77, 82]. Numerical investigations of thin-shell buckling, such as linear buckling analysis using finite element software, have found that the closely-spaced eigenvalues of thin shell structures under axial compression indicate their imperfection sensitivity [83–85].

A practical solution to the imperfection sensitivity of hollow shells under axial compression was to use empirically-derived correction factors [73, 77], such as those of Weingarten et al. [79]. This correction factor γ accounted for the geometry of the shell and takes the form:

$$\gamma = 1 - 0.901 \left[1 - \exp\left(-\frac{1}{16} \frac{r}{t} \right) \right], \tag{2.4}$$

where r and t are the inner radius and thickness of the shell, respectively.

Correction factors such as these became the cornerstone of NASA analysis manuals for hollow shells in axial compression [72, 86], which are extremely useful for launch vehicle design. However, these correction factors gave very conservative estimates for the critical loads [72, 73, 86], often leading to over-designed structures that are heavier than needed. In aerospace applications, heavier structures are detrimental to aircraft performance and lead to increased fuel burn [14].

In 1964, Tennyson conducted extensive studies using polymer shells which included a layer of photoelastic material [78, 87, 88]. The photoelastic layer allowed Tennyson to see the stress fields present in the material while the shells were compressed axially [89]. The cylinders for his experiments were fabricated using spin casting, producing shells with very tight geometric tolerances and which were also virtually imperfection free. Strain gauges were also equally spaced around the circumference of all shells under load. Through his experiments, Tennyson was able to achieve experimental buckling loads that were within 1% of the theoretical values (Equation 2.2). From these studies, it was concluded that it is possible to obtain buckling loads close to theoretical values if the cylinders are manufactured to strict tolerances, include few material imperfections, and are aligned carefully to the axis of loading. This proved that making near-perfect shells would alleviate the imperfection sensitivity of hollow shells [80, 87, 88].

The theories of hollow-shell buckling are well established and have been verified through experimental investigations. However, modern applications for shells require that the shell be filled with another, less stiff material. This leads to the study of filled-shell buckling, which relies on the behaviour of hollow-shell buckling to describe the shell's behaviour.

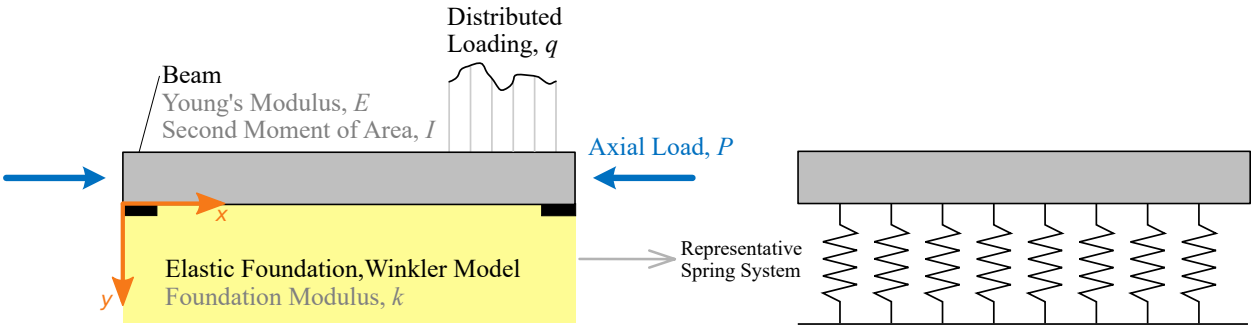

Figure 2.9: A beam with a Young's modulus E and second moment of area I is lying on an elastic foundation under an axial load P and has a distributed loading q. The elastic foundation can be represented as a Winkler foundation with modulus k, and this can be depicted as a bed of springs.

2.7 Filled-Shell Local Shell Buckling

Modelling filled-shell local shell buckling requires separate treatment of the shell and filler (or core) behaviour. While the hollow-shell theories are utilized to describe shell behaviour, various models representing the core have been derived in the literature. Many of these models utilize the aspects of Hetenyi's theories for beams on elastic foundations [90]. This topic is discussed first prior to delving into filled-shell buckling literature.

2.7.1 Beams on Elastic Foundations

A beam of unit width lies on an semi-infinite elastic material or "foundation," as shown in Figure 2.9. The beam is subject to an axial load P and distributed loading q. The foundation material with modulus k is modelled as a bed of independent springs, such that the transverse deflection at any point in the foundation is independent of the deflections at any other point [82, 90, 91]. This spring-like foundation model is often called the Winkler model [92, 93]. The original beam-on-foundation model focuses on the deformations of the beam [90], and does not consider the stresses or deformations in the foundation. In this case, the foundation modulus k is adequate to describe the behaviour of the elastic foundation. However, in certain cases the stress distribution within the core is also desired, and for these cases various stress functions have been developed to describe the core behaviour [82, 91, 92].

The governing equation of the beam on the elastic foundation shown in Figure 2.9 is:

$$EI\frac{d^4y}{dx^4} + ky + P - q = 0, \tag{2.5}$$

where E and I are the Young's modulus and second moment of area of the beam, respectively; k is the foundation modulus or spring constant for the spring layer, and q and P are the distributed load and axial load applied to the beam, respectively.

Beam on elastic foundation theories have been utilized in the treatment of face wrinkling composite beams [24, 94], and also for some analyses of hollow-shell buckling by treating the surrounding shell material

around a shell slice as a foundation [34, 35, 73, 90, 95]. By assuming certain behaviours of the foundation, various other models can be derived which can include modifications of Winkler's model [82, 91, 92]. Some of these have accounted for the shear behaviour of the foundation material, as well as non-infinite foundations.

Many of the existing models derived using the theories of beams on elastic foundations became the groundwork for theoretical treatment of filled-shell local shell buckling [96, 97].

2.7.2 Literature on Filled-Shell Buckling

The problem of local shell buckling of filled cylindrical shells was not studied until the early 1960's. Driven by the need to understand buckling of solid propellant rockets under axial loads [5, 72, 97–101], various authors undertook theoretical and experimental investigations.

The earliest attempt at a filled-shell buckling theory by Myint in 1966 [97] emulated the approach used by von Karman and Tsien [35]. It was assumed that the core acts as a Pasternak foundation, or a Winkler layer which accounts for both the transverse deflections in the core as well as the shear interactions between the shell and the core [91, 92]. The filled-shell buckling equation derived in this way yields:

$$\sigma_{\mathrm{M}} = \frac{1}{\sqrt{3(1-\nu^2)}}\sqrt{1+\frac{kr^2}{Et}}+\frac{gr}{Et^2}, \tag{2.6}$$

where σ_{M} is the axial buckling stress of the filled cylinder, k is the modulus of the spring layer, E is the Young's modulus of the shell material, ν is its poisson's ratio, g is the modulus of the shear layer, and r and t are the radius and thickness of the shell, respectively.

This equation is similar to the hollow-shell local shell buckling not only because of the similarity between this procedure and that of von Karman and Tsien [35], but also because Myint assumed that the behaviour of the shell for filled-shell buckling follows that of hollow-shell buckling. Since Myint's theoretical development, this treatment of the shell behaviour for filled-shell buckling has continued to remain this way for the majority of filled-shell buckling models in the literature.

Although the Myint model accounts for the shear behaviour of the shell-core system (i.e. g in Equation 2.6), it was later shown by various other studies that the shear interactions between the shell and the core were negligible [96, 98–100]. A more recent development in filled-shell buckling utilizes a foundation model derived by Gough et al. [82], which was originally intended for buckling of face sheets on sandwich panels subject to axial compression. This filled-shell buckling model was derived by Karam and Gibson [98] as:

$$P_{cr} = 2\pi Et^2\left(1+\frac{r}{2t}\frac{E_c}{E}\right)\left[\frac{1}{12(1-\nu^2)}\frac{r/t}{(\lambda_{cr}/t)^2}+\frac{(\lambda_{cr}/t)^2}{r/t}+\frac{2(E_c/E)}{(3-\nu_c)(1+\nu_c)}\frac{\lambda_{cr}}{t}\frac{r}{t}\right] \tag{2.7}$$

where E is the Young's modulus of the shell, E_c is the Young's modulus of the core material, t is the shell thickness, r is the shell inner radius, ν is the Poisson's ratio of the shell, ν_c is the Poisson's ratio of the core material, and λ_{cr} is the critical buckling wavelength. The critical wavelength must be found by determining

the positive real root of the quadratic equation given by $\partial P_{cr}/\partial\lambda = 0$.

The buckling load of Equation 2.7 is derived through modifying the hollow-shell derivations of Timoshenko [34] and Lorenz [37] to account for the presence of a core material with foundation modulus as defined by Gough [82]. A comparison between Equations 2.7 and 2.6 reveals that the Karam and Gibson theory neglects shear interactions.

Various other theoretical investigations also provided models for filled-shell local shell buckling. Seide [96] and Kounandis [102] used Donnell's Equation (Equation 2.3) [74, 75] to derive the local shell buckling load of a filled cylindrical shell, with Seide treating the core material as a Winkler spring layer [91]. Reddy and Wall [103] focused on the effects of the density of the filler material for foam-filled cylindrical shells, while using a model that incorporated the angle of the "hinges" of the buckling folds caused by local shell buckling. Malyutin et al. [104] and Weingarten et al. [100] each produced different theoretical models, both of which utilized an eigenvalue-solving method. The application of filled-shell buckling was also extended to concrete-filled steel or polymer tubes [105, 106], where it was found that the high compressive strength of a concrete core substantially increased the buckling resistance of the tubes.

Experimental investigations were also undertaken in an attempt to validate the aforementioned theories, and to investigate the phenomenon of filled-shell buckling. The majority of the experiments were performed using metal tubes filled with polymer or polymer-like foams [5, 103, 104, 107–109], intended to mimic the structure of solid propellant rockets or natural materials like plant stems. The theoretical model of Karam and Gibson [98] was also used to estimate the axial buckling strength of porcupine quills [69, 70]. Reddy and Wall investigated the energy absorption of filled shells [103], and were primarily interested in the optimal core stiffness where the energy absorption was maximized. Some finite element studies were also undertaken to understand the post-buckling behaviour of filled shells [100].

Through these experiments, it was reported that the filler material prevented or hindered the formation of diamond indents (non-axisymmetric buckling deformations previously shown in Figure 2.8). This caused concertina folds to appear more readily in filled shells than for hollow shells of the same geometry. It was also found that a better agreement between theory and experiment occurred with shells when the thickness-to-radius ratios were large [5, 69, 70, 107, 110], due to the fact that buckling loads for thick shells are less prone to imperfection sensitivity. While the strengthening effect of the core is more apparent for thinner shells [103], imperfection sensitivity still persists. Although Seide originally derived different theoretical models for both axisymmetric and non-axisymmetric buckling in filled shells [96], this effect was not found to cause differences in buckling loads as found through experiments.

The graph in Figure 2.10 shows data from the aforementioned experiments investigating filled-shell buckling, all of the experiments using tubes filled with a foamed polymer. The exception to these are the studies done by Yang et al [69, 70], which were conducted using porcupine quills. The theoretical predictions of Karam and Gibson [98] and Seide [96] are also shown. The experimental buckling loads are presented as normalized values relative to the hollow-shell buckling equation (Equation 2.2), while both the shell material

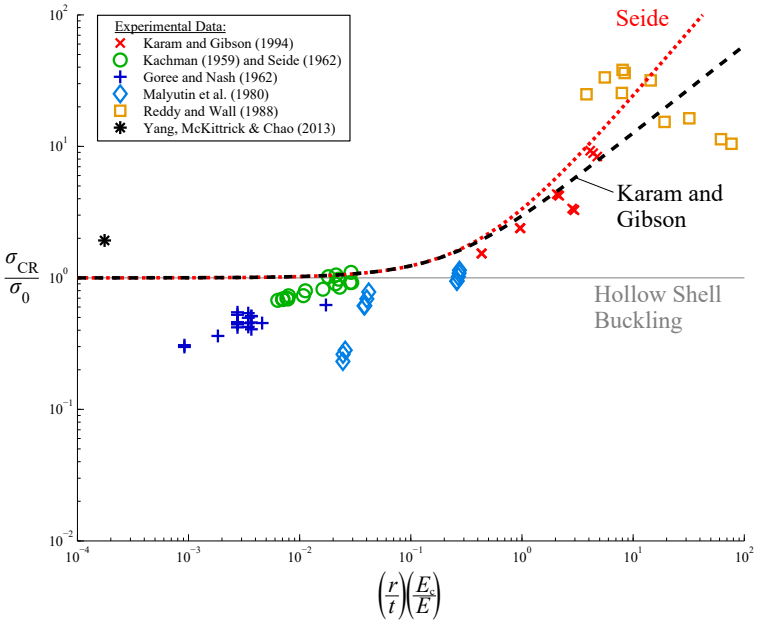

Figure 2.10: Graph of experimental results from investigations of axial buckling of filled cylindrical shells, plotted against the theoretical models for filled-shell buckling. The buckling stress σ_{CR} has been normalized against hollow local shell buckling equation, σ_0 (Equation 2.2) [adapted from Karam and Gibson [5]].

and geometry are considered in the non-dimensional parameter used as the abscissa.

The trends in the theoretical curves of Seide and Karam and Gibson generally agree with the experimental data, with the Seide model overpredicting all of the experimental values except those of Reddy and Wall. For shells with lower thicknesses (left end of Figure 2.10), there is less agreement between the predictions and experimental results. This indicates that the imperfection sensitivity of thinner filled shells persists as it does with hollow shells [73, 76, 78, 79, 102]. The experiments conducted by Reddy and Wall [103] involved different foam densities, whereas the other experiments used shells with different geometries.

The theoretical investigations of filled-shell buckling have focused on elastic buckling of thin shells with a soft elastic core. However, for thicker shells both with and without a core, inelastic local shell buckling becomes the dominant mode of failure.

2.8 Inelastic Buckling

While a majority of theoretical efforts investigate shell buckling phenomena assuming elastic material behaviour, some practical applications of buckling demand that inelastic behaviour be taken into account. This occurs when buckling takes place beyond the yield strength of the shell material.

Both the elastic and plastic behaviours of a linear-elastic work-hardening material can be represented diagramatically on a stress-strain curve as shown in Figure 2.11. While a material is behaving elastically, it is susceptible to elastic buckling. This means that removal of any load at the inception of buckling will cause all buckling deformations to disappear, causing the shell to return to its undeformed shape [78, 87].

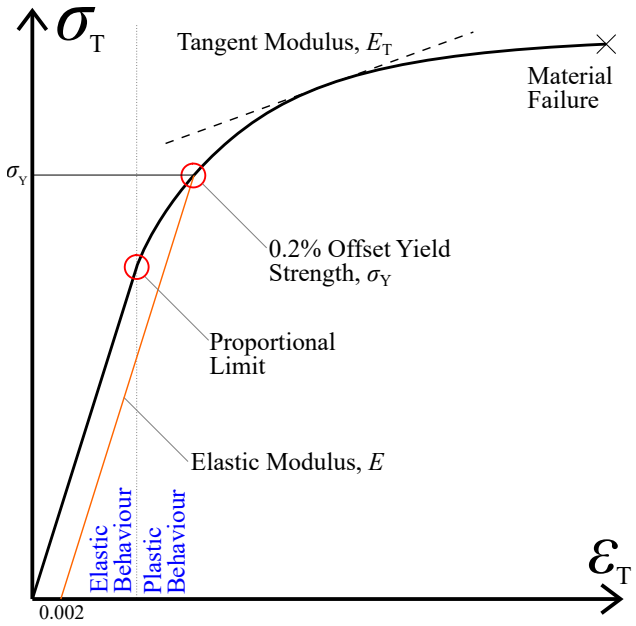

Figure 2.11: An annotated true stress-strain curve diagram showing regions of elastic and plastic behaviour. The methods of calculation for the Elastic Modulus E and tangent modulus E_T are shown.

The experiments conducted by Tennyson to investigate the imperfection sensitivity of hollow shells under axial loads included unloading buckled shells to confirm that buckled deflections disappeared, thus confirming elastic buckling. For elastic buckling predictions, the buckling loads can be calculated using values of Young's moduli found in material data sheets [34].

A material that is behaving plastically can fail by buckling inelastically, and this may occur before the material achieves its ultimate strength [1, 4, 34]. The proportional limit as shown on Figure 2.11 is the end of the linear-elastic region of the stress strain curve and the beginning of plastic behaviour. Like any plastic deformation, plastic buckling deformations are non-recoverable upon removal of the load as energy has been dissipated through plastic flow [18]. The Young's modulus E cannot be used to calculate inelastic buckling loads accurately. Instead either the tangent modulus (E_T) or the reduced modulus (E_R) must be used. The tangent modulus is found by calculating the instantaneous slope of the stress-strain curve, as shown in Figure 2.11, while the reduced modulus uses the tangent modulus along with a representation of the strut's cross section [34].

The inelastic buckling load can be calculated by replacing the Young's Modulus E with either E_T or E_R. However due to a difference in stress on opposite sides of a buckled shape (i.e. the concave and convex sides), using the tangent modulus can result in conservative estimates for buckling loads [111, 112]. The reduced modulus is intended to alleviate this issue, but it is more difficult to work with in practice and must be recalculated for different strut cross-sections.

Calculating the tangent and reduced modulus requires an analytical representation of a material stress-strain behaviour. While the Ramberg-Osgood curve fitting procedure is a generally-accepted representation of material stress-strain behaviour [113], the Voce curve fit remedies some of the shortcomings of the

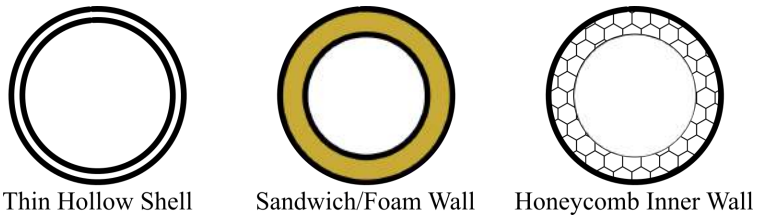

Figure 2.12: Illustrations of optimal compression member cross-sections from existing literature

Ramberg-Osgood model [114] as it is a continuous model between stress and strain with no transition area. The Voce model takes the form [1, 4, 114]:

$$\sigma_{\mathrm{T}} = B_{\mathrm{v}} - (B_{\mathrm{v}} - A_{\mathrm{v}}) \exp(-C_{\mathrm{v}} \epsilon_{\mathrm{T}}), \tag{2.8}$$

where σ_{T} is the true stress, ϵ_{T} is the true strain, and A_{v}, B_{v} and C_{v} are fitting constants of the model. Like other material stress-strain models, the Voce model can be used to find the tangent modulus at any stress.

2.9 Optimization

Optimization of metal-coated polymer microtrusses has focused on several areas. These include topology optimization of the microtruss structure [21, 115], grain size optimization of the metal coating [1, 4], and optimization of the struts for maximum load-bearing capability with minimum mass [45]. While not originally intended for microtrusses, investigations into optimizing general compression members have also been undertaken.

As the electrodeposition process requires tailoring of the process controls in order to produce nanometals, these same controls can be used to control the grain size of the produced nanocrystalline materials. Referring to Figure 2.5, optimization of metal-coated microtrusses can be done by controlling four length scales: the length of the struts l, the coating thickness t, the strut radius r and the grain size of the electrodeposited nanometal [1, 4, 33]. The ability to select the grain size of the deposited nanocrystalline metal gives a very fine degree of control over the behaviour of metal-coated polymer structures. Optimization of metal-coated microtruss structures while accounting for inelastic behaviour of the metal coating has also been undertaken [1, 4].

Looking at compression members, an analytical study was undertaken by Budiansky [45] to determine the minimum mass for a strut under an axial load. He showed that the optimal compression strut cross-section is that which has a sandwich wall with a hollow core [45], as shown in the centre of Figure 2.12. However, given the scale of the microtrusses being manufactured [4, 21, 33], as well as the manufacturing difficulties associated with this sandwich-wall cross section, it is difficult to use this cross section in a microtruss. An alternative is to utilize hollow cylindrical cross sections which can be designed to have low weights comparable to that of sandwich-wall cylindrical cross sections. The buckling sensitivity of hollow shells to

imperfections, especially at low shell thicknesses, makes this an impractical solution after knockdown factors are accounted for. For this reason, filled shells are recommended for their reduced sensitivity to imperfections [98, 103, 104, 107].

An optimization study of foam-filled metal cylinders loaded in axial compression was also undertaken [116] with a focus on very thin shells and low loads. Through this study, the optimal core stiffness ratio was determined for a given axial load. This same study revealed, however, that a metal shell with a hollow honeycomb core wall (right side of Figure 2.12) would outperform a hollow shell or a foam-filled shell in axial compression. This is a similar finding to that of Budiansky [45], as well as studies where optimization of sandwich panels was undertaken [117].

Some other studies have focused on other optimization aspects of foam-filled compression members. For instance, after conducting experiments on foam-filled metal shells, Reddy and Wall undertook numerical studies to determine the optimal foam density that provides the maximum specific energy absorption for a filled shell in axial compression [103]. It has also been revealed that a foam-filled cylinder can hold more energy than a hollow cylinder of the same mass, and the energy stored in filled-shell is more than that given by the individual energies of the core and shell added together [69, 82]. Examination of natural materials such as plant stems, bird feathers and porcupine quills have found that these naturally-made structures often have higher buckling strength-to-weight ratios than man-made structures [23, 69, 98, 118, 119]. As such, these natural materials provide inspiration to make more efficient compression members.

As of this writing, there are no relevant optimization studies which investigate the area of metal shells filled with solid polymer cores. It is this area that this research project intends to investigate, specifically geometries and loads relevant to metal-coated polymer microtrusses.

2.10 Summary

Metal-coated polymer microtrusses offer the high-strength benefits of nanocrystalline metals and the lightweight aspects of polymer materials. Although nanocrystalline metals are most reliably produced through electrodeposition methods, 3D printed polymer microtrusses must first be metallized using an electroless procedure. While electroless methods are well-developed, adhesion between the electroless metal layer and their polymer substrates is imperfect.

The dominant failure modes of metal-coated polymer microtrusses are compressive instabilities of the struts. These instabilities include both global buckling and local shell buckling. For local shell buckling of filled cylindrical shells under axial compressive loads, the shell behaviour is described by hollow-shell theory. The core decreases the imperfection sensitivity of the shell while also providing increased buckling strength. The majority of filled-shell experimental investigations have focused on foam-filled tubes, with the relevant theoretical models intended for this material combination. Optimization efforts of hollow- and filled-shell structures has been undertaken in several areas, but none have looked at polymer-filled metal shells in detail.

Chapter 3

Energy Model of an Elastic Cylinder Subject to an Axially Varying Axisymmetric Load

3.1 Introduction

Metal-coated polymer microtrusses are a lightweight complement to the current generation of aircraft structures. These hybrid structures are produced by electrodepositing nanocrystalline metal onto a 3D printed polymer preform, taking advantage of both the high-strength benefits of nanocrystalline metal [28–30] and the mass-efficient properties of microtruss topologies [1, 4, 21]. Three-point bending tests of metal-coated polymer microtrusses demonstrated that compressive instabilities dominate the failure modes of their struts, which have cylindrical cross-sections [4]. Therefore, the behaviour of metal-coated polymer cylinders is studied in order to understand the compressive instabilities of the hybrid microtruss structures.

Local shell buckling and global buckling are the compressive instabilities exhibited by metal-coated polymer cylinders under axial loads [4], and by extension metal-coated polymer microtrusses when subject to three-point bending loads. Of these mechanisms, local shell buckling of polymer-filled metal shells is less understood. The behaviour of hollow cylindrical shells undergoing local shell buckling has been studied extensively [34–37, 66, 75, 79, 87, 88], but filled-shell buckling has not been studied in the same depth. An undeformed filled cylindrical shell is shown in Figure 3.1(a), while a filled shell undergoing local shell buckling is shown in Figure 3.1(b). Though no studies specifically examine the buckling of solid polymer-filled metal shells, there have been several theoretical and experimental studies investigating the local-shell buckling of foam-filled shells [96, 98, 103, 104, 107, 109]. These foam-filled shell models utilize hollow-shell theory to describe the behaviour of the shell, and it has been shown that the inclusion of a core reduces the propensity of the shell to buckle.

Each of the filled-shell studies use different approaches in modelling the core behaviour [96, 98, 103, 104, 107, 109]. Of note is the filled-shell model developed by Karam and Gibson [98], currently the best-available buckling model for filled shells subject to axially compressive loads. Their model utilizes a core model developed by Gough et al [24, 82], originally derived for face sheet buckling of composite sandwich panels. However, the Gough model is two-dimensional and does not account for stresses in the circumferential direction. As the Karam and Gibson model relies on the Gough model, their model is not axisymmetric. In addition, the Karam and Gibson model cannot be used for more complicated filled-shell buckling situations, such as those where the core is hollowed out along its axis or a metal-coated polymer cylinder where the

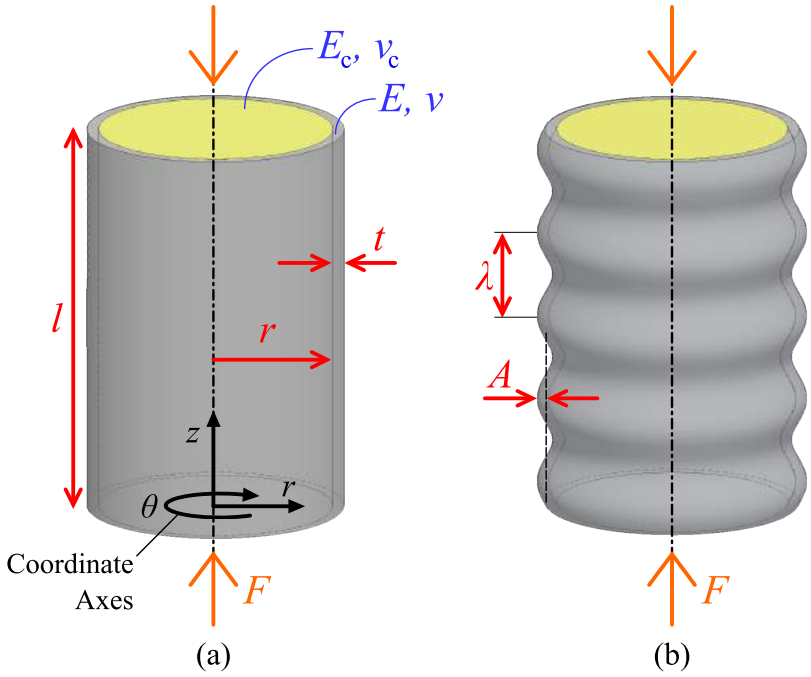

Figure 3.1: (a) A metal-coated polymer cylinder under an axial load F prior to buckling deformations. The cylinder has a length l, shell thickness t and inner radius r. The shell and core have Young's Moduli E and E_c while their respective Poisson's ratios are ν and ν_c. The coordinate axes for reference are z, r and θ. (b) A metal-coated polymer cylinder undergoing buckling with buckle wavelengths λ and buckle amplitude A.

shell and core are not adhered to each other.

To predict the buckling load of a metal-coated polymer cylinder, the theories of hollow-shell buckling [34, 35, 37] are utilized for the metal shell. However, as with previous filled-shell approaches [96, 98, 103, 104, 107, 109] a model is required for the polymer core. The Southwell model [6, 38, 39] enables calculation of the stress state in an elastic cylinder subject to an axisymmetric load. The Southwell model can be used to determine the stresses in a solid polymer cylinder as it undergoes deformations consistent with the sinusoidal local shell buckling of a surrounding shell. The stress state in a cylinder is determined as a function of two stress potentials, and unlike the Gough model this provides stresses in three dimensions [6, 38, 39]. Due to the nature of its governing equations, the Southwell model cannot be solved analytically and so a stress solution is found numerically through computational methods. Because this stress model is intended for the specific case of a cylinder under axisymmetric loads, the Southwell model is less expensive computationally compared to using general finite element software, as a lower mesh resolution can be used. In addition, a custom-written script intended for solving the Southwell model for the particular case of an axisymmetric loading would enable much faster solution times compared to general finite element software.

The goal of this work is to predict the axial load at which a shell filled with elastic material will exhibit local buckling. Analysis of strain energy is a convenient approach to such a prediction. It is assumed that an elastic core material is perfectly bonded to a thin elastic shell. When the shell begins to buckle locally under an axial load, the core material deforms in accordance with the shell deflection. Timoshenko [34] provides an analysis of the buckling of a hollow shell; in this chapter a novel approach to modelling the

core will be explicated. First, the Southwell model for a cylinder subjected to axisymmetric loading will be described. Next, this model will be coupled to the deformations associated with shell buckling through an appropriate choice of boundary conditions. This enables the determination of the elastic stress field in the core material at the onset of buckling, and hence the elastic strain energy in the core. The Southwell model is next verified through high-resolution finite element analysis to ensure that the stresses calculated match those determined through finite element simulations. A representation of the energy state of the core is then developed by determining the relationship between the strain energy and the geometric and material parameters of the problem. This is done by fitting an analytic function to the strain energy values calculated using the Southwell model. This improves the efficiency and enables differentiation of the model. The resulting function can therefore be used for strain energy predictions in a gradient-based optimization context, where sensitivities are required.

3.2 Model of the Core Behaviour

Predicting the axial buckling load for a metal-coated polymer cylinder requires the use of hollow-shell buckling theories [34, 35, 37] to describe the shell behaviour along with an accurate model to represent the core behaviour. Previous predictions for filled-shell buckling have modelled the core behaviour by utilizing the theories of beams on elastic foundations [96, 97], or have adapted the approaches intended for buckling of face sheets on composite sandwich panels [24, 82, 98]. However, the past models for the core are not axisymmetric as they do not account for the stresses in all relevant coordinate directions. Specifically, the circumferential direction is not included in the Gough model, on which the Karam and Gibson model relies. In this section, the procedure used for developing a new core model is detailed. Using the energy method of Timoshenko [34] to predict the local buckling load of the elastic shell, this new model of the core will be used to derive an axial buckling load prediction for a filled cylindrical shell.

The buckling load is to be determined for a metal-coated polymer cylinder under an axial load, as shown in Figure 3.1(a). The appearance of the filled shell while it is undergoing buckling is shown in 3.1(b). In determining the axial buckling load, the following assumptions hold:

- the shell and core are perfectly bonded;
- both the shell and core materials behave elastically;
- the buckling displacements are sinusoidal;
- there are many waves that form when the shell buckles; and
- the core conforms to the buckled shape of the shell.

When the shell and core are fully adhered, local buckling of the shell causes radial displacements on the surface of the core. In order to determine the strain energy in the core caused by these displacements, a model for the stress state of the core is required. The Southwell stress model will be used to determine the

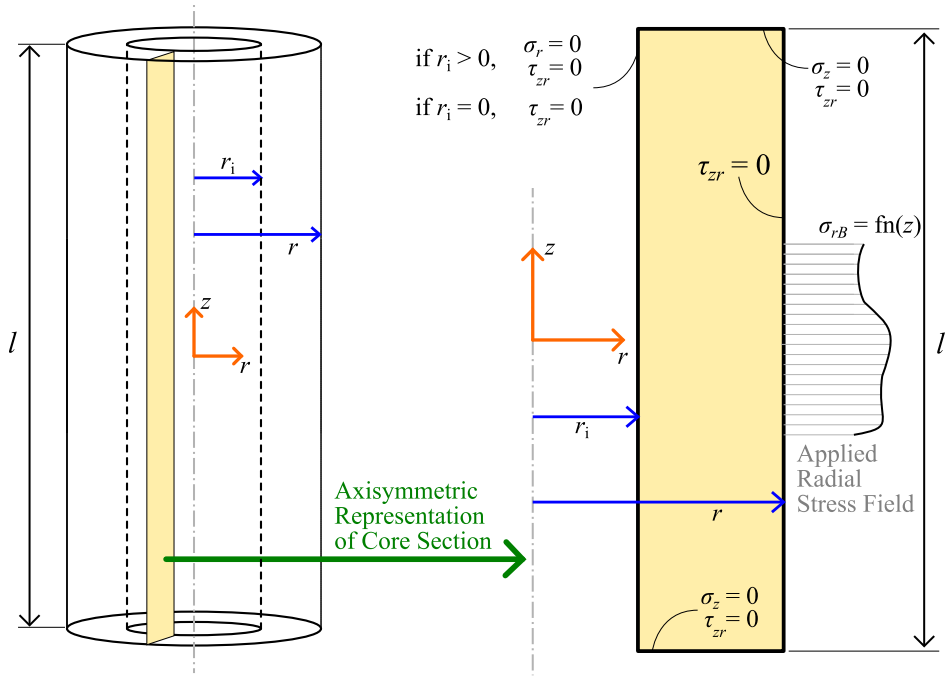

Figure 3.2: A polymer core with length l, inner radius r_i and outer radius r. An axisymmetric section is detailed showing the boundary conditions as relevant for the Southwell model (diagram adapted from Southwell [6]).

stress state in the core as it is subjected to sinusoidal radial displacements, and these stresses will be used to determine the strain energy in the core.

3.2.1 The Southwell Model

Southwell [39, 120] created a model that employs a stress potential function to calculate the stress field in an axisymmetrically-loaded isotropic elastic cylinder. Although the present aim of using the Southwell model is to determine the stress state in a solid polymer cylinder under axisymmetric radial loads, the model can be used to describe the stress states of either solid or hollow cylinders. A general cylinder geometry is shown in Figure 3.2, showing a hollow cylinder with inner radius r_i, outer radius r and length l. An axisymmetric section of this cylinder is detailed, with a radial stress field σ_rB applied at the outer surface of the cylinder. Along the edges of this axisymmetric section shown in Figure 3.2, the shear stress $\tau_{zr} = 0$, while the axial stresses $\sigma_z = 0$ at the top and bottom of the section (or top and bottom of the cylinder). These boundary conditions hold when the cylinder is hollow ($r_\text{i} > 0$), and will change when the cylinder is solid ($r_\text{i} = 0$) as shown in Figure 3.2. The Southwell stress model provides the stress state of the cylinder by solving for the stress state of the axisymmetric section shown in the Figure.

The present goal to determine the stress state of a solid cylinder (i.e. a polymer core of a filled shell) as it is subject to sinusoidal radial displacements. As the Southwell model is a stress model, it requires stress boundary conditions, as shown in Figure 3.2. The radial buckling displacements will be transformed into appropriate sinusoidal stress fields in order to adapt the Southwell model to the requirements of filled-shell buckling. In addition, the equations arising from the Southwell model require a numerical solution, and so

the axisymmetric domain to be studied must be discretized; the methods of discretization and meshing will be detailed in Section 3.2.3.

The Southwell model presents a more direct approach to solving for the core behaviour compared to classical finite element analysis. The model is uniquely suited to solving for the stress states in axisymmetrically-loaded cylinders. Solutions to the stress states of cylinders can be solved quickly and accurately using relatively low-density meshes. A finite element solution for similar geometries and loading conditions would require high resolutions to match the accuracy of the Southwell model. Thus, the use of a custom-written program developed solely for analysing core geometries of interest provides more efficient solutions than using general purpose finite element software.

Previous models for filled-shell buckling are intended only for fully-filled cylinders and when the shell and core are perfectly bonded [82, 96, 98, 103, 104, 107, 109]. The Southwell model can be used to determine the stress state in a cylinder subject to any axisymmetric loading cases, regardless of the cylinder geometry. This allows for the study of filled shells with hollow cores or cylinders where the shell and core are not adhered, two important cases which have not been studied previously in the area of filled-shell buckling.

3.2.2 Governing Equations for the Southwell Model

The governing equations to the Southwell model will be discussed in this section, followed by the methods used for discretizing these equations. The process of adapting the Southwell model for a polymer core subject to radial displacements will also be detailed.

The Southwell model provides the stress field in an axisymmetrically loaded cylinder, as shown in Figure 3.2. This requires rearranging the compatibility and equilibrium equations so that they are a function of two stress potential functions. First, the compatibility and equilibrium equations are written in terms of a single stress function ζ as follows [6, 38, 39, 121]:

$$\begin{aligned}
\sigma_r + \sigma_\theta &= \frac{1}{r}\frac{\partial^3 \zeta}{\partial r \partial z^2}, \\
\sigma_r - \sigma_\theta &= r\frac{\partial}{\partial r}\left(\frac{\partial^2 \zeta}{\partial z^2} - 2\nu\nabla^2\zeta\right), \\
\sigma_z &= -\frac{1}{r}\frac{\partial}{\partial r}\left(\frac{\partial^2 \zeta}{\partial z^2} - (1+\nu)\nabla^2\zeta\right), \text{ and} \\
\tau_{zr} &= \frac{1}{r}\frac{\partial}{\partial z}\left(\frac{\partial^2 \zeta}{\partial z^2} - (1+\nu)\nabla^2\zeta\right),
\end{aligned} \tag{3.1}$$

where σ_r, σ_z, σ_θ are the radial, axial and circumferential stresses respectively; τ_{zr} is the shear stress; and ν is the Poisson's ratio of the cylinder material. The details on the derivations of these equations are contained in [36] and [38]. Due the assumption of axisymmetric behaviour, the stress components $\tau_{r\theta}$ and $\tau_{z\theta}$ vanish everywhere. The stress function ζ satisfies the equation:

$$\nabla^4 \zeta = 0, \tag{3.2}$$

where ∇ is the gradient operator. Two more stress functions ϕ and ψ are introduced which are functions of the first stress function ζ:

$$\phi = \nabla^2 \zeta \quad \text{and} \quad \psi = \frac{\partial^2 \zeta}{\partial z^2} - (1+\nu)\nabla^2 \zeta. \tag{3.3}$$

The boundary conditions shown in Figure 3.2 as well as the functions for the stresses in Equations 3.5 allow for finding a constant value of ψ on all the boundaries of the axisymmetric domain. In this way, the value of ψ is 0 along the boundary.

Utilizing Equations 3.1 through 3.3, the equilibrium equations for ϕ and ψ are found to be [6, 38, 121]:

$$\begin{aligned} &\frac{\partial^2 \phi}{\partial r^2} - \frac{1}{r}\frac{\partial \phi}{\partial r} + \frac{\partial^2 \phi}{\partial z^2} = 0, \quad \text{and} \\ &\frac{\partial^2 \psi}{\partial r^2} - \frac{1}{r}\frac{\partial \psi}{\partial r} + \frac{\partial^2 \psi}{\partial z^2} = \frac{\partial^2 \phi}{\partial z^2}. \end{aligned} \tag{3.4}$$

A numerical solution to Equations 3.4 provides the values of ϕ and ψ in the cylinder. The methods for this will be detailed in the next section. The individual stress components can be calculated using their equations written in terms of ϕ and ψ:

$$\begin{aligned} \sigma_r &= \frac{1}{r}\left(\frac{\partial \phi}{\partial r} + \frac{\partial \psi}{\partial r}\right) - \frac{1}{r^2}[\psi + (1-\nu)\phi], \\ \sigma_\theta &= \frac{\nu}{r}\frac{\partial \phi}{\partial r} + \frac{1}{r^2}[\psi + (1-\nu)\phi], \\ \sigma_z &= -\frac{\nu}{r}\frac{\partial \psi}{\partial r}, \quad \text{and} \\ \tau_{zr} &= \frac{1}{r}\frac{\partial \psi}{\partial z}. \end{aligned} \tag{3.5}$$

3.2.3 Discretization of Equations for a Numerical Solution

A general analytical solution is not obtainable for the Southwell model. A finite differencing solution was developed by Allen et al. [6, 38, 121] which utilizes second-order central differencing throughout the domain. The axisymmetric section of the cylinder shown in Figure 3.2 is discretized using evenly spaced nodes, as shown in Figure 3.3. The node spacing in the radial and axial directions are a and b respectively. For the following equations, the node numbering follows the indexing pattern shown in Figure 3.3, with node 0 referring to the centre node of the pattern and nodes 1 through 4 indexed counter-clockwise starting from the bottom of the pattern. A discretized set of the stress function equilibrium equations (Equations 3.4) is determined for every single node in the domain, providing a matrix of undetermined coefficients. This is solved using standard matrix solution techniques which are readily available, such as those in MATLAB.

The equations for the stress functions ϕ and ψ (Equations 3.4) are discretized as follows:

$$\begin{aligned} \phi_1 + \phi_3 - 2\phi_0 + \left(\frac{a_s}{b_s}\right)^2 (\phi_2 + \phi_4 - 2\phi_0) - \frac{a_s^2}{2r_0 b_s}(\phi_2 - \phi_4) = 0, \quad \text{and} \\ \psi_1 + \psi_3 - 2\psi_0 + \left(\frac{a_s}{b_s}\right)^2 (\psi_2 + \psi_4 - 2\psi_0) - \frac{a_s^2}{2r_0 b_s}(\psi_2 - \psi_4) + 2\phi_0 - \phi_1 - \phi_3 = 0. \end{aligned} \tag{3.6}$$

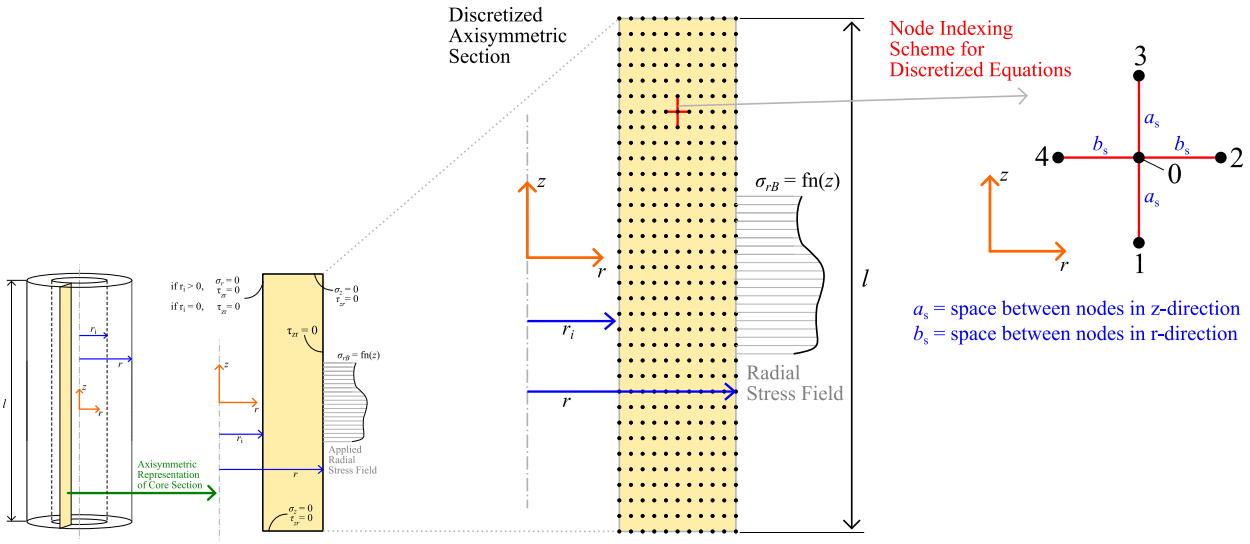

Figure 3.3: Node spacing and indexing pattern used for the axisymmetric section of the polymer core. The entire section is discretized using node spacings a in the z-direction and b in the r-direction. The node numbering follows a conter-clockwise pattern starting with node 1 at the bottom.

In these equations a_s and b_s are the grid spacings in the radial and axial directions respectively, r_0 is the radial position at the node of interest, and ϕ_0, ϕ_1, etc., ψ_0, ψ_1, etc. refer to the values of ϕ and ψ at various nodal locations as shown in Figure 3.3.

Due to the boundary conditions of the domain (as seen in Figure 3.2), the value of ψ is zero on all boundary nodes [6, 38]. To determine the values of ψ in the interior nodes, as well as the values of ϕ everywhere in the domain, requires the use of the boundary σ_r specified by the applied stress field σ_{rB}. Along the outer edge of the cylinder where $r_0 = r_\mathrm{o}$, the equation used to find the nodal values of ϕ is [6, 38]:

$$2(\phi_4 + \psi_4) - \phi_0 \left[2 - \frac{2(1-\nu)b_\mathrm{s}}{r_0}\left(1 - \frac{b_\mathrm{s}}{2r_0}\right)\right] + 2b_\mathrm{s}r_0\left(1 - \frac{b_\mathrm{s}}{2r_0}\right)(\sigma_{r\mathrm{B}})_0 = 0, \tag{3.7}$$

where the values of $(\sigma_{rB})_0$ are non-zero along the region where values of σ_{rB} are specified, and zero everywhere else. Equation 3.7 replaces the second of Equations 3.6 along the outside edge of the domain, where $r_0 = r_\mathrm{o}$. At the other three boundaries of the domain, the node numbering pattern used in Equations 3.6 and 3.8 will lead to spurious node references, as some nodes to which reference is made will not exist. At these domain extremities, second-order directional differencing is used in place of central differencing.

This discretization scheme generates one set of Equations 3.6 for every node in the domain. Along the outer edge where $r_0 = r_\mathrm{out}$, Equation 3.7 is used. Solving the resulting matrix of coefficients using standard matrix-solving algorithms provides values of ϕ and ψ. These can then be used to determine the values of the stress components (Equation 3.5), which are also discretized using second-order central differencing:

$$(\sigma_r)_0 = \frac{1}{2br_0}\left[(\phi_2 - \phi_4) + (\psi_2 - \psi_4)\right] - \frac{1}{r_0^2}[\psi_0 + (1-\nu)\phi_0],$$
$$(\sigma_\theta)_0 = \frac{\nu}{2br_0}(\phi_2 - \phi_4) + \frac{1}{r_0^2}[\psi_0 + (1-\nu)\phi_0],$$

$$(\sigma_z)_0 = -\frac{1}{2br_0}(\psi_2 - \psi_4), \quad \text{and}$$
$$(\tau_{zr})_0 = \frac{1}{2ar_0}(\psi_1 - \psi_3). \tag{3.8}$$

These stresses, once calculated, provide the complete stress state of the cylinder in Figure 3.2 when subject to a radial stress field $\sigma_{r\mathrm{B}}$. The stress distribution can also be used to determine the strain fields and the resulting strain energy in the cylinder.

3.2.4 Adapting the Southwell Model to Filled-Shell Buckling

The present aim is to develop an energy model for the polymer core in a metal-coated polymer cylinder when the metal shell is buckling (refer to Figure 3.1(b)). The Southwell stress model will be used to develop a model which provides the strain energy of a solid polymer cylinder as it undergoes sinusoidal radial deflections. This model will be used to determine the buckling load of a metal-coated polymer cylinder subject to an axial compressive load.

A cylinder subject to an axial load F has a length of l, core radius r and shell thickness t is shown in Figure 3.1(a). When the load reaches a critical value, the shell buckles along its length as shown in Figure 3.1(b). The buckle wavelengths are sinusoidal and are axisymmetric about the circumference of the cylinder. Each wave has a wavelength of λ and a peak amplitude of A as shown in Figure 3.1(b). The metal shell and polymer core are assumed to be perfectly bonded, thus as the shell buckles the shell and core will have the same radial deformations at the interface. These radial deformations have the expression:

$$w = A \sin \frac{m\pi z}{l}, \tag{3.9}$$

where w is the radial displacement at some axial position z, and m is the number of half waves.

The general form of the Southwell model was developed for the hollow cylinder of Figure 3.2. However, the stress state of a solid polymer cylinder must be determined. A limitation of the Southwell model is that it requires stress boundary conditions. While it would be ideal to use displacement boundary conditions in the form of Equation 3.9, a stress boundary condition must be specified. Sinusoidal displacements lead to sinusoidal stress fields [24, 82], and so a sinousoidal stress field is introduced to mimic the form of the applied displacements. This stress field takes the form:

$$\sigma_{r\mathrm{B}} = \sigma_0 \cos\left(\frac{m\pi z}{l}\right), \tag{3.10}$$

where σ_0 is a given stress amplitude. When applied to a solid polymer cylinder of length l and radius r as shown in Figure 3.4, this stress field causes radial deflections in the form of Equation 3.9. An axisymmetric section of this cylinder is shown in detail, showing the stress field σ_{rB} applied to the outer edge of the domain. The stress state and strain energy of this cylinder is to be determined by using the Southwell model

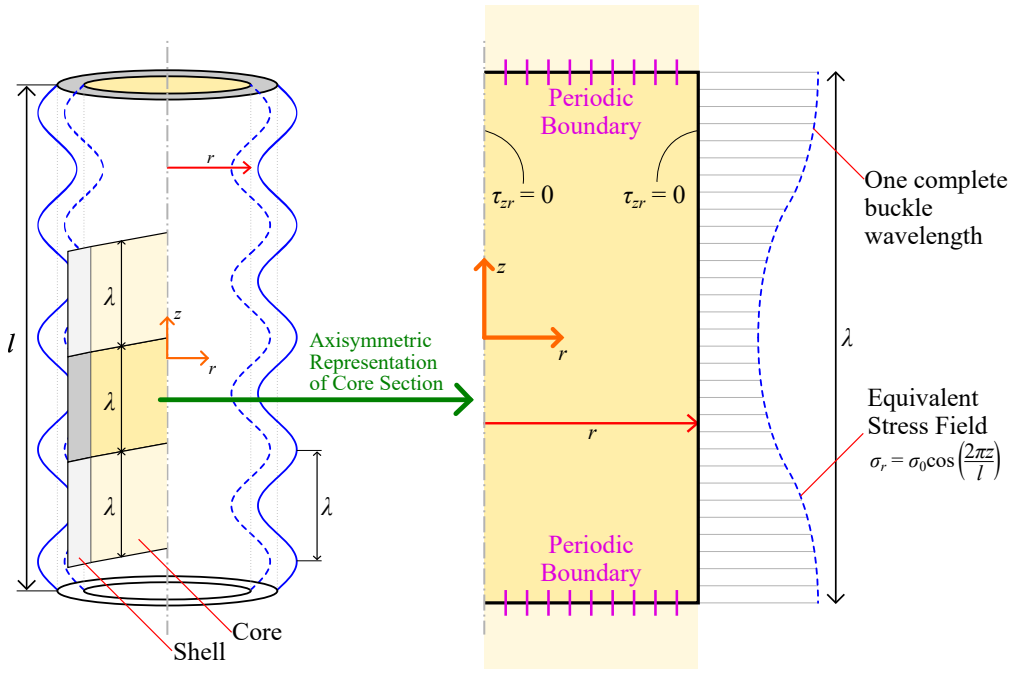

Figure 3.4: A cylinder of length l and radius r undergoing buckling deformations, where the buckle waves have length λ. An axisymmetric section of length l of the polymer core is examined, and a sinusoidal stress field is applied to this section to cause sinusoidal buckling deflections

to analyse this axisymmetric section.

As seen in the axisymmetric section of the cylinder of Figure 3.4, the length of the domain to be studied is λ, or one wavelength of the applied radial stress and the buckled shape. Periodic boundary conditions ensure that a calculation for one buckle wavelength can be used when multiple waves are present. It is assumed that during buckling there will be many waves, consistent with experiments and models of hollow shell buckling [34, 35]. For long cylinders, the end effects are also assumed to be negligible.

The Southwell model determines the stress state for one cylinder geometry and one loading condition. For the purposes of determining the axial buckling load of a metal-coated polymer cylinder, the energy state of a solid cylinder subject to sinusoidal radial stresses must be determined for any cylinder geometry. The relationship between the strain energy and the buckle wavelength λ must also be determined. To determine these relations while also maintaining the generality of the resulting model, the stress state of the geometry in Figure 3.4 must be found for various domain geometries (i.e. many values of λ/r) and several load magnitudes values σ_0. The model developed in this way will be used to calculate the strain energy of the core as a function of the buckle wavelength λ and the geometric dimensions of the cylinder.

3.3 Finite Element Verification and Mesh Convergence Studies

Prior to any further model development, a verification of the Southwell model for a cylinder subject to a radial stress field will be determined (i.e. Figure 3.4). A finite element analysis of the axisymmetric periodic

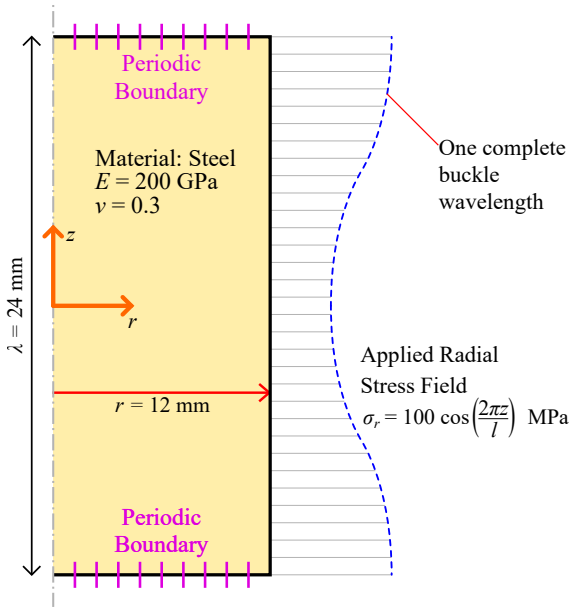

Figure 3.5: Diagram showing setup of a finite element simulation using Abaqus for an axisymmetric section of a polymer core. The axisymmetric section represents a core section of wavelength λ and a radius r of 12 mm, subject to a radial stress field σ_r. The stress field encompasses a full wavelength λ, thus matching the length of the domain. The section has periodic boundary conditions, and the material properties of the core are those of steel (E_c = 200 GPa, ν_c = 0.3)

domain will be performed and compared to results determined from the Southwell model. In addition, a mesh convergence study will be undertaken to establish the ideal mesh density for accurate results.

Verification studies were carried out using Abaqus in order to confirm the accuracy of the Southwell stress model. These studies included a comparison of the stress distributions and strain energies predicted by both the Southwell model and Abaqus. Mesh convergence studies were also undertaken in order to determine an adequate mesh density for the Southwell model to ensure accurate results.

3.3.1 Finite Element Verification of Southwell Model

Finite element verification was carried out using an axisymmetric cylinder section with a length of 24 mm and a radius of 12 mm, as shown in Figure 3.5. This chosen geometry is similar to that used by Allen and Southwell when they described the implementation of the Southwell model [6, 38, 39]. A sinusoidal radial loading with an amplitude σ_0 of 100 MPa was applied to this domain (refer to Equation 3.10), and the material properties of steel were used. Periodic boundary conditions were also used to match the loading case of Figure 3.4, and only one wavelength was modelled (i.e. λ = 24 mm)

The Southwell model was implemented in MATLAB to solve for the stresses in a cylinder represented by the axisymmetric section shown in Figure 3.4. The mesh density is set by prescribing the number of nodes in the radial direction. The node count in the axial direction is then determined by keeping the aspect ratio for the node spacing as close to 1 as possible. In Abaqus, an axisymmetric domain was generated for the same geometry and meshed with quadrilateral elements having aspect ratios of 1. The radial, circumferential, axial and shear stresses were calculated using both the Southwell model and Abaqus. The strain energies

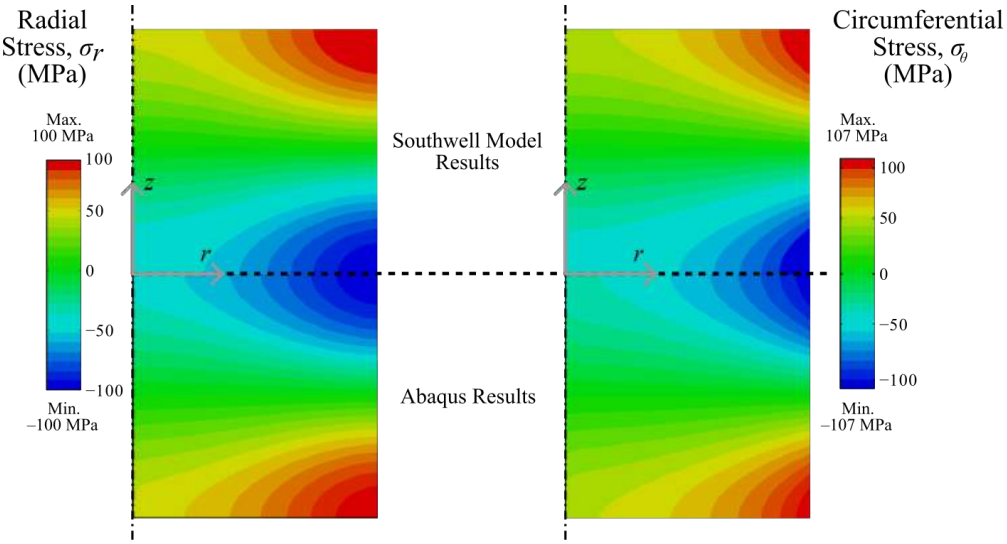

Figure 3.6: Radial and circumferential stresses as calculated for a steel cylinder using Abaqus (below) and a MATLAB implementation of a Southwell model (above) for a cylinder with dimensions of 24 mm in the z-direction and 12 mm in the r-direction. The cylinder is loaded with a sinusoidal radial stress with a magnitude $\sigma_0 = 100$ MPa.

were also determined.

Figure 3.6 shows the radial and circumferential stresses, respectively, as calculated by the axisymmetric Abaqus simulation and the MATLAB implementation of the Southwell model. About 80 000 nodes were used for the Southwell model solution, while approximately 150 000 nodes were used in Abaqus (or roughly 150 000 elements). As seen in the Figure, there is a good agreement between the stresses predicted by Abaqus and the Southwell model. Although the stress distributions are slightly different when comparing the Abaqus results and Southwell model, the total strain energies calculated for each case are very similar: the Abaqus simulation predicted 12.32 J while the Southwell Model gave 12.29 J.

Similar stress comparison studies were conducted for many cylinder geometries, loading conditions, and material properties to ensure that the results were similar for changing conditions. These results as well as those shown in Figure 3.6 confirm that the Southwell model is valid. As the intention is to determine the strain energy of a cylinder using the Southwell model, a mesh convergence study was also undertaken to determine when the strain energy becomes independent of the number of nodes.

3.3.2 Mesh Convergence Studies

A mesh convergence study was undertaken to determine the mesh density required to obtain accurate results with little mesh dependence. The same geometry and loading conditions as shown in Figure 3.6 was used (axisymmetric domain with radius of 12 mm and length of 24 mm), and the MATLAB implementation of the Southwell model was utilized. As previously done for the verification studies, the spacing between nodes was made to be as square as possible to achieve an aspect ratio of 1 (equivalently, $a = b$ as seen in Figure 3.3). The strain energy values calculated using the Southwell model were normalized against the strain energy calculated from the Abaqus verification simulation of the same geometry (i.e. 12.32 J).

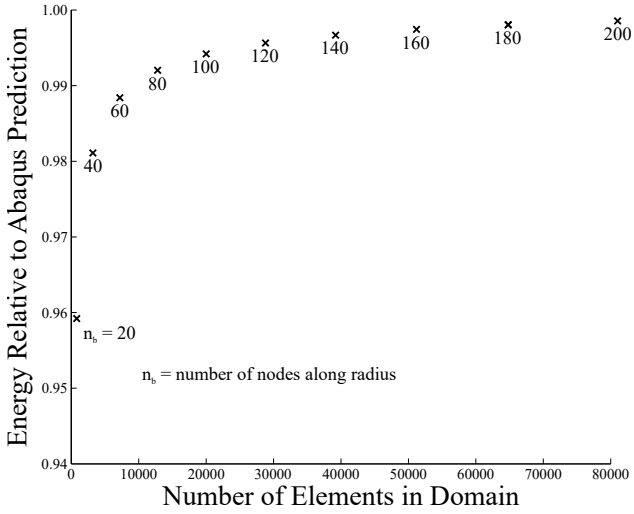

Figure 3.7: A graph showing the results of mesh convergence studies. The energy predictions relative to Abaqus energy calculation for various node counts are shown, with the number of nodes in the radial direction shown for reference.

Figure 3.7 shows calculated values of the strain energy from the Southwell model solutions as implemented in MATLAB. The values are shown for increasing mesh densities and have been normalized against the internal energy calculated from the Abaqus simulation for the case shown in Figure 3.5. The number of nodes in the radial direction is also provided for each relative energy quantity shown on this graph. It is seen that as the number of nodes approaches 30 000, there is less than 1% difference between the energies predicted by the Southwell model and Abaqus. When the number of nodes approaches 80 000 there is less than a 0.5% difference. Based on the results of this mesh refinement study, it was determined that over 150 nodes through the radius (or over 80 000 nodes in total) are required to obtain accurate results for each Southwell model execution.

The Abaqus verification studies show that the Southwell model is valid. In addition, mesh refinement studies show that over 80 000 nodes (or 150 nodes in the radial directions) are required to achieve accurate strain energy calculations from the Southwell stress model. This model will now be used to develop a strain energy prediction model for a polymer core when subject to sinusoidal radial stresses. Once developed, this will be used to predict the axial buckling load of a metal-coated polymer cylinder.

3.4 Core Model Development

The Southwell model implementation in MATLAB has been verified using finite element analysis, and mesh refinement studies have been undertaken to determine the minimum number of nodes required for accurate results. The Southwell model is now utilized to develop a model which predicts the strain energy in a polymer core subject to sinusoidal radial displacements. These radial displacements are the consequence of the shell buckling as shown in Figure 3.1(a); the assumed adhesion between the shell and core means their radial displacement distributions are identical. The Southwell model requires stress boundary conditions, and thus

the sinusoidal radial displacements are transformed into an equivalent stress field.

As the desired model is to be utilized for any core geometry and buckle wavelengths, the strain energy will be determined for various buckle wavelength values and changing core dimensions. A function is fit to the strain energy predictions to create a general core model. The resulting model must be differentiable so that it can be used to calculate the axial buckling load of a metal-coated polymer cylinder through an energy-based method.

3.4.1 Strain Energy Data Generation Using the Southwell Model

A core model is to be developed in order to determine the axial buckling load of a filled shell. The Timoshenko method [34] was previously used to determine the buckling load of a hollow shell, and it will be utilized to determine the filled-shell buckling load. As the Timoshenko method is an energy-based approach that requires the strain energy as a function of the buckling displacement magnitude A, the strain energy of the core will be modelled.

The strain energy of the core will be calculated for the polymer core geometry and loading conditions as shown in Figure 3.4. The radial stress magnitude σ_0 and buckle wavelength-to-radius ratio λ/r will each be varied, and the energy recalculated for new values of these variables. Values of λ/r between 0 and 10 are used, while the radial stress magnitudes σ_0 is varied between 50 MPa to 400 MPa. For the radial stress loading, one complete wavelength is used as shown in Figure 3.4 (i.e. $m = 2$ in Equation 3.10). In varying λ/r and σ_0, the objective is to obtain strain energy information for the polymer core such that a general model can be developed for any core geometry and stress magnitude.

The calculated values of the strain energy U are divided by the cylindrical volume represented by the axisymmetric section in Figure 3.4. The resulting values of $U/(\pi r^2 \lambda)$ plotted as a function of λ/r is shown in Figure 3.8. Since a stress boundary condition is required for the Southwell model (refer to Figure 3.2), a relationship must be determined between the displacement amplitude A and the stress magnitude σ_0. A graph of the normalized displacement magnitude A/r is plotted as a function of λ/r in Figure 3.9. The energy and displacement amplitude values were calculated using the material properties of VisiJet Crystal ($E_c = 1.5$ GPa, $\nu_c = 0.35$) [122].

In the graphs shown in Figures 3.8 and 3.9, there are two distinct regions: one of linearly increasing energy density at lower λ/r values, and an asymptotic value of energy density at higher λ/r values. As indicated on the Figures, the end of the linear behaviour occurs at a transition point of $(\lambda/r)_{\text{tr}} = 2.5$, beyond which there is a brief transition region followed by the asymptotic region. The same behaviour and transition point is seen for all load magnitudes (σ_0), while further investigations revealed that the transition value of $(\lambda/r)_{tr} = 2.5$ is unaffected by material properties. Because elastic local shell buckling leads to buckle waves which have small wavelength-to-radius ratios [5, 78], the trends that hold in the linear region of $0 < \lambda/r < 2.5$ are of interest (specifically when $\lambda/r \ll 2.5$). The core model will be developed using the strain energy data in this linear region. However, a more useful method of representing the data must be

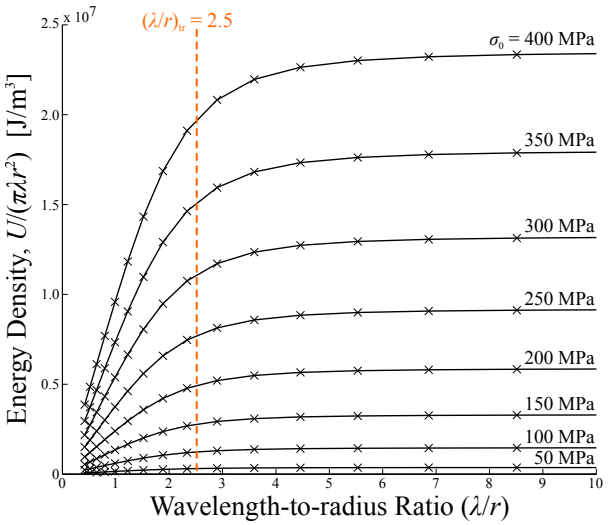

Figure 3.8: Calculated energy density values as a function of dimensionless wavelengths for increasing load magnitudes. Data is valid for a VisiJet Crystal cylinder, and all values were found using the Southwell model.

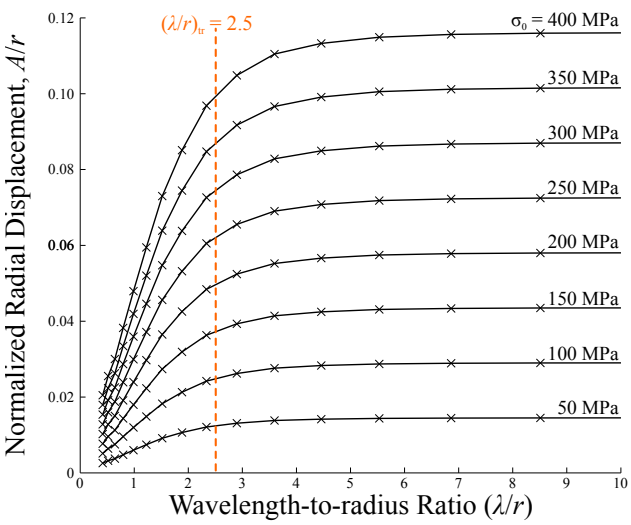

Figure 3.9: Calculated dimensionless radial displacement magnitudes as a function of dimensionless wavelengths for increasing load magnitudes. Data is valid for a VisiJet Crystal cylinder, and all values were found using the Southwell model.

developed first.

In order to determine the relations needed, the strain energy and displacement magnitude information contained in Figures 3.8 and 3.9 is plotted as a function of the stress amplitude σ_0. Figures 3.10 and 3.11 show the values of $U/(\pi r^2 \lambda)$ and A/r, respectively, as a function of σ_0. As λ/r is increased beyond 2.5, the energy density values in Figures 3.10 and 3.11 no longer increase, leading to lines which lie on top of each other in the graphs. These overlapping lines correspond to the asymptotic regions in Figures 3.8 and 3.9, where further increases in λ/r beyond 2.5 lead to asymptotic increases in $U/(\pi r^2 \lambda)$ and A/r. As the core model is to be developed for the behaviour when $\lambda/r < 2.5$, these asymptotic regions (or similar energy density values in Figures 3.10 and 3.11) will not be considered. The behaviour observed in Figures 3.10 and 3.11 will be used in developing the relations for the model.

3.4.2 Trend Analysis and Core Model Development

A model is desired that predicts the strain energy in the core U as a function of the buckle wavelength λ, the displacement magnitude A and the radius r. Relations are to be determined from trends in the calculated strain energies, which are shown graphically in Figures 3.8 through 3.11. The core model must be an analytical function and must also be a differentiable function of the displacement magnitude A, so that the change in strain energy as a function of the displacement amplitude can be found. This will allow the use of the Timoshenko energy method [34] to determine the buckling load of an axially-loaded metal-coated polymer cylinder.

The Southwell model was used to determine the strain energy in a polymer core subject to sinusoidal radial displacements by transforming these into equivalent stress fields. However, the core model must provide the strain energy in the core U as a function of the displacement magnitude A. Thus, a relationship

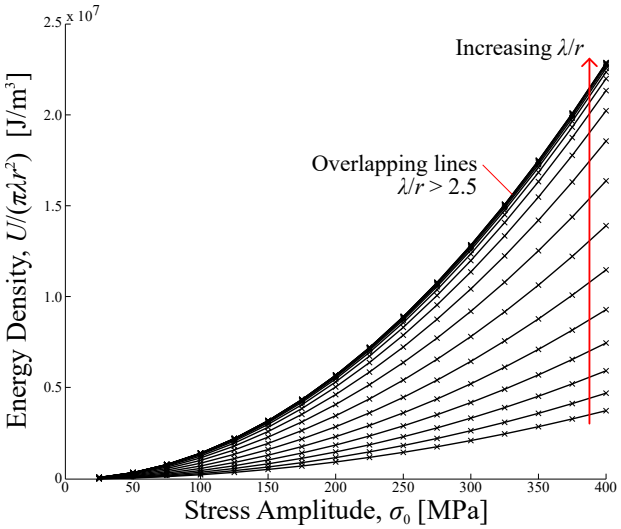

Figure 3.10: Calculated energy density values as a function of load magnitude for increasing dimensionless wavelengths. Data is valid for a VisiJet Crystal cylinder, and all values were found using the Southwell model.

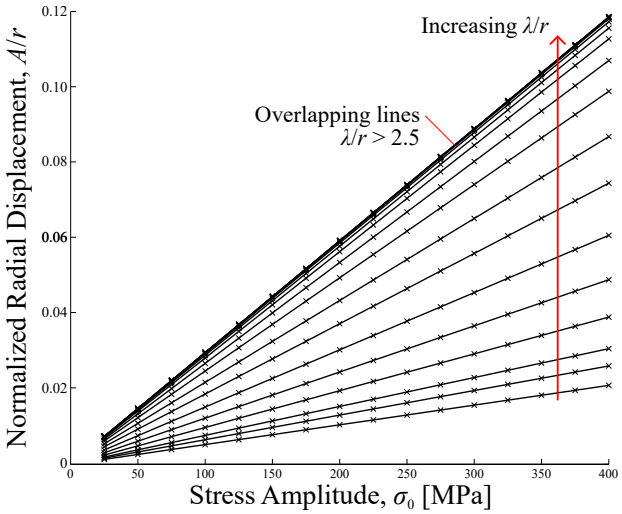

Figure 3.11: Calculated dimensionless radial displacement magnitude as a function of load magnitudes for increasing dimensionless wavelengths. Data is valid for a VisiJet Crystal cylinder, and all values were found using the Southwell model.

between U and A is required that is not a function of the load magnitude σ_0. Figures 3.10 and 3.11 show plots of the energy density $U/(\pi r^2\lambda)$ and the maximum normalized radial displacement A/r, respectively, plotted against the load magnitudes values σ_0. Through inspection it is seen that a quadratic relationship exists between $U/(\pi r^2\lambda)$ and σ_0, while there is a linear relationship between A/r and σ_0. Looking only at the behaviour when $\lambda/r < 2.5$, a general quadratic expression relating $U/(\pi r^2\lambda)$ and σ_0 is:

$$\frac{U}{\pi\lambda r^2} = K_2\sigma_0, \tag{3.11}$$

where K_2 is the quadratic fit constant. Similarly, the linear relationship between the A/r and σ_0 can be expressed as:

$$\frac{A}{r} = K_1\sigma_0, \tag{3.12}$$

where K_1 is the linear fit constant. When λ/r is much lower than the transition value 2.5, the constants K_1 and K_2 are linearly related to λ/r through:

$$K_2 = K_3\frac{\lambda}{r} \quad \text{and} \quad K_1 = K_4\frac{\lambda}{r}, \tag{3.13}$$

where K_3 and K_4 are the parameters which relate the quadratic and linear fit co-efficients, respectively, to λ/r.

The values of $U/(\pi r^2\lambda)$ and A/r have been calculated for one complete buckle wavelength, or when $m = 2$ in Equations 3.9 and 3.10. Thus the expressions contains in Equations 3.11 through 3.13 are valid for one complete buckle wavelength, or the loading condition shown for the axisymmetric cylinder section in Figure 3.4. Using Equations 3.11 through 3.13, the expression for the energy of one complete wavelength in

a solid cylinder (or core) under an axisymmetric radial stress as seen in Figure 3.4 is found to be:

$$U = \frac{K_3}{K_4^2} A^2 \pi r = K A^2 \pi r, \tag{3.14}$$

where U is the internal energy, A is the radial displacement magnitude of buckling, and $K = K_3/K_4^2$ is the model fit coefficient. In this equation, the stress magnitude σ_0 has been eliminated, and the core model is only a function of K, A and r. The value of K is valid for one set of core material properties, and must be recalculated when the core material changes.

It is of interest to note that the core energy is not a function of the buckle wavelength λ, though varying values of λ/r were used in calculating strain energy magnitudes using the Southwell model. This indicates that for a elastic core undergoing sinusoidal buckling radial deformations, the resulting energy in the core is not a function of the buckle wavelength.

Because Equation 3.14 is the expression for the energy of one wavelength, it must be corrected to account for multiple waves. Since m is the number of half-waves, the total energy of a cylinder under m half waves is found to be:

$$U_c = \frac{m}{2} K A^2 \pi r, \tag{3.15}$$

where U_c is the internal energy of the core. This expression holds while λ/r is much lower than 2.5, which is the case for elastic buckling of filled shells with an elastic core. This core energy expression is required for a complete buckling analysis of a filled-shell system when using an energy-based method, similar to the method used by Timoshenko [34] in developing hollow-shell buckling theory. While the material properties of VisiJet crystal were used to obtain the data as shown in Figures 3.8 through 3.11, the relations shown in Equations 3.11 through 3.13 are valid regardless of material chosen.

As seen in the form of Equation 3.15, the strain energy of the core is not a function of the buckle wavelength λ. Further analysis using the Southwell model MATLAB code, as well as finite element analyses, revealed that for small wavelengths the value of U is indeed insensitive to λ. This implies that, if the values of λ and r are chosen such that $\lambda/r < 2.5$, only one calculation using the Southwell model is needed for a given core material. In this way, the value of K is found by rearranging Equation 3.15:

$$K = \frac{2U}{m A^2 \pi r}. \tag{3.16}$$

The material properties of VisiJet crystal were used to determine the strain energy and radial displacement amplitudes. Using the calculation shown in Equation 3.16 leads to the same value of K as found if using the methods outlined in Section 3.4.2. This single-calculation method provides a quicker method of calculating the model constant K for the core energy model, enabling expedient calculation of the constant as the core material is changed.

3.5 Conclusions

An energy-based method is to be used in determining the axial buckling load of a metal-coated polymer cylinder. The behaviour of the metal shell is governed by hollow-shell buckling theory, but the behaviour of the polymer core requires a differentiable analytical model. When a filled cylindrical shell undergoes buckling deformations, the shell buckles in a sinusoidal pattern. As it is assumed that the metal shell and the polymer core are perfectly adhered, their displacements are coupled. Thus it was of interest to develop an energy model of the core as it is subject to sinusoidal radial displacements. In this chapter, a new core model has been developed which accurately accounts for the stresses in the polymer core of a metal-coated polymer cylinder as the cylinder undergoes sinusoidal buckling deformations. This model will be used to represent the core behaviour of a filled-shell system for buckling analysis.

An implementation of the Southwell stress model was utilized in order to develop this new core model. This stress model calculates the triaxial stress components, unlike the Gough at al. model used by Karam and Gibson which only calculates the stresses in two coordinate directions. The Southwell model cannot be solved through analytical means; hence, a finite difference method was implemented using MATLAB. The core model was derived from functions fitted to Southwell model strain energy calculations, such that the energy of a solid cylinder under axisymmetric sinusoidal radial displacements can be found for any cylinder geometry and buckle wavelength. Each core model constant is valid only for one core material.

The resulting core model is a true axisymmetric representation of the core behaviour. When implemented, this core model is expected to provide more accurate load predictions than previous models for filled-shell buckling. In addition, the versatility of the Southwell model allows for more complicated core geometries such as hollow cores, or lack of adhesion between the shell and the core. Furthermore, the buckling model utilizing the present core model enables the optimization of cylinder geometries for mass minimization purposes.

Chapter 4

Local Buckling of an Elastic Shell Filled with a Solid Elastic Cylinder

4.1 Introduction

Metal-coated polymer microtrusses are a low-weight alternative to all-metal structures, offering the high-strength benefits of nanocrystalline metal and the low weight of polymer materials. A thorough understanding of their behaviour is required prior to using these hybrid structures in practical applications. Because three-point bend tests on hybrid microtruss structures have shown that their failure mechanisms are dominated by compressive instabilities [1, 4], the failure modes of local shell buckling and global buckling are being investigated. Due to the cylindrical shape of the microtruss struts, the focus will be on understanding the compressive failure modes of metal-coated polymer cylinders in axial compression.

Earlier investigations into the failure mechanisms of metal-coated polymer microtrusses assumed that the polymer material acted purely as parasitic mass [1, 4]. These past studies did not accurately account for the polymer core when it is subject to sinusoidal radial displacements, the observed shape when local shell buckling of the metal shell takes place [5, 66, 78, 109]. Theoretical and experimental investigations of foam-filled tubes, where the core material was accurately accounted for, have shown that the foam core hinders the onset of buckling and provides increased axial strength [69, 98, 103, 107]. These models make use of well-tested hollow-shell concepts in describing the behaviour of the shell [34, 35, 74]

There are, however, no models which are intended specifically for tubes with solid polymer cores instead of foamed cores. While some of the existing models may be adequate, they utilize foundation models intended for composite sandwich panels [24, 82], and are thus not true axisymmetric representations of the core behaviour. Given the shortcomings of presently existing models, there is a necessity for an improved model that is relevant to metal-coated polymer microtruss structures – or more specifically, their struts – which accurately describing the behaviour of both the metal shell and polymer core.

The Southwell model characterizes the stress distributions in a cylinder subject to axiysmmetric stresses [6, 38, 39]. In the preceding chapter, the Southwell model was used to develop a simple method to predict the internal energy of a polymer cylinder subject to sinusoidal radial stresses. The intention was to represent the core of a polymer-filled metal shell as the shell undergoes sinusoidal buckling displacements.

In this chapter, predictions of the buckling load for a metal-coated polymer cylinder will be derived utilizing this core model. Additionally, finite element analysis will be undertaken to verify this model and to

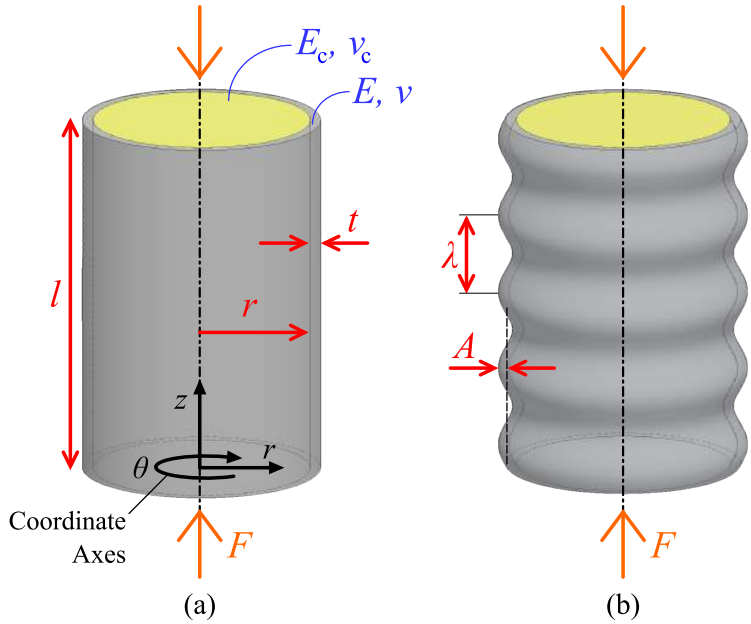

Figure 4.1: A filled shell when undeformed (left) and buckled (right). The filled shell is under an axial load F with length l, shell thickness t and inner radius r. The shell has material properties E and ν while those of the core are E_c and ν_c. When buckled, the buckle waves have wavelength λ and amplitude A.

determine whether the stresses in the core during buckling match those predicted by the Southwell model. Although there are some differences in the stresses predicted by the Southwell model, the buckling loads are nevertheless accurately predicted and the model performs better than the best-available foam-core model.

4.2 Axial Buckling Load for Metal-coated Polymer Cylinder

A metal-coated polymer cylinder subject to an axial load F is shown in Figure 4.1(a). The shell has a Young's modulus E and Poisson's ratio ν, while the corresponding properties of the core material are E_c and ν_c, respectively. The cylinder has a length of l and a shell thickness of t, while both the shell inner radius and core outer radius are designated as r. At some critical load, the shell buckles with buckle wavelengths λ and wave amplitude A as shown in Figure 4.1(b). An energy analysis considering the separate energy contributions of the shell and core will be used to determine this critical load. The assumptions used while determining the buckling load are as follows:

- the shell and core are perfectly bonded;
- both the shell and core materials behave elastically;
- the buckling displacements are sinusoidal;
- there are many waves that form when the shell buckles;
- the core conforms to the buckled shape of the shell; and
- the thickness of the shell is small compared to the radius (i.e. $t/r \leq 0.1$).

While undergoing buckling deformations as shown in Figure 4.1(a), the strain energy is accumulated due

to the bending and circumferential stretching of the shell. The shell bending energy is the energy associated with bending of longitudinal sections of the shell as they undergo sinusoidal buckling deformations, while the stretching energy results from the stretching or compressing of the shell circumferential sections as they expand or contract to accommodate the bending. The energy contained in the core is due to the radial displacements caused by the buckling of the shell. These buckling displacements are transferred from the shell to the core due to their adhesion, and have the sinusoidal shape [34, 35, 97, 98]:

$$w = A \sin \frac{m\pi z}{l}, \tag{4.1}$$

where A is the amplitude of the radial deflections, m is the number of buckle half waves along the length l of the shell, and z is the axial coordinate as seen in Figures 4.1(a) and (b). Equation 4.1 is the same assumed displacement used in the derivation of the core energy term of Chapter 3. The shell bending energy U_b is [34, 37]:

$$U_\mathrm{b} = \int_0^l \frac{D^*\kappa}{2} \mathrm{d}x = \frac{\pi E r t^3}{12(1-\nu^2)} \frac{m^4\pi^4}{l^4} \frac{A^2 l}{2} \tag{4.2}$$

where:

$$\kappa = w'' = \frac{\mathrm{d}^2 w}{\mathrm{d}x^2} = \frac{A^2 m^4 \pi^4}{l^2} \sin^2\left(\frac{m\pi x}{l}\right) \quad \text{and} \quad D^* = 2\pi r \frac{Et^3}{12(1-\nu^2)}.$$

κ is the curvature of the shell surface undergoing buckling deformations, while D^* is the flexural stiffness of a curved plate [34, 123]. The circumferential stretching energy U_c is [34]:

$$U_\mathrm{c} = \int_0^{2\pi} \int_r^{r+t} \int_0^l \int_0^{\varepsilon_\mathrm{rc}} \sigma_\mathrm{rc} r \mathrm{d}\varepsilon \mathrm{d}z \mathrm{d}r \mathrm{d}\theta = \frac{\pi E t A^2 l}{2r^2}, \tag{4.3}$$

where the stress field σ_rc results from the radial strains (ε_rc) caused by buckling deformations:

$$\sigma_\mathrm{rc} = E\varepsilon_\mathrm{rc} = E\frac{1}{r} A \sin\left(\frac{m\pi z}{l}\right).$$

Finally, the core energy as determined in Chapter 3 is:

$$U_\mathrm{p} = \frac{m}{2} K A^2 \pi r. \tag{4.4}$$

During buckling, the total internal energy (U_i) of a cylindrical shell with a polymer core is the sum of the shell bending energy (Equation 4.2), the shell circumferential stretching energy (Equation 4.3), and the core energy (Equation 4.4). The external energy (U_e) is due to the applied axial force F as indicated in Figure 4.1. These two energy terms, respectively, are:

$$U_\mathrm{i} = U_\mathrm{b} + U_\mathrm{c} + U_\mathrm{p} = \frac{\pi E r t^3}{12(1-\nu^2)} \frac{m^4\pi^4}{l^4} \frac{A^2 l}{2} + \frac{\pi E t A^2 l}{2r} + \frac{m}{2} K A^2 \pi r \tag{4.5}$$

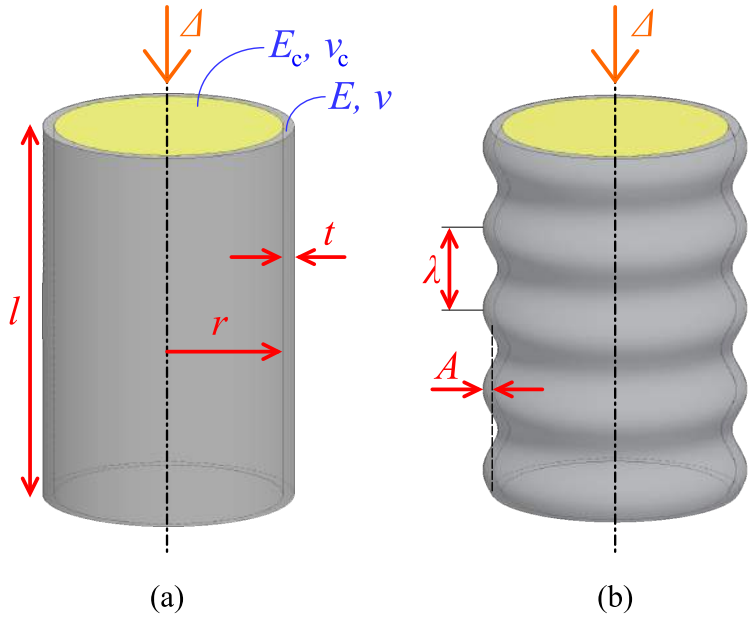

Figure 4.2: (a) A filled cylinder with length l, radius r and shell thickness t under an axial displacement Δ. The shell has material properties E and ν while the core properties are E_c and ν_c. (b) The buckled shape of the shell at a critical value of Δ. The buckle waves have wavelength λ and amplitude A.

and

$$U_e = \frac{Fm^2\pi^2A^2}{4l}. \tag{4.6}$$

4.2.1 Bifurcation Point and Buckling Load Derivation

A shell subject to an axial displacement Δ is shown in Figure 4.2(a). Conservation of energy stipulates that the internal energy of the shell (sum of U_b and U_c) is always equal to the external energy (U_e) for any displacement Δ. At a critical Δ, the increment in energy required to cause buckling of the cylinder is equal to the energy increment required for continued axial compression without buckling:

$$\frac{\partial U_i}{\partial \Delta} = \frac{\partial U_{ic}}{\partial \Delta} = \frac{\partial U_e}{\partial \Delta}, \tag{4.7}$$

where U_i is the internal energy of the filled cylinder as it undergoes buckling and U_{ic} is the internal energy under continued axial compression. Equation 4.7 identifies the bifurcation point of a cylindrical shell under an axial displacement. Any further increase in the applied axial displacement Δ (or equivalently the axial load F) will either lead to an increase in load without buckling (i.e. undeformed geometry of Figure 4.2(a)) or the appearance of buckle waves (Figure 4.2(b)). For ideal cylinders buckling will not take place, however imperfections will always cause a thin-shelled cylinder to buckle rather than continue to compress [73, 78, 124].

After the formation of buckling wrinkles, the axial displacement Δ and the radial displacement amplitude A are related geometrically through:

$$\Delta = \frac{A^2m^2\pi^2}{4l}. \tag{4.8}$$

Using this relation, a part of Equation 4.7 can now be rewritten as a function of A instead of Δ:

$$\frac{\partial U_{\mathrm{e}}}{\partial A} = \frac{\partial U_{\mathrm{i}}}{\partial A}. \tag{4.9}$$

This enables the use of the energy expressions (Equations 4.2 through 4.6). Using Equations 4.5 (U_{i}) and 4.6 (U_{e}) and applying the operation in Equation 4.9, the elastic buckling load of a metal-coated polymer cylinder in axial compression is found to be

$$F = \frac{2\pi^3 r E t^3}{3(1-\nu^2)}\frac{1}{\lambda^2} + \frac{Et}{2r\pi}\lambda^2 + \frac{Kr}{\pi}\lambda \tag{4.10}$$

where $\lambda = 2l/m$ is the buckling wavelength, as shown in Figure 4.2(b). The total load for a cylindrical shell under an axial load includes the loads carried by the core and that of the shell. Equation 4.10 only describes the buckling load in the metal shell, without accounting for the load borne by the polymer core. Applying a factor to account for the relative stiffness and geometry of the shell and the core, the buckling equation for a metal-coated polymer cylinder is:

$$F = \left(1 + \frac{E_{\mathrm{c}}}{E}\frac{r}{2t}\right)\left[\frac{2\pi^3 r E t^3}{3(1-\nu^2)}\frac{1}{\lambda^2} + \frac{Et}{2r\pi}\lambda^2 + \frac{Kr}{\pi}\lambda\right]. \tag{4.11}$$

Equation 4.11 applies for any value of λ. However, for a cylinder with known geometry and material properties, there is only one value of λ that is physically permissible, and its value leads to the buckling load. The critical λ value is found by minimizing the value of F, which entails finding the positive real root of the 4th-order polynomial expression $\partial F/\partial\lambda = 0$ as given by:

$$\frac{Et}{r\pi}\lambda^4 + \frac{Kr}{\pi}\lambda^3 - \frac{4\pi^3 r E t^3}{3(1-\nu^2)} = 0. \tag{4.12}$$

Once found, the critical value of λ is substituted into Equation 4.11 to give the critical load.

4.2.2 Recovery of the Hollow-Shell Buckling Equation

The hollow-shell local shell buckling equation (refer to Equation 2.2 of Chapter 2) can be recovered from Equation 4.11 when the core constant K is zero (i.e. when the core is removed). First, K is eliminated to give:

$$F_{\mathrm{HS}} = \frac{2\pi^3 r E t^3}{3(1-\nu^2)}\frac{1}{\lambda_{\mathrm{HS}}^2} + \frac{Et}{2r\pi}\lambda_{\mathrm{HS}}^2. \tag{4.13}$$

The solution for λ is found from the equation $\partial F/\partial\lambda = 0$ as:

$$\lambda_{\mathrm{HS}} = \left(\frac{12(1-\nu^2)}{r^2 t^2}\right)^{1/4}, \tag{4.14}$$

which, when substituted into 4.13 gives

$$F_{\mathrm{HS}} = \frac{2\pi E t^2}{\sqrt{3(1-\nu^2)}}. \tag{4.15}$$

This equation is most familiarly written as a stress:

$$\sigma_{\mathrm{HS}} = \frac{Et}{r\sqrt{3(1-\nu^2)}}. \tag{4.16}$$

Equation 4.16 is the classical hollow-shell local shell buckling equation [34, 35, 37, 39, 75]. Its isolation from Equation 4.11 demonstrates that the filled-shell buckling model is fundamentally sound.

4.3 Predicted Behaviour of Axially Compressed Filled Shells

In order to compare the hollow-shell (Equation 4.15) and the filled-shell models (Equation 4.11), their predictions are compared graphically. The Karam and Gibson filled-shell buckling model [98] will also be used for reference.

Another model used for comparison purposes is the plane stress buckling model. Timoshenko and Goodier [123] determined that for a solid polymer cylinder loaded axisymmetrically, constant and equal radial and circumferential stresses are present at every cross section of the cylinder. Since this is a plane stress condition, the corresponding model is referred to as the plane stress model. The plane stress condition is a minimum value for the critical buckling load of a filled shell, when full adhesion between the shell and core is assumed.

Prior to calculating values for the model constant K, values of E_{c} were determined by choosing ratios of the core-to-shell Young's modulus E_{c}/E and by using a the Young's Modulus of a known shell material. The shell was assumed to be nanocrystalline nickel manufactured by RePliForm [7]; this is a common metal produced through electrodeposition [28]. The ratios of the Young's moduli were chosen to represent ABS (i.e. $E_{\mathrm{c}}/E = 0.01$) and LDPE ($E_{\mathrm{c}}/E = 0.001$). The values of the shell and core Poisson ratios used for calculations were 0.3 and 0.35 respectively. Using these material properties, $K = 0.0199$ when $E_{\mathrm{c}}/E = 0.01$, and $K = 0.00199$ when $E_{\mathrm{c}}/E = 0.001$. These values of K were used to determine load predictions using the new filled-shell buckling model.

Figure 4.3(a) is a plot of the critical buckling load (Equation 4.11) for $E_{\mathrm{c}}/E = 0.01$, while that for $E_{\mathrm{c}}/E = 0.001$ is in Figure 4.3(b). Included in both of these figures are the loads predicted by the Karam and Gibson model [98], the plane stress model and the hollow-shell model (Equation 4.15). As seen in Figures 4.3(a) and 4.3(b), the new elastic model predicts slightly higher critical loads than the Karam and Gibson model. Both predict failure loads much larger than those predicted by the plane stress model, a lower bound for filled-shell buckling. When the shell thickness-to-radius ratio of the shell is very high (i.e. very close to 0.1 in both graphs), the buckling load is dominated by the shell behaviour. At these high values of shell thickness, the hollow-shell and all three of the filled-shell models predict nearly equal loads because they can

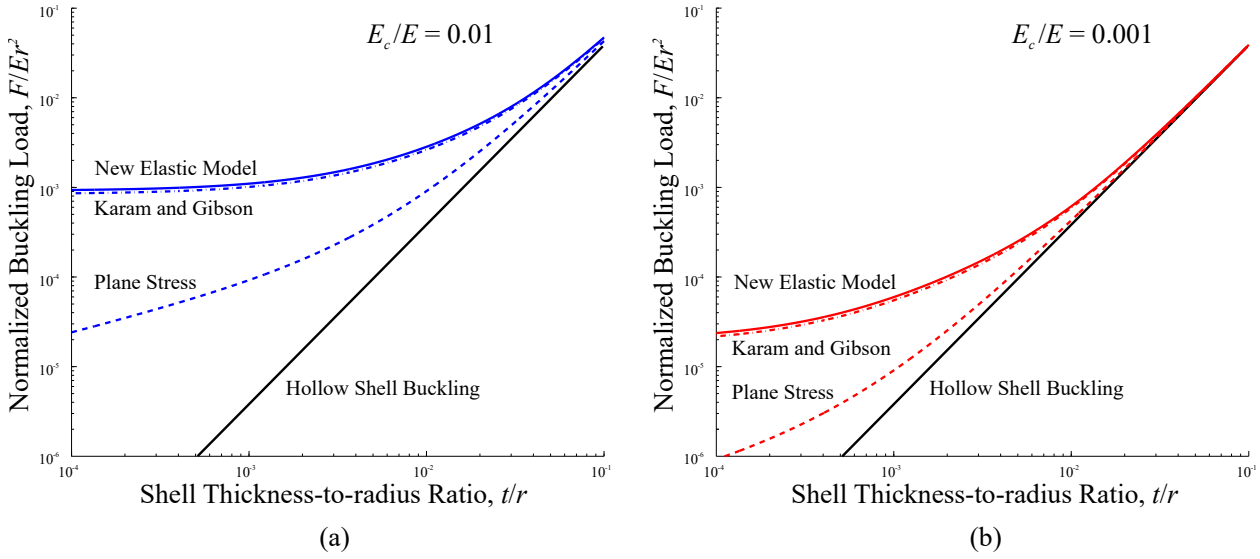

Figure 4.3: Predictions of the buckling load found for the new elastic model, Karam and Gibson model and the hollow-shell model plotted against increasing shell thickness-to-radius ratios for (a)$E_c/E = 0.01$ and (b)$E_c/E = 0.001$

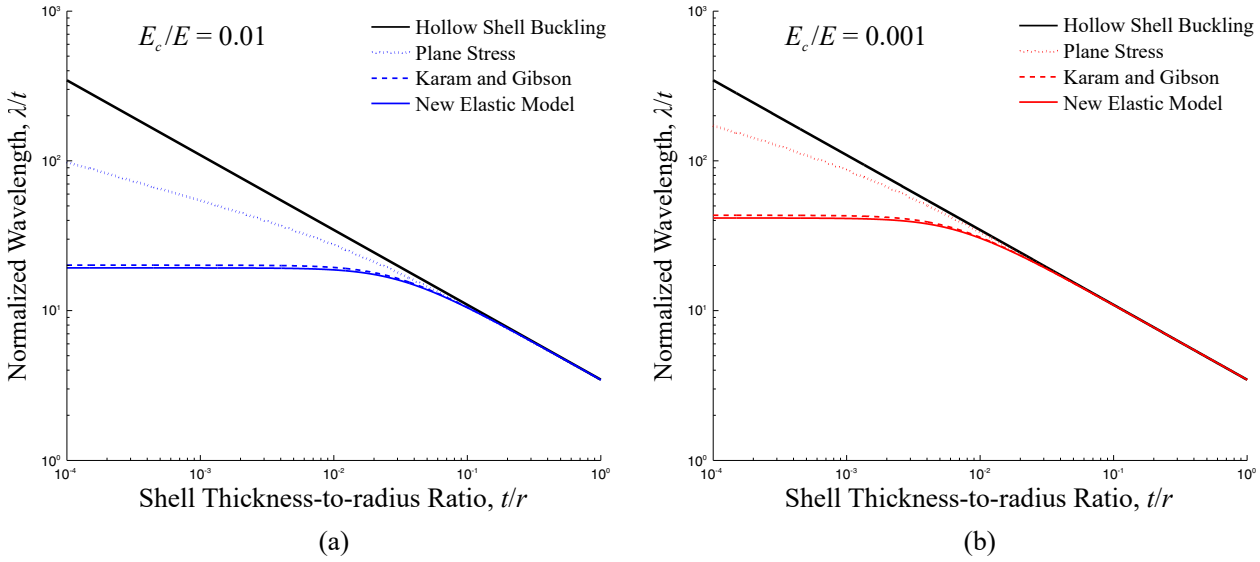

Figure 4.4: Predictions of critical wavelength for the new elastic model, Karam and Gibson model and the hollow-shell model plotted against increasing shell thickness-to-radius ratios for (a)$E_c/E = 0.01$ and (b)$E_c/E = 0.001$

all be reduced to the Timoshenko expression (Equation 4.15) for local shell buckling.

Figures 4.4(a) and 4.4(b) show the critical ratio of buckling wavelength to shell thickness (λ/t) as a function of the ratio of shell thickness-to-radius (t/r), for the high ($E_c/ = 0.01$) and low ($E_c/ = 0.001$) values of the relative core stiffness, respectively. The predictions for the new elastic model, the plane stress model, the Karam and Gibson model and the hollow-shell model are plotted in these figures. The normalized wavelength-to-thickness ratio shown in these graphs, λ/t, is the critical wavelength needed to cause buckling. Its value is essential to determining the buckling load of a cylinder.

For the new elastic model, the predicted wavelengths (λ/t) are unaffected at lower values of shell

thickness-to-radius. This behaviour is mirrored in the Karam and Gibson model. However λ/t decreases quickly and eventually approaches the normalized wavelength value of hollow-shell buckling, which is when the filled-shell and hollow-shell load predictions become equal. As seen for the predicted loads in Figures 4.3(a) and 4.3(b), the effect of the core is insignificant at higher t/r values.

The values of the predicted wavelengths are noticeably higher for the plane stress model when compared to the Karam and Gibson and new elastic models; conversely the plane stress model predicts lower loads. From this observation, as well as from the behaviours of λ/t for the new model and the Karam and Gibson model, it can be deduced that higher loads correspond to smaller buckle wavelengths for both filled and hollow shells.

The higher predicted loads of the new model are in accordance with the increased energy that this model predicts. The circumferential stress component (refer to Equation 3.5 in Chapter 3) is not calculated for the Karam and Gibson model, as the Gough model they utilize for the core behaviour only accounts for the axial, circumferential and shear stress components. Though the energy contribution of the circumferential stress is small compared to these components, its exclusion in the Karam and Gibson model contributes to lower predictions of buckling load.

4.4 Finite Element Verification of the New Elastic Model

A verification of the buckling loads was conducted using linear buckling analysis in Abaqus; this is also referred to as modal analysis. This analysis was used to verify the loads predicted by the new model as shown in Figures 4.3(a) and 4.3(b) as well as the predicted wavelengths of Figures 4.4(a) and 4.4(b). However, in order to verify the stresses predicted by the Southwell model, post-buckling analysis was used.

4.4.1 Buckling Load Verification through Modal Analysis

Buckling analysis was undertaken using the eigenvalue buckling solver in Abaqus in order to validate the buckling loads predicted by the new model. The general eigenvalue buckling problem is used to find the buckling loads of a structure by determining when its stiffness matrix becomes singular provided given applied displacements or loads [83]. The solutions of the eigenvalue buckling problem provide the bucking loads and the buckled shapes of the structure. Due the large number of degrees of freedom in a finite element problem, the eigenvalue buckling solutions must be determined through an iterative process that would otherwise be computationally expensive to calculate directly [83].

As the eigenvalue buckling problem requires a load or applied displacement, a perturbation was applied in the form of an axial displacement δl at one end of the cylinder as seen in Figure 4.5, while the opposite end of the cylinder was fixed axially. Both ends of the cylinder were permitted to displace radially. A range of ratios of the length to the radius of the cylinder were selected, and these were generated using the criteria given in Table 4.1.

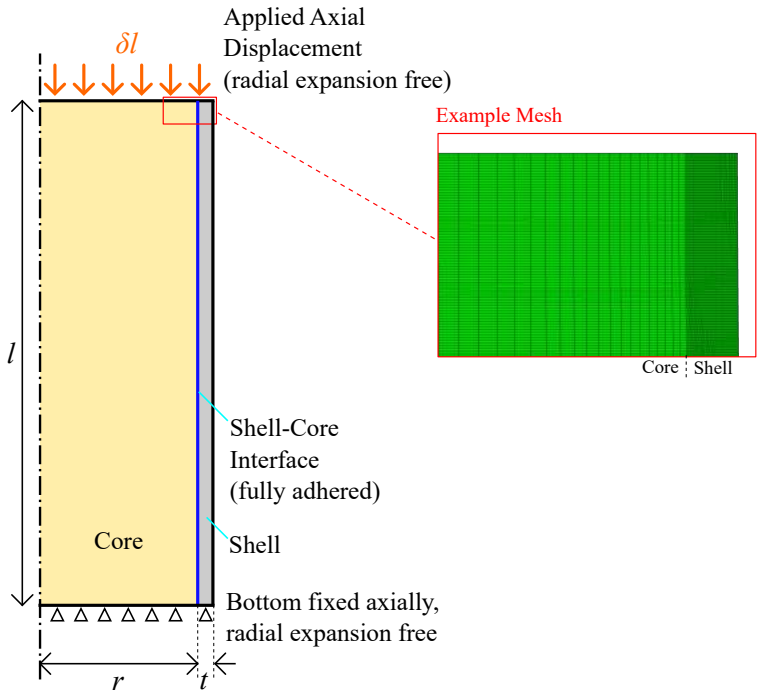

Figure 4.5: Diagram showing the configuration of a finite element simulation using Abaqus for an axisymmetric section of a filled shell with length l, radius r mm and shell thickness t. The section is loaded with an applied axial displacement δl. An example mesh is also shown, with decreasing mesh density towards the cylinder centreline.

Table 4.1: List of criteria for the cylinder geometries chosen for verification simulations of fundamental model using Abaqus.

Quantity	Chosen values
Thickness-to-radius ratios (t/r)	0.005, 0.0075, 0.01, 0.025, 0.05 and 0.1
Length-to-radius ratios*(l/r)	Between 5 and 35, in increments of 5
Relative core stiffness ratio (E_c/E)	0.01 and 0.001

* Length of cylinder fixed at 50 mm

The Lanczos algorithm [83] was used to solve for the eigenvalues and corresponding eigenvectors for the element stiffness matrix of the discretized axisymmetric domain (see Figure 4.5). The eigenvalues found from the Abaqus results are compared to the predicted loads and wavelengths shown in Figures 4.3 and 4.4, respectively. As an axial displacement was the applied perturbation for the modal analysis, the resulting eigenvalue provided the displacement at which the shell buckled. Using models of elasticity and the geometry of the cylinder, the buckling force can then be determined:

$$F_\mathrm{b} = \pi((r+t)^2 - r^2)E\frac{\delta l_\mathrm{b}}{l} + \pi r^2 E_\mathrm{c}\frac{\delta l_\mathrm{b}}{l}, \tag{4.17}$$

where δl_b is the eigenvalue solution from the Abaqus analysis and F_b is the resulting buckling load.

The geometries were meshed in such a way to ensure that there were at least 5 elements through the thicknesses of the coatings as seen in Figure 4.5. The first eigenvalue calculated by the solver was taken to indicate buckling. In order to verify that the eigenvalues were insensitive to cylinder length, the modal analyses were completed for ratios of length-to-radius (l/r) ranging between 5 and 35. The ratios of thickness-to-radius (t/r) studied for the modal analysis ranged between 0.005 and 0.1. Ratios of t/r below

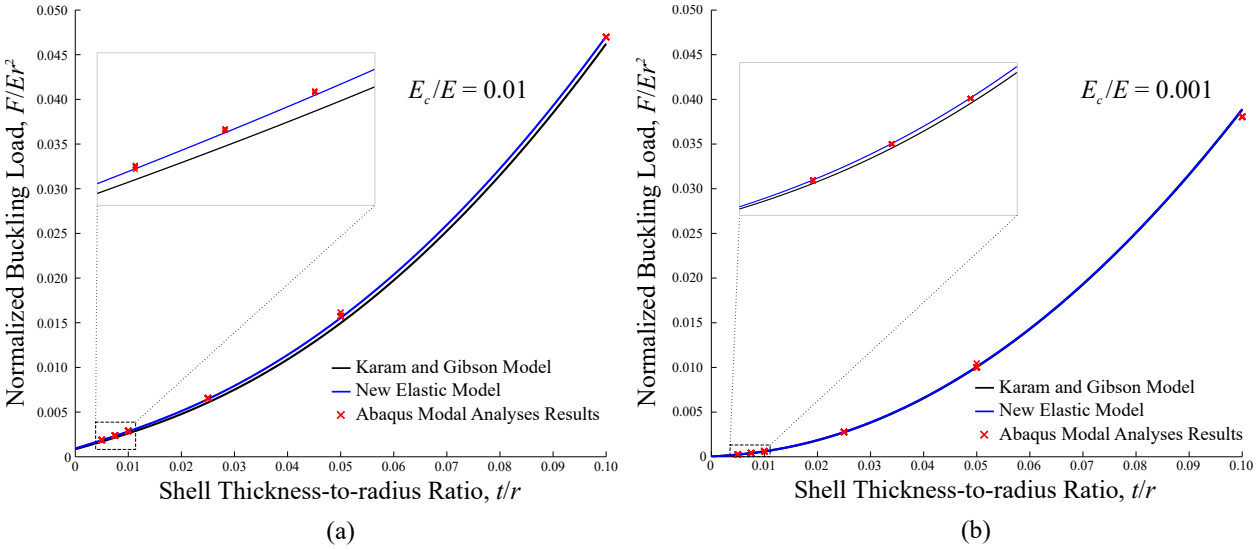

Figure 4.6: Predictions of the buckling load determined from Abaqus modal analyses compared to theoretical models for (a)$E_c/E = 0.01$ and (b)$E_c/E = 0.001$

0.005 indicate very low shell thickness values which may be impractical to manufacture for hybrid microtruss structures, while those above 0.1 are outside the scope of the thin-shell assumption used for the derivation of the new elastic buckling model. Beyond this value, the predicted loads of the model are less accurate.

Figures 4.6(a) and (b) show graphs of the calculated buckling loads as predicted by Abaqus along with the theoretical buckling loads predicted by both the new elastic model and the Karam and Gibson model. Figure 4.6(a) shows the results for $E_c/E = 0.01$, while Figure 4.6(b) shows the results for $E_c/E = 0.001$. Both Figures include insets showing detail at lower values of the ratio of shell thickness-to-radius (t/r) where the data appear to overlap (i.e. data points on the graph are nearly coincident). Where applicable, the overlapping Abaqus data points indicate solutions at different ratios of length-to-radius (l/r) for the same t/r. This overlap in Abaqus data is not present for all ratios of shell thickness to radius; it is due to slight differences in mesh characteristics as the ratio of length-to-radius is changed (e.g. different element counts).

As seen in Figure 4.6(a), for $E_c/E = 0.01$ both the Karam and Gibson model and the new model predict lower loads than the Abaqus results. The Karam and Gibson model predicts loads that are up to 10% less than those predicted by Abaqus, while the new elastic model predicts loads that are no more than 3% less than the Abaqus results. The agreement between the Abaqus results and the Southwell model improves at higher values of the shell thickness to radius (t/r).

The results in Figure 4.6(b) show that when $E_c/E = 0.001$ there is a better agreement between the Abaqus results and the Southwell model model. The Karam and Gibson model also has better predictions at this lower E_c/E value, as the diminished core stiffness reduces the core contribution during buckling. However it is seen that at $t/r = 0.1$, both theoretical models over-predict the buckling load relative to the Abaqus results. The Karam and Gibson model is a better predictor of the load at this higher t/r value.

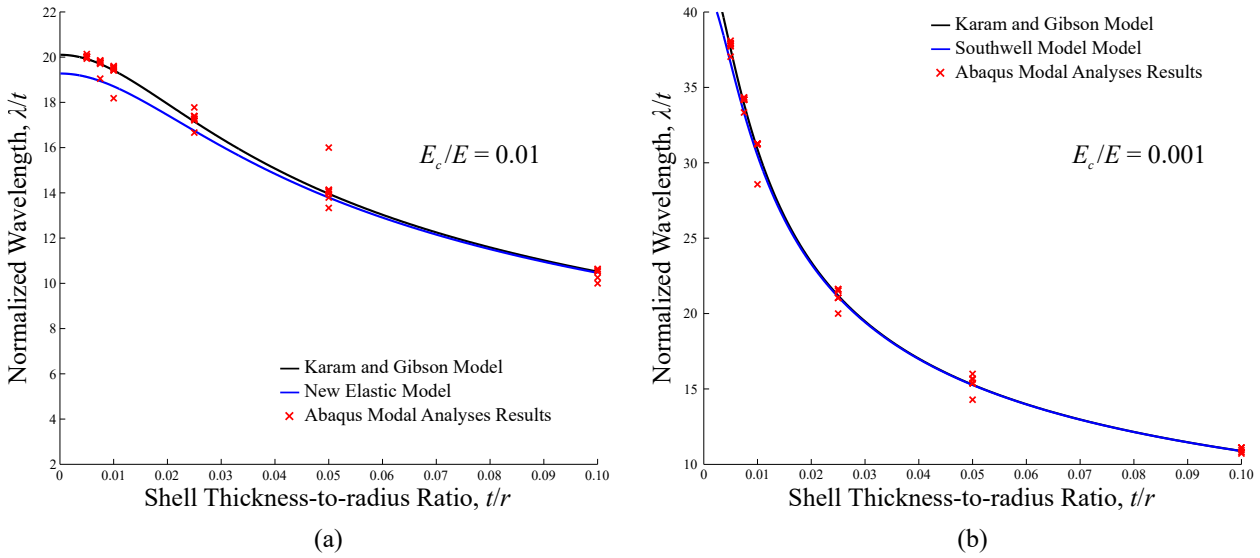

Figure 4.7: Predictions of the critical wavelengths determined from Abaqus compared to theoretical predictions for (a)$E_c/E = 0.01$ and (b)$E_c/E = 0.001$

The difference between the new model and the Abaqus results can be attributed to an incorrect model constant K, which arises from poor function fits when developing the core model. Nevertheless, the new model is still an improvement over the Karam and Gibson model, which does not predict the buckling loads relative to Abaqus as well. It is likely that this is due to the underlying assumptions of the Karam and Gibson model, such as the lack of its inclusion of the circumferential stresses due to its reliance on the Gough model [82].

The predictions of the wavelengths (λ/r) are shown in Figures 4.7(a) for $E_c/E = 0.01$ and Figure 4.7(b) for $E_c/E = 0.001$. The values from the Abaqus simulations were obtained by counting the number of buckling lobes (m) and using the relation $\lambda = 2l/m$ to get the wavelengths. Because m is an integer value, there is more scatter to the predicted values from Abaqus relative to the theoretical values. This is because the wavelength λ was calculated by counting the waves from buckled shapes obtained from Abaqus, whereas the values calculated for theoretical predictions assume that m is continuous. The Abaqus λ/r values gravitate towards the Karam and Gibson predictions for both E_c/E values, indicating that their model is a more accurate prediction for the buckled wavelength.

It is of interest to note that for each geometry assessed, several eigenvalues were requested for the buckling analyses conducted in Abaqus. For a given geometry, the eigenvalues obtained were very close to each other: the first and sixth eigenvalues were within 2% of each other. In addition, the number of waves in each resulting mode shape were very similar, with only differences in the buckle wave amplitudes marking the differences between the eigenvalues. The closeness of the eigenvalues indicates the sensitivity of filled-shell buckling loads to the imperfections of the shell geometry [83], while the similarity of the mode shapes illustrates that the buckling load is not strongly dependant on the buckled shape of the shell.

Based on the modal analysis for values of E_c/E of 0.01 and 0.001, it is seen that the new model is a

more accurate predictor of buckling load while the Karam and Gibson model predicts the wavelengths of the buckles more accurately.

4.4.2 Verification of Stress Distributions

While the modal analysis provides the buckling loads and mode shapes, it is of interest to also determine the stresses in the cores of metal-coated polymer cylinders subsequent to the emergence of buckling deformations (as in Figure 4.1(b)) and compare this to the values obtained in the MATLAB implementation of the Southwell model (as developed for Chapter 3). Eigenvalue or modal analysis in Abaqus is used to determine the critical loads and buckled shapes of structures [83], but cannot be used to determine the stress state in the resulting buckled geometries. This necessitates the use of post-buckling analysis, whereby imperfections are deliberately introduced to cylinder geometries in order to induce buckling in standard finite element analysis. Without the use of imperfections, the cylinders would continue to undergo axial straining without buckling taking place.

As was done for the modal analyses, an axisymmetric section of a cylinder is loaded axially as shown in Figure 4.5. The boundary conditions were identical to those used for the modal analysis, and the meshes previously generated for each cylinder geometry were reused. The modal analyses provided the axial displacement of each geometry at which buckling was incipient. For the post-buckling analysis, the axial displacements applied to the cylinders utilized the values found from the modal analyses.

The undeformed mesh of each cylinder was deliberately made imperfect by offsetting the nodes using the information from buckled shapes obtained from the modal analyses. This was done using a series of buckled shapes, and the imperfections applied in this way were controlled by varying the scale factors of each mode shape. Table 4.2 lists the scaling factors used for the first six mode shapes for each geometry. Utilizing more than six eigenmodes did not affect the results of the post-buckling analyses, while larger scaling factors led to lower buckling loads than previously found from the modal analysis.

The geometries studied for the modal analysis were also analysed using post-buckling analysis (hence the same meshes could be used). The loads determined from the results of the modal analysis were verified through post-buckling analyses. All of the loads obtained in this manner were very similar to their modal analysis counterparts, and are thus not given in this section. However, an examination of the stress

Table 4.2: Scaling factors used for each eigenvalue, as applied to the geometries used for post-buckling analyses in order to generate imperfect meshes.

Eigenvalue/Mode #	Scaling Factor
1	5.000×10^{-3}
2	2.500×10^{-3}
3	1.250×10^{-3}
4	6.250×10^{-4}
5	3.125×10^{-4}
6	1.562×10^{-4}

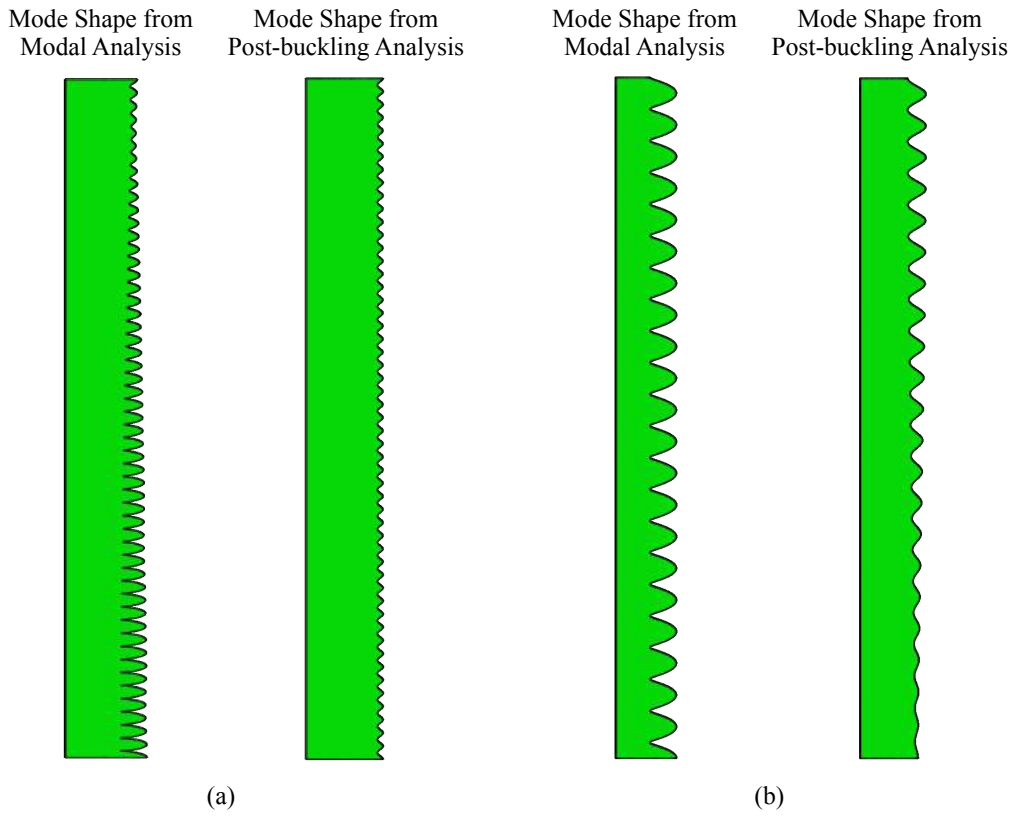

Figure 4.8: Mode shape from modal results and deflected shape from post-buckling analysis for (a) $t/r = 0.01$, $l/r = 10$ and (b) $t/r = 0.05$, $l/r = 15$. The core relative stifness $E_c/E = 0.01$ for both cases, and the radial deformations have been exaggerated.

distributions for some geometries will be given, as well as comparisons of some deformed shapes of several geometries analysed.

Figure 4.8(a) shows the first buckling mode from a modal analysis performed for $l/r = 10$ and $t/r = 0.01$, while also showing the buckled shape for a simulation of post-buckling behaviour. Figure 4.8(b) shows the buckled shapes for $l/r = 10$ and $t/r = 0.05$, again for both simulations. The value of E_c/E for both figures is 0.01. It is seen that the number of buckle waves is similar for both the modal and post-buckling simulations. This is most likely due to the fact that the modal analysis was the basis for the imperfections used for the post-buckling analyses. Although the imperfection pattern for the geometries was a weighted sum of the first six mode shapes (refer to Table 4.2), these figures illustrated that the buckled shapes are still similar to the first mode shape. Recall that the axial load as determined from the first eigenvalue (which corresponds to the first mode shape as shown in Figures 4.8(a) and (b) was compared against the predictions of the filled-shell models shown in Figures 4.6 and 4.7.

While a stress analysis of the core subsequent to the emergence of buckling displacements for several select geometries was undertaken, only the results pertaining to $l/r = 10$ and $t/r = 0.01$ are shown ($r = 5$ mm and $l = 50$ mm). This is the same geometry whose buckled shapes are shown in Figure 4.8(a). The stress distributions in the core as obtained from the post-buckling simulations and the Southwell model are shown in Figure 4.9. In this Figure, the radial and axial stresses for $l/r = 10$, $t/r = 0.01$ and $E_c/E = 0.01$

are shown. Only one wavelength λ of the cylinder is shown for clarity. In addition, only the outer 2 mm of the core is shown as the rapidly decreasing stresses towards the core centreline mask the stress activity at the core outer sections. The axial stress for the Southwell model solution was changed by -40 MPa to account for pure axial loading of the core, as this effect is not accounted for in the Southwell stress solution.

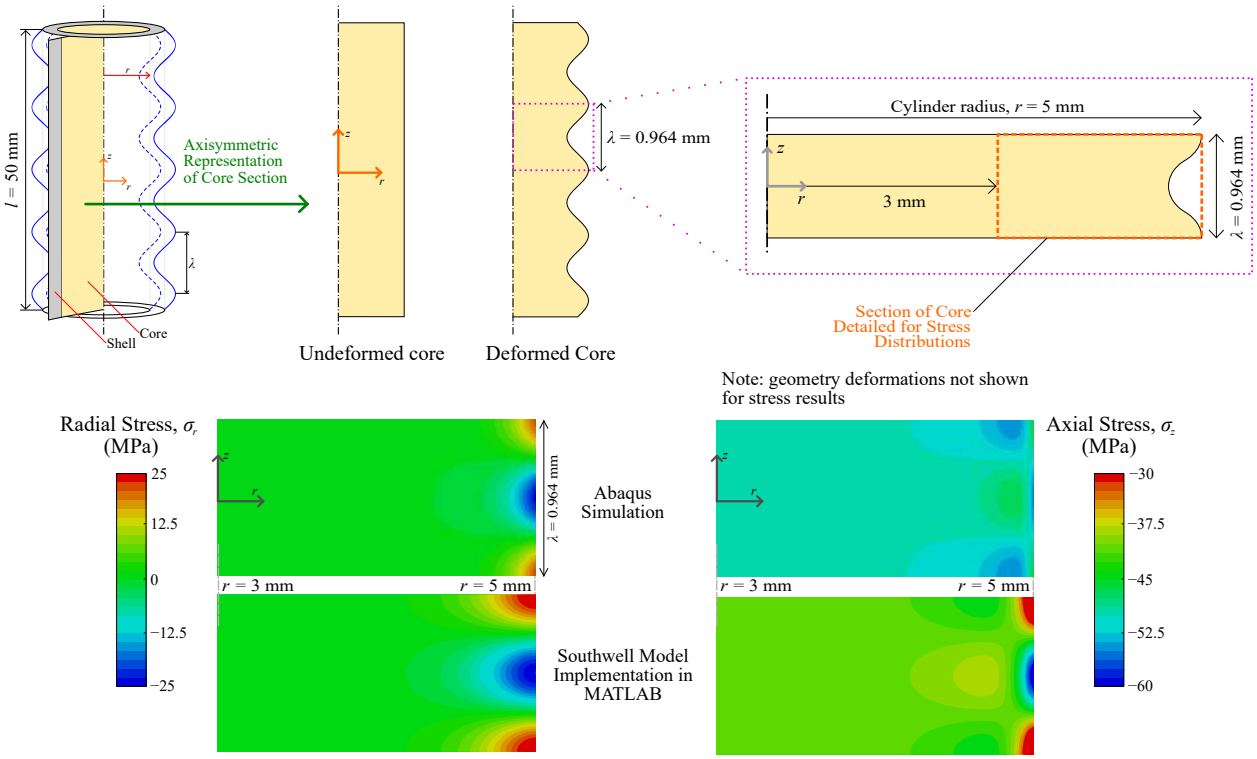

Figure 4.9: Radial (left) and axial (right) stress distributions in the core calculated from the Southwell Model (top) and Abaqus post-buckling analysis (bottom) for a geometry with $l/r = 10$, $t/r = 0.01$ and $E_c/E = 0.01$. Note that only one wavelength of the geometry is shown, and only the outer 2 mm of the core as shown in the diagram above.

For the core sections shown in Figure 4.9, the stress distributions determined for the radial and axial directions are similar in appearance for both the Abaqus and Southwell model solutions. Although the radial stress fields are more spread out in the radial direction for the Southwell model solution, the minimum and maximum values of the radial stresses obtained from both the Abaqus and Southwell solutions are the same. However, there are notable differences in the axial stress solutions. While the distributions of the axial stresses in both the Abaqus and Southwell model solutions are visually similar, the values of these stresses are not. The minimum axial stress determined from both results is -60 MPa. However, the axial stress value at $r = 3$ mm is -50 MPa while the value found from the Southwell model is -45 MPa. The stress values at $r = 3$ mm represent the stress state far away from the influence of buckle deformations at the outer surface of the core.

It is believed that this discrepancy in the axial stress distributions is due to a Poisson effect that is not accounted for in the Southwell model, despite the -40 MPa change to the results prior to comparisons. An inspection of the strain energy contributions of the core (as determined using the Southwell model) reveals

that the radial stress has the highest contribution to the strain energy, followed by the shear strain energy. The contribution of the axial strain energy is lower than both the radial and shear strain contributions. In addition, the buckling load calculated by the new elastic model matches that from the Abaqus modal analysis and the present post-buckling analysis. This implies that the differences in the axial stress distributions do not markedly affect the results of the buckling loads.

Despite the differences in the axial stresses obtained from the Abaqus and Southwell model solutions, the circumferential and shear stress distributions, which have not been shown here, compare well for the Southwell model and Abaqus results. The maximum absolute shear stress for the same core section shown in Figure 4.9 is found to be 10 MPa, and this value is found through both the Abaqus and Southwell solutions.

The radial stress distributions for this geometry were found to be similar for the Abaqus and Southwell model solutions. The differences in the axial stress distributions are attributable to a Poisson effect in the core that is not accounted for in the Southwell model solution. As the contribution of the axial strain energy to the total core strain energy is less than other strain energy components, these differences in the axial stresses do not affect the results of the buckling load estimates obtained from Abaqus. As such, despite the differences in the axial stresses, the buckling load calculations obtained from Abaqus verify the predictions obtained using the new elastic model.

4.5 Conclusions

The buckling load for a metal-coated polymer cylinder (or a filled shell) in axial compression has been derived. This new model predicts slightly higher buckling loads than the Karam and Gibson model, currently the standard for the buckling of foam-filled cylinders. For very thick shells, the contribution of the core to the buckling load becomes insignificant, and the loads approach the theoretical hollow-shell buckling load.

Through Abaqus modal analysis, it was shown that the new model is in better agreement with buckling loads found through finite element analysis compared to the Karam and Gibson model. The buckle wavelengths, however, are better predicted by the Karam and Gibson model. A stress analysis undertaken utilizing post-buckling analysis showed that the radial stresses agree well with those predicted by the Southwell model. However, while the axial stress distributions are visually similar for the Abaqus results and Southwell model, the stress magnitudes are not identical even after accounting for the added axial load in the Abaqus simulations (which is not originally present in the Southwell model). Despite this difference in magnitudes, the buckling loads found through Abaqus are in better agreement with the new model than with the Karam and Gibson model.

Although the Karam and Gibson model does not match as well with the results found through Abaqus, it is a simpler model to implement in practice. Were one to require an analysis of a known geometry, the Karam and Gibson model would be much more efficient than the model described here. The advantage of the new model lies in its adaptability to other conditions that are very important in filled-shell buckling.

Chapter 5

Local Buckling of an Elastic Shell Filled with a Solid Elastic Cylinder without Interfacial Adhesion

5.1 Introduction

Metal-coated polymer microtruss structures take advantage of mass-efficient microtruss topologies while utilizing the high-strength benefits of nanocrystalline metals [4]. These structures are produced by 3D printing a polymer preform followed by coating this preform with nanocrystalline metal. During the metal-coating process, an electroless step is necessary in order to create a thin layer of metal on the polymer surface. This provides a conductive surface for the electrodeposition of nanocrystalline metal. While the bond between the electroless metal layer and the nanocrystalline metal is strong, the adhesion between the electroless metal and the polymer surface is known to be imperfect [22, 59]. The quality of the bond between the electroless metal and the polymer is affected by several factors. These can include the ambient temperature during the electroless process [57], the cleanliness of the polymer surface [22, 58], the difference in Young's moduli between the metal and polymer [63] and the chemistry of the polymer [59].

A key assumption of the elastic model (Chapter 4) is that the core and the shell are perfectly bonded. The imperfect bond between the metal and polymer (specifically the electroless layer and the polymer) results in lower critical loads than would be expected with a fully-adhered metal shell and polymer core [62, 63]. With full adhesion, the metal shell and surface of the polymer core move as one unit. The core increases the buckling resistance of the filled shell compared to a hollow shell of the same geometry. Without adhesion, the core still provides added resistance to buckling, but does not provide as much support compared to a fully-adhered filled-shell. The terms "shell" and "coating" refer to the electroless and electrodeposited metal together, as the bond between these metal layers is not of concern.

The lack of adhesion requires modification of the model. While the shape of the shell subject to buckling deformations remains unchanged, only the radial deflections which push the core inward will affect the shape of core, while those that would have pulled the core outward do not affect the core. Lack of adhesion between the shell and the core reduces the axial buckling strength of a filled shell. However, even without adhesion, a filled shell will buckle at a higher load compared to a hollow shell of the same shell geometry.

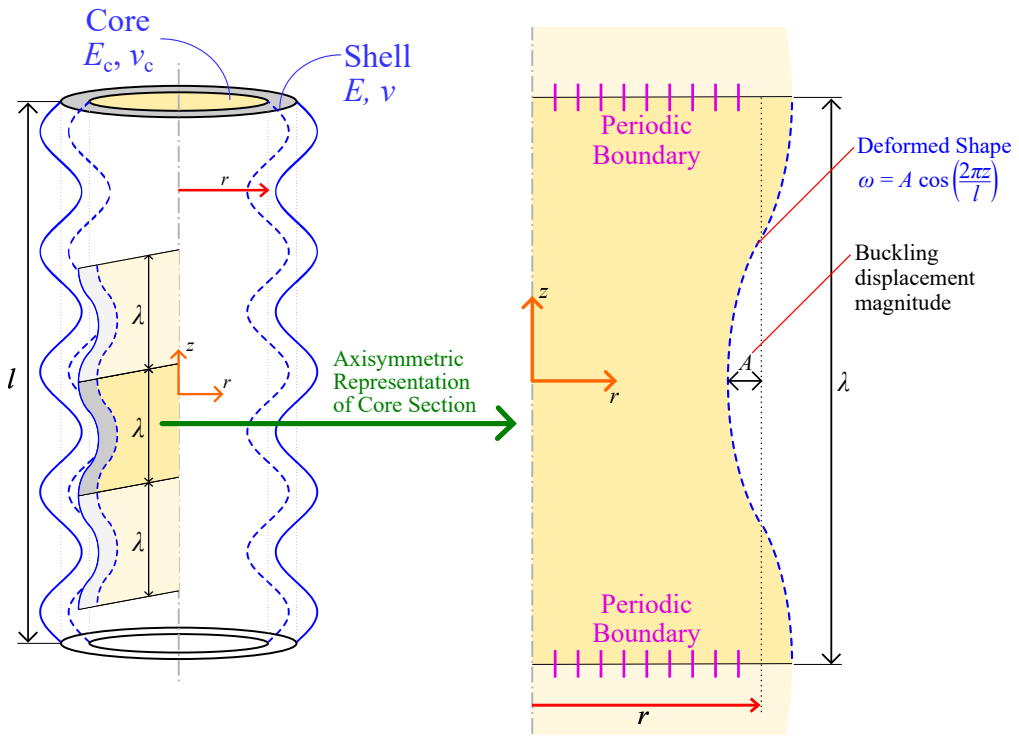

Figure 5.1: A fully-adhered filled cylindrical shell of length l and radius r undergoing buckling deformations. The buckle wavelengths have length λ and amplitude A. An axisymmetric section of the core with length λ and periodic boundary conditions is shown in detail.

5.2 Modelling the Core for Non-adhesion

Although the coating is not adhered to the core, the shell is assumed to maintain its sinusoidal deformations when it buckles. However, the lack of adhesion between the metal coating and polymer core results in the transfer of less energy to the core compared to fully-adhered conditions. This is because the core undergoes less deformation compared to when the shell and core are fully adhered.

During buckling of a fully-adhered filled shell under axial load, the outer surface of the core moves in tandem with the shell. Figure 5.1 depicts the deformed shape of a filled cylinder while buckling, and also the resulting deformed shape of an axisymmetric section of the core undergoing sinusoidal radial displacements. These displacements are a consequence of the buckling displacements of the shell transferred to the core, due to the adhesion between the shell and core. As the shell moves towards or away from the cylinder centreline, so too does the core. The magnitude of the radial displacement of the buckle waves is A, and the radial displacement of the surface of the core takes the form:

$$w = A\sin\frac{m\pi z}{l}, \tag{5.1}$$

where m is the number of buckle half waves along the length l of the shell, and z is the axial coordinate as seen in Figure 5.1. The core section in Figure 5.1 has length λ, the same as that of the buckle waves. The periodic boundary conditions ensure that a model of this axisymmetric section is relevant for any section of

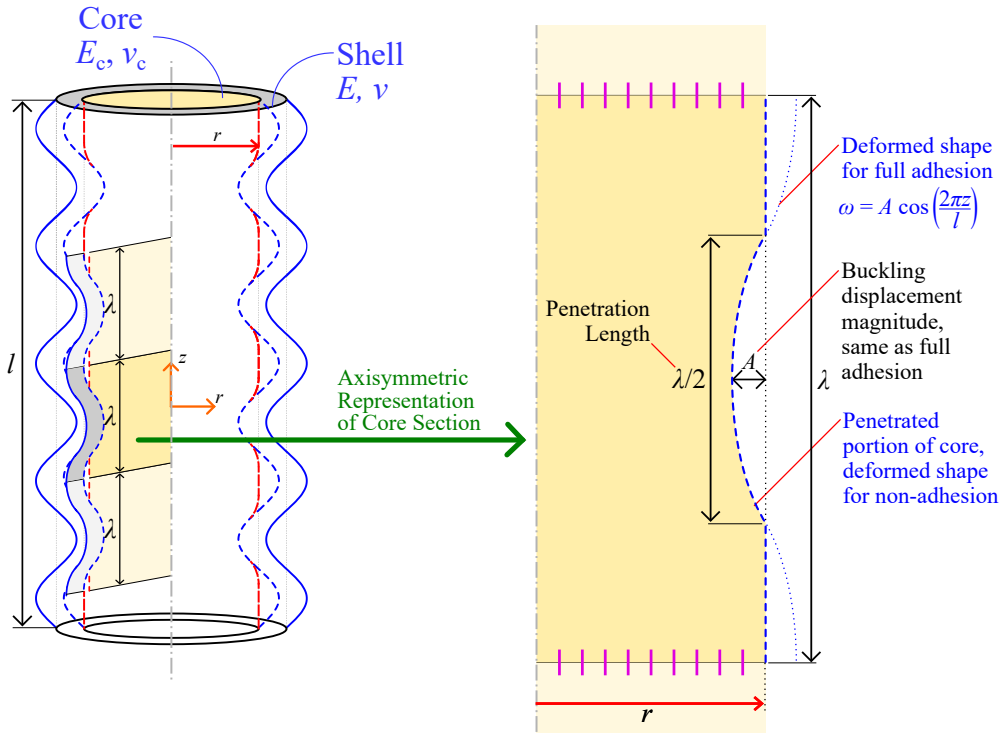

Figure 5.2: A non-adhered filled cylindrical shell of length l and radius r undergoing buckling deformations. The buckle wavelengths have length λ and amplitude A. An axisymmetric section of the core with length λ and periodic boundary conditions is shown in detail. Full penetration of the core is assumed.

the core subject to buckling displacements. This is important when developing the model for the core, as was detailed previously in Chapter 3.

Without adhesion between the shell and core, only the movements of the shell that push into the core are transferred to the core, as shown in Figure 5.2. Comparing Figures 5.1 and 5.2 shows that only the radial displacements of the shell that move in the $-r$ direction are transferred to the core. Half of the shell buckle wavelength penetrates the core, as given by the dimension $\lambda/2$ in Figure 5.2. Because of the reduced interaction region of the core in Figure 5.2 compared to core movement under a fully-adhered shell and core (Figure 5.1), the strain energy accumulated in the core without adhesion conditions will be less than that compared to full adhesion.

5.2.1 Full penetration and partial penetration

The deformed shape of the core depicted in Figure 5.2 assumes that there is full penetration of the buckled shell into the core, so that all shell displacements in the $-r$ direction are transferred to the core. It is of interest to also examine when it is energetically efficient for the shell to expand radially outward uniformly in addition to buckling sinusoidally, instead of for the core to deform inward. This particular case is referred to as "partial penetration," and is depicted in Figure 5.3. The core and the average position of the shell are now separated by a distance r' as depicted in the Figure, and the penetration depth of the radial deflections becomes A'. When $r' = 0$, there is "full penetration" of the shell into the core as the shell buckles, as

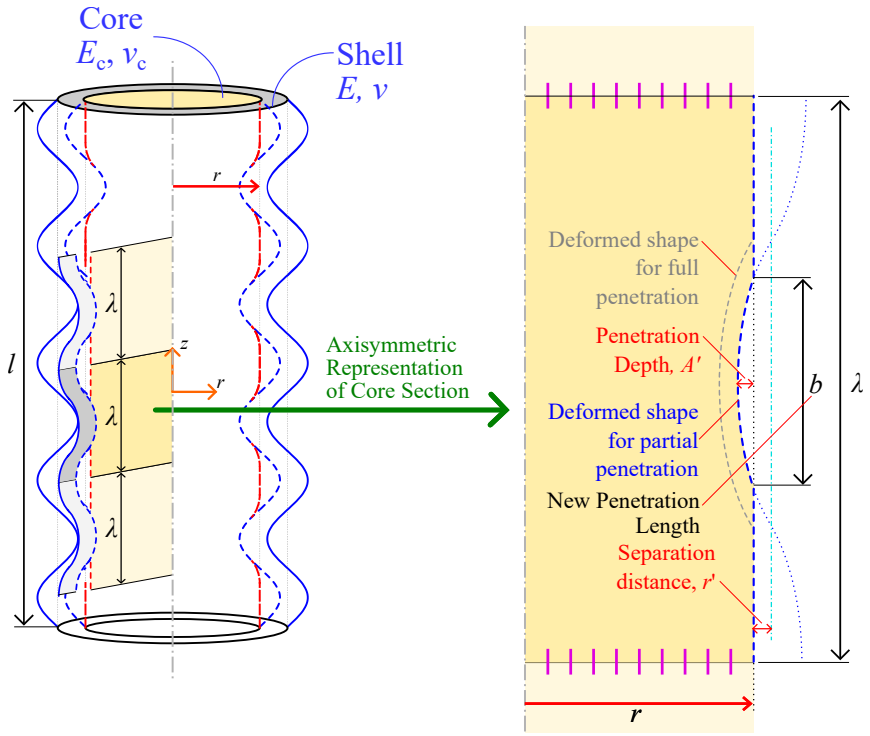

Figure 5.3: A partially-adhered filled cylindrical shell of length l and radius r undergoing buckling deformations. The buckle wavelengths have length λ and amplitude A. An axisymmetric section of the core with length λ and periodic boundary conditions is shown in detail.

previously shown in Figure 5.2. The penetration length b, as shown in Figure 5.3, represents the portion of the half-buckle wavelength which penetrates the core. It reaches a maximum value of $\lambda/2$, when full penetration takes place as given in Figure 5.2. In order to quantify the effects of partial penetration, a new variable b/λ is introduced to represent the degree of partial penetration under non-adhesion conditions. The quantities of b/λ and r' are related geometrically through:

$$\frac{r'}{A} = \sin\left[\pi\left(\frac{1}{2} - \frac{b}{\lambda}\right)\right], \tag{5.2}$$

while the quantity A' is related to A and r' through

$$A' = A - r'. \tag{5.3}$$

As the value of b/λ can be used to completely describe the degree of penetration for a non-adhered filled-shell under partial penetration conditions, b/λ is treated as its own variable for the non-adhesion model.

5.3 Development of Non-adhered Core Model

The Southwell model employs a stress potential function to calculate the stress field in an axisymmetrically-loaded isotropic cylinder [39, 120]. It was previously utilized in Chapter 3 to determine the stress state of

a core under full-adhesion conditions (i.e. as in Figure 5.1). The Southwell model was used in order to determine the constant, K. The equation used to find this fitting constant was given as:

$$K = \frac{2U}{mA^2\pi r}, \tag{5.4}$$

where U is the internal energy in an axisymmetric section of the core, m is the number of half-buckle waves, A is the radial displacement magnitude (as shown in Figure 5.1) and r is the radius of the core. The radial displacements applied to the core are shown in Figure 5.1, and they take the form of Equation 5.1.

A limitation of the Southwell model is its reliance on stress boundary conditions [6, 38, 39]. To circumvent this, a MATLAB function was developed that determines the stress amplitude required to obtain a prescribed displacement amplitude A. In this way, A and r can be set for a given core geometry (refer to Figure 5.1), and the value of K (the fitting constant) can be found through Equation 5.4 for one buckle wavelength (i.e. $m = 2$). For the fundamental (or full-adhesion) case in Chapter 4, K was simply a constant which is independent of the buckle wavelength λ. However, the behaviour of a cylinder when there is no adhesion between the shell and the core causes K to become a function of the penetration variable b/λ.

In order to determine the behaviour of a core under non-adhesion conditions, the value $U/(A^2\pi r)$ was found for many λ/r values. This process was repeated for various b/λ between 0 and 0.5, representing the limiting conditions of no penetration and full penetration respectively. Using the data generated with these varying geometric values, a model for a non-adhered core was developed. As was done in Chapter 3 for a fully-adhered core, this was done for two different relative core stiffness values (E_c/E) of 0.01 and 0.001. The material properties for the shell and core are indicated in Figure 5.3.

The results for the energy analysis are given here for $E_\mathrm{c}/E = 0.01$ only. Only final fit parameters for $E_\mathrm{c}/E = 0.001$ will be provided. Figure 5.4 shows the graph for $U/(A^2\pi r)$ plotted against λ/r for values of b/λ ranging between 0 and 0.5. As indicated with lines of best fit in this Figure, there is approximately a linear relationship between $U/(A^2\pi r)$ and λ/r for every b/λ. An examination of the lower part of Figure 5.4(a) is shown in Figure 5.4(b), showing that the linear fits also hold at lower b/λ.

From the graphs of Figures 5.4(a) and (b), it is seen that the slopes and vertical-axis intercepts of the linear fits change with b/λ. Denoting the slopes as K_s and the intercepts as K_i, the fit function K is:

$$K\left(\frac{b}{\lambda}, \frac{\lambda}{r}\right) = K_\mathrm{s}\left(\frac{b}{\lambda}\right) + K_i\left(\frac{b}{\lambda}\right)\frac{\lambda}{r}. \tag{5.5}$$

The values of K_s and K_i are functions of b/λ, as shown in the figure. A graph containing values of K_s and K_i is given in Figure 5.5 for the best fit lines plotted previously in Figures 5.4(a) and 5.4(b). As seen in Figure 5.5, the values of K_s and K_i are very small as b/λ becomes small (i.e. $b/\lambda < 0.2$). An exponential fit weighted towards the low b/λ values allows for adequate interpolation of K_s and K_i values. These exponential fits for K_s and K_i take the form:

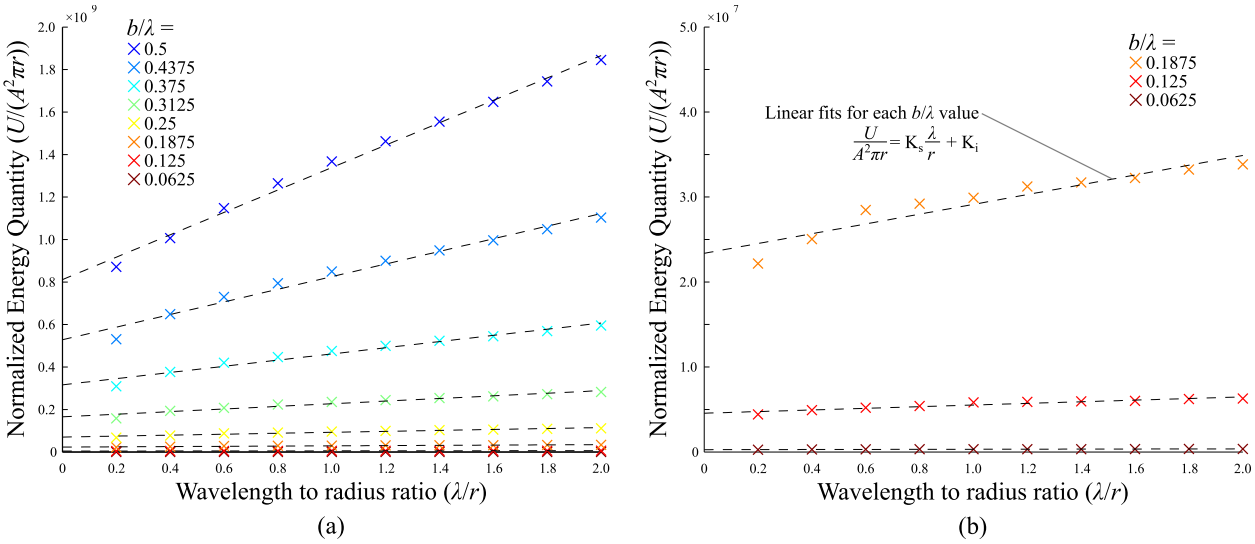

Figure 5.4: (a) Normalized energy quantity $U/(A^2\pi r)$ plotted against the wavelength-to-radius ratio λ/r for increasing b/λ values. The data pertains to a core with $E_c/E = 0.01$. (b) Normalized energies for low b/λ values only, showing that the linear fit (Equation 5.6) still holds for these low b/λ values

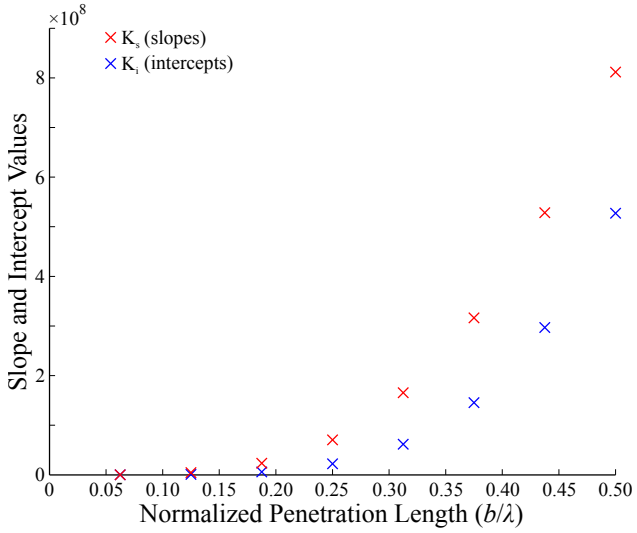

Figure 5.5: K_s and K_i values plotted against increasing values of b/λ for $E_c/E = 0.01$ (refer to Equation 5.6).

$$K_s = a_1 \exp\left(-\left(\frac{\frac{b}{\lambda} - b_1}{c_1}\right)^2\right) \quad \text{and} \quad K_i = a_2 \exp\left(-\left(\frac{\frac{b}{\lambda} - b_2}{c_2}\right)^2\right), \tag{5.6}$$

where a_1, b_1, c_1, a_2, b_2 and c_2 are the fit constants from the exponential fits as found using least-squares curve-fitting algorithms. Equations 5.6 and 5.5 together provide the energy model for a core subject to sinusoidal deflections for a non-adhered filled shell undergoing axial buckling. The model can be used to represent the conditions of varying penetration (i.e. b/λ can vary) or full penetration (i.e. $b/\lambda = 1/2$).

Using the form of K as shown in Equation 5.5 and utilizing the original form of U_p as given in Equation 3.15 of Chapter 3, the form of U_p for a core under non-adhesion conditions takes the form:

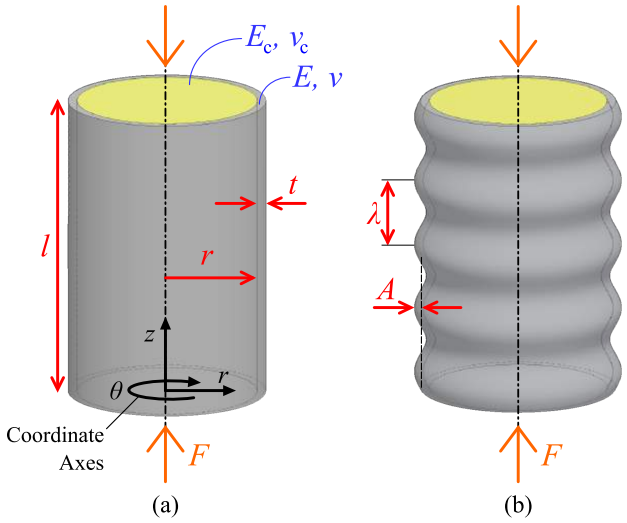

Figure 5.6: A filled shell when undeformed (left) and buckled (right). The filled shell is under an axial load F with length l, shell thickness t and inner radius r. The shell has material properties E and ν while those of the core are E_c and ν_c. When buckled, the buckle waves have wavelength λ and amplitude A.

$$U_p = \frac{m}{2}\left(K_s + K_i\frac{\lambda}{r}\right)A^2\pi r, \tag{5.7}$$

where the multiplier $m/2$, as for the fully-adhered case, extends this energy model to account for many buckle waves. Equation 5.7 provides the energy for a core subject to partially-penetrating sinusoidal radial displacements of length b/λ.

5.4 Buckling Load for a Non-Adhered Filled Shell

A filled shell is under an axial load F is shown on the left of Figure 5.6. The shell has a thickness t, radius r and length l. When buckling takes place, the shell buckles with waves of length λ and amplitude A. The buckling load for the non-adhered shell in axial compression is derived as detailed in Chapter 4. The assumptions are the same as those used in Chapter 4, with the exception of full-adhesion. It is instead assumed that there is no adhesion between the shell and the core, and any sliding contact between the shell and core is frictionless as it is assumed that any frictional effects will not affect the buckling behaviour. The energy contributors involved in the calculation of the buckling load include:

- the longitudinal bending load of the shell due to sinusoidal buckling deformations (U_b),
- the circumferential stretching of the shell due to these same buckling deformations (U_c), and
- the contribution of the core energy due to buckling deformations pushing into the core (U_{c2}), given in Equation 5.7).

When partial penetration of the core takes place (Figure 5.3), another energy term must be included. As the shell and core separate with distance r', this causes additional circumferential stretching of the shell. The energy associated with this additional circumferential stretching is:

Table 5.1: Values of the fitting constants for (K_s, K_i) found from core model analysis. The reference value for E (125 GPa) is that of nanocrystalline nickel manufactured by RePliForm [7].

E_c/E	a_1	b_1	c_1	a_2	b_2	c_2
0.01	6.932×10^8	0.6020	0.1842	7.299×10^8	0.5212	0.1711
0.001	7.086×10^7	0.8698	0.6153	8.434×10^7	0.3325	0.7655

$$U_{c2} = \frac{\pi E t A^2 l}{r} \sin^2 \left[\pi \left(\frac{1}{2} - \frac{b}{\lambda} \right) \right]. \tag{5.8}$$

The expressions for U_b and U_c have been presented in Chapter 4 in Equations 4.2 and 4.3 respectively. The internal energy of the filled shell is the sum of the circumferential energy (Equation 5.8) as well as U_b, U_c and U_p. The external energy is due to the applied axial load F as shown in Figure 5.6, and its expression is given in Equation 4.6 of Chapter 4.

Using the derivation method of Chapter 4, the buckling load for the non-adhesion case is:

$$F = \left(1 + \frac{E_c}{E}\frac{r}{2t}\right) \left[\frac{2\pi^3 r E t^3}{3(1-\nu^2)} \frac{1}{\lambda^2} + \left[\frac{Et}{r} \left(\frac{1}{2} + \sin^2 \left(\pi \left(\frac{1}{2} - \frac{b}{\lambda} \right) \right) \right) + K_s \right] \frac{1}{\pi} \lambda^2 + \frac{K_i r}{\pi} \lambda \right]. \tag{5.9}$$

Due to the dependence of non-adhesion buckling on the degree of penetration b/λ, λ is also a function of b/λ. Thus the critical load F is a function of the wavelength λ, b/λ, and the material properties and geometric values in Equation 5.9. The buckling load is thus found by minimizing Equation 5.9 for both λ and b/λ.

5.4.1 Non-Adhesion Buckling Load Behaviour

The behaviour of the non-adhesion buckling load (Equation 5.9) is compared to that of the fundamental model (Equation 4.11 in Chapter 4) and the hollow-shell model [34–37]. The fitting constants found for the non-adhesion case are shown for two values of E_c/E in Table 5.1. The reference value of E is that of nanocrystalline nickel given by RePliForm Inc (125 GPa) [7]. In order to find the values of b/λ and λ, a non-linear solver was used to determine their values which lead to the lowest buckling loads for given shell geometry and material properties. This behaviour is compared to that of a non-adhered filled shell with full-penetration (i.e. $b/\lambda = 0.5$).

The values of the non-dimensional critical loads for the fundamental, non-adhesion, and hollow-shell models are provided in Figure 5.7(a) and (b) for E_c/E values of 0.01 and 0.001 respectively. The critical wavelengths pertaining to these same models are shown in Figures 5.8(a) and (b). The critical loads and wavelengths have been given for both the full penetration case ($b/\lambda = 0.5$ in Figure 5.2) as well as for varying penetration ($0 \leq b/\lambda \leq 0.5$ in Figure 5.3). As b/λ is a variable of the buckling problem, its values are given graphically in Figure 5.9.

As seen in Figure 5.8(a) for $E_c/E = 0.01$, the normalized buckle wavelengths (λ/t) corresponding to the full-penetration case are lower than those of the non-adhesion case with varying penetration. For both values of E_c/E (Figures 5.8(a) and 5.8(b)), the critical wavelengths are smaller than for hollow shell

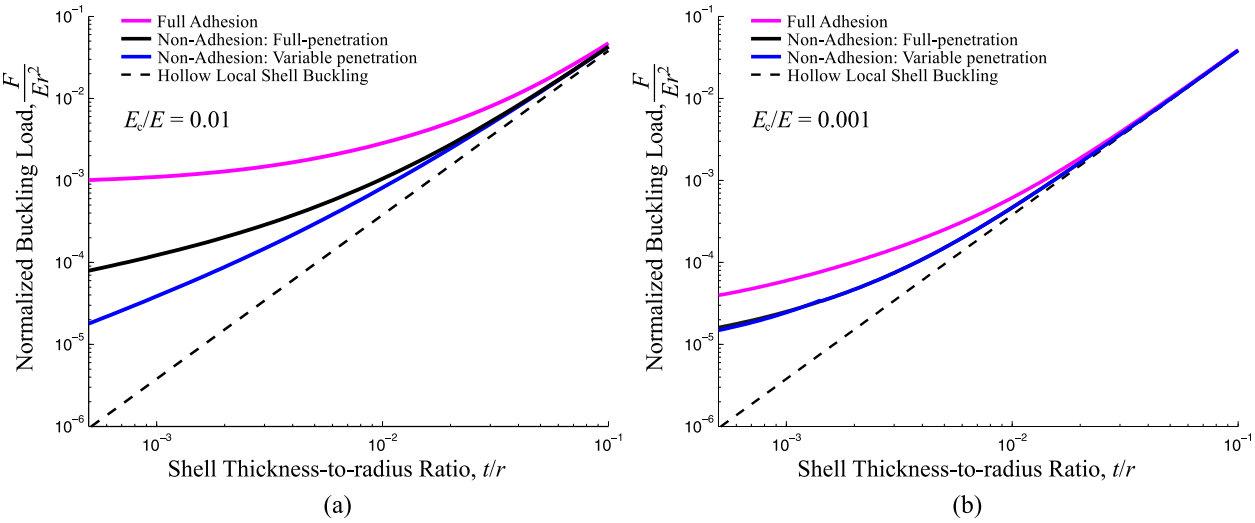

Figure 5.7: Predictions of buckling loads for the non adhesion (variable penetration and full penetration), fundamental and hollow shell models as functions of t/r for (a)$E_c/E = 0.01$ and (b)$E_c/E = 0.001$

buckling, indicating that this is a permissible response. A λ/t greater than that of the hollow shell model would imply that the buckling loads are lower than the hollow shell buckling load.

The core stiffness, however, plays a strong role in the transition from full penetration to varying penetration. As seen in Figure 5.8(b) for $E_c/E = 0.001$, the λ/t curves for variable penetration and full-penetration are nearly coincident with each other, indicating that this lower stiffness cores it is more energy efficient for the core to be fully penetrated than for varying penetration to occur. This is confirmed upon inspection of Fig 5.9, which shows that b/λ is very close to 0.5 (i.e. full penetration). In the opposite limit of a rigid core, the penetration must be zero.

The plots of the buckling load for $E_c/E = 0.01$ in Figure 5.7(a) indicate that the buckling loads for full and varying penetration are below that of the full adhesion case, as would be expected. There is a noticeable difference between the full penetration and varying penetration loads when $E_c/E = 0.01$ (Figure 5.7(a)), corresponding to changing values of b/λ for this core stiffness value in Fig 5.9. However, the dependence of the buckling load on b/λ disappears when $E_c/E = 0.001$. The load behaviours of the variable penetration and full penetration cases are nearly identical in Figure 5.7(b), except at very low values of t/r.

In summary, the non-adhesion model with variable penetration predicts very low loads compared to full-penetration conditions when E_c/E is 0.01. However, for less stiff cores (i.e. E_c/E of 0.001) the full penetration and varying penetration assumptions produce the same results. The behaviour of the non-adhesion model is verified next using finite element simulations.

5.5 Finite Element Verification of Non-Adhesion Buckling Loads

Abaqus simulations were used to verify the predicted loads and critical wavelengths calculated using the non-adhesion model. As the non-adhesion model requires that the shell and core remain unbonded, contact

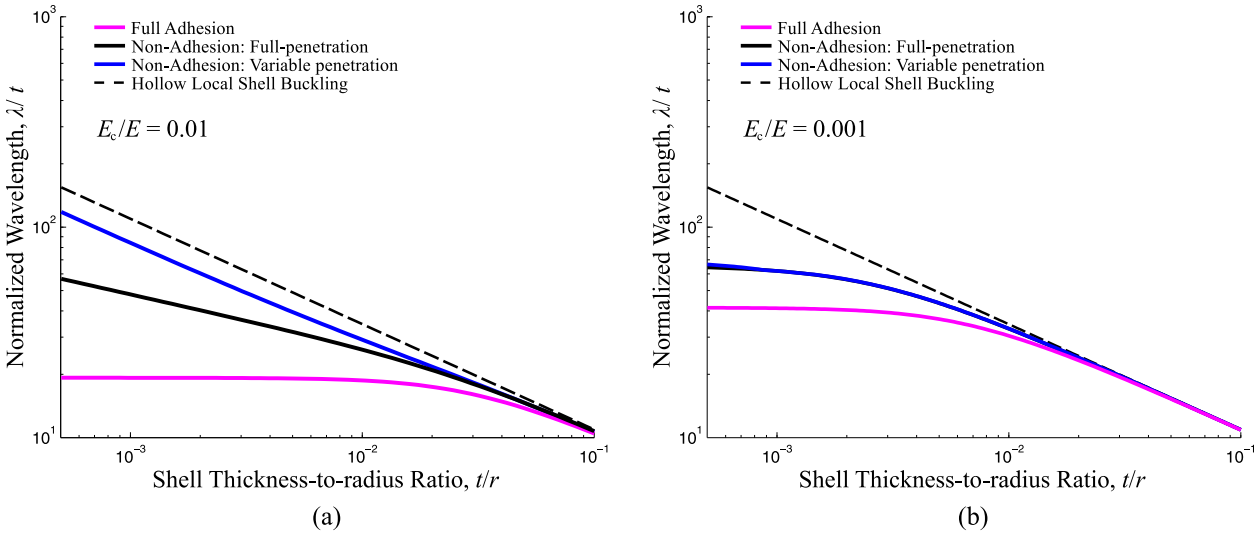

Figure 5.8: Predictions for the critical wavelengths for the non adhesion, fundamental and hollow shell models as functions of t/r for (a)$E_c/E = 0.01$ and (b)$E_c/E = 0.01$

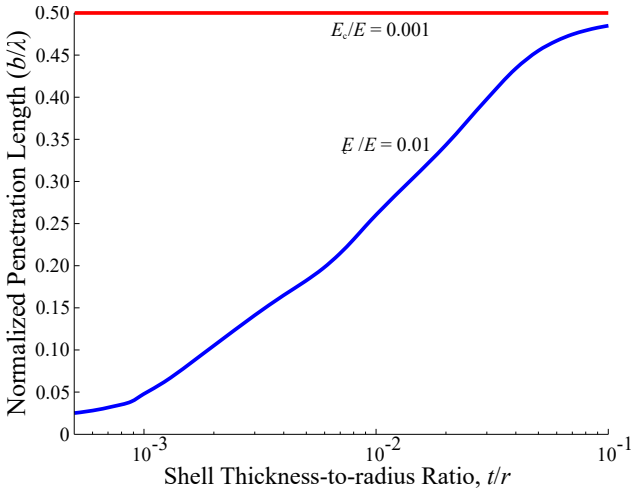

Figure 5.9: Critical values of b/λ for $E_c/E = 0.01$ and 0.001 as a function of t/r for the non-adhesion model with varying penetration. The values are those found for the critical loads and wavelengths found in Figures 5.7 and 5.8.

definitions were required for these simulations in order to ensure a correct representation of the shell and core. However, because of the inclusion of contact definitions, modal analysis could not be performed as the eigenvalue solvers in Abaqus assume pairs of surfaces with contact definitions remain in their base states [83].

Figure 5.10 shows the setup used for the finite element simulations. The simulations were performed using an axisymmetric representation of a filled cylinder, while the loads were applied through the use of a displacement boundary condition at the cylinder top surface (shown as an edge in Figure 5.10). As for the simulations for the fundamental case, axisymmetric simulations allowed for reduced processing times and was used due to the independence between buckling modes (refer to Section 2.7.2 of Chapter 2). However, any non-axisymmetric buckling behaviour is lost.

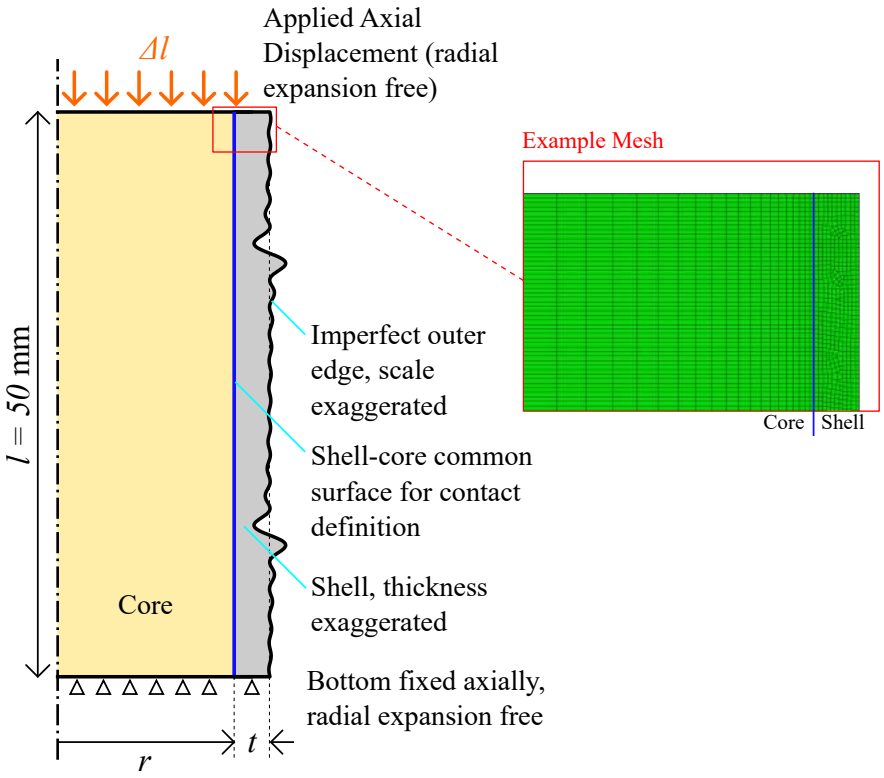

Figure 5.10: Diagram showing setup of an Abaqus simulation for an axisymmetric section of a filled shell with length $l = 50$ mm, radius r and shell thickness t. A contact definition is used for the shell-core common surface, while the shell is loaded with an axial displacement at the top surface. A sample mesh is also provided, showing the use of tetrahedral and quadrilateral elements due to the induced imperfections in the shell.

Imperfect shell geometries were required in order to induce local shell buckling. Imperfections were generated by using a sum of several buckling mode shapes with varying amplitudes. The maximum imperfection peak amplitude was limited to $0.01t$, or 1/100th of the thickness of the shell. The imperfection curve was only applied to the shell outer edge, as shown in Figure 5.10. This ensured that the common shell-core surface was geometrically flat to generate an adequate contact pair.

Contact definitions were required for these simulations in order create the necessary conditions for a non-adhered shell-core system. Contact was defined using the built-in general contact mode in Abaqus, which allows the software to determine the best contact algorithms. The contact properties were chosen such that there was hard normal contact, but translational movement between the surfaces was allowed and remained frictionless. This is in accordance with the assumptions used for the buckling model. Moreover, no sliding occurs at the inception of buckling, which is the focus of the finite element investigations.

Meshes were generated to have at least 5000 to 8000 elements along the length of the cylinder and at least 5 elements through the thickness of the coating. Due to the the imperfect outer edge of the coating, both triangular and quadrilateral elements were used. The geometries for the simulations were chosen using the criteria as given previously in Table 4.1, through which a total of 72 geometries for the simulations were generated. The use of various l/r values allowed for a sensitivity analysis of the buckling load to the l/r ratio, while also ensuring that many values for the wavelength λ could be obtained for each t/r value. All

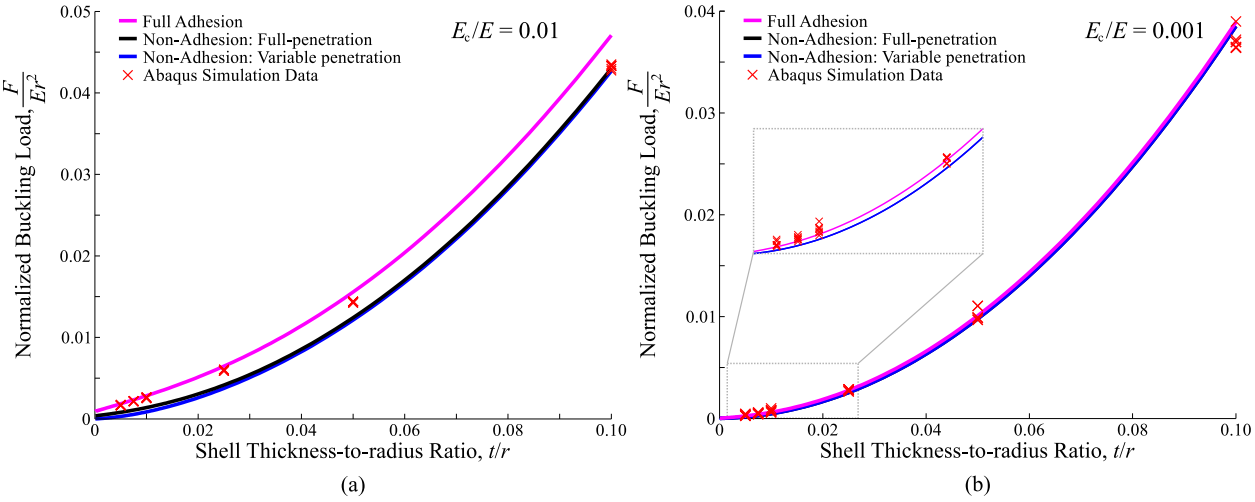

Figure 5.11: Predictions for the buckling loads as functions of t/r for various theoretical models and from Abaqus simulations for (a)$E_c/E = 0.01$ and (b)$E_c/E = 0.01$.

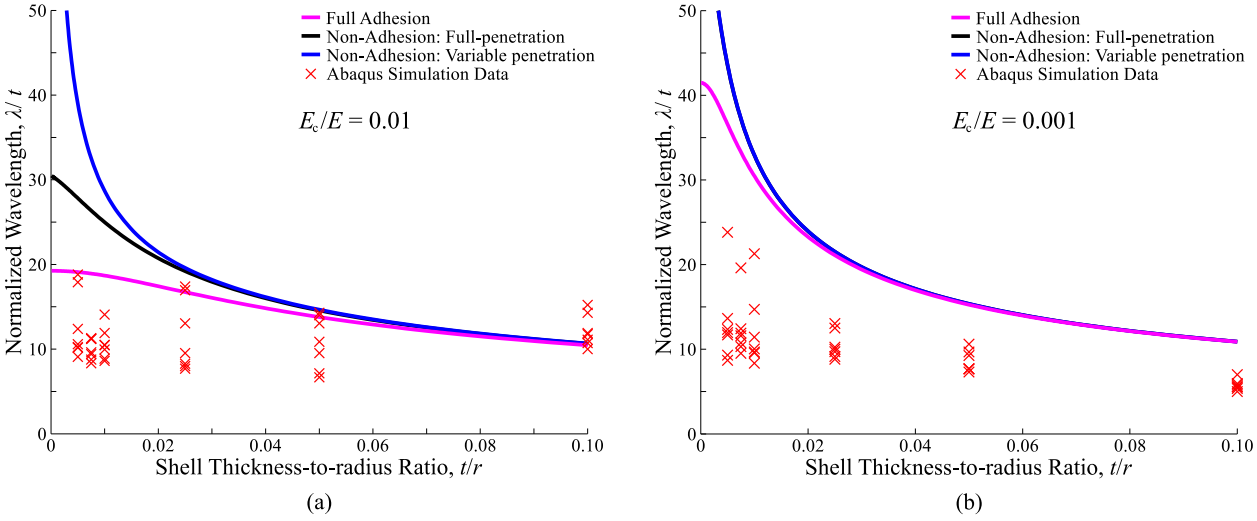

Figure 5.12: Predictions for the buckling wavelengths as functions of t/r for various theoretical models and from Abaqus simulations for (a)$E_c/E = 0.01$ and (b)$E_c/E = 0.01$.

geometries had a length of 50 mm.

5.5.1 Results of Finite Element Verification

As was done for the Abaqus verification results of Chapter 4 (Section 4.4), the buckling loads were calculated from the Abaqus results using Equation 4.17. The calculated loads are presented graphically and compared to the models shown in Figure 5.7.

Figure 5.11(a) shows the Abaqus predictions for the buckling loads as functions of t/r along with the two non-adhesion models (full penetration and varying penetration) as well as for the fundamental model for $E_c/E = 0.01$, while Figure 5.11(b) shows the corresponding information for $E_c/E = 0.001$. As expected, there is little scatter in the load predictions with changing l/r (as shown by overlapping data points),

indicating the buckling load is insensitive to this parameter as predicted by the model.

For the intermediate core stiffness ($E_c/E = 0.01$ as shown in Figure 5.11), there is a closer agreement at lower t/r between the fundamental predictions and the loads found through Abaqus. However, as t/r increases, the buckling loads agree more closely with the non-adhesion models. At the higher t/r, the predictions of the full penetration and varying penetration models are similar. However, at lower t/r, the varying penetration model predicted much lower critical loads than the Abaqus calculations. The reduced agreement between the model and simulation data at low t/r values suggests an opposite trend compared to that of the model (refer to Figure 5.9). The model suggests that there is lower penetration (i.e. lower b/λ) at lower t/r values for the variable penetration model when $E_c/E = 0.01$. The loads predicted through simulations, however, are consistently lower than loads predicted for full-adhesion (fundamental) simulations in Abaqus (refer to Figures 4.6(a) and 4.6(b) in Chapter 4), indicating that there is a loss of load-bearing capability. The degree to which loss of load carrying capacity is captured by the non-adhesion model is inadequate as ascertained through the Abaqus simulation data. It is possible that this is due to the assumed deformed shape used for the non-adhesion model or even the methods chosen to represent the behaviour (for instance the use of the variable b/λ).

This disagreement between the Abaqus simulation data and the loads predicted by the non-adhesion models is narrowed when $E_c/E = 0.001$, as expected given the reduced importance of the core. As seen in Figure 5.11(b), there is increased agreement between the loads as found through the simulations and those given by the fundamental and varying penetration models. A detail of the data at low t/r (shown in the inset of Figure 5.11(b)) reveals how the loads are still closer to the fundamental model, as was the case for $E_c/E = 0.01$. However, the Abaqus loads are closer to the non-adhesion model than for $E_c/E = 0.01$ (Figure 5.11). Because the reduced stiffness of the core already narrows the difference between the non-adhesion and fundamental models, it is also likely that this may be a contributing factor in narrowing the gap between the loads as found through finite element simulations and the predicted loads from the model.

For $E_c/E = 0.01$, the lack of agreement between the Abaqus results and non-adhesion models is further seen upon inspection of the λ/r plots. Figures 5.12(a) and 5.12(b) show the wavelengths predicted by Abaqus during buckling. The full-penetration, varying penetration, fundamental and hollow-shell models are also shown on these Figures for comparison. Each data point on these graphs represents the wavelength as calculated using $\lambda = 2l/m$, and there is scatter in the data points is because discrete numbers for wave counts (i.e. m) are being compared to theoretical values originally calculated as continuous quantities. When the cylinders become very long (i.e. large l/r), the number of waves would be high enough that this scatter would be less apparent, but geometries with these l/r values would be more susceptible to global buckling.

The low wavelengths as predicted by Abaqus (shown in Figures 5.12(a) and 5.12(b)) compared to the non-adhesion model (and further the fundamental model) indicate that there is a disagreement between the models and the simulations. As the buckling load is dependent upon the critical wavelength, an estimate of the buckling wavelength is required in order to accurately estimate the buckling load. Typically, higher λ/t

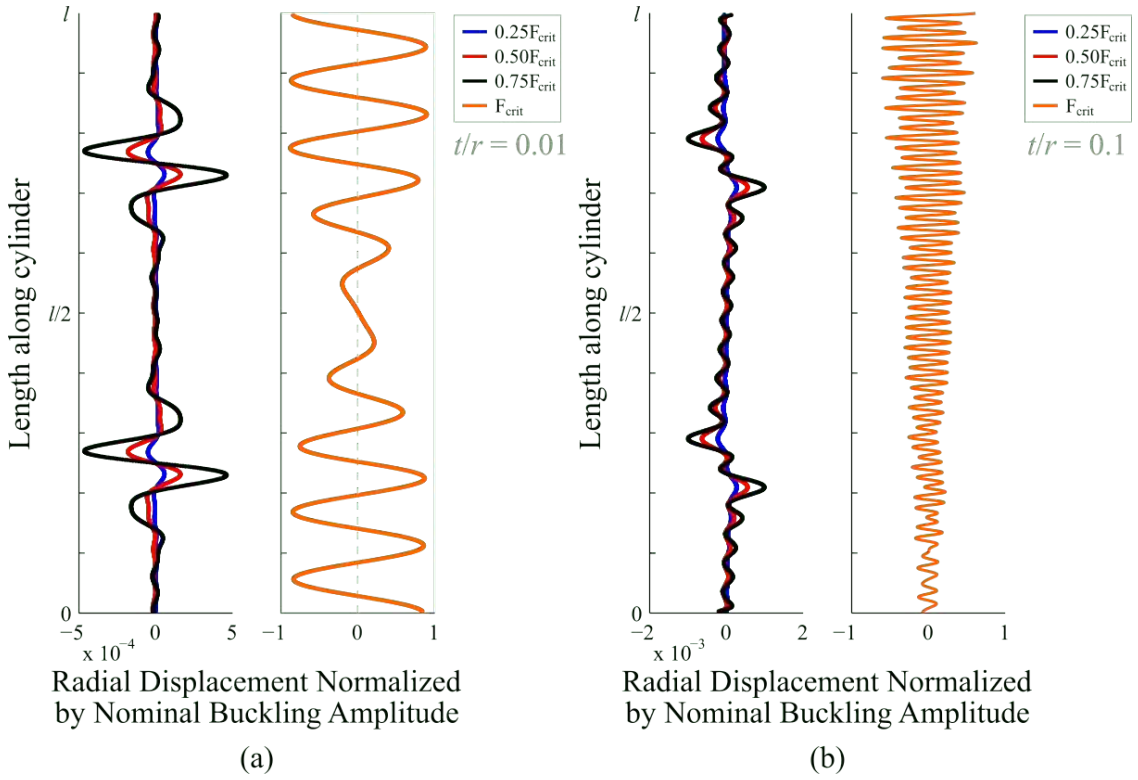

Figure 5.13: Buckling shape progression of the outer edge of the shell for (a)$t/r = 0.01$ and (b)$t/r = 0.1$, in quarter-load increments of the critical load. The data pertains to filled cylinders with $E_c/E = 0.01$ and $l/r = 10$; the final buckled shape of the shell is independent of the imperfection configuration.

values correspond to lower buckling loads and *vice versa*. Thus the higher λ/t predictions of the non-adhesion models are an underlying factor contributing to the lower load estimates compared to the Abaqus results.

5.5.2 Comparing Buckled Shapes between fundamental and Non-Adhesion Abaqus Simulations

Because of the disconnect between the theoretical load predictions and those obtained through Abaqus simulations for non-adhered filled shells, it was warranted to investigate the buckled shapes of some of the geometries found for both the non-adhesion simulations as well as those done previously to validate the fundamental model. The shape of the outer surface of the shell was examined throughout the process of a finite element analyses for several geometries, and their shapes compared with those found from fundamental simulations completed previously.

Figure 5.13(a) shows examples of the buckling progress of the surface of the outer shell over the course of a simulation for $t/r = 0.01$, while Figure 5.13(b) shows the same for $t/r = 0.1$. For both of these Figures, the core relative stiffness was $E_c/E = 0.01$. The lines drawn in these Figures represent the shape of the outer-most shell edge as the simulations progressed at 1/4 increments in load relative to the critical load. The initial waveform in the shapes prior to buckling shows the growth of the initially-generated imperfection pattern applied to the outer cylinder edge (as shown previously in Figure 5.10). In both cases, buckling is

shown to be very abrupt, with no noticeable difference in the progression towards the final buckled shapes between the different values of t/r. These buckled shapes were shown to be nearly identical on the surfaces of the core for these same geometries, indicating that there was no change in the penetration length b/λ with changes in t/r and that the penetration length did not change as the critical load was approached. Of note is that the final buckled shapes of the shells is not dependent upon the initial imperfections.

A comparison between the buckled shapes of the shells for non-adhesion and full adhesion simulations was also done. Figure 5.14 shows the buckled shapes of the shells as found for $t/r = 0.01$ and 0.1 for both non-adhesion and full-adhesion (fundamental) simulations ($E_c/E = 0.01$ for both sets of geometries). While the number of waves initially appears similar for the same t/r values at first glance, a count of the number of half-waves m shows that there are slightly fewer waves for non-adhesion simulations than there are for comparable full-adhesion simulations. This indicates that there is a difference in the behaviour when adhesion between the shell and core is not present, leading to lower buckling loads for the non-adhesion system. The difference in the number of waves is more apparent for thicker shells, as seen on the right side of Figure 5.14.

Of note is the flattened portion towards the centre of the cylinder length for the non-adhesion simulations for both of the t/r values in Figure 5.14. Though not shown here for brevity, this effect is present on many of the other simulated geometries for the non-adhesion analyses. These flattened areas lead to a change in the buckled shape of the shell compared to those found for fundamental, and may be a contributing factor in the variance observed between the Abaqus results and the model. The flattened regions indicate that there is likely an edge effect present on the top and bottom of the shell, which is currently unaccounted for in the model as the buckled shape of the shell assumes a uniform sinusoidal buckled shape for the shell with no changes in wavelength or amplitude along the length of the shell.

5.5.3 Discussion of Disagreement between Abaqus and Analytical Results

The Abaqus results have shown that while non-adhesion is a factor in reducing the buckling load compared to fundamental case, the reduction in the buckling load is not as detrimental compared to the predictions by the analytical model for practical values of core stiffness (i.e. $E_c/E = 0.01$). The buckling loads predicted by Abaqus simulations are closer to full-penetration load predictions at lower t/r, while the wavelengths are much lower than those predicted by the non-adhesion models for all t/r values investigated. Furthermore, there is little evidence of varying penetration in the simulations despite the prediction of low penetration at lower t/r values for $E_c/E = 0.01$.

There are several reasons as to why this disagreement exists. The most likely of these is that the assumed deformed shape is wrong, thereby giving incorrect energy predictions. The flattened regions near the centres of cylinders may cause non-uniform sinusoidal buckles (Figure 5.14), leading to different buckled shapes than assumed for the buckling load derivations. It is also possible that free radial expansion of the core (i.e. due to the separation distance r' in Figure 5.3) causes added Poisson-related effects, which increases

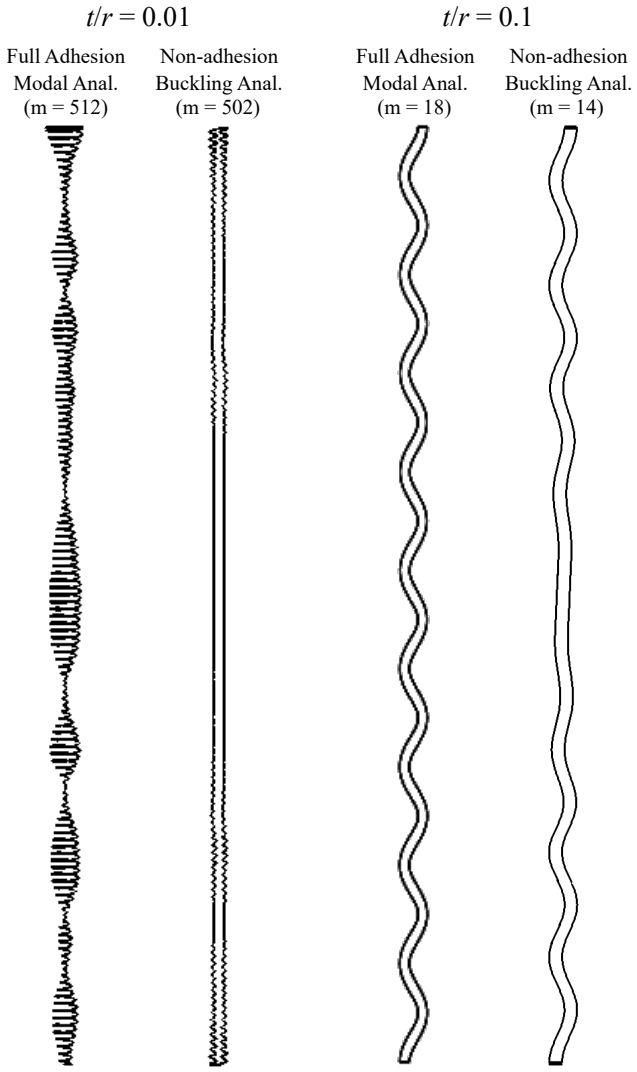

Figure 5.14: A comparison of the buckled shapes of the shells as obtained from Abaqus verification studies for full-adhesion and non-adhesion. All images are provided for $l/r = 10$, with comparisons made for $t/r = 0.01$ and 0.1.

the buckling loads for the low t/r geometries than what is predicted by the model. If present, this effect would be less prevalent at higher shell thickness values whereby the shell would restrict the movement of the core. This would explain the decrease in load closer to the non-adhesion model as t/r increases.

While less likely, it is also possible that some frictional effects are present which are not being accounted for in the buckling load analysis or the simulations. It is to be reiterated that the simulations were run with frictionless tangential contact, which makes this factor even less likely. The end conditions may also play more of a role for non-adhesion than originally accounted for in the buckling load analysis.

Despite the shortcomings of this model, it is seen that although the buckling loads predicted by the non-adhesion model are lower compared to the Abaqus simulation data, the non-adhesion predictions provide a lower bound to the buckling loads of non-adhered filled-shell systems. While practical coated cylinders will likely include partially-adhered metal coatings, the lower bound determined from this model

is nevertheless helpful for design purposes of filled-shell systems under axial compression. It is possible that the simplifications used for this buckling problem (i.e. uniform buckling pattern, use of only one variable to describe penetration length) may not be suitable as the situation may be more complex than can be accounted for by this model.

5.6 Conclusions

A novel model for the axial buckling load of a non-adhered filled-shell system was developed which accounts for a variable penetration depth of a non-adhered buckled shell into a core. This variance in the penetration depth was predicted to lead to lower buckling loads for filled shells with lower thickness-to-radius ratios. Finite element verification of the model, however, found that the buckling loads predicted by the non-adhesion model are lower than the simulated loads. This may be due to the incorrect predictions of the buckle wavelength, likely caused by an incorrectly assumed buckled shape or some misrepresentation of the energy within the shell-core system. It is also possible that the end conditions of a non-adhered shell-core system may have much more of an influence than anticipated. Nevertheless this model presents a lower bound on the buckling load of a non-adhered filled-shell subject to axial compression, nd is a starting point for more complicated problems involving partial adhesion of metal coatings on polymer cylinders.

Chapter 6

Local Buckling of an Elastic Shell Filled with a Hollow Elastic Cylinder

6.1 Introduction

Hybrid microtruss structures provide the high-strength benefits of nanocrystalline metals while utilizing the mass-efficient topology of a microtruss [1, 4, 21]. These structures are produced by 3D printing a polymer microtruss preform and electrodepositing nanocrytalline metal onto the polymer surface. The strength of these structures are governed by compressive instabilities of the cylindrical struts, which are modelled as metal-coated polymer cylinders. Failure mechanisms for metal-coated polymer cylinders have been developed in the preceding chapters, however in these previous models the core geometry remains unchanged. Previous studies treated the polymer as a parasitic mass, and optimization studies on hybrid microtruss structures found that the most mass-efficient designs eliminated the polymer preform [1, 4]. However, as hollow-shell structures are inherently sensitive to imperfections [73, 78, 79, 81], keeping some amount of the polymer core is advantageous for buckling performance. A polymer core which is bored out along its axis is termed a "hollow core", and the buckling of hollow-core filled shells is the topic of this chapter.

The majority of models and experimental programs examining filled-shell buckling have focused on the buckling of a shell containing a solid core [69, 70, 96–99, 101, 103–107]. Rationales behind these studies included investigating natural materials such as porcupine quills [69, 70, 118], developing models for solid propellant launch vehicles [97, 104], and quantifying the effects of steel tubes filled with concrete [105, 106]. Beams on elastic foundations [90, 93] are often utilized as models where the core is treated as bed of independent springs. Others have modelled the core using the same stress distributions as those found in cores of composite sandwich panels where the face sheets are buckling [24, 82, 91, 125].

The investigation of hollow-core filled shells is a less-examined area. One reason for this is the difficulty associated with accurately representing the behaviour of a hollow core. A previous examination of hollow-core buckling utilized assumed stress distributions within the core [5, 116], whereby the stresses in the core were decayed towards the cylinder axis. As the Southwell model is used to solve for stress distributions in solids of revolution [6, 38, 39], it can be used to develop a more accurate model for the hollow core in a filled shell undergoing buckling. However, for a filled shell with a hollow core, this core model is only valid when only the shell buckles. Figure 6.1(a) shows an undeformed filled shell with a hollow core, while Figure 6.1(b) depicts local shell buckling, the case for which a hollow-core model is essential. A second type of buckling

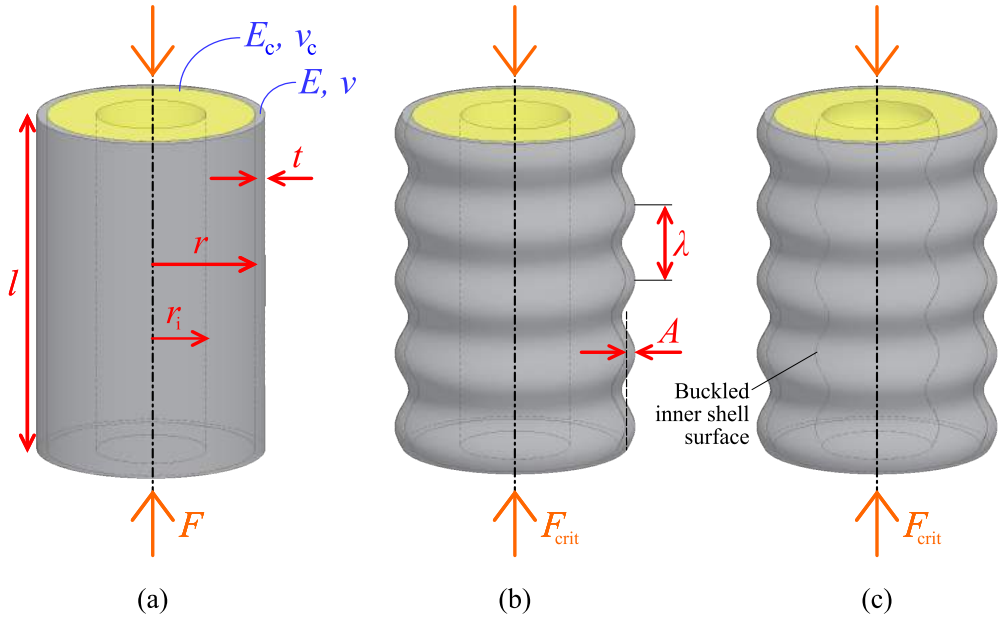

Figure 6.1: Diagrams of a filled cylindrical shell with a hollow core. (a) A filled shell with thickness t, radius r, inner radius r_i and length l under an axial load F. The shell has Young's modulus E and Poisson's ratio ν while the corresponding properties of the core are E_c and ν_c. (b) Depiction of hollow-core local shell buckling with buckle wavelength λ and radial displacement amplitude A. (c) Depiction of simultaneous buckling of the shell and hollow core.

shown in Figure 6.1(c), referred to as simultaneous buckling, where the shell and core buckle in unison.

This chapter details predictions for both the shell buckling load (Figure 6.1(b)) and simultaneous buckling load (Figure 6.1(c)). The former requires a model for the energy behaviour of a hollow core subject to sinusoidal radial displacements, which will be obtained using the Southwell stress model. Finite element analysis will be used to verify these models and determine if the transition point from simultaneous buckling to local shell buckling is consistent with that determined by the models.

6.2 The Hollow-Core Model

The development of a core model requires an understanding of the behaviour of a hollow-core geometry subject to radial sinusoidal displacements. These displacements are the consequence of local shell buckling, as shown in Figure 6.1(b). The core model is essential for determining the local shell buckling load of a filled shell with a hollow core. The model is not required for determining the simultaneous buckling load, as shown in Figure 6.1(c); this will be found using a separate analysis. While undergoing local shell buckling, the shell behaviour is described by the hollow-shell model [34–37].

The sinusoidal buckling pattern along the length of a cylinder, as shown in Figure 6.1(a), is assumed to be axisymmetric around the cylinder circumference. Neglecting the end conditions of the cylinder, a representative axisymmetric section with periodic boundary conditions represents the behaviour of the entire cylinder. A filled shell with a hollow core undergoing local shell buckling is shown in Figure 6.2, and an axisymmetric section of the hollow core is in the same figure. The buckle waves have length λ and

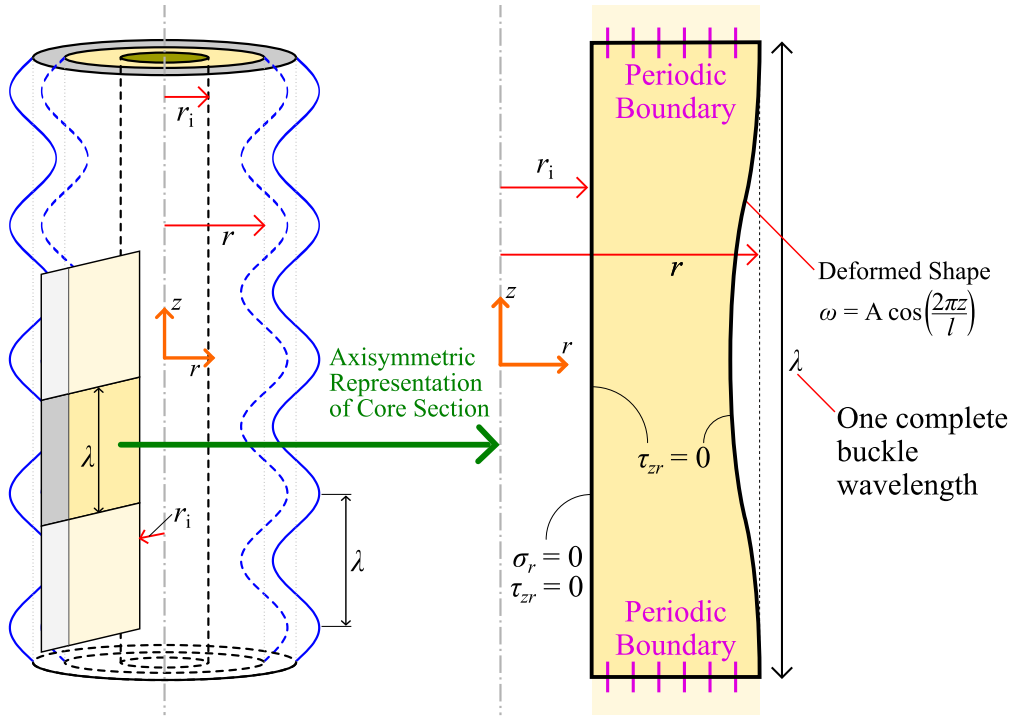

Figure 6.2: A filled shell with a hollow core undergoing buckling deformations, and an axisymmetric section of the core of length λ. The behaviour of this axisymmetric section as solved using the Southwell model is representative of the entire hollow core.

displacement amplitude A. The applied displacement on the antisymmetric core section in Figure 6.2, as well as the length of this core section, are $A\cos(2\pi z/l)$ and λ, respectively. Periodic boundary conditions are used for the axisymmetric core section, as the periodic nature of the sinusoidal buckling waves and the assumption of many waves during buckling allow for the core behaviour to be represented using one wavelength. As shown in the Figure, the inner hollow section of the core has radius r_i, while the core-shell interface radius is r. A new parameter $\overline{h}$ is introduced which takes the value r_i/r, and is referred to as the hollowness factor of the core. Its values range between 0 and 1, representing fully filled and completely hollow cores, respectively. In the limit of $\overline{h} = 1$, the shell is completely hollow.

Using the Southwell model and the associated equations [6, 38, 39, 121], the stress state inside this representative domain of the core (Figure 6.2) can be found. The solutions to the Southwell model equations requires stress boundary conditions as it is a solution to the stress state of an axisymmetric domain. For the hollow core section shown in Figure 6.2, these are provided by the conditions of the cylinder, while the outer surface will be subject to a stress field σ_0 previously given in Equation 3.10 of Chapter 3. The stress field on the outer core surface provides a sinusoidal radial load with a form similar to that of the sinusoidal displacement shown in Figure 6.2. For the fundamental model (Chapters 3 and 4), this was found to provide an accurate representation of the buckling displacements.

It is desirable to have a model for the core section of Figure 6.2 which calculates strain energy for any given values of the buckle wavelength λ, the hollowness factor $\overline{h} = r_i/r$ and radius r. This requires that the stress state of the core be found, followed by the calculation of the strain fields in the relevant coordinate

directions. The strain energy can then be calculated for a known applied radial load magnitude σ_0. Similar to the behaviour of the non-adhesion model in Chapter 5, the core model for hollow-core filled-shell buckling is a function of the buckle wavelength λ. Thus, calculations must be done for many buckle wavelengths and for various core geometries in order to develop a complete model for the core.

A model for the core will be developed which will provide the energy in a polymer hollow core subject to a sinusoidal radial displacement with magnitude A. This will be a function of the hollowness factor $\overline{h}$ and the buckle wavelength λ. In order to develop this model, the internal energy of the core section shown in Figure 6.2 is to be found for $\overline{h}$ values between 0 (fully filled shell) and 1 (completely hollow shell), for normalized buckle wavelengths (λ/r) between 0 and 1. Buckle wavelengths ratios higher than 1.0 are unnecessary as these higher values would imply physically unobtainable wavelengths, which are not observed in elastic local shell buckling of filled shells [98, 104].

6.2.1 Data Generation

When the core was a solid polymer cylinder (Chapter 3), the internal energy of the solid polymer core subject to a sinusoidal displacement was determined. The equation for the fit co-efficient K took the form:

$$K = \frac{U}{A^2 \pi r}, \tag{6.1}$$

where U is the internal energy of the core, A is the buckling displacement magnitude as shown in Figure 6.2(b) and r is the outer radius of the core. For solid polymer cores, there is no dependence between the energy and the buckle wavelength λ. However, for a hollow core, the fit-coefficient is instead a function of the hollowness factor and the ratio of buckle wavelength-to-radius, i.e. $K(\overline{h}, \lambda/r)$. The form of this function must be determined in order to develop the form of the function $K(\overline{h}, \lambda/r)$.

As the Southwell model requires stress boundary conditions [6, 38, 39, 121], an algorithm was written which finds the required stress amplitude to generate a desired buckling displacement. A fixed value of $A/\lambda = 0.01$ was chosen to normalize the value of A across all geometries studied. The value of $U/(A^2\pi r)$ was found for geometries with $\overline{h}$ varying between 0 and 1, each of these examined with λ/r values ranging between 0 and 1. Figure 6.3 shows the values of $U/(A^2\pi r)$ as a function of λ/r for the various values of $\overline{h}$. The information presented in these Figures was generated using $E_c/E = 0.01$, with $E = 125$ GPa corresponding to the value for nanocrystalline nickel [7]. There is little difference in the energies for the various $\overline{h}$ values when λ/r is close to zero. However, the energy stored in the hollowest cores (i.e. $\overline{h}$ close to 0) is reduced significantly as λ/r becomes larger. This is to be expected as there is less energy contained in hollower cores.

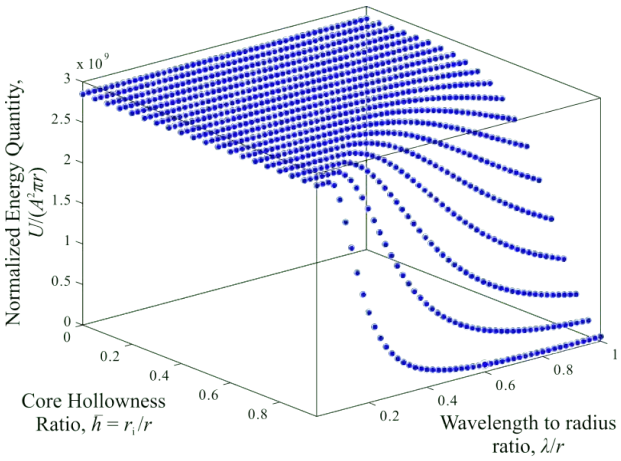

Figure 6.3: Energy behaviour as a function of the buckle wavelength λ/r and core hollowness factors $\overline{h}$.

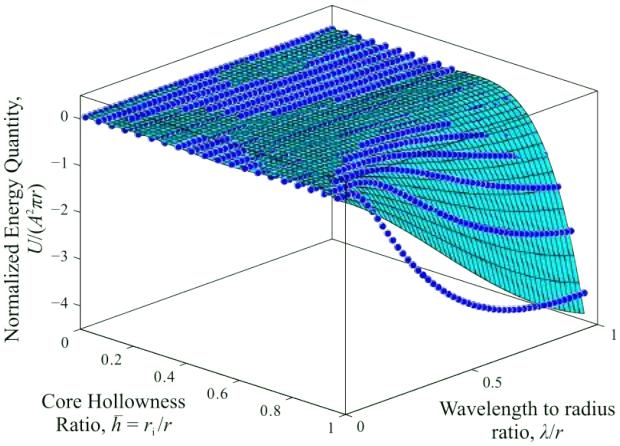

Figure 6.4: Energy behaviour as a function of the buckle wavelength λ/r and core hollowness factors $\overline{h}$, and fitted surface of Equation 6.2.

6.2.2 Model Development

A function must be fit to the data shown in Figures 6.3 so that the energy in a hollow core can be found for any core geometry and buckle wavelength. In addition, the model for the energy behaviour of the core must be a differentiable function of A, as this allows the model to be used when determining the buckling load for a filled shell with a hollow core.

For the data shown in Figures 6.3, the function found to fit this data was a least-squares fitted, 5^{th}-order two-dimensional polynomial of the form:

$$\begin{aligned} K\left(\overline{h},\ \frac{\lambda}{r}\right) = K_{\text{f}} \exp\Bigg[& p_{00} + p_{10}\overline{h} + p_{01}\frac{\lambda}{r} + p_{20}\overline{h}^2 + p_{11}\overline{h}\frac{\lambda}{r} + p_{02}\left(\frac{\lambda}{r}\right)^2 + p_{30}\overline{h}^3 + p_{21}\overline{h}^2\frac{\lambda}{r} + \\ & p_{12}\overline{h}\left(\frac{\lambda}{r}\right)^2 + p_{03}\left(\frac{\lambda}{r}\right)^3 + p_{40}\overline{h}^4 + p_{31}\overline{h}^3\frac{\lambda}{r} + p_{22}\overline{h}^2\left(\frac{\lambda}{r}\right)^2 + p_{13}\overline{h}\left(\frac{\lambda}{r}\right)^3 + \\ & p_{04}\left(\frac{\lambda}{r}\right)^4 + p_{50}\overline{h}^5 + p_{41}\overline{h}^4\frac{\lambda}{r} + p_{32}\overline{h}^3\left(\frac{\lambda}{r}\right)^2 + p_{23}\overline{h}^2\left(\frac{\lambda}{r}\right)^3 + p_{14}\overline{h}\left(\frac{\lambda}{r}\right)^4 + p_{05}\left(\frac{\lambda}{r}\right)^5\Bigg] \\ = K_{\text{f}} \exp(\hat{K}), & \end{aligned} \tag{6.2}$$

where K_f is the fundamental model constant for the core material (obtained from using Equation 6.1 for a solid core as in Chapter 3), K is the fitting function for the hollow core, and $\hat{K}$ contains the contracted two-dimensional polynomial. As Equation 6.2 implies, this is a logarithmic fit to values of $U/(A^2\pi r)$ normalized against the fundamental model energy quantity for a solid polymer core of the same material. The graph of this fitting function together with the original data is shown in Figure 6.4. Using Equation 3.15 in Chapter 3, the energy function for a hollow core of any degree of hollowness can then be expressed as:

$$U_{\text{p}} = K\left(\overline{h},\ \frac{\lambda}{r}\right)\frac{m}{2}A^2\pi r, \tag{6.3}$$

where m is the number of half-buckle waves. Other than the representation of K as the two-dimensional polynomial in Equation 6.2, this energy expression is similar to that found for full adhesion (Equation 3.15 in Chapter 3). The $m/2$ multiplier accounts for many buckle waves encountered in a complete cylinder, instead of just one wave as represented by the core domain Figure 6.2.

It is to be noted that while the value of $\overline{h}$ is required in order to find a value for K, it is not a parameter of the energy minimization problem. Allowing $\overline{h}$ to be a variable for energy minimization would cause the hollow-shell buckling solution to be obtained, and not solutions for different core hollowness factors. Thus, the value of $\overline{h}$ is chosen prior to the energy minimization, as this value defines the geometry of the core.

6.3 Critical Buckling Loads for Filled Shells with Hollow Cores

The axial local shell buckling load for a filled cylindrical shell with a hollow core (Figure 6.1(b)) is found by determining the minimum energy required when buckling is incipient [34, 73, 77]. The buckling load is found as a function of the critical buckling wavelength for the shell, which is part of the energy minimization solution. Since a thin hollow core can also lead to buckling of the shell and core simultaneously (Figure 6.1(c)), this is another critical load of a filled shell with a hollow core. The derivation for both of these critical loads will be detailed in this section, followed by a comparison of these buckling loads to existing theories for filled-shell buckling.

6.3.1 Critical Buckling Load for Shell Buckling

A filled cylindrical shell with a hollow polymer core is subject to an axial load F, as shown in Figure 6.1(a). The shell has Young's modulus E and Poisson's ratio ν, while the corresponding material properties of the core are E_{c} and ν_c. The shell has a thickness of t, while the shell-core common surface has radius r. The hollow core has inner radius r_{i} while the cylinder has length l. The buckle waves have length λ and axial displacement magnitude A, as shown in Figure 6.1(b).

While undergoing buckling, the strain energy accumulates in the shell due to bending U_{b} and the circumferential stretching energy U_{c}. The shell bending energy refers to the energy contained under the bending action of longitudinal sections of the shell as they undergo sinusoidal buckling deformations (Equation 4.2 in Chapter 4), while the circumferential stretching energy is the circumferential tension or compression of the shell hoop sections [34] (Equation 4.3 in Chapter 4). The core energy U_{p} is the energy of the core subject to radial sinusoidal displacements, and has the form given in Equation 6.3.

The procedure and assumptions for deriving the local shell buckling load for a filled shell with a hollow core are the same as those used previously for a filled shell with a solid core (refer to Section 4.2 of Chapter 4). In this way, the local shell buckling load for a filled shell with a hollow core is given as:

$$F = \left(1 + \frac{E_{\mathrm{c}}}{E}(1-\overline{h}^2)\frac{r}{2t}\right)\left[\frac{2\pi^3 r E t^3}{3(1-\nu^2)}\frac{1}{\lambda^2} + \frac{Et}{2r\pi}\lambda^2 + \frac{r}{\pi}K\left(\overline{h},\ \frac{\lambda}{r}\right)\lambda\right]. \tag{6.4}$$

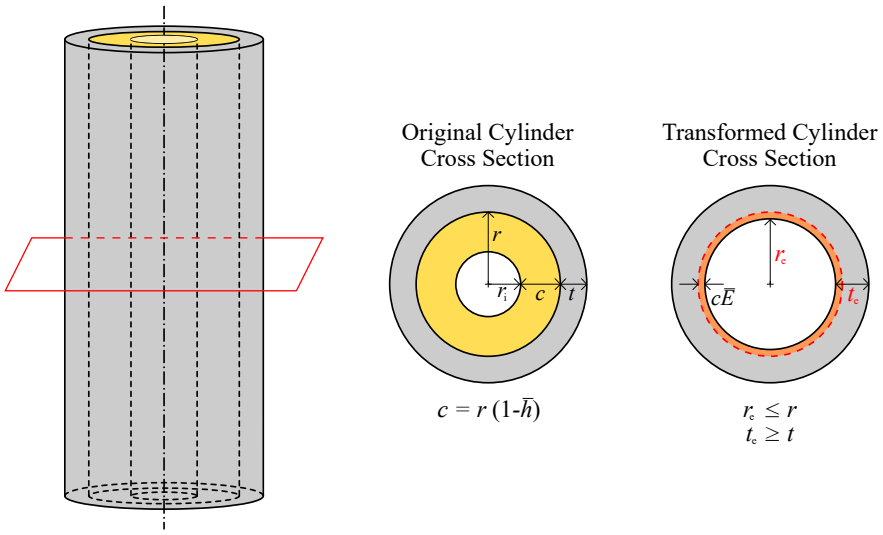

Figure 6.5: Diagram showing original and transformed cross sections of filled cylinder with hollow core. The dimension c is introduced while new dimensions r_e and t_e result from this method of transformed sections

This equation is nearly identical to that of the buckling equation for a filled shell with a solid polymer core (Equation 4.11 in Chapter 4), except that the correction term leading the equation now accounts for the presence of a hollow core instead of a completely filled core and the fitting constant K is now the function $K(\overline{h}, \lambda/r)$ (Equation 6.2).

Equation 6.4 applies for any buckle wavelength λ. However for a given cylinder with known material properties and geometry as shown in Figure 6.1(a), only one value of λ yields the lowest load. This critical λ is found by finding the positive real root of the expression $\partial F/\partial\lambda = 0$. Once found, the critical value of λ is substituted into Equation 6.4 to give the critical load for a filled cylindrical shell with a hollow core. Because $K(\overline{h}, \lambda/r)$ contains the buckle wavelength λ, this precludes an analytical solution for λ and a numerical solution for λ is required.

6.3.2 Critical Buckling Load for Simultaneous Buckling

When the core is sufficiently hollow, the thin membrane that remains after much of the core is removed does not act as enough of a foundation to absorb radial deflections of local shell buckling. Instead, it buckles in tandem with the shell as in Figure 6.1(c), often at a buckling load closer to the hollow-shell buckling load. The thin remaining core effectively acts to thicken the metal shell. The method of transformed sections [67] can be utilized to find the effective thickness of the thin remnant of the core as it supplements the shell, as shown in Figure 6.5. The hollow core cross section with dimensions of r_i and r is transformed into an equivalent section using a modulus-weighed transformation. The new cross section for the shell has new dimensions t_e, r_e and $c = r(1 - \overline{h})$. Using the new section, a new hollow-shell buckling load for a filled cylinder with a hollow core can be found. This will be done by modifying the existing equation for local shell buckling of a hollow shell.

The hollow-shell local buckling equation is [34, 35, 37, 74]:

$$\sigma_0 = \frac{E}{\sqrt{3(1-\nu^2)}}\frac{t}{r},$$

where σ is the buckling stress, E is the Young's modulus of the shell material, ν is its Poisson's ratio, t is the thickness of the shell as shown in Figure 6.5 and r is the inner radius of the shell. As a load, F_0, this expression becomes:

$$F_0 = \frac{2\pi E t^2}{\sqrt{3(1-\nu^2)}}. \tag{6.5}$$

The addition of the inner layer of core material, as in Figure 6.5, leads to an effective thickening of the shell. However, due to differences in material properties between the shell and core, the polymer core contributes less to the total shell buckling strength because of its smaller stiffness. The effective thickness of the shell, using a modulus-weighted transformed section for the core [67], is:

$$t_\mathrm{e} = t + r(1-\overline{h})\frac{E_\mathrm{c}}{E} = t + c\overline{E}, \tag{6.6}$$

while the transformed inner radius is

$$r_\mathrm{e} = r - r(1-\overline{h})\frac{E_\mathrm{c}}{E} = r - c\overline{E}. \tag{6.7}$$

The term $\overline{E} = E_\mathrm{c}/E$ in Equations 6.6 and 6.7 is the ratio of the core stiffness to that of the shell. The method of solution for the simultaneous buckling load follows that of Timoshenko [34] for hollow shells. The flextural stiffness $D = E/(1-\nu^2)$ [123] is modified for the core contribution [5]:

$$D_\mathrm{sb} = \frac{E}{1-\nu^2}\left[\frac{t^3}{12} + t\left(c + \frac{t}{2} - y_0\right)^2 \frac{c^3\overline{E}^3}{12} + c\overline{E}\left(y_0 - \frac{c}{2}\right)^2\right],$$

where the centroid y_0 is defined as:

$$y_0 = \frac{\left(c + \frac{t}{2}\right)t + \frac{c^2\overline{E}}{2}}{t + c\overline{E}}.$$

The expression for D_sb is utilized in the buckling stress equation derived by Timoshenko [34]:

$$\sigma_\mathrm{SB} = \frac{2}{r_\mathrm{e}t_\mathrm{e}}\sqrt{ED_\mathrm{sb}t_\mathrm{e}},$$

which as a load is written as:

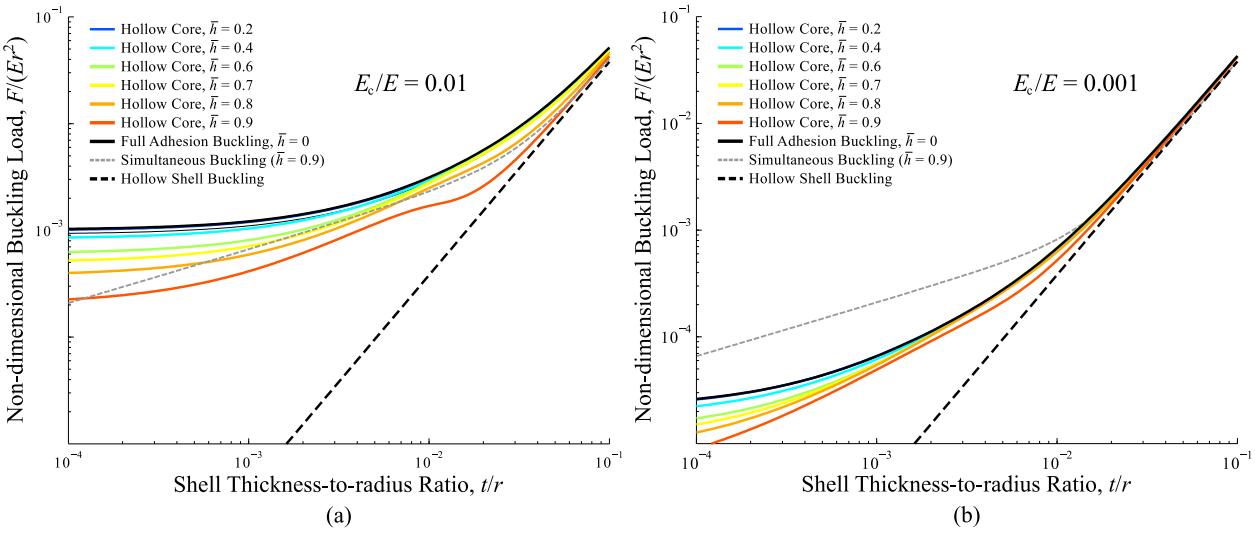

Figure 6.6: Predictions for the buckling load for a range of hollowness factors $\overline{h}$ as a function of t/r for (a)$E_c/E = 0.01$ and (b)$E_c/E = 0.001$. The predictions for simultaneous buckling for $\overline{h} = 0.9$ and the hollow-shell buckling are also shown.

$$F_{SB} = 4\pi E \left\{ \frac{t + \overline{E}(1-\overline{h}^{\,2})}{1-\nu^2} \left[\frac{t^3}{12} + t\left((1-\overline{h}) + \frac{t}{2} - y_0\right)^2 + \frac{(1-\overline{h})^3\overline{E}^3}{12} + (1-\overline{h})\overline{E}\left(y_0 - \frac{(1-\overline{h})}{2}\right)^2 \right] \right\}^{1/2}. \tag{6.8}$$

This is the load at which simultaneous buckling of the shell and core takes place (Figure 6.1(c)).

6.4 Hollow-core Buckling Load

The buckling load for a filled shell with a hollow core will be found as a function of t/r for two different core stiffness values ($E_c/E = 0.01$ and 0.001, where $E = 125$ GPa). The behaviour is compared to hollow-shell buckling (Equation 6.5), and will be verified through modal analyses using Abaqus. The value of E was chosen to be that of nanocrystalline nickel with an average grain size of approximately 65 µm [7].

Figure 6.6(a) shows the non-dimensional critical loads for $E_c/E = 0.01$ as a function of λ/t for the fundamental model and for filled shells with hollowed cores of various hollowness ratios $\overline{h}$. The hollow-core model is equivalent to fundamental filled-shell model for $\overline{h} = 0$, and thus the fundamental model is an upper bound on the load for the hollow-core model. Figure 6.6(b) shows the non-dimensional load curves for $E_c/E = 0.001$. The simultaneous buckling load (Equation 6.8) is only shown for $\overline{h} = 0.9$ in Figure 6.6(a), as $\overline{h}$ values higher than this lead to the simultaneous buckling load being higher than the corresponding hollow-core load.

There is a decrease in the load carrying capacity of the shell as t/r decreases, and also while $\overline{h}$ decreases. There is a more distinct decrease in load at lower $\overline{h}$ with smaller t/r, implying that a hollow core is more

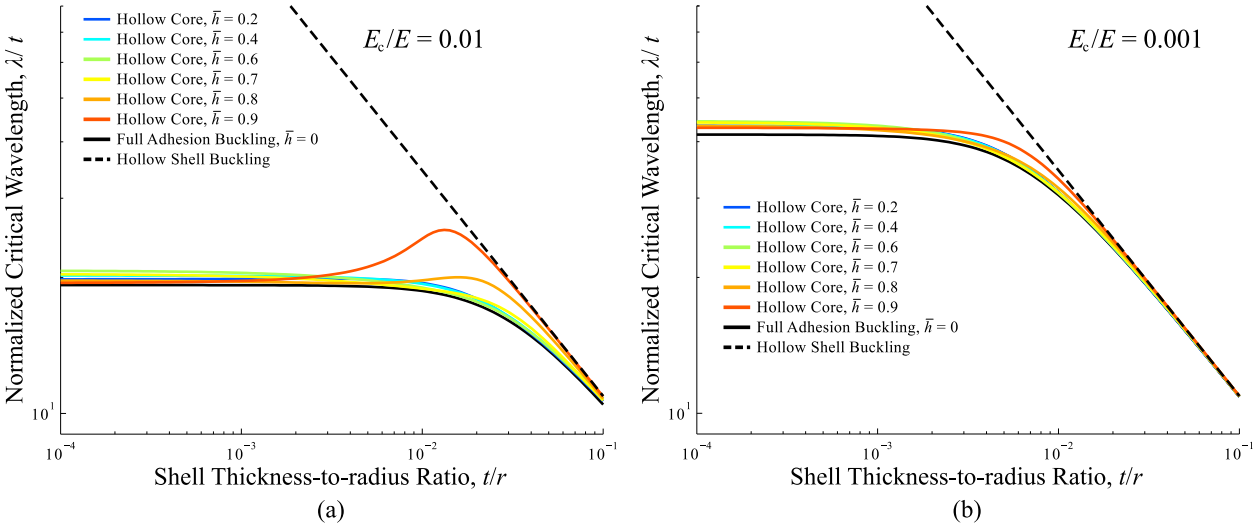

Figure 6.7: Predictions of the critical wavelengths for various core hollowness factors $\overline{h}$ as a function of t/r for (a)$E_c/E = 0.01$ and (b)$E_c/E = 0.001$.

detrimental to the strength of the filled shell for smaller shell thickness values. For $E_c/E = 0.01$ (Figure 6.6(a)) it is seen that near $t/r = 0.01$, there is a marked decrease in the buckling load when $\overline{h} = 0.9$, while there is a less-pronounced decrease in the buckling load at lower values of $\overline{h}$. The cause for this sudden decrease in the buckling load is not known, however it is hypothesized that this reduction is due to the hollow core approaching the hollow-shell buckling load for the same t/r. While it is possible that there is some interaction occurring between the hollow-shell and simultaneous buckling modes, the hollow-core shell model (Equation 6.4) is not intended to account for any interaction of this nature. The load predictions in Figure 6.6(a) shows that the simultaneous buckling model predicts lower loads than the hollow-core model when t/r is very small; this is not where this drop in the hollow-core load occurs. The simultaneous buckling load is also lower when t/r is very large.

For the hollow-core shell buckling predictions, the same trends hold for this more compliant core (6.6(b)) when compared to the behaviour of the predictions for $E_c/E = 0.01$ (Figure 6.6(a)). However, the simultaneous buckling load predictions for $\overline{h} = 0.9$ are much higher than the corresponding hollow-core behaviour. This implies that as the core becomes more compliant, the hollow-core shell buckling load will become dominant while the simultaneous buckling mode is of less importance.

Figures 6.7(a) and (b) show the non-dimensional critical wavelengths for $E_c/E = 0.01$ and 0.001, respectively, for values of $\overline{h}$ for which the critical loads were shown in Figures 6.6(a) and (b). Although the loads for hollow-core shell buckling are well above those predicted for hollow-shell buckling for $E_c/E = 0.01$ (Figure 6.7(a)), there is a potential for the shell to have nearly the same buckle wavelength as would be seen for a hollow shell without any supporting core material. The appearance of the corresponding load predictions for $\overline{h} = 0.9$ in Figure $E_c/E = 0.01$ (Figure 6.7(a)), may explain the large bulge in the load behaviour seen previously in Figure 6.6(a): because the wavelength predictions for hollow-core shell buckling are closer to those of hollow-sell behaviour, these loads are tending to equality for $t/r \approx 0.015$.

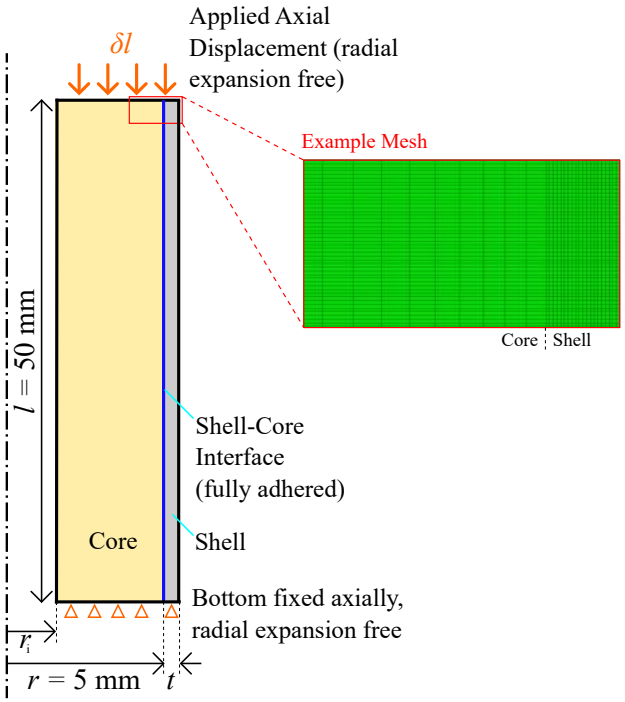

Figure 6.8: Diagram showing the setup of an Abaqus simulation for an axisymmetric section of a filled shell with a hollow core. The section has with length $l = 50$ mm, radius $r = 5$ mm, shell thickness t, and inner radius r_i determined by the value of $\bar{h}$. The top is loaded with a displacement δl, while the bottom cannot move axially. Radial expansion is allowed on both the top and bottom. An example of a meshed geometry is also provided.

6.5 Finite Element Verification of the Hollow-core Model

The critical values of load for a filled shell with a hollow core were verified using modal analyses in Abaqus. The criteria used for geometry selection is given in Table 6.1. The length-to-radius ratio of the cylinder was kept at 10, deemed to be an appropriate ratio based on the actual geometries of coated microtruss structures [4, 21]. With the criteria in Table 6.1, a total of 120 geometries were generated and their buckling loads found using modal analysis in Abaqus.

Figure 6.8 shows the finite element simulation setup for the hollow core simulations. A section of the filled shell was used to represent the axisymmetric behaviour of the entire cylinder, which means that buckling deformations determined would be axisymmetric about the cylinder circumference. The top and bottom edges of the cylinder were allowed to move radially. The radius r was fixed at 5 mm while the cylinder length was chosen to be 50 mm, yielding the desired criterion l/r value of 10. A displacement was applied to the top edge as shown in Figure 6.8, and the resulting eigenvalues from the analysis are the displacements at which buckling occurs. All geometries were meshed using quadrilateral elements, with at least 7 elements through the thickness of the shell. The mesh was generated such that elements had an aspect ratio of nearly 1.0 inside the shell area, with larger aspect ratio elements used in the core to reduce computation time. An example mesh is shown in the inset of Figure 6.8.

The Abaqus subspace eigenvalue solver was used to find the buckling modes, with three modes re-

Table 6.1: List of criteria for the cylinder geometries chosen for verification simulations of hollow-core model using Abaqus.

Quantity	Chosen values
Thickness-to-radius ratios (t/r)	0.005, 0.0075, 0.01, 0.025, 0.05 and 0.1
Length-to-radius ratios $^{*}(l/r)$	10
Hollowness ratios ($\overline{h}$)	Between 0 and 0.9, in increments of 0.1
Relative core stiffness ratio (E_c/E)	0.01 and 0.001

* Fixed at 10 for hollow-core verification simulations, with $r = 5$ mm and $l = 50$ mm.

quested. The resulting values returned by the solver indicate the displacements at which buckling would occur. The number of half-waves from each mode shape was used to compare the number of buckle waves and their wavelengths to theoretical estimates.

6.5.1 Comparison of Modal Analysis Solutions to Analytical Values

The simulations run for every case converged, yielding three eigenvalues and corresponding mode shapes for every geometry. For each case, all three eigenvalues were very close in value, the difference between the highest and lowest eigenvalues being less than 0.5% for the majority of the geometries. This implies that many buckling modes are possible for the hollow shell structures near the critical load, and that the buckling loads required to attain these modes are very close to each other or that multiple modes may be superimposed upon one another at the critical load [83–85]. This observation also further illustrates that the buckling load is independent of the mode shape, an observation which holds true for hollow shell buckling [34, 35, 37, 75] and for filled-shell buckling (Chapter 3). Due to the number of results obtained from the finite element simulations, several graphs are presented to compare and contrast the differences between the simulation results and the analytical buckling loads.

Figures 6.9(a) and (b) show the load predictions for a hollow core with $\overline{h} = 0.3$, for core stiffness values of $E_c/E = 0.01$ and $E_c/E = 0.001$ respectively. The load predictions for the relevant geometries as determined from Abaqus modal analyses are also shown on these graphs. The hollow-core analytical predictions and Abaqus results for $\overline{h} = 0.6$ are shown in Figures 6.9(c) and (d), while the same data for $\overline{h} = 0.9$ is shown in Figures 6.9(e) and (f). Although Abaqus simulations were performed for every 0.1 increment of $\overline{h}$ (refer to Table 6.1), only these graphs are presented for brevity.

It is seen in Figures 6.9(a) and (b) that the analytical predictions are very close to the loads calculated from finite element analyses, for both of the core stiffnesses. However, as seen in Figures 6.9(c) through (f), there is a larger disagreement between the simulation data and the analytical results as $\overline{h}$ becomes larger, or as the core becomes more hollow. This discrepancy is magnified more for a stiffer core (Figures 6.9(a), (c), and (e)), implying that a stiffer core has more of an effect on the buckling load of a filled shell with a hollow core. This is a trend also seen in the underlying analytical model for hollow core shell buckling.

The loads obtained from simulation data are higher than those predicted by the analysis, the opposite of what would be expected during finite element verification of a model. Typically, the maximum energy that can be calculated from finite element simulations will always be less than the theoretical calculation

for the same result [126]. Given that the hollow core model was derived using an energy model for the core, this could imply a fault in the data used to create the this model or in the curve-fitting procedures used to generate the fit function K (Equation 6.2).

Considering the number of waves as shown in Figures 6.10(a) and (b), for $E_c/E = 0.01$ and 0.001 respectively, there is better agreement with the results for the more compliant core ($E_c/E = 0.001$) than there is for a stiffer core ($E_c/E = 0.01$). The spread of the data points in Figure 6.10(a) ($E_c/E = 0.01$) is much pronounced more than for the lower stiffness case. Specifically, for $\overline{h} = 0.9$ and $t/r = 0.01$, the wavelength predicted for buckling is much higher than that predicted by hollow-shell buckling. The large wavelengths for this geometry are a likely indicator that simultaneous buckling of the shell and core is taking place (refer to Figure 6.1 (b)), even though the hollow core load is lower for this t/r as shown in Figure 6.6(a). A closer look at the mode shapes is warranted to investigate this. The spread in the predicted wavelengths can be reduced by using longer cylinders for the simulations, however this will lead to cylinder geometries where Euler buckling will be more energetically preferable and thus will not be physically representative for local shell buckling.

The complete set of simulation data is shown in Figures 6.11(a) and (b) for core relative stiffnesses of $E_c/E = 0.01$ and 0.001 respectively. These two Figures show values of the buckling loads calculated from the simulations normalized against the load prediction from the fundamental model for a completely filled shell (Equation 4.11 of Chapter 4, or when $\overline{h} = 1$ in Equation 6.4). The predicted loads corresponding to the hollow-core shell buckling load for $\overline{h} = 0.9$ are also plotted on these figures together with the simultaneous buckling load for the relevant E_c/E values. The spread of the simulation data as $\overline{h}$ increases is apparent for each value of t/r, indicating a larger decrease in the buckling load as the core becomes more hollow. This same trend is matched by the analytical values of the hollow-core shell buckling load (refer to Figures 6.6(a) and (b)). In addition, the buckling loads predictions from Abaqus are larger than the corresponding predictions from the hollow-core model for $\overline{h} = 0.9$, indicating that the simulated data is bounded by the predicted loads.

6.5.2 Comparison of Buckled Mode Shapes

It is of interest to examine the buckled mode shapes of some of the geometries to aid in determining when the dominant buckling failure mode will change from hollow-core shell buckling (Figure 6.1(b)) to simultaneous buckling of the shell and core (Figure 6.1(c)). For some geometry $\overline{h}$, there is a given t/r at which it is more energetically efficient to have the core buckle in tandem with the shell instead of the shell buckling alone.

Figures 6.12(a) through (c) show various buckled mode shapes for hollow shells with t/r values of 0.005, 0.05 and 0.1, respectively. For each of these three Figures, the mode shapes corresponding to $\overline{h}$ values of 0 (fully filled), 0.5 and 0.9 are shown. For each geometry, the mode shapes shown are those corresponding to the first eigenvalue that was found through Abaqus modal analysis. All Figures correspond to a material combination of $E_c/E = 0.01$, as simultaneous buckling is not a dominant mode of failure when $E_c/E =$

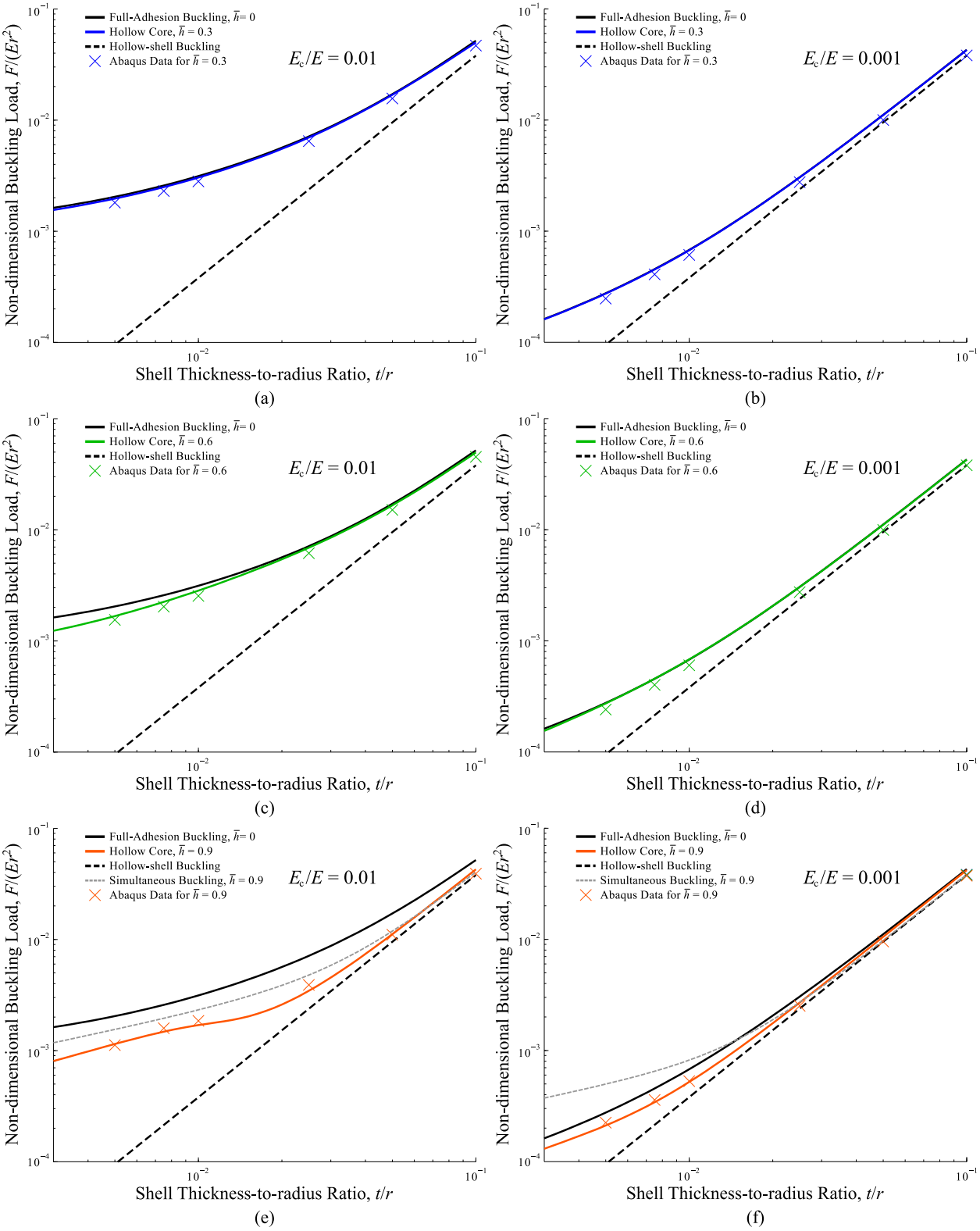

Figure 6.9: Predictions for the buckling load from Abaqus simulations for filled shells with hollow cores for (a) $\overline{h} = 0.3$ and $E_c/E = 0.01$; (b)$\overline{h} = 0.3$ and $E_c/E = 0.001$; (c)$\overline{h} = 0.6$ and $E_c/E = 0.01$; (d)$\overline{h} = 0.6$ and $E_c/E = 0.001$; (e)$\overline{h} = 0.9$ and $E_c/E = 0.01$; and (f)$\overline{h} = 0.9$ and $E_c/E = 0.001$.

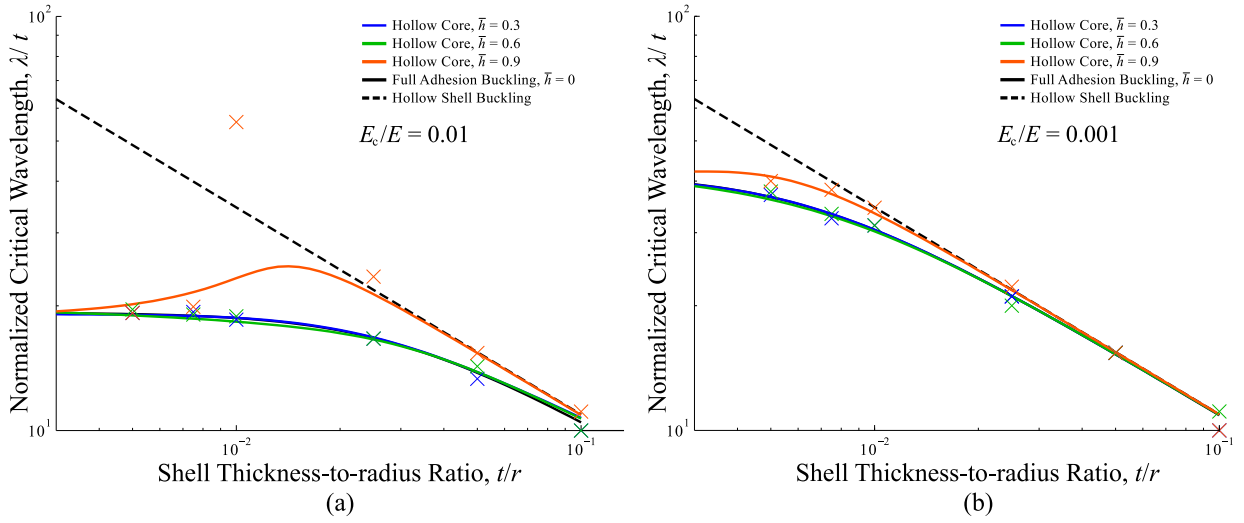

Figure 6.10: Predictions of critical wavelengths from Abaqus for filled shells with hollow cores with $\overline{h}$ = 0.3, 0.6 and 0.9 for (a)$E_c/E = 0.01$ and (b)$E_c/E = 0.001$. The predicted loads for the hollow shell and full adhesion models are also shown for comparison.

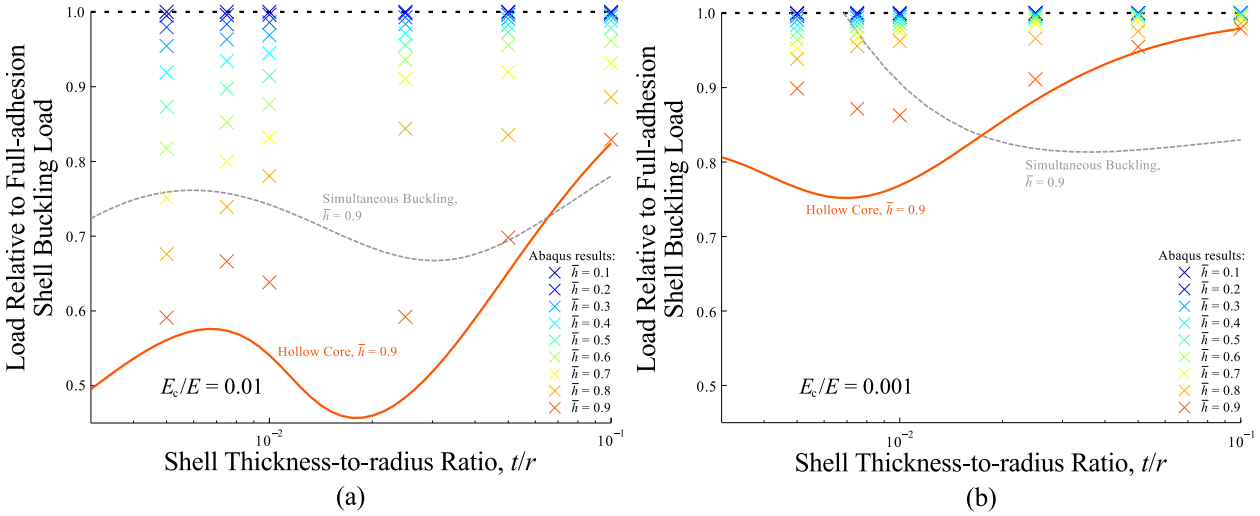

Figure 6.11: Predictions for the buckling loads relative to fundamental model load of same t/r for hollow-core model, simultaneous buckling model and Abaqus simulations for (a)$E_c/E = 0.01$ and (b)$E_c/E = 0.001$.

0.001 (refer to Figure 6.6(b)).

For each individual t/r value, there is a reduction in the number of waves as $\overline{h}$ increases, with a corresponding increase in the wavelength of the waves. This is due to the shifts in the behaviour of the cylinder as it moves from filled-shell ($\overline{h} = 0$), to hollow-core ($0 < \overline{h} < 1$) and finally to hollow-shell ($\overline{h} = 1$). For the same t/r, hollow-shell buckling is accompanied by the same or greater wavelengths as filled-shell buckling (refer to Figures 6.10(a) and (b)).

While the number of waves is a function of cylinder geometry and failure mechanism, the low-frequency mode shape fluctuations are not dependant on the geometry of the cylinder, but rather are unique to the eigenvalue for each specific geometry. The fluctuations are not mesh dependant as there is a large number of quadrilateral elements, and the calculated mode shapes changed little after the geometries were meshed

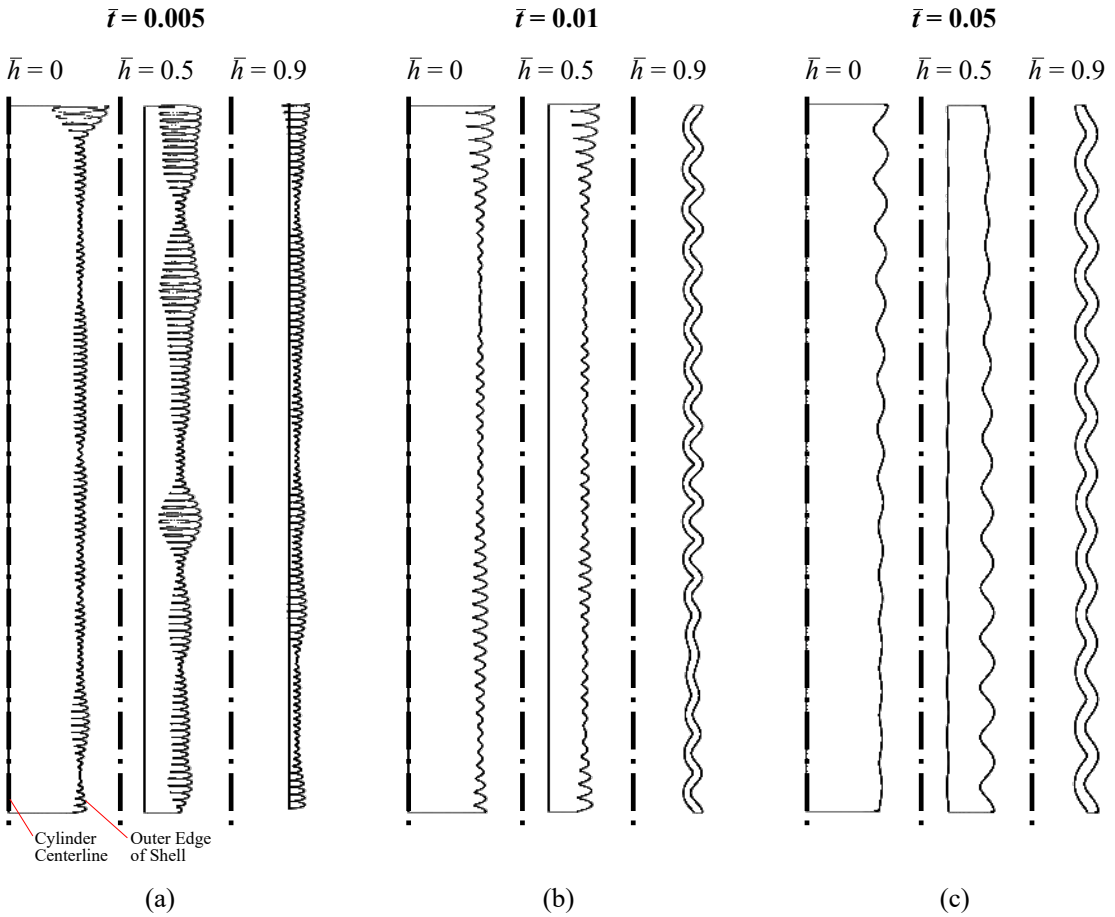

Figure 6.12: Buckled shapes for three hollowness factor ratios $\overline{h}$, shown for a core stiffness ratio $E_c/E = 0.01$ and thickness-to-radius ratios of (a)$t/r = 0.005$, (b)$t/r = 0.01$ and (c)$t/r = 0.05$.

with over 200 000 elements. In addition, the boundary conditions play a strong role in these fluctuations, as restricting radial movement at the top and bottom of the cylinders leads to more symmetrical mode shapes.

For very thin coating thicknesses, or $t/r = 0.005$ (Figure 6.12(a)), buckling of the shell always takes place even when the core is very hollow ($\overline{h} = 0.9$ in the right-most part of the figure). However starting at $t/r = 0.01$ (Figures 6.12(b) and 6.12(c)), a hollow core with $\overline{h} = 0.9$ will lead to simultaneous buckling, where the shell and core buckle in tandem. This leads to larger buckle wavelengths than those predicted by the hollow core shell buckling model, and very close to or exceeding those predicted by the hollow-shell model. Given the appearance of the buckle mode shape for $\overline{h} = 0.9$ in Figure 6.12(b), the outlying calculated wavelength previously highlighted in Figure 6.10(a) (for $t/r = 0.01$) is justified given that complete buckling has occurred for this geometry and material combination. This contrasts to the load predictions of Figure 6.6(a), which shows that hollow-core shell buckling has a lower load and thus should dominate for $t/r = 0.01$. The sharp drop in the hollow-core load prediction for $\overline{h} = 0.9$ may indicate an interaction load between the hollow-core shell buckling and simultaneous buckling loads, even though these loads do not intersect near $t/r = 0.01$. The lack of an intersection near this t/r may indicate that some fine-tuning is necessary for the core model for hollow-core shell buckling prediction. Figures 6.12(a) through 6.12(c) also show that as the

shell thickness becomes very large, simultaneous buckling will always occur for filled shells with very hollow cores ($\overline{h} \geq 0.9$), an observation confirmed by the theoretical behaviour of the hollow-core shell buckling and simultaneous buckling predictions (Figures 6.6(a) and (b)).

6.6 Concluding Remarks

A model for the buckling behaviour of an axially-loaded polymer-filled metal shell with a hollow core has been developed. This required a model which predicts the strain energy in a hollow core undergoing sinusoidal radial deflections, which was used in conjunction with the energy contributions from a shell undergoing buckling deformations in order to determine the local shell buckling load. The load required to cause simultaneous buckling of the shell and core together was also derived. Finite element simulations verified the hollow-core shell buckling load behaviour, while also highlighting some of the weaknesses of the model. Namely, the analytical predictions are lower than the Abaqus results for more hollow core geometries, while the transition from shell buckling to simultaneous buckling is not captured as well in the model. These simulations also showed that simultaneous buckling can lead to wavelengths which are larger than those corresponding to hollow-shell buckling for the same shell geometry. In addition, the simulations revealed that the buckling loads for hollow-core filled shells may be lower than those predicted by the model, and this may warrant a closer look at the curve-fit used for the core model.

Future investigations into filled shells with hollow cores should possibly look at more complex fitting models for the core energy behaviour. This should alleviate the current issue whereby the transition to simultaneous buckling is not being found accurately. In addition, future studies should also consider the role that end conditions have in the mode shapes calculated from finite element simulations.

Chapter 7

Local Buckling of an Inelastic Shell Filled with a Solid Elastic Cylinder

7.1 Introduction

The models for buckling presented thus far have assumed that buckling takes place for filled shells with elastically-behaving shell and core materials. The models have been presented for elastic buckling of metal-filled shells (Chapter 4), for shells and cores that are not adhered (Chapter 5), and hollow cores (Chapter 6). A practical treatment of filled shells subject to axial loads warrants inclusion of the buckling behaviour while the shell material behaves inelastically. This chapter will describe such a model for local shell buckling.

While subject to axial compression, buckling failure of both hollow and filled cylindrical shells can occur before or after the initiation of plastic yield in the shell material. During elastic buckling, all buckling deformations are recovered if the load is removed immediately after the initiation of buckling [78, 112]. Inelastic buckling, however, results in deformations that are not always recoverable after buckling has been initiated. This type of buckling takes place before ultimate material failure of the shell [1, 4, 34]. For shells made of metal, this is after the end of the linear-elastic region on a stress-strain curve.

There are several studies investigating the inelastic behaviour of hollow shells subject to axial compression [77, 124, 127]. Analytical and experimental investigations of filled shells have focused on elastic behaviour [96, 98–100, 104, 107]. Two studies examined the inelastic behaviour of filled shells without accounting for the core [1, 4, 116]; one of these studies considered the yield strength of the shell without accounting for its inelastic behaviour explicitly [116].

For elastic local buckling predictions of thick shells filled with polymer cores (Chapter 4), the load-bearing capacity of the core leads to elastic local shell buckling loads that exceed the yield strength of the metal. As polymer materials require higher strains to yield then metals, the polymer core remains elastic even as the shell behaves inelastically. A new model for inelastic buckling of filled shells will remedy this shortcoming of thick shells while still assuming that the core material behaves elastically. The development of an inelastic model allows for validation of filled-shell predictions through experiments by using geometries with thicker shells. The use of thicker shells in experiments is expected to alleviate the imperfection sensitivity inherent in shell buckling, an effect which is magnified when the shell thickness is small [73, 78, 79, 81].

This chapter presents an extension to the fundamental buckling model of Chapter 4, which will allow for buckling load predictions for inelastically-behaving shells filled with solid elastic cores. As was done for

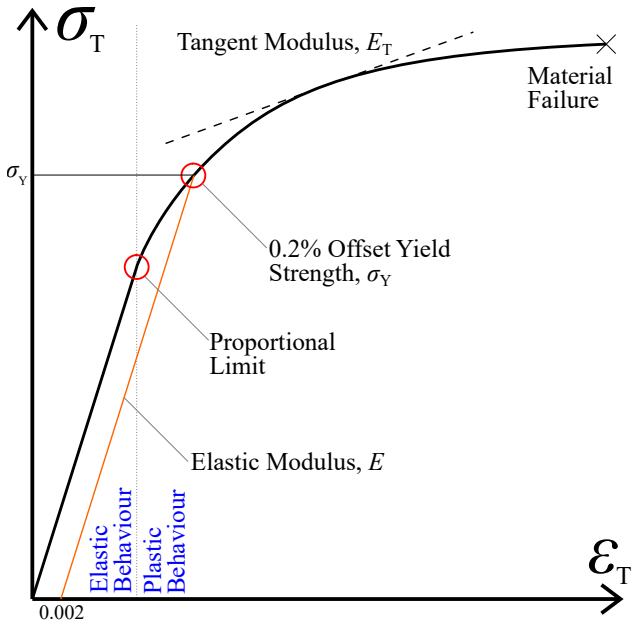

Figure 7.1: Annotated true stress-strain curve diagram showing regions of elastic and plastic behaviour, along with labels for Young's modulus E and the tangent modulus (E_T).

the fundamental model, the Timoshenko energy treatment of the shell [34] is used in conjunction with the strain energy model of the core developed in Chapter 3. To represent the behaviour of the shell material when it is behaving inelastically, an analytical representation of its stress-strain behaviour is required. The Voce material model is used for this purpose, and a description of it is provided. Using the value of the shell material modulus given by the Voce model, the fundamental model is modified for inelastic behaviour. Verification of this inelastic model is carried out through the use of non-linear finite element analysis.

The results of the finite element verification studies illustrate that the new inelastic model is accurate for a wide range of shell thickness-to-radius ratios. However, for filled shells that contain less stiff core materials, the inelastic model is less accurate for very high shell thickness-to-radius ratios.

7.2 Inelastic Material Behaviour and the Voce Material Model

To accurately calculate the inelastic buckling load for a filled shell under an axial load, an analytical material model is required. The rationale behind this is explained here, followed by a description of the Voce material model.

The elastic and plastic behaviours of a linear-elastic work-hardening material can be represented on a stress-strain curve as shown in Figure 7.1. At the inception of elastic buckling, the removal of any load will cause all buckling deformations to disappear, and the shell will return to its original shape [78, 87]. Typically, elastic buckling loads are calculated using Young's moduli found in material data sheets [34, 65]. Inelastic buckling, conversely, occurs before the ultimate strength of a material is reached [1, 4, 34]. The proportional limit as shown on Figure 7.1 denotes the end of the linear-elastic region of the stress strain

curve and the beginning of inelastic (or plastic) behaviour. Like any plastic deformation, inelastic buckling deformations are non-recoverable upon removal of the load as energy has been dissipated through plastic flow [18].

To calculate inelastic buckling loads, the Young's modulus E is replaced with either the tangent modulus E_{T} or the reduced modulus E_{R}. The tangent modulus is found by calculating the instantaneous slope of the stress-strain curve, as shown in Figure 7.1, while the reduced modulus uses the tangent modulus along with a representation of the cylinder cross section [34, 112]. While the reduced modulus is more complicated to calculate in practice, it is also more accurate for some models of inelastic buckling [111, 112]. For the present analysis, the tangent modulus is used for inelastic buckling predictions due to its simplicity.

7.2.1 The Voce Material Model

In order to calculate the tangent modulus for the shell material, it is desired to have a smooth fit between for its stress-strain behaviour. The Ramberg-Osgood model [113] uses a power law relationship between stress and strain, introducing a transition region between the elastic and inelastic behaviours of the material. Conversely, the Voce model provides a smooth fit between stress and strain without any transition region [114]. The Voce model requires the engineering stresses and strains to be in true stress-strain space, as seen in Figure 7.1. The conversion from engineering to true stress and strain can be done using [18]:

$$\sigma_{\mathrm{T}} = \sigma_{\mathrm{E}}(1+\varepsilon_{\mathrm{E}}) \quad \text{and} \quad \varepsilon_{\mathrm{T}} = (1+\varepsilon_{\mathrm{E}}), \tag{7.1}$$

where σ_{T} is the true stress, ε_{T} is the true strain, σ_{E} is the engineering stress and ε_{E} is the engineering strain. The Voce function takes the form [1, 4, 114]:

$$\sigma_{\mathrm{T}} = B_{\mathrm{v}} - (B_{\mathrm{v}} - A_{\mathrm{v}})\exp(-C_{\mathrm{v}}\varepsilon_{\mathrm{T}}), \tag{7.2}$$

where A_{v}, B_{v} and C_{v} are the fitting constants. The Voce model can be used to find the tangent modulus E_{T} at any stress value by differentiating Equation 7.2 with respect to ε_{T} [114]:

$$E_{\mathrm{T}} = C_{\mathrm{v}}(B_{\mathrm{v}} - \sigma_{\mathrm{T}}). \tag{7.3}$$

In order to calculate the inelastic buckling load, the elastic modulus E is set to E_{T} as given in Equation 7.3. The constants in Equation 7.2 can be determined for given material through a least-squares fit to experimental data.

7.3 Inelastic Buckling Load for a Filled Shell

A model for the prediction of the inelastic buckling load for a filled shell with a solid polymer core is presented here. This modified version of the fundamental buckling model (Chapter 4) makes use of the Voce material model for nanocrystalline nickel.

7.3.1 Voce Material Model for Nanocrystalline Nickel

Stress-strain data were obtained for nanocrystalline nickel (nNi) from RePliForm [7]. This data were produced through tensile tests of electrodeposited nNi specimens. The average grain size of this nanometal was 65 nm as determined by transmission electron microscope (TEM). A micrograph is in Figure 7.2.

Figure 7.3 shows the stress-strain data for the nanocrystalline nickel and the least squares fit to Equation 7.2. Table 7.1 shows the Young's modulus corresponding to this material along with the Voce coefficients for the curve in Figure 7.3. Equation 7.3 is used with the co-efficients in Table 7.1 to represent the material behaviour of the metal shell. Since the value of A_v is significantly smaller than the other coefficients, its value is set to 0.

7.3.2 Model for Inelastic Buckling

The development for the buckling load prediction for a filled cylinder with an inelastically-behaving shell material follows the method utilized in Chapter 4. Figure 7.4 shows a diagram of a filled cylinder of length l, radius r and thickness t subject to an axial load F. The core has Young's modulus of E_c and Poisson's ratio of ν_c, while the same properties of the shell are E and ν. The derivation of the inelastic buckling load uses the following assumptions:

- the core remains elastic at all times,
- the shell buckles with a sinusoid shape along its length,
- there are many waves during buckling,
- the shell is thin compared to the radius of the cylinder ($t/r < 0.1$), and
- the shell and core are perfectly bonded.

Due to the final assumption, the surface of the core takes on the same shape as the shell during buckling. Because the core remains elastic, the Southwell model (previously discussed in Chapter 3) is used to predict the behaviour of the core.

Table 7.1: Mechanical properties and Voce fit parameters for nanocrystalline nickel, as determined from stress-strain data provided by RePliForm [7]. The coefficient of determination (R^2) for the parameters is 0.9937.

Young's Modulus, E (GPa)	Poisson's Ratio	Yield Strength, σ_y (MPa)	A_v (MPa)	B_v (MPa)	C_v
125.0	0.3	1180	1.766×10^{-6}	1615	107.3

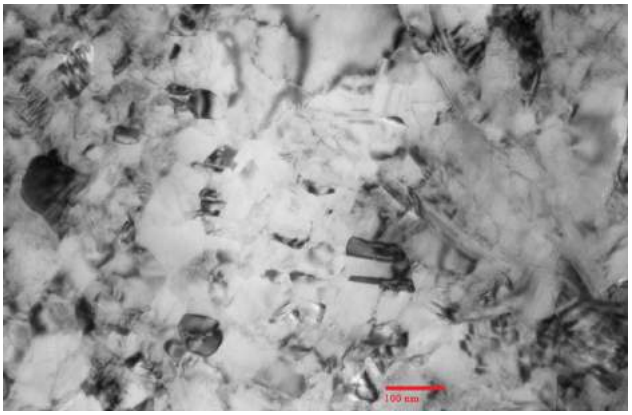

Figure 7.2: Micrograph captured using a transmission electron microscope during grain-size measurements of RePliForm nanocrystalline nickel. The average grain size found was 65 nm.

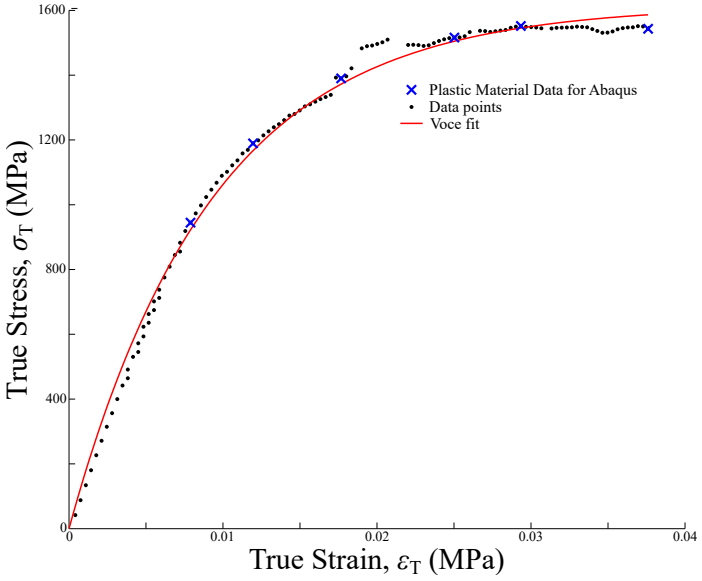

Figure 7.3: Stress strain data for nanocrystalline nickel (nNi) [7] and Voce exponential fit corresponding to this data (the fit coefficients are in Table 7.1).

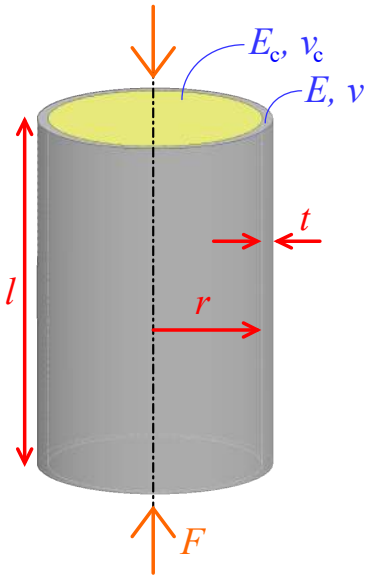

Figure 7.4: A filled cylinder under an axial load F with a length l, inner radius r and shell thickness t. The shell has Young's modulus E and Poisson's ratio ν while those of the core are E_c and ν_c.

Prior to deriving the buckling load F, the value of E is replaced with E_T (Equation 7.3). The stress σ_T is the load on the shell divided by the shell area. Thus the value of E_T becomes:

$$E_T = C\left(B - \frac{F_s}{2\pi r t}\right), \tag{7.4}$$

where F_s is the load on the shell only. The load carried by the core will be determined separately.

A filled shell in axial compression undergoing incipient local shell buckling experiences bending and circumferential stretching (refer to Equations 4.2 and 4.3 in Chapter 4). Modifying these equations for inelastic behaviour by replacing E with E_T gives:

$$U_{bi} = \frac{\pi E_T r t^3}{12(1-\nu^2)}\frac{m^4\pi^4}{l^4}\frac{A^2 l}{2} = \frac{t^2 C(2\pi r t B - F_s)}{24(1-\nu^2)}\frac{m^4\pi^4}{l^4}\frac{A^2 l}{2} \quad \text{and} \tag{7.5}$$

$$U_{\mathrm{ci}} = \frac{\pi E_{\mathrm{T}} t A^2 l}{2r} = C(2\pi r t B - F_{\mathrm{s}})\frac{A^2 l}{4r^2}. \tag{7.6}$$

The core energy term remains unchanged from the full adhesion fundamental model (Equation 3.14) as it is does not rely on the material properties of the shell. Performing the same operations as in Section 4.2 of Chapter 4 and isolating for F_{s} gives:

$$F_{\mathrm{s}} = \left[\frac{2\pi^3 r t^3 B_{\mathrm{v}} C_{\mathrm{v}}}{3(1-\nu^2)}\frac{1}{\lambda^2} + \frac{t B_{\mathrm{v}} C_{\mathrm{v}}}{2r\pi}\lambda^2 + \frac{Kr}{\pi}\lambda\right]\left[1 + \frac{\pi^2 t^2 C_{\mathrm{v}}}{3(1-\nu^2)}\frac{1}{\lambda^2} + \frac{C_{\mathrm{v}}}{4\pi^2 r^2}\lambda^2\right]^{-1}. \tag{7.7}$$

The values for K are obtained from the model that represents the core behaviour as developed in Chapter 3. Equation 7.7 applies for any λ value, however only one critical λ value exists for a given cylinder with known material properties. This critical λ value is found by finding the positive real root of $\partial F/\partial\lambda = 0$ [34, 77, 98].

The core provides added axial strength to the shell. For inelastic shell behaviour, the core contribution to the total cylinder load is determined by using the axial strain in the shell along with linear elastic expressions for the core behaviour. This strain, ε, in both the core and the shell is found by rearranging the Voce relation of Equation 7.2 to give:

$$\varepsilon = -\frac{1}{C}\ln\left[\frac{B - \dfrac{F_s}{2\pi r t}}{B - A_v}\right]. \tag{7.8}$$

Finally, the total axial load for the filled shell is determined by adding the shell and core loads together:

$$F = F_s + E_{\mathrm{c}}\varepsilon\pi r^2, \tag{7.9}$$

where E_{c} is the Young's modulus of the core, and ε is determined using Equations 7.8 and 7.7.

7.3.3 Inelastic Buckling Behaviour for a Filled Shell

The behaviour of the inelastic model is compared to the fundamental elastic model of Chapter 4, as well as to the inelastic buckling load for hollow shells. The latter was derived by Lausic et al. [1, 4]:

$$F_{\mathrm{hi}} = \frac{2\pi r t^2 C B}{\sqrt{3(1-\nu^2)} + Ct}. \tag{7.10}$$

Figure 7.5(a) shows the behaviour for various buckling loads for $E_{\mathrm{c}}/E = 0.01$, while Figure 7.5(b) shows the same loads for $E_{\mathrm{c}}/E = 0.001$. The corresponding graphs of λ/t are shown in Figures 7.6(a) and (b) for $E_{\mathrm{c}}/E = 0.01$ and 0.001 respectively. On the graphs of Figures 7.5, buckling predictions are given as a function of shell thickness-to-radius ratio (t/r) for the inelastic filled-shell (Equation 7.9) and elastic filled-shell (Chapter 4, Equation 4.11), inelastic hollow-shell load (Equation 7.10) and elastic hollow-shell

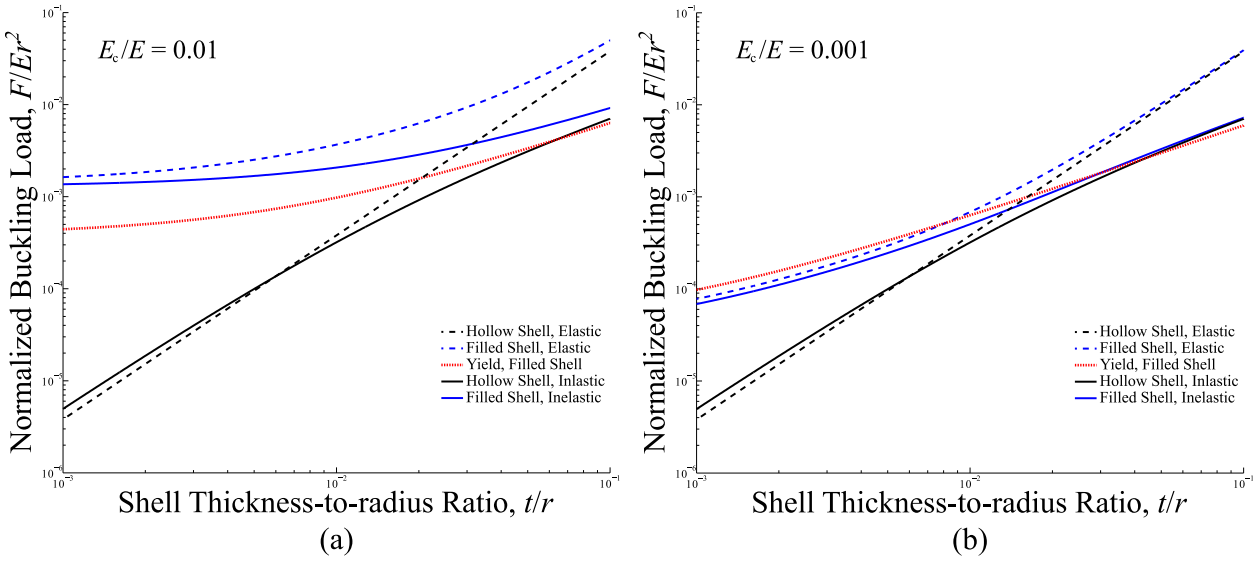

Figure 7.5: Predictions of the inelastic buckling load for filled cylinders as a function of t/r for (a)$E_c/E = 0.01$ and (b)$E_c/E = 0.01$. The predictions for the elastic and inelastic hollow and filled shell models are shown, along with the yield loads of a filled cylinder.

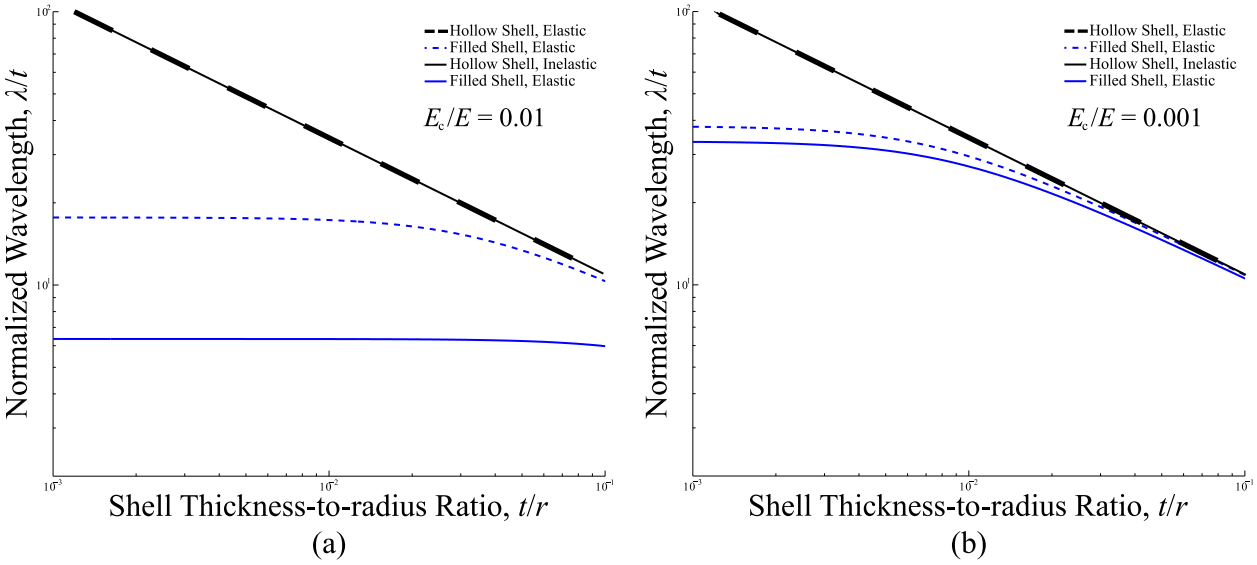

Figure 7.6: Predictions of the inelastic buckling load for filled cylinders as a function of t/r for (a)$E_c/E = 0.01$ and (b)$E_c/E = 0.01$. The predictions for the elastic and inelastic hollow and filled shell models are shown, along with the yield loads of a filled cylinder.

models [34]. The load to yield for a filled shell is also given as a reference.

As seen in Figure 7.5(a), both predictions of the elastic and inelastic filled-shell load for $E_c/E = 0.01$ are all above the yield load for the entire range of t/r on this graph. This implies that metal-coated polymer cylinders with very stiff cores (i.e. $E_c/E \gtrsim 0.01$) will readily lead to inelastic shell buckling for a wide range of shell thickness-to-radius ratios. This is supported by Figure 7.5(b) for $E_c/E = 0.001$, which shows that yielding of the shell does not begin until $t/r \approx 0.03$ for this reduced core stiffness.

The graphs of λ/t (Figures 7.6(a) and (b)) show the critical wavelengths for elastic and inelastic buckling of both hollow and filled shells. Inelastic behaviour of a filled shell causes the critical buckling

wavelengths to be lower than for elastic buckling. However, for a hollow shell, it is seen that the buckling wavelengths for both elastic and inelastic buckling are the same. This difference between hollow- and filled-shell buckling wavelengths is because the critical wavelength of filled-shell buckling depends on the shell material properties, whereas this is not the case for hollow-shell buckling [34]. Hence, as the shell behaviour changes from elastic to inelastic, the critical wavelength changes as well.

Figure 7.6(b) illustrates that the model for inelastic buckling of a filled shell with $E_c/E = 0.001$ yields wavelengths that are much closer to elastic buckling wavelengths, which lead to the predicted loads being closer to the loads for elastic buckling. This is confirmed by the inelastic filled-shell loads in Figure 7.5(b), which are closer to their elastic counterparts compared to the corresponding predictions shown in Figure 7.5(a) for $E_c/E = 0.01$. Inelastic buckling for filled shells with more compliant cores will occur at loads that are much closer to the hollow shell loads, showing the reduced importance of the core as its relative stiffness is reduced. For both $E_c/E = 0.01$ and 0.001, inelastic buckling predictions are below the elastic hollow-shell buckling model when t/r is very large. However, for smaller t/r, Figure 7.5(b) reveals that the inelastic load for $E_c/E = 0.001$ predicts a lower load than the elastic filled-shell model. This is a limitation of the inelastic model: to represent the complete axial behaviour of a filled shell, elastic shell buckling should take place for thin shells and this should transition smoothly to the inelastic buckling behaviour at higher thickness values.

7.4 Finite Element Verification

Finite element verification was carried out using Abaqus. Axisymmetric cylinder geometries were represented using a fixed radius r of 10 mm while varying cylinder length l and coating thickness t to generate different values of length-to-radius (l/r) and thickness-to-radius (t/r). A total of 18 geometries were generated using six t/r values of 0.005, 0.0075, 0.01, 0.025, 0.05 and 0.1, each of these used with l/r values of 5, 15 and 25. An example of a typical finite element configuration is shown in Figure 7.7 with a sample section of a mesh for one geometry. All geometries were discretized using a minimum of 5×10^6 elements, with at least 8 elements through the shell thickness. The cylinders were loaded axially by applying a displacement δl at the top edge of the axisymmetric section (i.e. the top surface of the cylinder), as shown in Figure 7.7. The top and bottom edges – representing the top and bottom surfaces of the cylinder – were allowed to expand in the radial direction as the axial displacement was applied. The material properties of nNi were used for the shell (refer to Table 7.1) while a ratio of E_c/E controlled the Young's modulus of the core. To be consistent with the results in Figures 7.5(a) and (b), the values of E_c/E used were 0.01 and 0.001.

Two cases were calculated for each geometry. First a modal analysis was performed to extract eigenvalues and mode shapes for elastic buckling of the geometry using a linear perturbation analysis [83]. A static analysis followed, using material stress-strain data for nanocrytalline nickel as well as imperfections applied to the mesh using the modal data generated from the elastic buckling analysis. The imperfections were applied using a scaling factor for the first 6 mode shapes from the modal analysis, with the scaling

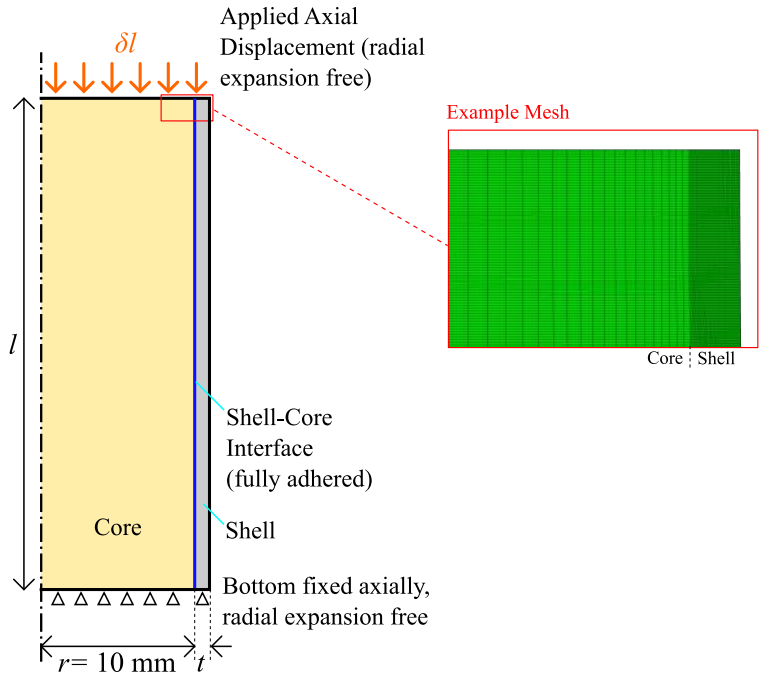

Figure 7.7: Diagram showing setup of an Abaqus simulation for an axisymmetric section of a filled shell with length l, radius $r = 10$ mm and shell thickness t. The inset shows an example of a mesh.

Table 7.2: Scaling factors used for each eigenvalue, as applied to the mesh for the analysis of inelastic buckling in Abaqus

Eigenvalue/Mode #	Scaling Factor
1	5.000×10^{-3}
2	2.500×10^{-3}
3	1.250×10^{-3}
4	6.250×10^{-4}
5	3.125×10^{-4}
6	1.562×10^{-4}

Table 7.3: Plasticity data for shell material used for Abaqus inelastic buckling simulations (refer to [83] for methods of use)

Plastic Strain	True Stress (Pa)
0	9.865×10^{8}
4.058×10^{-3}	1.189×10^{9}
1.011×10^{-2}	1.396×10^{9}
1.747×10^{-2}	1.517×10^{9}
2.179×10^{-2}	1.549×10^{9}
3.004×10^{-2}	1.537×10^{9}

factors listed in Table 7.2. These magnitudes were determined through a sensitivity analysis on hollow- and filled-shell simulations using similar geometries. The inclusion of mode shapes beyond the 6^{th} mode did not affect the results.

Abaqus utilizes material stress-strain data in the form of plasticity data. The plasticity data for nanocystalline nickel is given in Table 7.3 while the corresponding data points on the original nNi stress-strain data is shown in Figure 7.3. The eigenvalue buckling predictions did not use plastic material behaviour as the Abaqus eigenvalue solver cannot account for plasticity [83]. No plasticity information was used for the core as it is assumed to remain elastic. The displacement applied to the geometries for the static general analyses was determined through the eigenvalues returned by the preceeding buckling analyses.

7.4.1 Methods for Data Extraction

The criterion for failure in non-linear simulations is typically not apparent as it often is for elastic simulations [71]. As such a method was chosen to determine the point of failure for the verification simulations. A

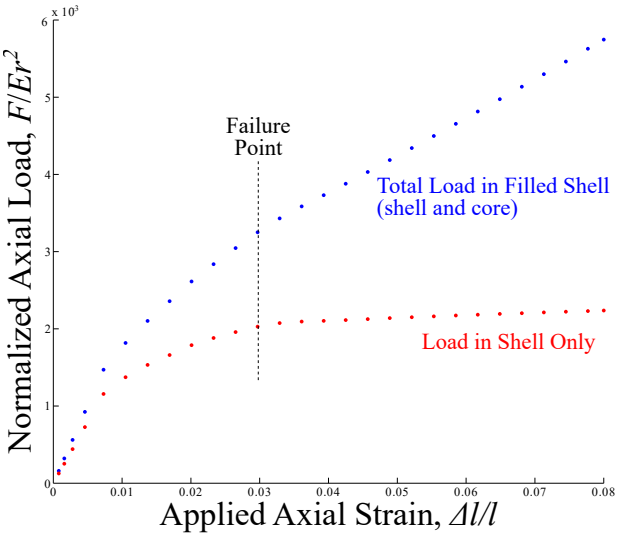

Figure 7.8: Force-displacement data extracted from an inelastic Abaqus simulation for $E_c/E = 0.01$, $t/r = 0.25$ and $l/r = 5$

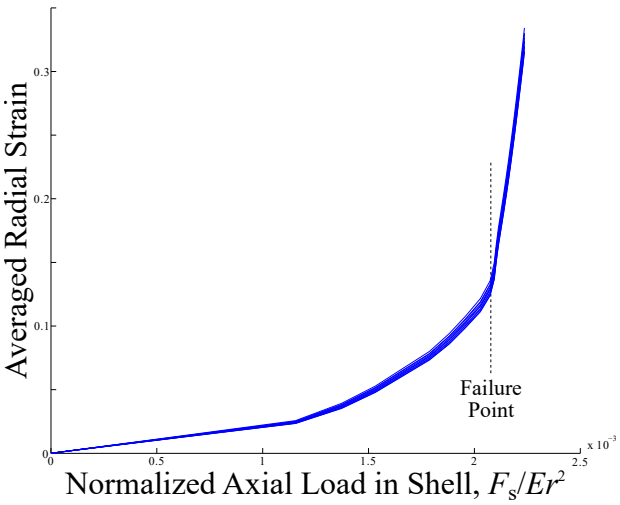

Figure 7.9: Averaged radial strains for selected outer edge nodes as extracted from an inelastic Abaqus simulation for $E_c/E = 0.01$, $t/r = 0.25$ and $l/r = 5$

reduction in the load-carrying capacity of the shell on a force-displacement diagram was deemed the point of failure. This was confirmed by a sharp increase in the radial deflections of buckle folds. To illustrate these failure criteria in practice, two figures will be provided.

Figure 7.8 shows the axial force plotted as a function of axial displacement, while Figure 7.9 shows the averaged radial strains calculated for several nodes on the outermost surface of the coating as a function of the axial force. For the latter figure, several nodes were selected at random along the outer coating edge and their radial strains determined. Figures 7.8 and 7.9 correspond to the simulation for $E_c/E = 0.01$, $t/r = 0.025$ and $l/r = 5$. The force-displacement graph (Figure 7.8) shows the data for both the complete cylinder as well as for the shell only. While there is a pronounced decrease in the shell force at the indicated failure point, there is not a pronounced decrease in the force in the entire filled shell. This sharp change in the force-displacement behaviour of the shell is where the cylinder has failed through inelastic buckling. The axial strains in Figure 7.9 illustrate how there is a large rise in radial displacement at the outer coating edge after the failure load is reached. These axial strains thus act as a confirmation of inelastic failure.

7.4.2 Verification Results

Figure 7.10(a) shows the non-dimensional loads obtained for the finite element verification simulations for $E_c/E = 0.01$, while simulation data for $E_c/E = 0.001$ is shown in Figure 7.10(b). On both Figures 7.10(a) and (b), the predictions for elastic buckling of a filled shell (Equation 4.11 in Chapter 4), inelastic buckling of a filled-shell (Equation 7.9) and inelastic buckling of a hollow shell (Equation 7.10) are included.

There is a very good agreement between the values obtained from Abaqus simulations and the predictions for an inelastic filled-shell with $E_c/E = 0.01$ (Figure 7.10(a)), indicating that the inelastic filled shell buckling model is sound. There is a slight scatter in the loads obtained from Abaqus due to the various l/r

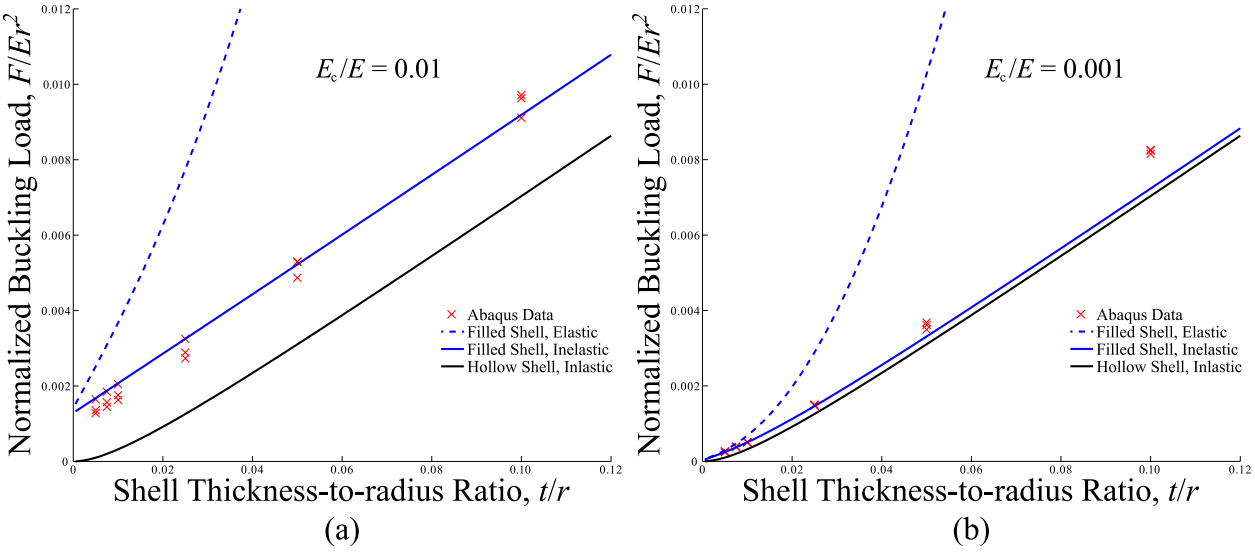

Figure 7.10: Predictions of the inelastic buckling loads for hollow shells, filled shells and the Abaqus simulation results as a function of t/r for (a)$E_c/E = 0.01$ and (b)$E_c/E = 0.001$.

values that were used. This is likely due to element counts inside the meshes and not due to the sensitivity of the buckling load to l/r. At $t/r = 0.1$ some of the values are greater than the predicted loads. This is likely because this is near the limits of the thin shell assumption (refer to Section 7.3.2), where the shell behaviour becomes dominant over that of the core. However, for $E_c/E = 0.001$ (Figure 7.10(b)) the values obtained from Abaqus are far above the predictions for inelastic shells starting at t/r values of 0.05 and above. The core behaviour may be more important than the inelastic model predicts, even when the core stiffness is substantially lower than that of the shell. Both of these deviations from the Abaqus results show that the inelastic model is not accurate for very thick filled shells (i.e. $t/r \geq 0.1$), but this is outside the assumed range of thicknesses for the inelastic filled-shell model.

The appearance of some of the final buckled shapes for the shells is shown in Figure 7.11 for several values of t/r. For comparison, the mode shapes corresponding to the first eigenvalue for the same values of t/r are shown in Figure 7.12. Buckled shapes for E_c/E values of 0.01 and 0.001 are shown in both figures. For all of the geometries studied, the first and tenth eigenvalues were within 1% of each other, an indication of the strong imperfection sensitivity of inelastic local shell buckling [71, 83–85].

The imperfect coating geometry, supplied by a weighted sum of the mode shapes (refer to Table 7.2), coalesced into large folds when $E_c/E = 0.001$, or into groups of folds at some location along the length when $E_c/E = 0.01$. This is more apparent for larger t/r values (i.e. $t/r = 0.05$ in Figure 7.11(b)). For both E_c/E values, the coalescence takes place well after the buckling load is exceeded (i.e. at very high axial strain values), as made apparent by comparing the values of δl in Figure 7.11 to the eigenvalues indicated in Figure 7.12. In addition, the visual appearance of the inelastic folds is similar to the first mode shape, which was given the highest weight factor in the imperfections. The appearance of the folds along the lengths of the cylinders is consistent with concertina buckle folds encountered in both hollow and filled metal shells tested

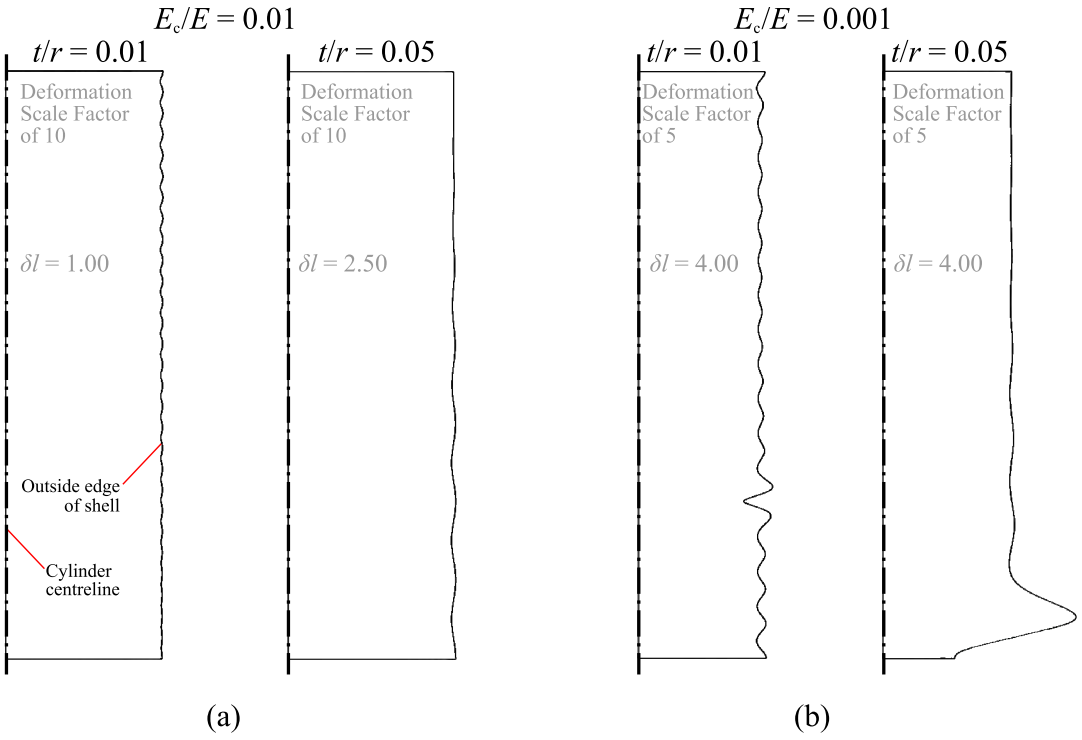

Figure 7.11: Buckled shapes for some geometries studied using inelastic Abaqus simulations for $l/r = 5$ ($r = 10$ mm) where a) $E_c/E = 0.01$ and b) $E_c/E = 0.001$. Note how the applied axial displacements compare to the eigenvalues for the elastic mode shapes in Figure 7.12.

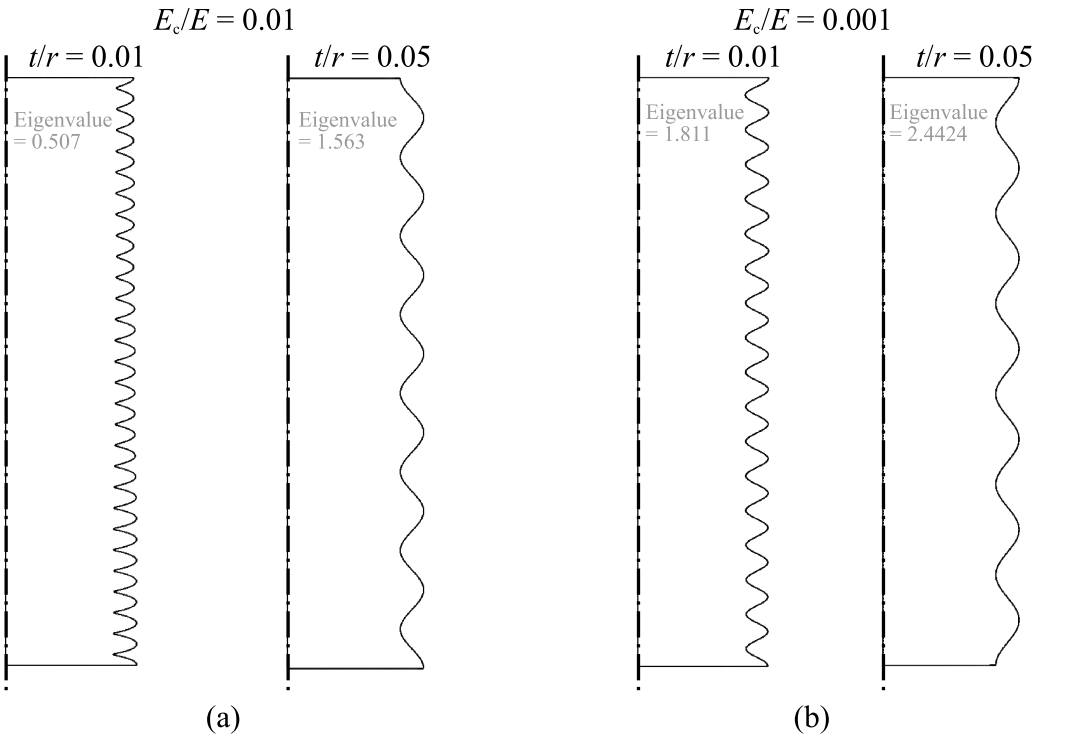

Figure 7.12: Elastic mode shapes for first eigenvalues as obtained for some geometries studied using Abaqus for $l/r = 5$ ($r = 10$ mm) where a) $E_c/E = 0.01$ and b) $E_c/E = 0.001$.

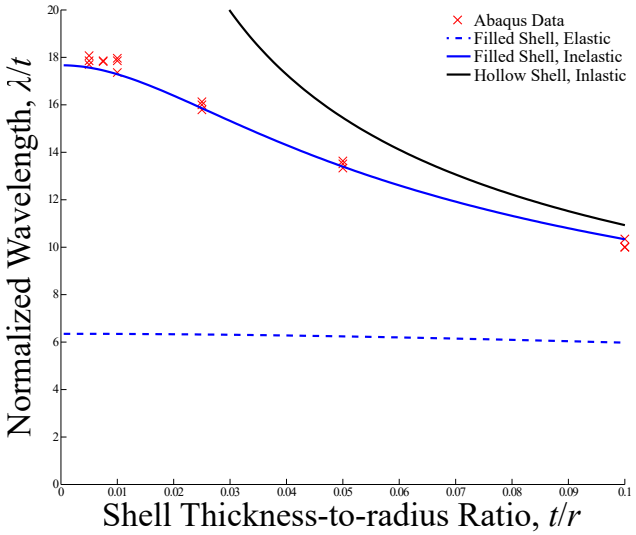

Figure 7.13: Predictions for inelastic critical wavelengths as determined through Abaqus for $E_c/E = 0.01$. The theoretical wavelengths for the hollow and filled shell theories are provided.

in experimental investigations [66, 98, 103].

Although the majority of the loads obtained from Abaqus simulations were in line with the predictions, it was not possible to verify the critical wavelengths for inelastic buckling. Since the critical wavelengths for elastic and inelastic buckling of filled shells are not the same (unlike those for hollow-shell buckling – refer to Figure 7.6), the use of mode shapes obtained through an elastic perturbation analysis was not guaranteed to give wavelengths corresponding to the inelastic model. This is illustrated in Figure 7.13, which shows the wavelengths from the simulations for $E_c/E = 0.01$. As seen in this Figure, all of the wavelength predictions from Abaqus are closer to those predicted by the elastic model. A second attempt to obtain the wavelengths was undertaken: to rule out the effect of the elastic mode shapes influencing the wavelength predictions, a less structured imperfection pattern was applied to the cylinders. The method of imperfection generation as used for verification of non-adhesion buckling loads was utilized (refer to Section 5.5 in Chapter 5). Using this second imperfection pattern resulted in radial growth of the buckle folds, with the wavelengths remaining unchanged as the axial load was applied. The buckling load in both of these was the same even as the final shape of the shell changed.

It is deduced from this behaviour that it is not the critical wavelength of a cylinder undergoing filled-shell buckling that affects the buckling load; instead, this load is more dependant upon the material behaviour of the shell. It is possible that the critical wavelength appears for a very short period at the inception of buckling, as this is observed in experimental investigations of hollow-shell buckling [66, 78, 87]. However, the limitations of Abaqus simulations made this difficult to investigate in detail.

7.5 Concluding Remarks

A model for inelastic local shell buckling of filled cylindrical shells has been developed. This utilizes the Voce material model to represent the behaviour of nanocrystalline nickel, one possible shell material that can be used for metal-coated polymer cylinders. The Voce material model was utilized to determine the instantaneous tangent modulus, which allowed for the existing elastic filled-shell buckling model to be modified for inelastic buckling. As the core is assumed to remain elastic, the model developed previously for the core was utilized again.

Verification using Abaqus finite element simulations was undertaken, using both elastic linear perturbation analysis to determine mode shapes for chosen cylinder geometries followed by a non-linear static analysis to determine the inelastic buckling load. The non-linear analyses used meshes with deliberately-introduced imperfections, which were determined using a weighted sum of the mode shapes found from the elastic perturbation analyses. Through these verification studies, it was deduced that the model is sound at lower thickness-to-radius ratios, but becomes less accurate as the thickness-to-radius ratio increases. The divergence from the model is more pronounced as the shell-to-core stiffness ratio is lowered, implying that the inelastic model may not be robust enough at higher thickeness-to-radius ratios. However these higher ratios are near the limits of the assumptions used in deriving the inelastic model. Despite the fact that the buckling loads were verified for a higher shell-to-core stiffness ratio, it was not possible to verify the critical wavelengths for this inelastic model.

Chapter 8

Experiments

8.1 Introduction

The dominant failure modes of metal-coated polymer microtruss structures are compressive instabilities [1, 4, 128]. These hybrid structures make use of mass-efficient microtruss topologies while utilizing the high-strength benefits of nanocrystalline metals. Metal-coated polymer cylinders (referred to as filled shells) are the struts of these structures, and studying their compressive instabilities leads to an understanding of the behaviour of hybrid microtruss structures. Of research interest is the local shell buckling mode of failure, as global buckling of bi-material struts is a better understood phenomenon. In previous chapters, filled-shell buckling models have been developed for various cylinder configurations and assumptions. These include a fully-adhered filled shell buckling elastically (Chapter 4), a filled shell where the shell and core are not perfectly adhered (Chapter 5), buckling of a filled shell with a partially hollow core (Chapter 6), and inelastic buckling of the shell (Chapter 7).

For the last of these models, many studies have examined the buckling behaviour of inelastic hollow shells [127, 129] while others provide predictions of the elastic buckling load of filled shells [5, 72, 97–101, 104–108]. However, studies that have investigated inelastic buckling of filled shells treated the polymer core as a parasitic mass, and did not properly account for the core behaviour [1, 4, 130]. Several of the filled-shell elastic buckling theories have been experimentally validated using tubes filled with polymer foams [5, 69, 70, 96, 103, 109]. These experimental programs obtained axial buckling loads that were within 90% of predictions, an agreement which decreases rapidly for cylinders with thinner shells (refer to Figure 2.10 of Chapter 2). Past experiments all utilized one or more methods to fix the ends of the cylinders during axial loading, including the use of sample geometries intended to fit neatly in a specific load frame or potting compounds to secure the ends [72, 78]. The intention of the clamped ends was to mitigate asymmetric loading of the shells, which can cause failure well below predicted loads given by models [73, 77].

Experimental investigations of filled-shell buckling phenomena have thus far been focused on foam-filled cylinders [5, 69, 70, 96, 103, 109]. The results of these experiments are less relevant to polymer-filled metal cylinders, where the core is not a foamed material. For this reason, it is of interest to undertake experimental studies of polymer-filled metal cylinders, as these would be more relevant to metal-coated polymer microtrusses. In addition, it is appealing to manufacture and test thick-shelled cylinders, as thinner shells are more susceptible to premature failure due to their increased sensitivity to imperfections [73, 78, 79, 81]. The use of thicker shells allows for comparison to the experimental results to the inelastic model

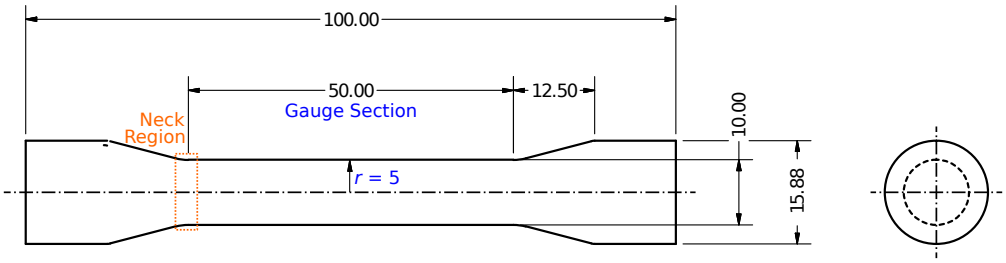

Figure 8.1: An annotated drawing of the dogbone geometry designed for compression tests with labels for the gauge section, its radius r and the neck region. All dimensions in mm.

for filled-shell buckling (Chapter 7), which provides more accurate loads than elastic buckling models for cylinders with thick shells.

This chapter presents the procedures and results of the experiments intended to explore the behaviour of metal-coated polymer cylinders subject to axial loads, the results of which will be compared with the inelastic buckling model developed in Chapter 7. As the inelastic model has been verified through finite element analysis, experiments allow for an examination of factors that are not considered in the model, such as asymmetric loading or imperfect cylinder geometries. In addition, the experimental data are compared to finite element simulations in order to ensure that the samples behave as expected. It will be shown that factors not considered in the theoretical derivation of buckling, such as non-uniform shell thicknesses or loading asymmetry, can severely affect buckling loads in practice.

8.2 Objectives of Experiments and Specimen Design

The objective of the experiments was to validate the predictions of inelastic buckling loads for filled cylindrical shells in axial compression by using specimens designed to fail through local shell buckling. The measured peak loads will be compared to predictions of the filled-shell inelastic model (Chapter 7), and to finite element simulations.

In contrast to the manufacturing method of foam-filled shells which first involves production of the shells prior to filling them with foam [5, 103, 107, 109], the present samples were produced by machining the polymer core followed by electrodeposition of a nanocrystalline metal coating. This was required as electrodeposition methods are currently the most viable and cost-effective method of producing high-quality nanocrystalline metal coatings [28–30].

8.2.1 Specimen Design and Manufacture

In designing specimens to investigate axial buckling, the intention was to reduce the likelihood of failure near the ends of the gauge section while ensuring that inelastic local shell buckling was the dominant failure mechanism. The geometry in Figure 8.1 was designed with this in mind while also maximizing the stresses in the gauge section. As seen in the figure, the sample geomtry has a dogbone shape, and the gauge section

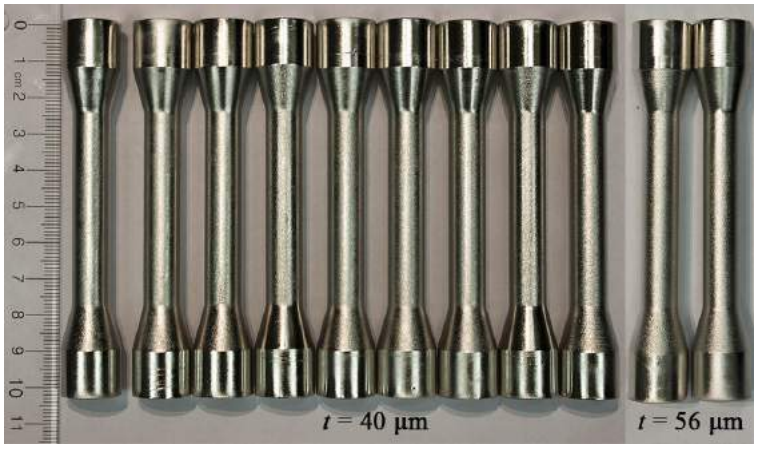

Figure 8.2: An image of all 11 samples as received from Integran with given nanocrystalline metal coating thickness t as indicated. The samples were coated all around with metal, including the top and bottom ends of the geometry.

Table 8.1: Coating thickness values as provided by Integran, the resulting thickness-to-radius ratios and quantities manufactured for experiment samples. A total of 11 samples were manufactured, two of which were coated with 56 µm of nNi while the rest were coated with 40 µm nNi.

Coating Thickness[a] (µm)	Thickness-to-Radius Ratio in Gauge Section, t/r	Quantity Manufactured
40	0.0080	9
56	0.0112	2
Total	—	**11**

[a] Coating thickness values provided by Integran

is a circular cylinder. This geometry was chosen after finite element studies were conducted to determine the shape of the neck region to reduce the von Mises stresses there.

The dogbone samples were machined out of ABS polymer and coated with nanocrystalline nickel (nNi). The proprietary surface cleaning and coating processes were performed by Integran Technologies. The choices of ABS polymer for the core and nNi for the coating provided a Young's modulus ratio of $E_c/E = 0.0176$, where E is the Young's modulus of the nNi coating (125 GPa) [7] and E_c is that of the ABS plastic (2.2 GPa).

A total of 11 samples were machined out of ABS and coated with nNi. An image of the samples as received from Integran is shown in Figure 8.2, while the coating specifications of these samples are provided in Table 8.1. Two of the samples were coated with 56 µm of nNi, while the remainder were coated with 40 µm nNi. These coating thickness values correspond to thickness-to-radius (t/r) values of 0.008 and 0.0112, respectively. Because verification of coating thicknesses required cutting sections from the samples, a microscopy investigation was undertaken after the experiments to confirm the thickness.

8.3 Experimental Procedure and Analysis Methods

The equipment used during experimental studies included a servo-hydraulic load frame, a laser extensometer, and two desktop computers to control the load frame and for data aquisition. Figure 8.3 shows a photograph of the load frame with one sample positioned in the frame, as well as the laser extensometer aligned with the

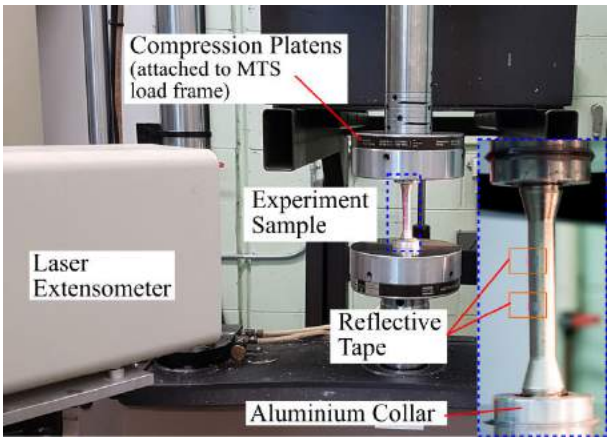

Figure 8.3: A photograph showing the equipment setup for the experiments. A laser extensometer is pointing at a sample positioned in compression platens, which are attached to the MTS load frame. The inset shows reflective laser tape used to mark the gauge length to be measured by the laser extensometer, as well as the aluminium collars used to hold the sample in place.

Figure 8.4: A dogbone sample mounted in aluminium collars prior to test. Note the weight on top to keep the sample pressed down as epoxy cures

sample. The load frame was an MTS 880 used in displacement-control mode and fitted with compression platens. The surfaces of the compression platens were checked for levelness after each sample was tested. Fibre optic lighting was used for increased illumination of the samples both during setup and testing.

The laser extensometer was an EIR LE-05 manufactured by Electronic Instruments Research. Reflective adhesive tape provided by the manufacturer was used to mark the gauge length being measured by the extensometer, as indicated in the inset of Figure 8.3. As the laser extensometer is a non-contact method of sensing displacement, the tape is required to indicate the gauge section.

The analog voltage output of both the load frame and the laser extensometer were provided to a computer running a virtual instrument (VI) programmed using National Instruments LabVIEW. The VI created text files containing the force from the load frame and the displacement recorded by the laser extensometer at 1 s intervals.

8.3.1 Sample Preparations and Testing Procedures

The dogbone samples were coated entirely with nNi, including the top and bottom ends of each sample. The ends of the samples were sanded using a sanding wheel fitted with 60 grit sand paper. This flattened the end surfaces, thereby ensuring better load alignment along the sample axis. Following this, the sample was mounted into two aluminium collars using epoxy as shown in Figure 8.4. This was done to enforce clamped end conditions and also to reduce loading misalignment. The practice of clamping the ends has been previously used in experiments involving axial compression of both hollow and filled shells [5, 72, 78, 96, 99, 107].

A LePage Speed Set two-part epoxy was used to pot the sample into the aluminium collars. Care was taken to ensure that the sample was potted in the centre of the collars, and a weight was placed on top of

specimens as the epoxy cured (as shown in Figure 8.4) to ensure that the surfaces of the collar and potted end were flush. Each end was potted separately, with a minimum time of 30 minutes given for each potting operation to allow the epoxy to cure fully. Samples were checked for alignment and levelness after each potting operation, and if necessary the potting operation was redone.

Once mounted in the aluminium collars, the prepared sample was positioned in the MTS load frame, as seen in Figure 8.3. The sample was bonded to the MTS machine platens using the same general-purpose epoxy. A small pre-load of 30–50 N was applied to each sample in order to keep it in place as the epoxy cured.

The behaviour of polymer materials is known to be strain-rate dependant [20, 131]. Prior compression tests on ABS samples were used to determine a suitable strain rate below which excessive strain-rate dependant behaviour would not be observed. This was determined to be $4 \times 10^{-5}\,\mathrm{s}^{-1}$, giving a cross-head displacement rate of $2 \times 10^{-3}\,\mathrm{mm/s}$ for the sample gauge length of 50 mm (refer to Figure 8.1).

The LabVIEW VI recorded force data obtained from the MTS machine and displacement readings from the laser extensometer. After each experiment, the aluminium collars were removed and cleaned of any epoxy so that they could be used for later samples. The surfaces of the compression platens were also cleaned and checked for levelness between experiments.

8.3.2 Microscope Examination of Coating Thickness

After the axial buckling experiments had been completed, the gauge sections of four of the 40 µm samples were cut to expose the coating-core interface. The sectioned samples were smoothed using 800 grit sandpaper to allow for easier viewing of the coating in an optical microscope.

An Olympus BX63 microscope was used for thickness measurements of the nNi coatings. Four locations around the circumference of each sample (at 90 degree spacings) were photographed in the microscope, and five measurements of the coating thickness were taken at each of these locations. This provided a profile of the coating thickness around the circumference for each of the sectioned samples while providing enough measurements to obtain average thickness values.

8.4 Results of Experiments

The failure mechanism for all specimens was inelastic local shell buckling of the coating, though not within the gauge section of the samples as desired. Buckling failure involved the rapid formation of a buckle fold along with a drop in the axial load of the sample as seen on a force-displacement diagram. The data gathered from experiments are presented in this section, along with photographs of several samples after being tested as well as the results of microscopy measurements of coating thickness. The data from experiments is compared to the inelastic model developed in Chapter 7.

Figure 8.5: A failed specimen showing an axisymmetric buckle fold near the neck region of the specimen. This is an undesirable failure location and indicative of high stresses in the neck region.

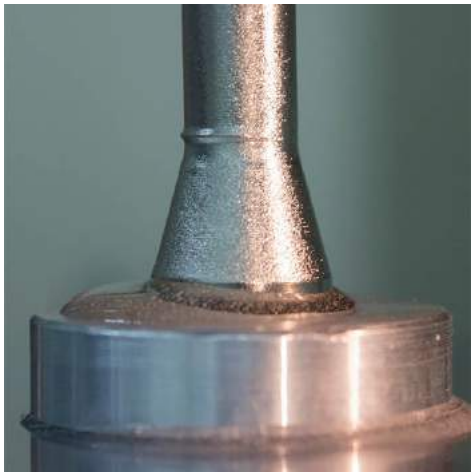

Figure 8.6: A failed specimen showing a non-axisymmetric buckle fold near the neck region of the specimen.

8.4.1 Appearance of Tested Samples

Figures 8.5 and 8.6 show images of specimens after being loaded past the point of failure. A buckle fold near the neck region of both samples indicates failure through local shell buckling. Nearly all of the samples tested had at least one buckle fold that formed near the neck region, with subsequent folds appearing at lower loads than the first fold. One sample that did not have a fold near the neck region instead failed at a much lower load than the rest of the specimens, indicating that misalignment had contributed to its early failure. The appearance of the buckle folds in the neck region reveals that the attempts at reducing stresses in this region were not successful: it would have been desirable to have failure in the gauge section.

The appearance of folds outside the gauge section also contributes to lower buckling loads than predicted by the inelastic model, as the neck region has a higher t/r compared to the gauge section. In addition, the varying geometry along the neck region provides a varying t/r, further complicating predictions using the buckling model.

Several of the samples which were not properly aligned with the axis of loading failed through Euler buckling, or through non-axisymmetric local shell buckling as seen in Figure 8.6. This was an indication of asymmetric loading which led to premature failure for these samples. Inspection of all the failed samples revealed that adhesion between the shell and the core was not a contributing factor to the failure of the specimens

8.4.2 Force-displacement Data from Experiments

Figure 8.7 shows the force-displacement data obtained from the experiments for all 11 samples. The failure load was the highest load encountered in the experiment for each sample, and the force-displacement data after failure have not been included. The failure loads are represented as endpoints on the individual sample

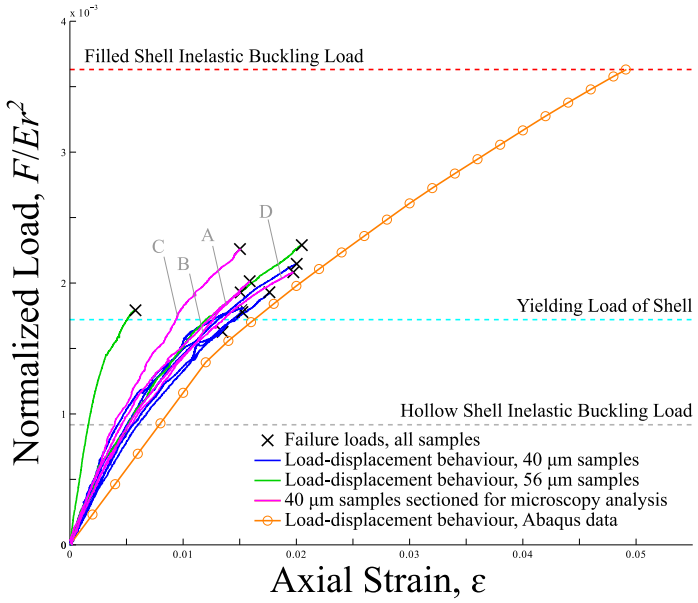

Figure 8.7: Force-displacement data obtained from the buckling experiments. The predicted inelastic buckling load is shown, along with the predictions for inelastic hollow shell buckling and the yield point of the metal coating. Force-displacement behaviour found from an Abaqus simulation for a 100 µm thick sample is also provided, and the highlighted curves (labelled A through D) were used for thickness measurements using microscopy analysis. The two samples with 56 µm of nNi are also indicated.

data curves. The two samples with 56 µm of nNi are highlighted to distinguish them from the 40 µm samples. Of the two 56 µm samples, the force-displacement behaviour of one was similar to the 40 µm samples, while the other had very different force-displacement behaviour. The failure loads of all samples are in the the same range, and do not appear to be dependant on the force-displacement behaviour or on the coating thickness. Error bars are shown for the failure loads only. This error is ±2% of the measured load F, and is due to the noise recorded from the LabVIEW VI during data acquisition.

Because of the uncertainty in the coating thickness of the samples as received from Integran, a microscopy measurement program was undertaken after all samples had been tested.

8.4.3 Microscopy Measurements of Sample Thickness

Four of the 40 µm samples were sectioned and their surfaces smoothed using 800 grit sandpaper. The sanding process was required in order to facilitate easier viewing of features while using an optical microscope. Sections were cut from the gage section of samples whose force-displacement behaviour is indicated in Figure 8.7, and have been labelled A through D for reference. Due to the large thickness of the metal coatings, it was not necessary to use an electron microscope for thickness measurements.

Figure 8.8 shows a micrograph of a section of Sample D as seen in the Olympus BX63 microscope at a magnification of 10×. Comparing the metal coating thickness to the scale bar indicates that the metal coating is approximately 100 µm thick.

More precise measurements were taken at 4 different locations around the circumference of each sample. The thickness measurements for the quadrant of Sample D in Figure 8.8 are shown at five points along

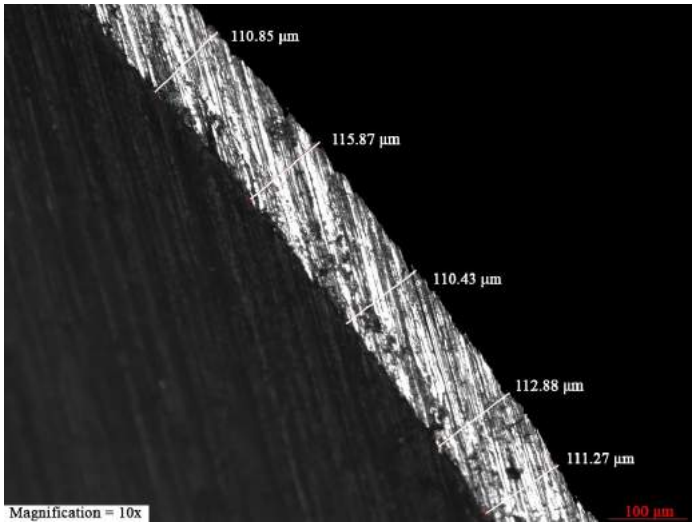

Figure 8.8: Micrograph of Sample D for quadrant 3 at 10× magnification (refer to Table 8.2). Measurements are shown along the thickness of the coating, with the average thickness calculated to be 112.26 µm.

Table 8.2: Thickness measurements as found for four locations, or quadrants, for four different sectioned samples. The mean measurements for each quadrant and the overall mean values are given. The samples used for microscopy analysis are indicated in Figure 8.7.

	Mean of 5 Thickness Measurements (µm)				Overall
Sample ID	Quadrant 1	Quadrant 2	Quadrant 3	Quadrant 4	Mean Thickness (µm)
A	109.46	102.25	87.17	122.05	105.23
B	121.81	123.79	124.12	127.86	124.40
C	144.06	95.34	99.14	143.65	120.55
D	123.25	128.74	112.26	90.85	113.78
				Average Thickness	**115.99**

the metal coating. Similar measurements were taken at 3 other quadrants for this sample. The average coating thickness of these five meausrements shown in the figure is 112.26 µm for this quadrant. The same measurement process was repeated for each of the 4 quadrants for all 4 samples tested. In this way, 16 sets of 5 thickness measurements were obtained.

Table 8.2 shows the averaged results of all the thickness measurements from the microscope investigations. The average thickness at the four quadrants of each of the samples is given, a mean thickness for each sectioned sample, and an average for all four samples. As seen from the values in the Table, the average thickness for the four samples together is approximately 116 µm, while the thickness can be up to 21 µm higher or lower at different points around the circumference of one sample. The average of 116 µm gives a new t/r of 0.0232 for the samples manufactured for these experiments.

While it is clear that the mean thickness of all samples is well above the nominal value of 40 µm, it is also seen that the coating thickness is not constant around the circumference of any of the four samples examined. This implies that the estimated thicknesses were not accurate, and that there is substantial variation of the coating thickness around the circumference of the samples. As the buckling loads of shells are highly sensitive to geometric imperfections [73, 76, 78, 79, 102], the variation in coating thickness around

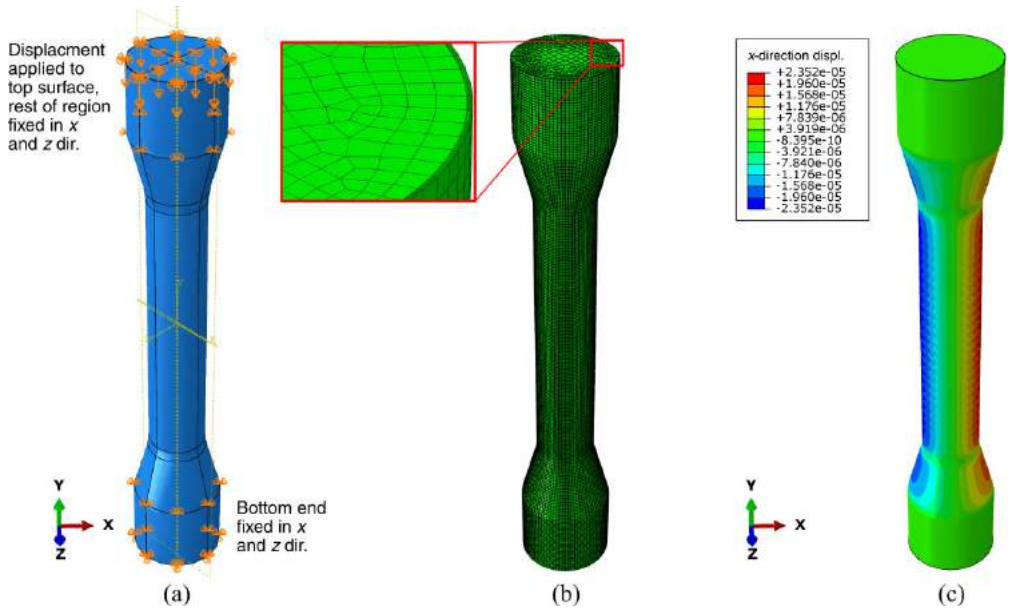

Figure 8.9: (a) Finite element simulation setup for a dogbone specimen with a 100 µm coating thickness. The sample is fixed at the all indicated positions except at the top where an axial displacement is applied. (b) The meshed geometry with 200 000 elements, and 5 elements through the coating thickness as shown in the inset. (c) Resulting displacements near the point of local shell buckling failure encountered in the simulation.

the circumference of all samples (including those not sectioned) likely contributed to deviations from the predicted buckling behaviour.

8.4.4 Comparing Results to Predictions

As seen in Figure 8.7, the predicted loads shown include the those for hollow-shell inelastic buckling (Equation 7.10 of Chapter 7) and filled-shell inelastic buckling (Equations 7.9 and 7.9 of Chapter 7). Load predictions were found using a thickness of 100 µm, while the yield point of the coating is also shown for reference. A lower value of the thickness was used than is given by the average value in Table 8.2 due to the uncertainty associated with the samples which were not sectioned for the microscope analysis. The stress-strain data for nNi as obtained from RepLiForm Inc [7] were used to calculate the inelastic buckling loads, utilizing the Voce fit parameters as shown previously in Table 7.1 of Chapter 7.

An Abaqus finite element simulation was also conducted using the dogbone geometry with a 100 µm coating for comparison to the force-displacement behaviour of the tested samples. Figure 8.9(a) shows the boundary conditions used for the finite element simulation, where the top end of the sample was compressed axially while both ends of the sample were not allowed to move in the x or z directions. These boundary conditions match those imposed through the use of the aluminium collars and the axial displacement applied using the MTS load frame. The dogbone geometry was meshed using over 200 000 first-order elements, with 5 elements enforced through the coating thickness as shown in the inset of Figure 8.9(b).

As previously done for the verification simulations of the inelastic buckling model (refer to Section 7.4 of Chapter 7), an elastic buckling simulation was first performed to determine the buckled shapes of

Table 8.3: Statistics of failure loads (in N) of the samples as found from the experiments. Results are given for the nine 40 µm samples, the two 56 µm samples and all 11 samples together.

	Coating Thickness		
	40 microns	56 micron	All samples
Maximum Observed Failure Load	5084	7155	7155
Minimum Observed Failure Load	7060	5599	5084
Mean Value of Observed Loads	6102	6377	6152
Standard Deviation	615	—	661
Inelastic Buckling Load	8657	9155	11 345*

* Calculated using coating thickness of 100 µm

the geometry. An imperfection pattern was generated using the first 6 elastic buckled shapes, which were used together with plastic material properties for the shell (refer to Tables 7.2 and 7.3 in Chapter 7). The resulting buckling pattern on the coating surface is shown in Figure 8.9(c). As done previously for the inelastic buckling simulations, another method of determining failure was required [71], as a sharp drop in force-displacement behaviour was not apparent.

The force-displacement behaviour of the Abaqus simulation is shown with the experimental data in Figure 8.7. This behaviour is more compliant than the experimental data, an indication that the coatings of the majority of the experimental samples may be thicker than the value of 100 µm used in both the theoretical predictions and the Abaqus simulations. However, the shape of the force-displacement curve generated from the Abaqus simulation is consistent with the general shapes of the force-displacement curves as obtained from the experimental data, showing that the behaviour of the samples was captured accurately by the Abaqus simulations despite the lower thickness value used for the analysis.

8.4.5 Finite Element Simulation of Off-axis Loading

Despite the use of aluminium collars for clamping the ends of the specimens during axial loading, there are very large deviations of the failure loads compared to the predictions for inelastic filled-shell buckling, as seen in Figure 8.7. While one reason for this is the non-axisymmetric coatings as found from the microscopy analysis, a finite element simulation using an off-axis load was performed to verify whether this causes premature failure.

The finite element simulation as previously shown in Figure 8.9 was modified to use an off-axis displacement loading that varied linearly in the xz plane. The mesh characteristics and material properties were unchanged for this modified simulation. Figure 8.10(a) shows the displacement magnitudes for both the pure axial loading simulation as previously shown in Figure 8.9(c), along with the results of the modified simulation (Figure 8.10(b)) at an axial strain value of 0.025. This corresponds to a point below the inelastic shell buckling load encountered for this geometry, as seen in the force-displacement diagram of Figure 8.7.

The deflected shape and displacements of the geometry in Figure 8.10(b) indicate that Euler buckling takes place well before local shell buckling when an off-axis load is applied to the specimen. The transition of the dominant failure mode from local shell buckling to global buckling depends on how pronounced the

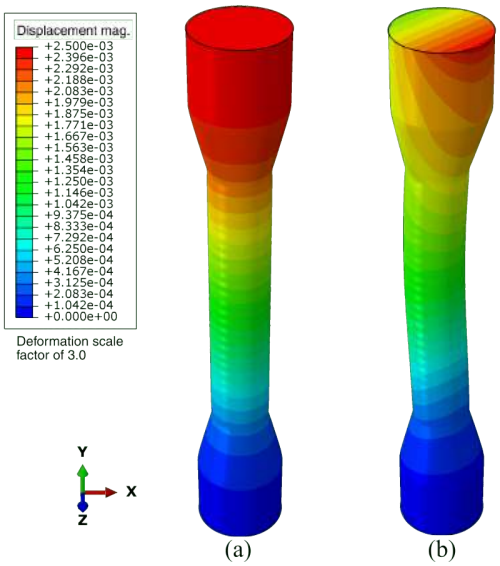

Figure 8.10: (a) Displacement magnitudes from a finite element analysis for the pure axial loading simulation as previously shown in Figure 8.9(a). (b) Displacement magnitudes from a finite element analysis where an off-axis loading is applied to deliberately cause Euler buckling of the sample.

mismatch is between the axis of the applied load and that of the sample geometry.

8.5 Discussion

While the aim of these experiments was to validate the inelastic model for filled shell buckling derived in Chapter 7, both the imperfections in the sample geometries as well as the asymmetry in the axial loading lead to buckling loads that were well below the predicted values. The buckling loads found through experiments were within 45-65% of the predicted buckling load. The sample which failed at 45% of the load predictions was below the yield strength of the nNi coating. For the same thickness-to-radius ratio as the present specimens (approximately 0.02 for the average measured thickness of 116 µm), experiments performed by Karam and Gibson were within 75% of their predictions [5].

Although the nominal coating thicknesses were 40 µm and 56 µm, microscopy investigations of four of the 40 µm samples revealed that the average coating thickness was at least 100 µm. Although there were two samples with a quoted thickness of 56 µm, their force displacement behaviours (Figure 8.7) are indicative of thicknesses closer to what was found in the microscopy investigations. It is also likely that the irregularity found in the four sectioned samples existed in all of the samples. As local shell buckling is highly sensitive to geometric imperfections of the shell [73, 76, 78, 79, 102], the large differences in coating thickness on different sides of the specimens likely caused large deviations from the predicted loads.

The asymmetry in loading was partially overcome through potting the samples into the aluminium collars (see Figure 8.4). As mentioned in Section 8.3.1, the levelness of the compression platens on the load frame was checked in between experiments. Given that the symmetry of the load was not checked

as extensively as was done by Tennyson [78, 88], the exact nature of the asymmetric loading could not be ascertained. However, premature buckling did take place for a few of the samples whereby Euler buckling took place concurrently with local shell buckling of the coating. The results of the off-axis loading simulations in Abaqus (Figure 8.10) have shown that this is a possible outcome when the loading is not symmetric about the circumference of the sample.

During the careful experiments of hollow-shell buckling performed by Tennyson [78, 87], strain gauges were positioned around the circumference of each tested specimens to ensure an axisymmetric distribution of the axial load. The aim of potting the ends of the present specimens in aluminium collars was to achieve axisymmetry in the load, but any mismatch between the load and geometry axes would lead to buckling loads below the predicted values. The strain distribution around the circumference of the samples was not tested as carefully as it was by Tennyson. Thus there is a high likelihood that there was loading asymmetry that led to premature shell buckling. It is the presence of imperfections in loading and geometry which drove the creation of empirical correction factors for hollow shells [72, 79].

Past experimental methods have focused heavily on the manufacturing methods of samples intended for either hollow or filled shell buckling analysis. Several of the experimental programs also involved manufacturing the specimens as a first step to ensure that few imperfections are present in the shells [5, 78, 107, 109]. For filled-shell experiments, the shells were manufactured first prior to being filled with a foam core. However, in the case of the present experiments, the core material was machined from ABS stock rod before nanocrystalline nickel was electrodeposited. This did not allow for inspection of the coating quality (i.e. that of the shell) prior to experiments being conducted, a practice which was carried out in previous experiments for both hollow and filled shell buckling [5, 78, 96].

There were not enough samples used for this study to indicate whether the deviations from the model are a regular occurrence for polymer-filled metal cylinders. Furthermore, the breadth of the data is not enough to warrant the creation of empirical correction factors for filled shells. Given the irregularity in the metal coatings along with the presence of asymmetric loading, both the sample manufacturing methods as well as experimental procedures will need to be refined prior to the undertaking of more validation programs for metal-coated polymer cylinders, whether this be for investigations of elastic or inelastic buckling.

8.6 Conclusions

Experiments were performed in an attempt to validate the load predictions of the inelastic filled-shell buckling model for metal-coated polymer cylinders loaded in axial compression. Specimens were made by using ABS dogbone-shaped specimens coated with an electrodeposited nanocrystalline nickel coating. The shape of the specimens was designed in conjunction with finite element studies in order to minimize von Mises stresses at the ends of the gauge section while maximizing stresses within the gauge section. The specimens were coated with a nominal coating thickness of 40 or 56 µm.

Prior to testing, each specimen was potted in aluminium collars using an off-the-shelf two-part epoxy. The intention was to alleviate asymmetric loading that can cause premature buckling of the samples, either through early Euler buckling or premature local shell buckling of the coating. The specimens were also bonded to the compression platens of the load frame for the same reasons.

Even though the samples had been designed to minimize stresses in the neck region, the majority of the samples failed with buckle folds appearing near this narrowing neck area. This implies that although care was taken to mitigate failure near at the ends of the gauge section, the higher stresses in this region still lead to buckling folds. Improper alignment of some specimens – either through inadequate potting techniques or poor compression platen levelling – also caused Euler buckling to occur before local shell buckling of the coating, a phenomenon that was confirmed through finite element analysis of the sample geometry under an off-axis load.

Microscopy investigations performed on sections cut from several tested samples revealed that the coating thicknesses were well above the nominal values: an average thickness of 116 µm was found among four samples sectioned compared with the 40 µm nominal thickness for these samples. Furthermore, the variation of the coating thickness of each of the samples sectioned revealed that the coating thickness for one sample could vary up to 25 µm around its circumference or over 20% of the average coating thickness.

As local shell buckling of axially compressed cylinders is highly sensitive to material, geometric and loading imperfections, it is likely that the above factors contributed to the poor agreement between the experimentally-determined failure loads for these specimens and the inelastic local shell buckling predictions. The failure loads for the the specimens with the highest buckling load were 35% away from the predicted inelastic failure load. There was little tearing of the coatings upon failure, indicating a good bond between the metal coating and the polymer surface and thus ruling out poor adhesion as a contributing factor. The undesirable Euler buckling and fold locations were due to poor specimen alignment and unforeseen effects of stress concentration near the narrowing sections of the samples, respectively.

Future test campaigns must include a thorough specimen design study prior to validating any filled shell models. In addition, more care must be taken to align the sample geometry axis to that of the loading direction, potentially requiring additional load frame attachments such as self-aligning compression platens. If possible, better coating methods must be developed to ensure a more even coating thickness around the circumference of samples. This may require various microscopy operations to ensure even coatings on cylindrical specimens prior to manufacturing the final specimens for experimental investigations of a similar nature.

Chapter 9

Mass Minimization of Axially-Loaded Filled Cylinders

9.1 Introduction

In designing aircraft, structural weight should be minimized in order to reduce fuel consumption. Simultaneously, strength, stiffness and safety must be maintained. Metal-coated polymer microtruss structures offer the low-weight capabilities of truss topologies together with the high strength and increased wear resistance of nanocrystalline metals. To make these hybrid structures more mass-efficient, a characteristic attractive for aircraft design, their efficiency can be improved through minimum mass design.

Hybrid microtruss structures are created by first building a polymer preform through 3D printing and subsequently electrodepositing a thin layer of nanocrystalline metal on the polymer surface [4, 21, 31]. These structures utilize the mass-efficient geometries of microtruss topologies, the advantageous second moment of area of a coated cylinder and the high strength of nanocrystalline metals. Analyses previously carried out by Lausic et al [1] focused on minimum mass configurations for polymer/nanocrystalline metal hybrid microtrusses. A consistent phenomenon found through three point bending tests was that failure was associated with buckling instabilities in the compression members. Failure occurred either through global Euler buckling of struts, or by local shell buckling of the nanocrystalline metal coating. Because the strut geometry of these microtrusses is cylindrical, the axial buckling load of metal-coated polymer cylinders has been investigated to understand the strut behaviour. The buckling behaviour of hollow-shell cylinders, polymer-filled cylinders and hollow-core cylinders have been previously examined in Chapters 4 and 6. This chapter examines the methods of optimizing cylinder geometries for minimum mass design.

Various studies have examined different facets of the mass efficiency of axially-loaded columns. In a general analysis of compression members, Budiansky [45] showed that the optimal member has a cylindrical cross-section. He further showed that a cylindrical section with a sandwich core and rigid face sheets on the inner and outer surfaces offers the best performance. As the study done by Budiansky was purely analytical, methods of producing these optimal compression members were not discussed. Optimization studies have also been conducted for cylinders filled with polymer foams by Dawson and Gibson [116]. It was shown that a foam-filled cylinder can be designed to fail simultaneously through elastic local shell buckling and material yielding if a sufficiently low ratio of shell-to-core moduli is selected. This study also accounted for cylinders with hollow polymer cores; however the cases considered were limited to cylinders with very small

shell thickness-to-radius ratios.

Polymer-filled metal shells have been examined by Lausic et al [1, 4], where geometries were optimized for minimum mass design. These studies focused primarily on the shell behaviour while treating the polymer core as a parasitic mass, and the optimization studies were carried out for metal-coated polymer cylinders loaded in axial compression. In these studies, the objective was to find both the ideal geometry as well as optimal grain size of the electrodeposited nanocrystalline metal [1, 4], the latter of which is controlled by tuning the parameters of the electrodeposition process [28–30, 41]. The results revealed that hollow cylinders are preferred for minimum mass design, while the grain size can be chosen according to the load-carrying capacity required. This load capacity is a trade-off between the elastic buckling load and the material yield strength: as the grain size of a nanocrystalline metal is decreased its Young's modulus will decrease while its strength increases [132].

Although Lausic et al. assumed that the polymer core was merely a parasitic mass, it is intuitive that the polymer provides a strength benefit beyond its axial load-bearing capacity by supporting the shell against buckling [96–98, 107, 116]. The present work (Chapters 4 through 7) also details the contributions that a polymer core provides. Though Dawson and Gibson [116] conducted a limited set of studies involving foam-filled cylinders, their work did not extend to thick cylinders. Additionally, while the work of Lausic et al. on grain-size optimization [1, 4] is relevant to the present work, their theoretical expressions for local shell buckling did not account for the presence of the polymer core. The present study addresses metal-coated polymer cylinders under axial loads with intermediate-to-high shell thickness (i.e. thickness-to-radius ratios above 0.01), while also accounting for the effects of the core. The analysis will compare the results for hollow-shell cylinders, filled-shell cylinders and hollow-core cylinders. As the length of filled cylinders is also varied for the optimization studies, global buckling becomes a dominant failure mechanism. Thus, in addition to the local shell buckling models developed in earlier Chapters, global buckling is considered as well.

For the present optimization studies, the mass minimization problem can be stated mathematically as:

$$\begin{aligned} \min_{\overline{r},\overline{t},\overline{h}} \quad & \overline{M}(\overline{r},\overline{t},\overline{h}) \\ \text{s.t.} \quad & \overline{F}(\overline{r},\overline{t},\overline{h}) - \overline{f} = 0, \end{aligned}$$

where the objective function $\overline{M}$ is the mass of the filled cylinder, $\overline{r}$ is the radius-to-length ratio of the cylinder, $\overline{t}$ is the thickness-to-radius ratio, $\overline{h}$ is the hollowness factor of the core, $\overline{F}$ is the expression for the failure load and $\overline{f}$ is a required axial load. All the variables are non-dimensional and the design variables of the optimization problem ($\overline{r}$, $\overline{t}$ and $\overline{h}$) are the geometric parameters for the cylinder.

The aim of the current optimization problem is to determine the minimum mass $\overline{M}(\overline{r},\overline{t},\overline{h})$ of a metal-coated polymer cylinder subject to an axial load $\overline{f}$, as it fails under the action of the mechanism described by $\overline{F}(\overline{r},\overline{t},\overline{h})$. Both the shell and core materials are assumed to behave elastically; inelastic behaviour is not

considered for this analysis. The material properties used for the shell are those of nanocrystalline nickel manufactured by RePliForm [7]. The core materials investigated included ABS, LDPE and Divnycell H200 foam. Cylinder configurations which are compared include hollow shells, fully filled cylinders and hollow core cylinders. To investigate the effect of the thin-shell assumption as used for derivation of the hollow-shell, filled-shell and hollow-core shell buckling models, a thick-shell buckling load is also derived for comparison purposes.

This chapter details the procedure used for minimum mass design of axially-loaded filled cylinders, and presents the results of these investigations. The optimization problem will first be outlined in detail, along with a description of the Lagrange multipliers method used for the solution. A set of non-dimensional variables is introduced to generalize the process and results of the optimization procedure. Next, an expression for the global buckling failure mechanism is derived for hollow and filled cylinders, including cores which vary in hollowness. As the mechanisms of local shell buckling, global buckling and simultaneous buckling are investigated, the expressions for these failure mechanisms are rewritten using the system of non-dimensional variables. To compare the results, trajectories of minimum mass are compared graphically for various cylinder configurations. Finally, the implications of the optimization results are provided.

The results of this analysis reveal that the optimal hollow-shell geometry will always have a lower mass than the optimal filled shell. When optimizing cylinders with hollow cores, the most mass-efficient geometry involves complete removal of the core (i.e. convergence to hollow-shell geometries). Although hollow shells may indeed be the most mass efficient, their susceptibility to imperfections makes them unreliable. In practical applications, stiffening elements are used to alleviate this sensitivity [73, 130]. However, for minimum mass design, cylinders filled with hollow polymer cores will likely provide lower masses than stringer-stiffened metal shells.

9.2 Optimization Problem Statement and Methods of Solution

The statement of the optimization problem is presented in this section, followed by a brief description of the Lagrange multipliers method. The optimization procedure is carried out using non-dimensional expressions, and so the optimization problem and the method of Lagrange multipliers are presented using non-dimensional variables. These non-dimensionalized variables are introduced first.

9.2.1 Non-dimensional Variables

To maintain a level of generality for the optimization process, a set of non-dimensional variables is introduced. The equations for the various failure modes will be provided using these non-dimensional terms, and the non-dimensionalized equations will be used for the optimization analysis.

Diagrams of hollow-shell, filled-shell and hollow-core cylinders under an axial load are shown in Figure 9.1. In these diagrams, the cylinders have shell thickness t and inner radius r, while the cylinder has a

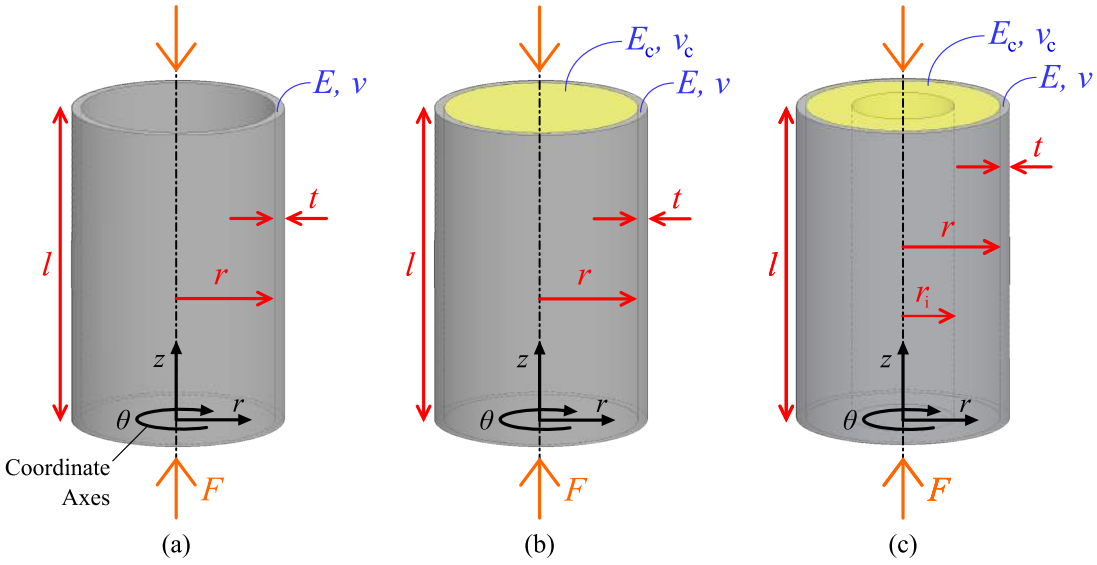

Figure 9.1: Diagrams of (a) hollow shell, (b) filled shell and (c) hollow core cylinders subject to an axial load F. The cylinders have a length l while the shells have thickness t and inner radius r. The hollow core cylinder has an inner radius r_i. The shell and core have Young's Moduli E and E_c while their respective Poisson's ratios are ν and ν_c.

length l. The Young's modulus of the shell is E while its Poisson's ratio is ν; the corresponding properties for the core are E_c and ν_c. The hollow core cylinder, shown in Figure 9.1(c) has an inner radius of r_i. While undergoing local shell buckling, as shown in Figures 9.1(a) through (c), the buckle folds have wavelength λ and amplitude A. Though not indicated in the figures, the cylinders each have a mass M. The non-dimensional parameters for load and mass, respectively, are given as:

$$\overline{F} = \frac{F}{El^2} \qquad \text{and} \qquad \overline{M} = \frac{M}{\rho l^3}. \tag{9.1}$$

Those for non-dimensional Young's modulus and material density are:

$$\overline{E} = \frac{E_c}{E} \qquad \text{and} \qquad \overline{\rho} = \frac{\rho_c}{\rho}, \tag{9.2}$$

while those for non-dimensional thickness, radius, hollowness factor and wavelength are:

$$\overline{t} = \frac{t}{r} \qquad \overline{r} = \frac{r}{l} \qquad \overline{h} = \frac{r_\mathrm{i}}{r} \quad \text{and} \quad \overline{\lambda} = \frac{\lambda}{t}. \tag{9.3}$$

These non-dimensional variables will be used when expressing the optimization problem statement as well as failure loads given in Section 9.4.

9.2.2 Optimization Problem Statement

The objective of optimizing a metal-coated polymer cylinder is to minimize its mass while it is subject to a given axial load. This optimization problem is:

$$\begin{aligned} \min_{x} \quad & M(x) \\ \text{s.t.} \quad & F(x) - f = 0 \end{aligned} \tag{9.4}$$

where the objective function M is the mass of the cylinder, F is the expression for the failure load and f is a required load carrying capacity. The materials of the cylinder are known, and only elastic behaviour is considered. The variables of the optimization problem x consist purely of the geometric parameters for the cylinder: its radius r, shell thickness t and its length l as seen in Figure 9.1. The mass of the cylinder M is:

$$M = \pi l(2rt\rho + r\rho_c(1 - \overline{h}^{\,2})), \tag{9.5}$$

where l is the cylinder length, r is the core outer radius, t is the shell thickness, $\overline{h}$ is the hollowness ratio, and ρ and ρ_c are the densities of the shell and core materials (respectively). Equation 9.5 can be used for hollow cylinders (when $\overline{h} = 1$), filled cylinders (when $\overline{h} = 0$) and hollow core cylinders (when $0 < \overline{h} < 1$). Using the non-dimensional variables given in Equations 9.1 through 9.3, this mass can be represented as:

$$\overline{M} = \pi\overline{r}^2(2\overline{t} + \overline{\rho}(1 - \overline{h}^{\,2})) \tag{9.6}$$

Using the non-dimensional variables, the optimization problem is:

$$\begin{aligned} \min_{\overline{r},\overline{t},\overline{h}} \quad & \overline{M}(\overline{r},\overline{t},\overline{h}) \\ \text{s.t.} \quad & \overline{F}(\overline{r},\overline{t},\overline{h}) - \overline{f} = 0, \end{aligned} \tag{9.7}$$

where $\overline{f} = f/El^2$ is the non-dimensionalized form of the required load f. The value of the force obtained from $F(\overline{r},\overline{t},\overline{h})$ is dependant on the wavelength λ (or its non-dimensional equivalent $\overline{\lambda}$). This wavelength value is determined by solving the equation $\partial\overline{F}/\partial\overline{\lambda} = 0$ for given values of $\overline{r}$, $\overline{t}$ and $\overline{h}$.

9.2.3 Method of of Lagrange Multipliers

An analytical solution to the optimization problem is ideal, as it will provide closed-form expressions which lead to optimal cylinder geometries when the material properties are known. The method of Lagrange multipliers is ideally suited to solving multi-variable optimization problems with one or more equality constraints [133]. To find the maximum and minimum values of the non-dimensional mass $\overline{M}$ subject to the load constraint as given in Equation 9.7, the values $\overline{r}$, $\overline{t}$ and $\overline{h}$ are found such that:

$$\nabla\overline{M}(\overline{r},\overline{t},\overline{h}) = \mu\nabla\overline{F}(\overline{r},\overline{t},\overline{h}), \tag{9.8}$$

where μ is a Lagrange multiplier. In some cases, the analytical solutions are intractable, necessitating the use of numerical solutions. Furthermore, there are instances where the optimal mass for given load may lead

to infeasible geometries, such as those where the core hollowness values $\overline{h}$ are above 1 or a solution provides negative values of the non-dimensional variables $\overline{r}$, $\overline{t}$, and $\overline{h}$.

For a complete description of the optimal geometries for each of the cylinder configurations, the optimality conditions for each of the non-dimensional load expressions (Section 9.4) must be found first, followed by the solutions for regions where two or more loads have equal values. The use of failure mechanism maps and minimum mass trajectories will aid in representing the failure modes and optimal cylinder geometries.

9.2.4 Failure Mechanism Maps

A failure mechanism map is useful to illustrate the influence of different material or geometric parameters on the failure mode of a structure. Failure mechanism maps are two-dimensional or three-dimensional graphs where the axes are non-dimensional material or geometrical parameters. As these parameters are varied, the map shows the active failure mechanisms for different designs [23]. A failure mechanism map is divided into regions, each of which has an active failure mechanism. The borders between the regions are where two or more failure mechanisms are activated by the same load. Failure mechanism maps are useful for determining the relationships between geometry or material properties and the dominant failure mechanisms. In addition, they can be utilized to show trajectories of minimum mass, which is the locus along which the mass of a structure is a minimum as the load is increased.

To develop a complete failure mechanism map for a metal-coated polymer cylinder subject to axial compressive loads, the information of all failure mechanisms is required. This includes both the local shell buckling and global buckling failure mechanisms, which are discussed in the next section.

9.3 Thick-shell Buckling and Global Buckling Failure

In undertaking optimization studies, it is necessary to determine the relevant failure modes. In addition, the results of different geometric configurations are to be examined. In this section, the failure loads for global Euler buckling of various shell configurations are provided. It is also of interest to examine the implications of removing the thin-shell assumption that is utilized in the hollow-shell buckling load derivation of Timoshenko [34]. The resulting "thick-shell" buckling load is also discussed in this section.

9.3.1 Thick-Shell Local Shell Buckling

Figure 9.1(a) shows a hollow cylinder under an axial load F. Its dimensions include its length l, radius r and shell thickness t. The shell material has a Young's Modulus E and Poisson's ratio ν. At a critical load F, the shell buckles along its length with wavelength λ and amplitude A, as shown in Figure 9.2(a). The buckling load for thin hollow cylindrical shells in axial compression is [34–37]:

$$\sigma_{\text{HS}} = \frac{Et}{r\sqrt{3(1-\nu^2)}}$$

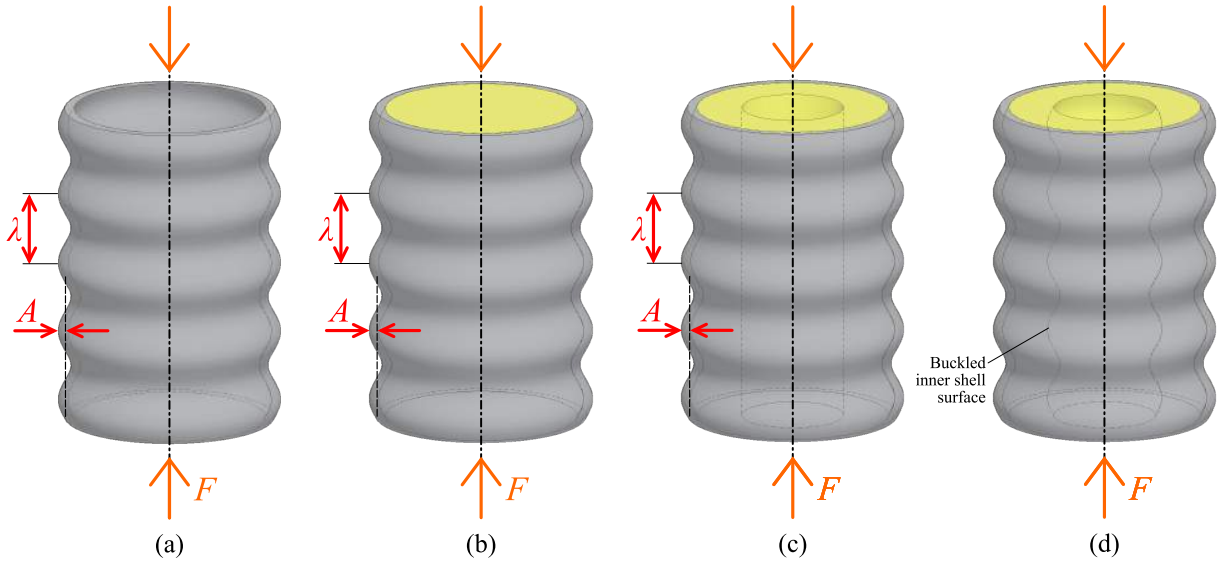

Figure 9.2: Diagrams of (a) hollow shell, (b) filled shell and (c) hollow core cylinders undergoing local shell buckling under an axial load F. The buckle folds have wavelength λ and amplitude A. (d) A hollow core cylinder undergoing simultaneous buckling.

where σ_{HS} is the axial buckling stress on the cylinder. This equation can be rewritten to give a buckling force [4]:

$$F_{\text{HS}} = \frac{2\pi E t^2}{\sqrt{3(1-\nu^2)}}. \tag{9.9}$$

The above equations are derived assuming that the shell is thin (i.e. $t/r \leq 0.1$) and therefore is less accurate as the shell thickness becomes large (when $t/r \geq 0.1$). Accounting for a thick shell requires a change in the derivation of the local shell buckling load.

As mentioned in Chapter 4, the strain energy for a cylindrical shell under an axial compression load includes its bending energy U_{b} (Equation 4.2) as well as the energy due to circumferential stretching U_{c} (Equation 4.3). The shell bending energy refers to the strain energy accumulated due to the bending of longitudinal sections of the shell as they undergo sinusoidal buckling deformations, while the circumferential stretching energy results from the tension or compression of the shell hoop sections to accommodate that bending. The external energy U_{e} (Equation 4.6) applied to the cylinder arises due to the axial compression load F as shown in Figure 9.1(a).

When deriving the hollow-shell buckling equation, an energy minimization procedure using U_{b}, U_{c} and U_{ex} leads to Equation 9.9. Originally, the expression for U_{c} assumes that the shell is very thin compared to the shell radius. Re-deriving this expression while removing the thin-shell approximation leads to:

$$U_{\text{c}} = \int_{\text{A}} \int_0^l \int_0^{\epsilon_{rc}} \sigma_{rc} r \, \mathrm{d}\epsilon \mathrm{d}z \mathrm{d}r \mathrm{d}\theta = \frac{\pi t(2r+t) E A^2 l}{4r^2}, \tag{9.10}$$

where

$$\sigma_{rc} = E\epsilon_{rc} = E\frac{1}{r} A \sin\left(\frac{m\pi z}{l}\right).$$

Here, ϵ_{rc} is the circumferential strain in the shell. The new expression for U_c (Equation 9.10) is used in conjunction with the unmodified expressions for U_b and U_e (Equations 4.2 and 4.6 from Chapter 4, respectively). Utilizing the same procedure detailed in Chapter 4, the thick-shell buckling load is:

$$F_{TL} = \frac{2E\pi^3 t^3 r}{\sqrt{3(1-\nu^2)}} \frac{1}{\lambda_{TS}} + \frac{Et(2r+t)}{4\pi r^2} \lambda_{TS}^2 \tag{9.11}$$

where the critical buckling wavelength is found by solving for λ_{TS} in the equation $\partial F_{TL}/\partial \lambda_{TS} = 0$:

$$\lambda_{TS} = \pi \left(\frac{8t^2 r^3}{3(1-\nu^2)(2r+t)} \right)^{1/4}. \tag{9.12}$$

The thick-shell local shell buckling equation (Equation 9.11) produces the same results as that of the thin-shell (Equation 9.9) when the shell thickness is small (i.e. $t/r \leq 0.01$). However, when the shell thickness is increased substantially, the thick-shell buckling load will give more accurate predictions.

9.3.2 Global Buckling

Global or Euler buckling dominates when a compression member has large aspect ratio. When a strut fails through global buckling, it forms visible curvature along its length at a critical load, often well before the strut material yield point. The global buckling load of a strut in axial compression is given by [34, 65]:

$$F_{GB} = \frac{\pi E I}{l^2}, \tag{9.13}$$

where F_{GB} is the global buckling load and I is the second moment of area of the strut cross-section. It is of interest to determine the global buckling load of a cylindrical strut loaded in axial compression, both with and without a polymer core. Figures 9.1(a) and (b) illustrate the dimensions of a hollow and filled cylinder, respectively.

Consider a thin hollow shell in axial compression (Figure 9.1(a)) undergoing global buckling. The second moment of area is approximated as:

$$I_{HS} = \frac{\pi}{4}[(r+t)^4 - r^4] = \frac{\pi}{4}(4r^3 t + 6r^2 t^2 + 4rt^3 + t^4) \approx \pi r^3 t. \tag{9.14}$$

This produces the global buckling equation for a thin hollow shell in axial compression:

$$F_{HG} = \frac{\pi^3 E r^3 t}{l^2}. \tag{9.15}$$

For a thick cylindrical shell, or equivalently by ignoring the thin-shell assumption, all terms from

Equation 9.14 are kept, leading to a global buckling load for a cylinder with a thick shell:

$$F_{\mathrm{TG}} = \frac{\pi^3 E(4r^3t + 6r^2t^2 + 4rt^3 + t^4)}{4l^2}. \tag{9.16}$$

When calculating the global buckling load for a filled cylinder (Figure 9.1(b)), the second moment of area includes the modulus-weighted second moment of area of the polymer core:

$$I_{\mathrm{FS}} = \frac{\pi}{4}\left(4r^3t + \frac{E_{\mathrm{c}}}{E}r^4\right). \tag{9.17}$$

This expression utilizes the thin-shell assumption. The use of I_{FS} produces the filled shell global buckling equation:

$$F_{\mathrm{FG}} = \frac{\pi^3 E r^3[4t + r\frac{E_{\mathrm{c}}}{E}]}{4l^2} \tag{9.18}$$

A final configuration of a filled cylindrical shell occurs when the core is partially removed as shown in Figure 9.1(c). Here, the shell has the same dimensions as previously shown in Figure 9.1(b), but now includes a core inner radius r_{i}. To normalize the hollow core geometry, the hollowness factor $\overline{h}$ is used (see Equations 9.3). For the hollow-core configuration, the second moment of area of the filled shell (Equation 9.17) is modified to account for this:

$$I_{\mathrm{HC}} = \frac{\pi}{4}\left(4r^3t + \frac{E_{\mathrm{c}}}{E}r^4(1 - \overline{h}^{\,4})\right). \tag{9.19}$$

This produces the hollow core global buckling equation:

$$F_{\mathrm{HCG}} = \frac{\pi^3 E r^3[4t + r\frac{E_{\mathrm{c}}}{E}(1 - \overline{h}^{\,4})]}{4l^2}. \tag{9.20}$$

Equation 9.20 reduces to Equation 9.18 when the core is completely filled (i.e. $\overline{h} = 0$) and to Equation 9.15 when the core is completely removed (i.e. $\overline{h} = 1$). Like the filled shell buckling load, the hollow core buckling load also utilizes the thin-shell approximation (i.e. $t/r \leq 0.1$).

9.4 Non-dimensional Load Expressions

The variables introduced in Equations 9.1 through 9.3 are used to non-dimensionalize the load expressions given in Section 9.3, as well as those introduced in earlier chapters.

9.4.1 Hollow Shell

For a thin hollow cylindrical shell (Figure 9.1(a)), the mass of the cylinder is given as:

$$M_{\mathrm{HS}} = 2\pi rtl\rho. \tag{9.21}$$

Using the non-dimensional variables given in Equations 9.1 through 9.3, the non-dimensional mass of a hollow metal cylinder is:

$$\overline{M}_{\mathrm{HS}} = 2\pi\overline{r}^2\overline{t}. \tag{9.22}$$

This is the same expression obtained when the mass expression introduced in Equation 9.5 is used with $\overline{h} = 1$. The failure modes associated with hollow-shell buckling are global buckling and local shell buckling. The global buckling load was previously found as Equation 9.15, while the local shell buckling equation was given in Equation 9.9. Using non-dimensional forms, their expressions are rewritten as:

$$\overline{F}_{\mathrm{HG}} = \pi^3\overline{r}^4\overline{t}, \quad \text{and} \tag{9.23}$$

$$\overline{F}_{\mathrm{HS}} = \frac{2\pi\overline{r}^2\overline{t}^2}{\sqrt{3(1-\nu^2)}}. \tag{9.24}$$

9.4.2 Thick Hollow Shell

The mass of a thick hollow shell is:

$$M_{\mathrm{TS}} = \pi\rho tl(2r + t). \tag{9.25}$$

It is represented non-dimensionally as:

$$\overline{M}_{\mathrm{TS}} = \pi\overline{r}^2\overline{t}(2 + \overline{t}). \tag{9.26}$$

Equations 9.16 and 9.11 provided the global and local shell buckling loads, respectively, for a thick hollow shell in axial compression. Using the non-dimensional parameters of Equations 9.1 through 9.3,

$$\overline{F}_{\mathrm{TG}} = \frac{\pi^3\overline{r}^4}{4}(4\overline{t} + 6\overline{t}^{\,2} + 4\overline{t}^{\,3} + \overline{t}^{\,4}), \quad \text{and} \tag{9.27}$$

$$\overline{F}_{\mathrm{TL}} = \overline{r}^{\,2}\left(\frac{2\pi^3\overline{t}}{\sqrt{3(1-\nu^2)}}\frac{1}{\overline{\lambda}^2_{\mathrm{TS}}} + \frac{\overline{t}^{\,3}(2+\overline{t})}{4\pi}\overline{\lambda}^2_{\mathrm{TS}}\right), \tag{9.28}$$

where

$$\overline{\lambda}_{\mathrm{TS}} = \pi\left(\frac{8}{3\overline{t}^{\,2}(1-\nu^2)(2+\overline{t})}\right)^{1/4}.$$

9.4.3 Polymer-Filled Shell

The mass of a metal shell filled with a polymer foam, as shown in Figure 9.1(b), is given as:

$$M_{\mathrm{FS}} = \pi l(2rt\rho + r\rho_c). \tag{9.29}$$

Representing this mass using the non-dimensional variables of Equations 9.1 through 9.3,

$$\overline{M}_{\mathrm{FS}} = \pi\overline{r}^2(2\overline{t} + \overline{\rho}). \tag{9.30}$$

This expression is also obtained by using $\overline{h} = 0$ in Equation 9.6. The equation for the global buckling load of a filled cylindrical shell was previously given in Equation 9.18. Its non-dimensional form is:

$$\overline{F}_{\mathrm{FG}} = \frac{\pi^3 \overline{r}^4}{4}[4\overline{t} + \overline{E}]. \tag{9.31}$$

For filled-shell local shell buckling, the load was previously derived in Chapter 4:

$$F_{\mathrm{FL}} = \left(1 + \frac{E_c}{E}\frac{r}{2t}\right)\left[\frac{2\pi^3 r E t^3}{3(1-\nu^2)}\frac{1}{\lambda_{\mathrm{FS}}^2} + \frac{Et}{2r\pi}\lambda_{\mathrm{FS}}^2 + \frac{K_{\mathrm{f}} r}{\pi}\lambda_{\mathrm{FS}}\right], \tag{9.32}$$

where the critical wavelength λ_{FS} is found by determining the root of $\partial F_{\mathrm{FL}}/\partial\lambda_{\mathrm{FS}} = 0$. This gives a 4th-order polynomial which can be solved for an exact value of λ_{FS}. The non-dimensional form of 9.32 is:

$$\overline{F}_{\mathrm{FL}} = \overline{r}^2\left(1 + \frac{\overline{E}}{2\overline{t}}\right)\left[\frac{2\pi^3\overline{t}}{3(1-\nu^2)}\frac{1}{\overline{\lambda}_{\mathrm{FS}}^2} + \frac{\overline{t}^3}{2\pi}\overline{\lambda}_{\mathrm{FS}}^2 + \frac{\overline{K}_{\mathrm{f}}\overline{t}}{\pi}\overline{\lambda}_{\mathrm{FS}}\right]. \tag{9.33}$$

9.4.4 Filled Shell with Hollow Core

The mass of a polymer-filled cylinder with the core partially bored out (as shown in Figure 9.1(c)) is:

$$M_{\mathrm{HC}} = \pi l(2rt\rho + r\rho_c(1 - \overline{h}^{\,2})).$$

Non-dimensionally, this mass can be represented as:

$$\overline{M}_{\mathrm{HC}} = \pi\overline{r}^2(2\overline{t} + \overline{\rho}(1 - \overline{h}^{\,2})).$$

These expressions were previously introduced in Equations 9.5 and 9.6. The hollow-core global buckling load was previously given in Equation 9.20. It is represented using non-dimensional variables as:

$$\overline{F}_{\mathrm{HCG}} = \frac{\pi^3\overline{r}^4}{4}[4\overline{t} + \overline{E}(1 - \overline{h}^{\,4})]. \tag{9.34}$$

The local shell buckling load of a filled shell with a hollow core, with hollowness factor $\overline{h}$ was previously given in Equation 6.4 of Chapter 6 as:

$$F_{\mathrm{HCL}} = \left(1 + \frac{E_c}{E}(1 - \overline{h}^{\,2})\frac{r}{2t}\right)\left[\frac{2\pi^3 r E t^3}{3(1-\nu^2)}\frac{1}{\lambda_{\mathrm{HC}}^2} + \frac{Et}{2r\pi}\lambda_{\mathrm{HC}}^2 + \frac{r}{\pi}K\left(\overline{h},\ \frac{\lambda_{\mathrm{HC}}}{r}\right)\lambda_{\mathrm{HC}}\right], \tag{9.35}$$

where K is defined previously in Equation 6.2 of Chapter 6. As with filled-shell local shell buckling, Equation 9.32, the critical wavelength is found by solving the equation $\partial F_{\mathrm{HCL}}/\partial\lambda_{\mathrm{HC}} = 0$. Unlike the filled-shell buckling equation, Equation 9.32, this does not yield a closed-form solution for λ_{HC}, necessitating the use

of numerical methods to find its value. The non-dimensional form of Equation 9.35 is:

$$\overline{F}_{\mathrm{HCL}} = \overline{r}^2 \left(1 + \frac{\overline{E}(1-\overline{h}^{\,2})}{2\overline{t}}\right)\left[\frac{2\pi^3\overline{t}}{3(1-\nu^2)}\frac{1}{\overline{\lambda}^2_{\mathrm{HC}}} + \frac{\overline{t}^{\,3}}{2\pi}\overline{\lambda}^2_{\mathrm{HC}} + \frac{\overline{K}\overline{t}}{\pi}\overline{\lambda}_{\mathrm{HC}}\right]. \tag{9.36}$$

where $\overline{K}$, the non-dimensional form of K, is given as:

$$\begin{aligned}\overline{K}\left(\overline{h},\overline{\lambda}_{\mathrm{HC}}\overline{t}\right) =& \overline{K}_{\mathrm{f}} \exp\Big[p_{00} + p_{10}\overline{h} + p_{01}\overline{\lambda}_{\mathrm{HC}}\overline{t} + p_{20}\overline{h}^{\,2} + p_{11}\overline{h}\overline{\lambda}_{\mathrm{HC}}\overline{t} + p_{02}(\overline{\lambda}_{\mathrm{HC}}\overline{t})^2 + \\ & p_{30}\overline{h}^{\,3} + p_{21}\overline{h}^{\,2}\overline{\lambda}_{\mathrm{HC}}\overline{t} + p_{12}\overline{h}(\overline{\lambda}_{\mathrm{HC}}\overline{t})^2 + p_{03}(\overline{\lambda}_{\mathrm{HC}}\overline{t})^3 + p_{40}\overline{h}^{\,4} + \\ & p_{31}\overline{h}^{\,3}\overline{\lambda}_{\mathrm{HC}}\overline{t} + p_{22}\overline{h}^{\,2}(\overline{\lambda}_{\mathrm{HC}}\overline{t})^2 + p_{13}\overline{h}(\overline{\lambda}_{\mathrm{HC}}\overline{t})^3 + p_{04}(\overline{\lambda}_{\mathrm{HC}}\overline{t})^4 + p_{50}\overline{h}^{\,5} \\ & + p_{41}\overline{h}^{\,4}\overline{\lambda}_{\mathrm{HC}}\overline{t} + p_{32}\overline{h}^{\,3}(\overline{\lambda}_{\mathrm{HC}}\overline{t})^2 + p_{23}\overline{h}^{\,2}(\overline{\lambda}_{\mathrm{HC}}\overline{t})^3 + p_{14}\overline{h}(\overline{\lambda}_{\mathrm{HC}}\overline{t})^4 + \\ & p_{05}(\overline{\lambda}_{\mathrm{HC}}\overline{t})^5\Big].\end{aligned} \tag{9.37}$$

A third failure mode for hollow-core cylinders is simultaneous buckling, as previously described in Chapter 6. Its appearance contrasts that of local shell buckling (Figure 9.2(c)) because the inner core wall buckles with the same shape as the shell, as seen in Figure 9.2(d). Its equation was given in Chapter 6 as:

$$\begin{aligned}F_{\mathrm{HCS}} = 4\pi E\Bigg\{&\frac{t+\overline{E}(1-\overline{h}^{\,2})}{1-\nu^2}\left[\frac{t^3}{12} + t\left((1-\overline{h}) + \frac{t}{2} - y_0\right)^2\right. \\ &\left.\frac{(1-\overline{h})^3\overline{E}^{\,3}}{12} + (1-\overline{h})\overline{E}\left(y_0 - \frac{(1-\overline{h})}{2}\right)^2\right]\Bigg\}^{1/2},\end{aligned} \tag{9.38}$$

where the centroid y_0 is defined as:

$$y_0 = \frac{\left((1-\overline{h}) + \frac{t}{2}\right)t + \frac{(1-\overline{h})^2\overline{E}}{2}}{t + \overline{E}(1-\overline{h})}. \tag{9.39}$$

The non-dimensional representation of Equations 9.38 and 9.39 are:

$$\begin{aligned}\overline{F}_{\mathrm{HCS}} = 4\pi\overline{r}^2\Bigg\{&\frac{\overline{t}+\overline{E}(1-\overline{h}^{\,2})}{1-\nu^2}\left[\frac{\overline{t}^{\,3}}{12} + \overline{t}\left((1-\overline{h}) + \frac{\overline{t}}{2} - \overline{y}_0\right)^2\right. \\ &\left.\frac{(1-\overline{h})^3\overline{E}^{\,3}}{12} + (1-\overline{h})\overline{E}\left(\overline{y}_0 - \frac{(1-\overline{h})}{2}\right)^2\right]\Bigg\}^{1/2}\end{aligned} \tag{9.40}$$

and:

$$\overline{y}_0 = \frac{\left((1-\overline{h}) + \frac{\overline{t}}{2}\right)\overline{t} + \frac{(1-\overline{h})^2\overline{E}}{2}}{\overline{t} + \overline{E}(1-\overline{h})}. \tag{9.41}$$

The above non-dimensional equations for thin hollow shells (Equations 9.22, 9.23 and 9.24), thick hollow shells (Equations 9.26, 9.27 and 9.28), filled shells (Equations 9.30, 9.31 and 9.33) and hollow-core shells (Equations 9.6, 9.34, 9.36 and 9.40) will be used in the optimization of an axially-loaded metal-coated

Table 9.1: Materials considered and their mechanical properties and density as utilized for optimization studies. The Young's Modulus, density and yield strength of each material is provided, while the non-dimensional ratios of E_c/E and ρ_c/ρ are also given for the core materials. Nanocrystalline nickel is the shell material for all the material combinations studied, while the core materials considered were ABS, LDPE and H200 foam.

Material	Young's Modulus (GPa)	E_c/E	Density (kg/m^3)	ρ_c/ρ	Yield Strength (MPa)
Nano Nickel[a]	125	—	8908	—	1180
ABS [b]	2.20	0.0176	1050	0.1177	44.81
LDPE	0.286	0.00230	940	0.1055	9.391
H200	0.288	0.00230	200	0.02245	4.850

[a] Nanocrystalline nickel with a grain size of 65 µm; properties obtained from RePliForm Inc. [7]
[b] Divinycell H200 foam; material properties taken as average of nominal and minimum values from [134].
[c] ABS and LDPE material properties obtained from [135, 136]

polymer cylinders.

The mass optimization is carried out by increasing the required load $\overline{f}$ and determining which failure mechanism or mechanisms leads to the lowest mass for that load (refer to Equation 9.7). The mass is calculated by determining the values of $\overline{r}$, $\overline{t}$ and $\overline{h}$ required to achieve the load $\overline{f}$ for each mechanism, and calculating the mass of the cylinders obtained in this way. The resulting mass trajectories are plotted on the failure mechanism maps for each cylinder configuration (filled shell, hollow core and hollow shell). The results of this optimization procedure are given in the next section.

9.5 Optimization Results

The optimization studies were only carried out for elastic failure modes. The failure mechanisms maps for each cylinder geometry are presented, along with the minimum mass trajectories for each case.

Table 9.1 lists the material properties used for the material combinations considered. Divinycell H200, a typical sandwich panel foam, is used to compare the performance of a high stiffness-to-weight core material against typical polymer materials. The material used for the shell in all cylinder configurations is nanocrystalline nickel, while $\overline{E}$ changes as the core material changes.

Failure mechanism maps will be used to illustrate the relationship between the dominant failure modes for different cylinder configurations. For a metal-coated polymer cylinder in axial compression, the primary failure mechanisms are global buckling and local shell buckling, while the design variables are the thickness-to-radius ratio $\overline{t}$ and the radius-to-length ratio $\overline{r}$. For hollow-core cylinders, the hollowness factor $\overline{h}$ is also a design variable. Minimum mass trajectories will show the locus of optimal cylinder designs. Both failure mechanism maps and minimum mass trajectories will be used to compare the optimal designs for the various cylinder configurations.

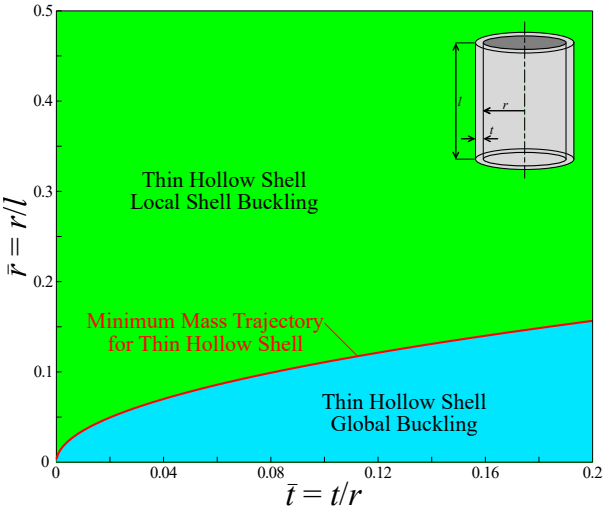

Figure 9.3: Failure mechanism map of a thin hollow shell subject to an axial compressive load. The design space is shown for a range of thickness-to-radius ratios $\bar{t}$ and radius-to-length ratios $\bar{r}$. The two dominant failure mechanisms are local shell buckling and global Euler buckling, while the minimum mass trajectory is along the boundary of these two failure mechanisms.

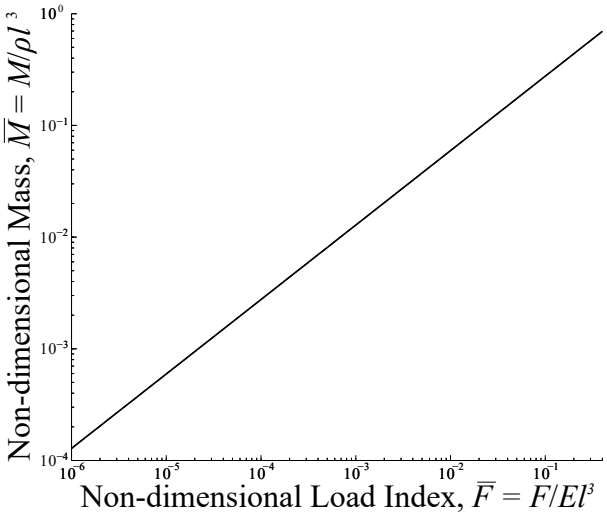

Figure 9.4: Minimum mass trajectory for a thin hollow shell subject to an axial compressive load, showing the non-dimensional optimal cylinder mass $\overline{M}$ as a function of the non-dimensional axial load $\overline{F}$. An optimal thin hollow cylinder will always fail concurrently through local shell and global buckling.

9.5.1 Optimization of Hollow Shells

Figure 9.3 shows the failure mechanism map for a hollow cylinder in axial compression. The relevant failure mechanisms are global buckling and local shell buckling. Equations 9.23 and 9.24 were used to calculate the failure modes, both of which utilize the thin-shell assumption. The optimal trajectory for minimum mass is shown on this Figure, and is plotted against the non-dimensional load index $\overline{F}$ in Figure 9.4. The minimum mass trajectory lies on the boundary between the global and local shell buckling failure modes because there is no feasible optimum for both the global and local shell buckling modes.

The thick hollow shell equations (expressed non-dimensionally in Equations 9.27 and 9.28) eliminate the thin-shell assumption used in classic local shell buckling (Equation 9.35). Figure 9.5 shows the failure mechanism map for a thick hollow shell in axial compression. Comparing this to Figure 9.3 reveals slight changes in the regions for global buckling and local shell buckling, namely the reduced area of the global buckling region. As for the thin-shell buckling behaviour, however, the minimum mass trajectory is once again along the boundary between global and local shell buckling. Despite the elimination of the thin-shell approximation, there is no feasible solution while optimizing for a thick hollow shell to fail through global buckling. However, a solution is found for thick-shell local shell buckling, as shown in the graph of Figure 9.6. The optimal for thick-shell local shell buckling occurs when $\bar{t}$ is well above 0.5, and hence its minimum mass trajectory is not shown on the failure mechanism map of Figure 9.5.

The graph of $\overline{M}$ plotted against $\overline{F}$ in Figure 9.6 includes the data from Figure 9.4 for thin hollow shells. The differences in the minimum mass trajectories are seen as the mass $\overline{M}$ of the cylinder (and therefore the shell thickness-to-radius ratio $\bar{t}$) becomes much larger, illustrating how the thick-shell assumption is more accurate for thicker shells.

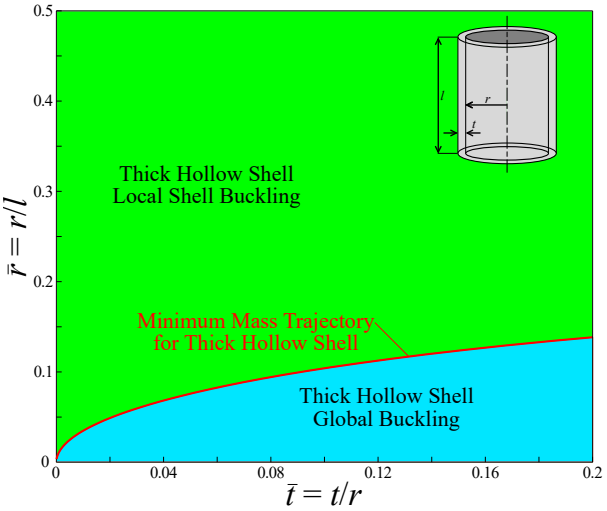

Figure 9.5: Failure mechanism map of a thick hollow shell subject to an axial compressive load. The design space is shown for a range of thickness-to-radius ratios $\bar{t}$ and radius-to-length ratios $\bar{r}$. The two dominant failure mechanisms are local shell buckling and global Euler buckling, while the minimum mass trajectory is along the boundary of these two failure mechanisms.

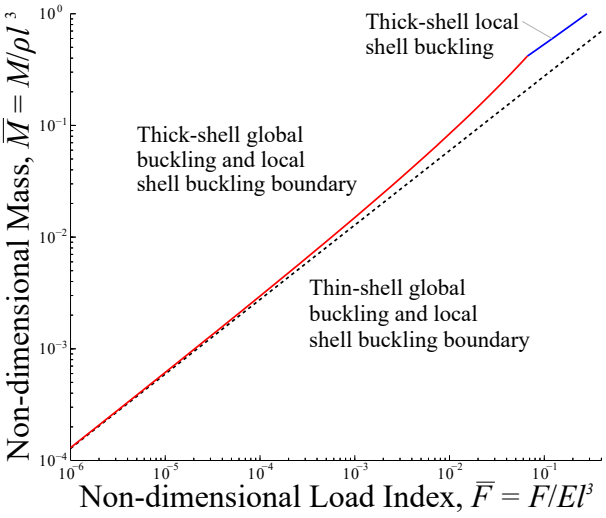

Figure 9.6: Minimum mass trajectory for a thin and thick hollow shells subject to an axial compressive load, showing the non-dimensional optimal cylinder masses $\overline{M}$ as a function of the non-dimensional axial loads $\overline{F}$. The trajectory for a hollow thin shell is found when local shell and global buckling take place concurrently, while the thick-shell trajectory transitions from concurrent local-global buckling to local shell buckling at higher loads.

From the results of the thin- and thick-shell analyses, it is determined that the minimum mass of a cylinder is achieved when a hollow cylinder is designed to fail concurrently through global and local shell buckling. When the loads become very large, local shell buckling is the preferred mode of failure corresponding to very thick-shelled cylinders.

9.5.2 Completely Filled Shell

As a core is now included in the geometry, the results will be presented for a nickel-coated ABS cylinder (i.e. $E_c/E \approx 0.02$), a nickel-coated LDPE cylinder (i.e. $E_c/E \approx 0.002$) and a foam-filled nickel cylinder ($E_c/E \approx 0.002$ with H200 foam). The material properties and densities for these materials are given in Table 9.1. The foam-filled cylinder (i.e. with H200 foam) is examined to compare the results of optimizing foam-filled cylinders against those with solid polymer cores.

The failure mechanism map and the minimum mass trajectory for a filled shell for a nickel-coated ABS cylinder is shown in Figure 9.7(a) while that of a nickel-coated LDPE and a foam-filled nickel cylinder is shown in Figure 9.7(b). On both of these figures, the dominant failure modes are local shell buckling (Equation 9.33) and global buckling (Equation 9.31). Unlike for a thin hollow shell, the minimum mass trajectory for a filled shell passes through the global buckling region, travels along the boundary between global and local shell buckling, and finally passes through the local shell buckling region. This is because there is a feasible solution in the global Euler buckling region for a filled shell, a solution not obtainable for a hollow shell.

Optimization of a filled shell in the global buckling region leads to a single thickness-to-radius ratio

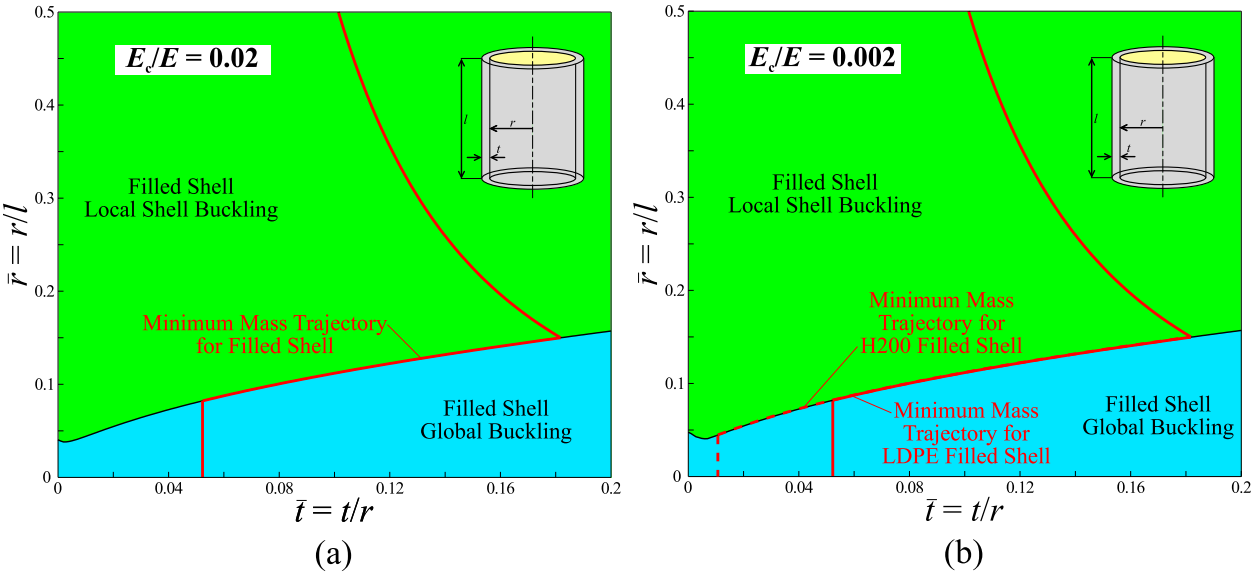

Figure 9.7: Failure mechanism map of filled cylinders subject to axial compressive loads with core materials comprised of (a) ABS ($E_c/E = 0.02$) and (b) LDPE and H200 foam ($E_c/E = 0.002$). For both failure mechanism maps, the design space is shown for a range of thickness-to-radius ratios $\bar{t}$ and radius-to-length ratios $\bar{r}$. The two dominant failure mechanisms are local shell buckling and global Euler buckling. The minimum mass trajectory transitions through these failure regions and along their boundary.

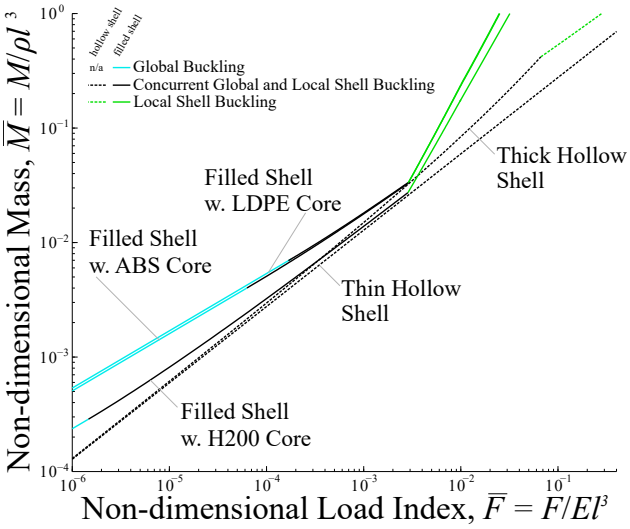

Figure 9.8: Minimum mass trajectories for thin-shell, thick-shell and various filled cylinders. The non-dimensional optimal cylinder masses $\overline{M}$ are given as a function of the non-dimensional axial loads $\overline{F}$. The optimal masses of all filled cylinders are below those of the hollow shells, except for a small region of the load $\overline{F}$.

$\bar{t}$ for a given set of material properties. The lower density of the H200 foam leads to a lower optimal $\bar{t}$ value for global buckling compared to ABS or LDPE cores (see Figure 9.7(b)), but otherwise the same optimal trajectories along the global-local-buckling boundary and through the local shell buckling regions. The optimal thickness-to-radius ratio $\bar{t}$ for the ABS and LDPE shells are very similar: 0.0539 for ABS ($E_c/E \approx 0.02$) and 0.0523 for LDPE ($E_c/E \approx 0.002$). The optimal trajectories for these two materials are nearly identical, indicating that the density of the core material has a strong influence on the optimal trajectory when global buckling is the preferred failure mode.

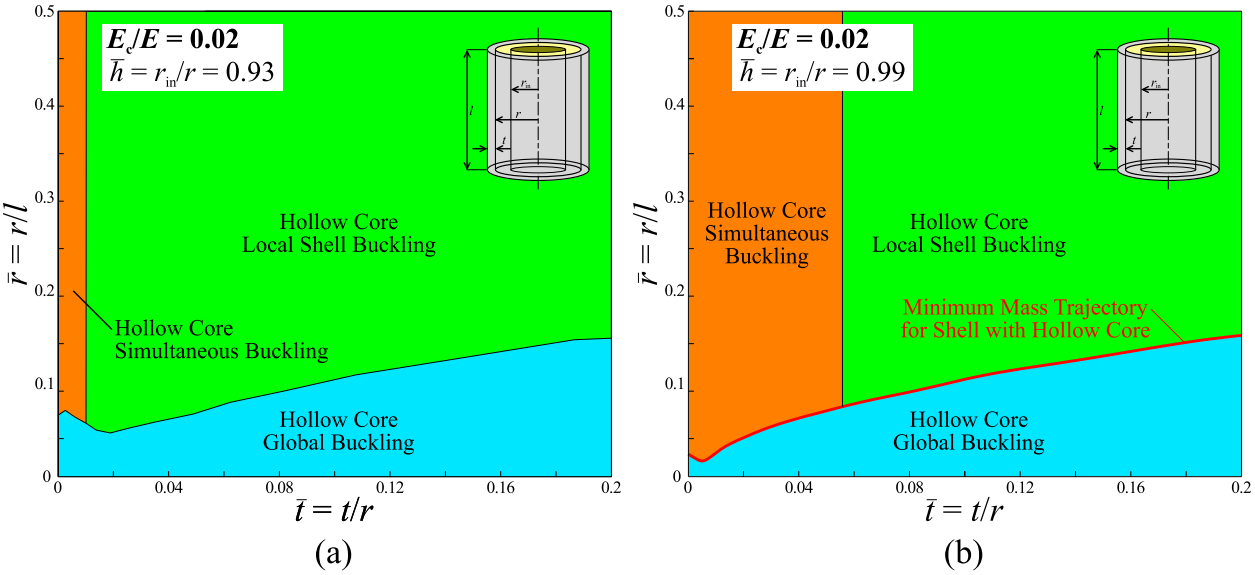

Figure 9.9: Failure mechanism map of an axially-loaded filled shell containing a hollow ABS core ($E_c/E = 0.02$) having a hollowness factor of (a)$\overline{h} = 0.93$ and (b)$\overline{h} = 0.99$. The design space is shown for a range of thickness-to-radius ratios $\overline{t}$ and radius-to-length ratios $\overline{r}$. The dominant failure mechanisms are local shell buckling, global Euler buckling, and simultaneous buckling. For $\overline{h} = 0.93$, there is no minimum mass trajectory. However, for $\overline{h} = 0.99$ the minimum mass trajectory follows the global-simultaneous buckling and global-local shell buckling boundaries.

Figures 9.8 shows the mass-versus-load (or $\overline{M}$ vs $\overline{F}$) plots for the various material combinations. Also shown on this Figure are the minimum mass trajectories for thin- and thick-shelled hollow cylinders. For minimum mass of a filled cylinder, the preferred failure mode at high loads is local shell buckling, as it is for thick-shelled hollow cylinders. However, the transition to local shell buckling occurs at a much lower load than it does for hollow cylinders. The global buckling region of the foam-filled cylinder has a smaller $\overline{F}$ range than the ABS or LDPE materials owing to the reduced $\overline{t}$ value as seen in Figure 9.7(b). Even compared to a metal cylinder filled with a low-density foam core, hollow shells are always preferred for minimum mass. In addition, the similar mass of ABS and LDPE negates the advantage of having a lower-stiffness core. If a less stiff core material is desired, a foamed polymer material such as H200 is more ideal.

9.5.3 Filled Shell with Hollow Core

The hollowness factor $\overline{h}$ (Equation 9.3) is a design variable when the a cylinder with a hollow-core is considered. A true representation of the failure mechanism map for this cylinder configuration would be three-dimensional, however for clarity several two-dimensional failure mechanism maps are presented.

Figure 9.9(a) shows a failure mechanism map for a metal-coated polymer cylinder in axial compression with a hollow polymer core having $\overline{h} = 0.93$. The minimum mass trajectory cannot be shown on this failure mechanism map as there is no optimal trajectory for this value of $\overline{h}$. Instead, the minimum mass trajectory is shown in Figure 9.9(b), which illustrates the failure mechanism map for $\overline{h} = 0.99$, when most of the core has been removed. Equations 9.34, 9.36 and 9.40 are used to calculate the failure modes for these failure mechanism maps. The minimum mass trajectory is shown to be along the simultaneous buckling and

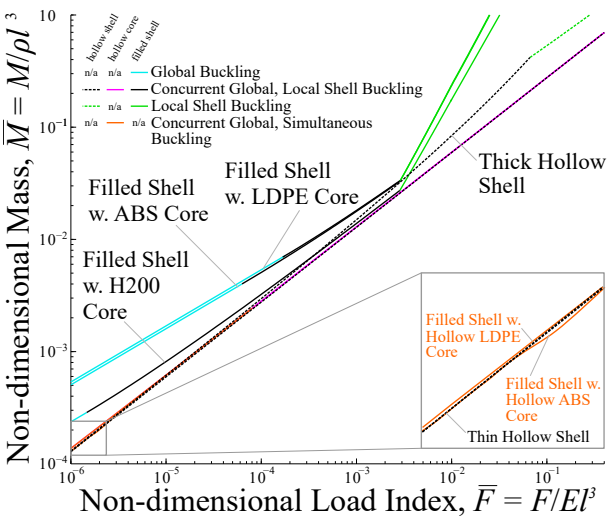

Figure 9.10: Minimum mass trajectories for thin-shell, thick-shell, filled-shell and hollow-core cylinders. The non-dimensional optimal cylinder masses $\overline{M}$ are given as a function of the non-dimensional axial loads $\overline{F}$. The inset shows detail at low $\overline{F}$, where the thin-shell and hollow-core trajectories are very close to each other.

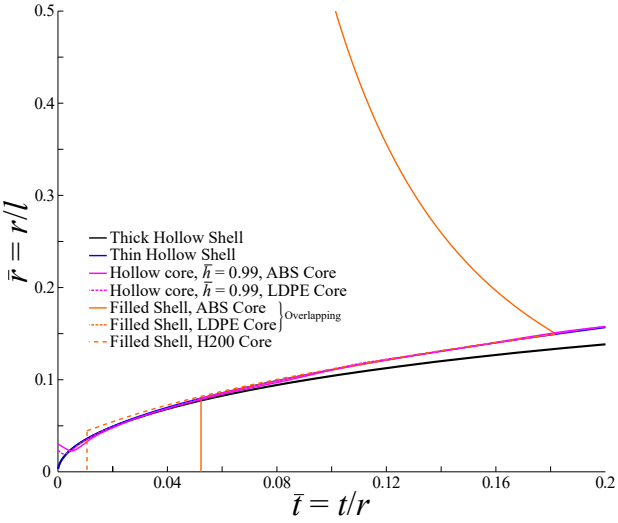

Figure 9.11: Minimum mass trajectories for thin-shell, thick-shell, filled-shell and hollow-core cylinders. The non-dimensional optimal cylinder thickness-to-radius $\bar{t}$ ratios and radius-to-length ratios are provided, corresponding to the same geometries shown in Figure 9.10. These are the same trajectories shown in the previous failure mechanism maps.

global buckling boundary at lower thickness-to-radius $\bar{t}$ values, and along the local shell buckling and global buckling boundary at higher $\bar{t}$ values. The value of $E_c/E \approx 0.02$ in both of these Figures, corresponding to a nickel-coated ABS cylinder. The failure mechanism maps are similar for $E_c/E \approx 0.002$ (LDPE and foam-filled cylinders) and are not shown here.

Although the method of Lagrange multipliers was presented in Section 9.2.3, the complexity of the equations for the hollow core local shell buckling and simultaneous buckling loads (Equations 9.36 and 9.40 respectively) makes the analytical solution for their optima less tractable. Instead, a numerical solution for the minimum mass trajectories for these failure loads was found. While the global buckling load for a hollow-core cylinder (Equation 9.34) did have an analytical solution, the result was infeasible.

Figure 9.10 shows the minimum mass trajectories in $\overline{M}$ vs $\overline{F}$ space for the hollow core case for both ABS- and LDPE-filled cylinders, with $\overline{h} = 0.99$. Because of the similarity of the results for the H200 foam and LDPE polymer solutions, the foam-filled cylinder is not included on this graph. However, the minimum mass trajectories for the filled-shell cases as well as the thin- and thick-shell cases are shown for comparison. The remaining core material for the hollow core cases (i.e. since $\overline{h} = 0.99$) causes a slight increase in the mass of a hollow-core cylinder compared to a hollow-shell, as seen in the inset of Figure 9.10. Because the the core is almost removed, there is little advantage to using an LDPE core. Instead of a slight decrease in mass when using an LDPE core (as found for the filled-shell configuration), the use of a less stiff core for a hollow-core cylinder negates the benefits of a less dense material, leading instead to an increase in mass for the same load-bearing capacity.

To compare the geometries for the various optimization cases, the minimum mass trajectories for the hollow-shell, filled-shell and hollow-core cases are drawn together in Figure 9.11 on $\bar{t}$ and $\bar{r}$ axes. As seen in

Table 9.2: Results of first case study where a 10 mm long strut has its radius specified, as given in the first column. The optimal cylinder geometries, failure loads and masses for thick hollow shells and ABS-filled cylinders are given.

Radius, r (mm)	**Optimal Thick Hollow Shell**			**Optimal Filled Shell with ABS Core**		
	t (µm)	F (N)	Mass (g)	t (µm)	F (N)	Mass (g)
0.5	10.8	5.57×10^5	0.0030	27.0	1.37×10^2	0.0496
1.5	124.1	7.48×10^7	0.0109	83.5	5.54×10^7	0.4534
2.0	652.6	2.18×10^9	0.8497	298.2	4.93×10^8	1.4632

Table 9.3: Results of first case study where a 10 mm long strut has its radius specified, as given in the first column. The optimal cylinder geometries, failure loads and masses for H200-filled and hollow-core ABS-filled cylinders are given.

Radius, r (mm)	**Optimal Filled Shell with H200 Core**			**Optimal Filled Shell with Hollow ABS Core** ($\overline{h}$=0.99)		
	t (µm)	F (N)	Mass (g)	t (µm)	F (N)	Mass (g)
0.5	8.0	4.25×10^5	0.0120	10.1	5.30×10^5	0.0030
1.5	272.4	3.88×10^8	0.7629	287.0	3.92×10^8	0.2425
2.0	298.2	4.30×10^8	1.1277	651.0	2.02×10^9	0.7314

this figure, the optimal design of a hollow-core cylinder at low $\overline{t}$ requires an increased $\overline{r}$. For this hollow-core geometry, there will be concurrent failure through simultaneous and global buckling at lower loads. The shape of the minimum mass trajectories for the hollow-core cases is consistent with the boundary between local shell buckling and global buckling in the filled shell cases (refer to Figures 9.7(a) and (b)). For the filled shell cases, the minimum mass trajectoriess are nearly identical whereas using a H200 foam core results in a lower thickness-to-radius ratio $\overline{t}$ – and thus a lower mass $\overline{M}$ – in the global buckling region.

It is deduced that when core material is an option (and not a requirement as in the filled-shell case), the optimal design necessitates the removal of the core entirely. The mass of the hollow-core cases are slightly above the thin-shell mass due to the small sliver of material remaining in the core. The hollow-shell cases provide the most mass-efficient designs for minimum mass cylinder construction. However, the optimal geometries for the hollow shells calculated for the present optimization studies do not take into account the imperfection sensitivity of local shell buckling loads for hollow shells.

9.6 Case Studies

To illustrate the results of these optimization results in practice, two case studies are presented. The first represents a typical strut geometry in a microtruss structure, while the second represents a larger column in compression. For these case studies, the optimal designs for the configurations of a hollow shell (using the thick-shell assumption), an ABS-filled shell, an H200-filled shell, and an ABS-filled shell with a hollow core are considered. Based on the results of the filled-shell optimization studies (Section 9.5.2), the filled-shell and hollow-core configurations with an LDPE core are expected to give similar mass values to their ABS-filled counterparts (refer to Figures 9.10 and 9.11). As such, an LDPE core is not considered for the case study.

For the first case, consider a 10 mm strut loaded in axial compression. Three different strut radii values are to be examined: 0.5, 1.5 and 2.0 mm. These values are shown in Tables 9.2 and 9.3. Using these radii

Table 9.4: Results of second case study where a 500 mm long strut is subject to a specified load, as given in the first column. The optimal cylinder shell thickness values, inner radii and masses for thick hollow shells and ABS-filled cylinders are given.

Load, F (kN)	**Optimal Thick Hollow Shell**			**Optimal Filled Shell with ABS Core**		
	t (µm)	r (mm)	Mass (kg)	t (µm)	r (mm)	Mass (kg)
40	290.7	20.6	0.172	790.5	14.7	0.678
90	436.1	23.6	0.298	967.2	17.9	1.015
200	656.4	26.9	0.516	1184	21.9	1.318

Table 9.5: Results of second case study where a 500 mm long strut is subject to a specified load, as given in the first column. The optimal cylinder shell thickness values, inner radii and masses for H200-filled and hollow-core ABS-filled cylinders are given.

Load, F (kN)	**Optimal Filled Shell with H200 Core**			**Optimal Filled Shell with Hollow ABS Core** ($\overline{h}$=0.99)		
	t (µm)	r (mm)	Mass (kg)	t (µm)	r (mm)	Mass (kg)
40	237.7	22.2	0.302	293.3	20.8	0.172
90	331.8	22.2	0.446	430.8	24.7	0.318
200	707.1	31.0	0.713	631.1	27.3	0.507

and a length of 10 mm, a radius to length value $\overline{r}$ can be calculated. From this, the optimal values of $\overline{t}$, $\overline{F}$ and $\overline{M}$ can be calculated using the optimization methods presently used. Alternatively, Figures 9.10 and 9.11 can also be used to find values for $\overline{t}$, $\overline{F}$ and $\overline{M}$.

The results of the first case study are provided in Tables 9.2 and 9.3, which give the optimal shell thickness t for the cylinder, the load F at failure and the mass M of the optimum strut. Table 9.2 provides the results for a hollow shell and ABS-filled shell, while Table 9.3 provides the results for an H200-filled shell and the hollow-core ABS-filled shell. The results of this case study confirm the results found from the non-dimensional optimization analysis: the optimal thick hollow shell provides the lowest mass for each of the radii considered, while the optimal filled shell always gives the highest mass. The optimal hollow-core configuration has a lower mass at the highest radius of 2.0 mm, however its shell thickness is very high (651 µm) and very close to the thick-shell optimal value of (652.6 µm). At this thickness-to-radius ratio, the thin-shell assumptions used for the hollow-core models are beyond their appropriate limits, and the mass of the thick shell value – although higher – is indeed the true optimum cylinder mass for this load.

While the optimum filled shell with an H200 foam core (Table 9.2) gives heavier cylinder masses than the thick hollow shells, they are considerably lighter at lower radii than ABS-filled cylinders (Table 9.3). At the higher radius of 2.0 mm, the shell thickness values of both filled shells are similar but the mass of the foam-filled cylinder is about 25% of the ABS-filled cylinder mass, owing to the lower density of the foam material. The low load of the ABS-filled cylinder at a radius of 0.5 mm is due to the buckling mode of global buckling, whereas combined global and local buckling is the failure mode when the radius is 1.5 or 2.0 mm.

For the second case study, a 500 mm strut is loaded at 40, 90 and 200 kN and the optimum cylinder mass is to be found. Tables 9.4 and 9.5 provide the optimal cylinder construction for the same cylinder configurations as the first case study. Since the load is now specified, the optimal shell thickness t and radius r is found along with the optimal cylinder mass M. The masses of the resulting cylinders are larger than

those found from the first case study due to the longer length requirement of this cylinder. As was found with the first case study, the optimal hollow shell still gives the lowest mass for all loads considered. Once again, the filled cylinder with a hollow ABS core has a slightly lower mass than the optimal thick-shelled cylinder; this is due to the thin-shell assumption used for the hollow-core calculations.

Although the results of these case studies demonstrate that the hollow-shell are predicted to provide the lowest mass designs, the imperfection sensitivity of hollow shells plays a strong role in determining their performance. This will be examined in a practical discussion of the results.

9.7 Discussion and Practical Considerations

The results of the optimization process can be summarized as follows:

1. If a hollow cylinder is loaded in axial compression, design it such that it fails concurrently through global and local shell buckling;
2. If a hollow cylinder is very thick or must sustain a high load, it should fail through local shell buckling;
3. If a filled cylinder is loaded axially, it should buckle globally if it is very long, fail by local shell buckling if very thick, and fail concurrently through global and local shell buckling otherwise; and
4. If a filled cylinder is loaded axially but its core thickness can vary, remove the core completely and treat it as if it were a hollow-shell cylinder as in items 1 and 2.

Of interest is the result obtained from the hollow-core cases, where optimization allows for varying core thickness (i.e. treating $\overline{h}$ as a variable). Instead of keeping a moderate amount of the core, the optimization revealed that the most mass-efficient designs do not utilize any core material. Only the shell remains, and the cylinder behaves as a hollow shell in axial compression. The optimization procedure performed by Dawson and Gibson [116] found that the core is desirable at lower loads. Thus at low loads a partially filled core is most mass-efficient (as per the results of Dawson and Gibson), while at high loads a hollow shell is preferred (as per the results of the present analysis). While the results of the hollow-core analysis lead to a design which does not contain a core, the nanocrystalline nickel coating requires a surface for electrodeposition [28, 30]. Thus for the shell to be produced, a polymer preform – even a very thin one – must be present.

The results of Lausic et al. [4] found that filled-shell cylinders would always lead to a higher mass than a hollow shell designed for the same load. This agrees with the present analysis for filled shells, where the core was represented with an accurate model compared to the analysis of Lausic et al. The aforementioned authors also found that a hollow shell will always be more mass efficient than a filled shell carrying the same load. The treatment of hollow shells in the present optimization studies, however, ignores the fact that local shell buckling loads of axially-loaded hollow shells are very imperfection-sensitive. As such, the optimal designs predicted for hollow shells in the present analysis will not hold their design loads [72, 73, 78, 79], leading to an increase in cylinder mass due to the utilization of thicker shells.

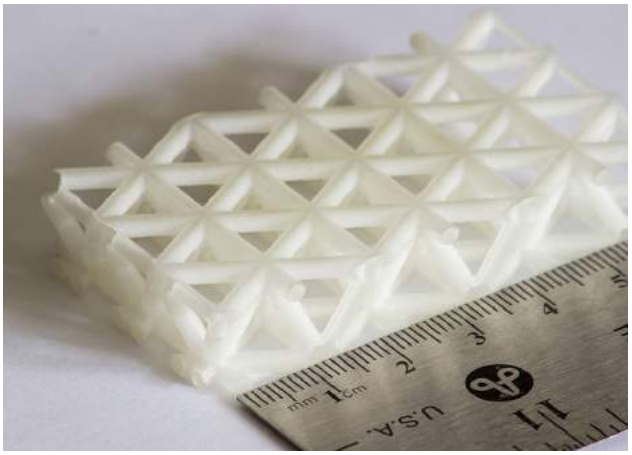

Figure 9.12: Photograph of a microtruss with hollow-core struts (hollowness factor $\overline{h} \approx 0.85$) produced through 3D printing methods. This microtruss can be coated with nanocrystalline metal, and the preform either later discarded or kept for added buckling support.

Imperfection sensitivities aside, for shell thicknesses that are optimal, the hollow-shell model is inaccurate because it ignores the behaviour of the core. This point can illustrated by considering the case study results for a cylinder designed to hold a 40 kN load (Table 9.4) and the graph which compares the behaviours of the filled-shell and hollow-shell models (Figure 4.3(a)). To hold this load, the results of Table 9.4 reveal that an optimum hollow shell requires a thickness-to-radius ratio of approximately 0.015. Looking at the graph of Figure 4.3(a), this corresponds to a non-dimensional load of approximately 2×10^{-3}, and a filled shell with a thickness-to-radius ratio of approximately 0.08 would be required to carry this same load. This large difference in geometry for the same load illustrates why the filled shell models are necessary: for the likely case where the core cannot be removed, the hollow-shell model will not accurately predict the behaviour of a polymer- or a foam-filled shell. The filled shell models will always account for the behaviour of the core, not only when predicting the load of the structure but also when undertaking optimization studies.

For the filled shells with hollow cores, some manufacturability aspects bear consideration. If it is desired to produce microtruss geometries with very hollow struts (i.e. $\overline{h} \geq 0.8$), high-quality 3D printing methods such as sterolithography can be used [26, 50]. Figure 9.12 shows a photo of 3D-printed polymer microtruss where the strut hollowness factor is very high ($\overline{h} = 0.85$ or higher). The finishing processes of these microtrusses involve removing the wax support material while taking care to not break the delicate struts. The full strength of this structure is only realized once it is coated with nanocrystalline metal, a process which would also require careful handling to avoid breakage.

If it is desired to completely remove the core, acid dissolution of 3D printed polymers has been shown to be a viable process [1]. Sulphuric acid or other strong acids can be used to preferentially dissolve the polymer preform in a metal-coated polymer structure. Depending on the polymer chemistry, the polymer core will be completely dissolved while the metal coating will remain. This dissolution process only works well for simpler structures (such as a single cylindrical strut or one unit cell of a microtruss). If the microtruss structure of Figure 9.12 were to be coated with metal, acid dissolution of the polymer preform would be

difficult, as the interior of the coated structure would be less accessible even if submerged fully in acid. Because of this and the inaccuracy of the hollow-shell model when predicting the behaviour of filled shells, the filled-shell models used for the present optimization studies are necessary.

Even if a microtruss with hollow metal struts is produced, the imperfection sensitivity of hollow shells will lead to significantly lower failure loads than those predicted by the hollow-shell buckling model. Studies with foam-filled cylinders have shown that filling a hollow shell reduces this sensitivity to imperfections to a large degree [98–100]. This resistance to buckling persists when part of the core is hollowed out (i.e. $\overline{h} > 0$), but removing too much of the core (i.e. $\overline{h}$ close to 1) results in the introduction of simultaneous buckling as a dominant failure mode (as seen in the failure mechanism map of Figure 9.9(a)). A filled or partially-filled cylinder will lead to more predictable loads for structures compared to hollow cylinders with the same thickness-to-radius ratios, even though these designs will be heavier than an ideal hollow shell intended for the same load carrying capacity. The improved predictability of filled shells is more desirable for engineered structures, where safety and reliability are often paramount.

In summary, the hollow-shell model should not be used to predict the behaviour of filled-shell structures, especially for shell thickness-to-radius ratios which are optimal, making the filled-shell models crucial. While a hollow cylinder is the most mass-efficient design, its imperfection sensitivity makes it unsuitable for many engineering applications, necessitating the use of shell stiffeners or thickening of the shell itself which will lead to sub-optimal structures [73]. A filled-cylinder allows for more readily-realized buckling loads, a characteristic which is preferable in engineering applications.

9.8 Concluding Remarks

This chapter examined optimization methods of metal-coated polymer cylinder to design low-mass nanocoated polymer cylinders. The results were determined for several cylinder configurations including hollow shells, completely filled shells and filled shells with hollowed-out cores. The thin-shell assumption was also assessed in this analysis, and it was shown to have a measurable effect when thicker shells were considered. Non-dimensional variables were used to generalize the results, and case studies were presented to illustrate their use.

The hollow-shell case – even with the thin-shell assumption disregarded – led to the most mass-efficient designs. Shells filled with ABS and LDPE were substantially heavier for the same load-carrying capacity. However, shells filled with Divinycell H200 foam, a low-density foam with properties similar to LDPE, lead to lower masses than ABS- or LDPE-filled cylinders. When allowing core hollowness to be a variable, as was done for the hollow core case, the optimal design always removed the core entirely. This reveals that even a small portion of the core leads to undesired mass from an optimal design standpoint.

However, for shell thicknesses that are optimal, the hollow shell model is incorrect because it does not account for the presence of the core. The complexity of a microtruss structure makes removal of the core

very difficult, and the use of the hollow shell model leads to inaccurate predictions for the behaviour of the structure. In addition, once the imperfection sensitivity of hollow shells is considered, it is clear that their use in practice will lead to much higher masses than predicted by the present optimization studies. For these reasons, the models developed from the present research as well as the optimum filled-cylinder designs given here are important.

Practical considerations for constructing hollow shells include the electrodeposition process of the nanocrystalline metal coating and, if possible, subsequent removal of the polymer core. The electrodeposition process needs a surface upon which to deposit metal, while removal of the core would be problematic for complex geometries such as those encountered in microtruss structures.

Future considerations for optimization of filled shells should take into account inelastic behaviour for both the shell and the core. This will lead to more accurate results for optimal designs, which may be more useful for further development and for use in practical structures. Analytical solutions to all of the above cases are also desirable so the results can be determined quickly once basic design specifications are known.

Chapter 10

Concluding Statements and Recommendations

The motivation for this research project was to understand the failure mechanisms of metal-coated polymer microtruss structures, which are dominated by compressive instabilities. As these structures have cylindrical struts, the failure mechanisms of metal-coated polymer cylinders under axial compressive loads were studied. The objectives of this research project included developing models for local shell buckling, examining the behaviour of the cylinders through experiments, and optimizing cylinder geometries for minimum mass design. With respect to these objectives, this final chapter of the thesis summarizes the key conclusions, reviews the key contributions, and proposes recommendations for future research directions.

10.1 Summaries

The conclusions for each chapter are reiterated here to summarize the main findings.

10.1.1 Elastic Core Model and Fundamental Buckling Model

Past studies examining the theoretical and experimental behaviour of foam-filled shells under axial loads utilized the models of beams on elastic foundations or the behaviour of foam cores in composite sandwich panels. Both of these approaches, however, only describe the stresses state in two coordinate directions, and thus do not lead to true axisymmetric representations of the polymer core behaviour for a filled shell. The best-available model for filled-shell buckling is that of Karam and Gibson [98], which utilizes the Gough sandwich panel model [82]. In contrast, the Southwell stress model [6, 38, 39] describes the stress state in three coordinate directions, and is intended for cylinder geometries subject to axisymmetric stresses. The Southwell model was implemented in MATLAB in order to calculate the stress state and strain energy of a polymer cylinder subject to sinusoidal radial stresses. Once the strain energies had been determined for a range of cylinder geometries and buckle wavelengths, an analytic fit was used to approximate the strain energy of an elastic core as a function of the core geometry and the buckle wavelength.

The new core model was used to develop an axial buckling load prediction for a metal-coated polymer cylinder by applying the energy method of Timoshenko [34]. Finite element verification revealed that this new elastic buckling model predicts the buckling loads slightly more accurately than the Karam and Gibson model [98]. In addition, a comparison between the stress distributions obtained from Abaqus buckling investigations and the Southwell model [6, 38, 39] revealed that the latter accurately describes the stress state of the core under buckling conditions, or when the shell and core are subject to sinusoidal radial

deflections due to the buckling of the shell and the assumed adhesion between the shell and the core. A main takeaway of the new model is that, while the Karam and Gibson model [82] is easier to implement in practice, the new elastic buckling model is more accurate than the current state-of-the-art. In addition, the versatility of the Southwell model allows for various core loading situations to be studied by changing the core geometry (i.e. by hollowing it along its axis) or different problem assumptions (i.e. when there is no adhesion between the shell and core). This versatility was harnessed to create more complex models later in the thesis.

10.1.2 Non-Adhesion Model

In previous investigations for filled-shell buckling, a key assumption for buckling load predictions is that the metal shell and polymer core are perfectly adhered. In many cases, such as for foam-filled cylinder construction, this is a reasonable assumption as the core is very well adhered to the shell. When metal-coated polymer cylinders are considered, however, adverse adhesion issues can be present. It is warranted to develop a buckling model for a filled-shell cylinder which assumes no adhesion between the shell and the core. In this situation, the core model developed for the fully-adhered shell core (or the fundamental model) must be modified for non-adhesion buckling.

A model for the core was created for the case when the shell and core are not adhered. This model only considers radial deflections which push the core inward towards the cylinder centreline. Any sinusoidal deflections which would move the core radially outward were disregarded, as these are not present when the shell and core are not adhered. A new non-dimensional variable, the penetration length, was introduced in order to express the energy of the shell as a function of how much the shell penetrates the core. As was done previously, the Southwell stress model was utilized to determine the energy state of the polymer core subject to non-adhesion buckling deformations. The resulting non-adhesion core model expresses the core strain energy as a function of the cylinder geometry, buckle wavelength and the penetration length. The energy-minimization procedure used for finding the buckling load was again utilized when determining the non-adhesion buckling load, with the penetration length becoming another variable of the problem. When compared to the full-adhesion buckling load, the non-adhesion buckling load is substantially lower, implying that the assumption of perfect adhesion has a large impact on buckling predictions.

Finite element investigations for non-adhesion buckling were carried out in Abaqus, using contact algorithms to model a non-adhered filled shell under axial loads. The buckling loads determined from these verification investigations were much higher than those predicted by the non-adhesion buckling model. This indicated that while the non-adhesion model provides a lower bound for metal-coated polymer cylinders with no adhesion, the model is not as accurate as was hoped. The cause for this discrepancy can be attributed to the assumed buckled shape of the shell: even though there is no adhesion between the shell and the core, it was assumed that the shell buckles along its length with uniform sinusoidal waves. The shapes of buckled shell geometries obtained from the Abaqus investigations showed buckling waves with non-uniform sinusoidal

shapes; their wavelengths and amplitudes were not consistent along the length of the cylinder. As the core model assumes uniform sinusoidal buckling along the length of the cylinder, the resulting predictions of the buckling behaviour would have been incorrect.

Although finite element investigations revealed that the non-adhesion model under-predicts buckling loads, the approach used to model non-adhesion buckling is nevertheless unique to this thesis project. The use of the Southwell model allowed for developing a core model for a non-adhered filled shell more readily. In addition, the non-adhesion model provides a practical lower bound for filled-shell buckling under adverse adhesion situations, a prediction which until this time has not been examined in the literature.

10.1.3 Hollow-core Model

Existing predictions for the buckling load of filled shells are intended for geometries where the core is completely filled. A more general model is necessary which accounts for core geometries where part of the core is hollow along the cylinder axis, or when its "hollowness factor" is changed. A core which is more hollow has a higher hollowness factor. While some previous studies have investigated hollow core behaviour, these studies used an estimate of the stress state for hollow cores. The Southwell model [6, 38, 39] allows for more accurate treatment of the hollow core buckling problem.

As done similarly for the fundamental and non-adhesion model, a new core model was developed for changing core hollowness factors. The versatility of the Southwell model [6, 38, 39] allowed for determining strain energies for various core geometries (i.e. as the hollowness factor is varied), and a function was fit to this strain energy data. This new hollow core model was used to determine the hollow core buckling load through the energy method of Timoshenko [34]. Higher core hollowness factors lead to cylinder geometries where buckling of the shell and core takes place together; this is simultaneous buckling. The loads predicted by the new hollow core model were verified through finite element investigations, while the transition point between hollow buckling and simultaneous buckling was determined as a function of the core stiffness and hollowness factor. Very hollow cores lead to filled-shell behaviours closely resembling those of hollow-shell buckling, and the effect of the core in these cases is negligible.

The creation of a hollow core buckling model is a novel contribution in the area of filled shell buckling. The buckling load can now be determined for cores which are partially hollow and not just those which are completely filled. Not only is this model more general for filled-shell buckling, it is more accurate than the previously-developed models for hollow core buckling due the use of the Southwell model for description of the core behaviour.

10.1.4 Inelastic Model

The models developed earlier in the thesis – as well as a large part of the existing literature – focus on the elastic buckling load for filled shells under axial loads. For very thick shells, elastic buckling load predictions become inaccurate due to yielding of the shell material at the high failure strains of these thicker shells. An

inelastic buckling model is needed for the cases. There have been notable investigations into the inelastic behaviour of hollow shells, but comparatively fewer studies into the inelastic behaviour of filled shells.

An inelastic buckling model was developed for axially-loaded filled shells. These predictions require the use of the tangent modulus, or a modulus determined by the tangent of the stress-strain behaviour of a material as it deforms inelastically. This requires a differentiable stress strain function for a material. The Voce relationship [114] is a function for the stress of a material given its strain, and is easily differentiated to provide the tangent modulus. As nanocrystalline material is the shell material for metal-coated polymer cylinders, the Voce fit constants were determined for nanocrystalline nickel. While inelastic behaviour was considered for the shell material, it was not considered for the polymer core as polymers have higher strains to yield compared to metals. As such, the elastic core model developed for the fundamental model was utilized to again represent the core behaviour. In contrast to the hollow shell inelastic buckling loads (determined previously by Lausic et al. [1]), the buckle wavelengths for inelastically-buckling filled shells are lower than their elastic counterparts. This indicates that the material properties of the core have a strong effect on both the elastic and inelastic behaviours of filled shells.

Verification studies using Abaqus determined that the inelastic buckling load predictions are accurate over a large range of cylinder geometries, but become inaccurate for extremely thick shells (i.e. those where the shell thickness-to-radius ratios exceed 0.1). Due to the methods used to verify the inelastic buckling loads, the wavelength predictions of the inelastic buckling model could not be verified, and will require an independent investigation. The determination of an inelastic buckling load is a unique contribution to the study of filled-shell buckling, as this area is often not explored in the study of filled shells.

10.1.5 Experiments

Filled-shell buckling models have previously been validated using foam-filled cylinders. As metal coated microtruss structures have solid polymer cores, the behaviour of metal-coated polymer cylinders is of interest. The buckling loads of cylinders with larger thickness-to-radius ratios are less sensitive to imperfections, so these geometries are preferred for manufacturing and experimental investigations. The behaviours of the cylinders found through experiments can be compared to the inelastic buckling model, which provides more accurate buckling loads for thicker shells.

For the experimental studies, dogbone-shaped specimens were machined from ABS plastic and coated with nanocrystalline nickel provided by Integran Technologies. The gauge sections of these samples had cylindrical cross sections, while the geometry of the specimens concentrated the stresses in this cylindrical section. The samples were tested in axial compression in a servo-hydraulic load frame. A constant displacement rate was used which had been determined through strain rate sensitivity investigations done prior to the experiments. Each dogbone specimen was clamped to the load frame prior to the start of each test to minimize the risk of asymmetric loading. The axial load and displacement was measured throughout each experiment, and the load was removed after a substantial reduction in load was observed (indicating failure).

Despite efforts to maintain symmetrical loading around the circumference of each specimen, some buckle folds were not axisymmetric about the circumference of the cylinders. In addition, none of the specimens tested failed in their gauge sections, despite careful specimen design prior to manufacturing. The highest buckling loads obtained during the experiments were within 65% of the theoretical values; by contrast, earlier experiments of filled shells by Karam and Gibson [5] for similar shell geometries achieved up to 75% agreement with theoretical values. Microscopy investigations also revealed that the coatings were not uniform around the circumference of each specimen. This non-uniformity along with the evidence of asymmetrical loading both likely led to the discrepancy between predicted and measured buckling loads.

The results of the experiments highlight the limitations of producing and testing metal-coated polymer structures, specifically those manufactured by electrodepositing nanocrystalline onto a polymer preform. The procedure to manufacture foam-filled cylinders involves first manufacturing the shell structure, followed by filling the shell with a foam compound and allowing this to set. The metal-coated polymer cylinders are manufactured in reverse: the polymer preform is machined or 3D-printed first, and the metal coating is then electrodeposited onto the polymer surface. The methods of manufacturing foam filled cylinders allow for inspection of the shell prior to filling them with foam, a process which cannot be done for metal-coated polymer cylinders without destructive inspection methods. In summary, the experiments showed that very careful preparations are required in order to validate filled-shell buckling models through experiment.

10.1.6 Mass Minimization of Filled Shells

In designing aircraft, structural weight should be minimized in order to reduce fuel consumption. This contributes to the goals of sustainable aviation while reducing operating costs for airlines. Nanocoated polymer microtrusses offer the mass-efficiency of microtruss topologies while providing the high strength of nanocrystalline metals. To realize the full benefits of these hybrid structures, optimization of the microtruss geometry can be carried out, which involves mass minimization of the cylindrical struts. Optimization studies have been previously undertaken for microtruss geometries by Lausic et al [1, 4]. However, the filled-shell models used for these studies did not use accurate treatments of the core. A study of hollow core geometries was previously done by Dawson and Gibson [116], but the results were limited to very thin shells.

An optimization study was carried out using the method of Lagrange multipliers, where the minimum mass of cylinders subject to a given range of axial loads was determined. Where necessary, numerical methods were used. The full-adhesion and hollow-core models were used for mass minimization, while the hollow-shell models were also used for comparison purposes. Both global and local shell buckling loads were considered, while simultaneous buckling was accounted for when analyzing hollow core cylinders. For the analysis, nanocrystalline nickel was the material chosen for the shell, while the core materials considered were ABS, LDPE and H200 Divinycell foam. The last of these materials allowed for comparisons between polymer-filled and foam-filled cylinders. The configurations examined for minimum mass optimization included hollow shells, completely filled shells and shells with hollow cores.

For the entire range of loads considered, hollow shells are always more mass-efficient than filled shells or shells with hollow cores. Cylinders with LDPE cores were more mass efficient than cylinders filled with ABS. The H200-filled cylinders had the lowest mass of the filled cylinders, highlighting the advantages of using foam-filled cylinders for minimum mass design. When the hollow-core model was used for mass minimization, the optimization results showed that the polymer core should be removed leaving only the metal shell behind. This indicates that even if the core hollowness factor is a variable, the optimal design for minimum mass is still a hollow shell.

For optimal cylinder geometries, the hollow shell model cannot be used to predict the behaviour of filled shells as it does not account for the presence of the core. If the hollow shell model were used in place of the presently-developed filled shell models, it would lead to shell designs which would be much thicker than needed. In addition, the practical use of hollow shells is limited by their imperfection sensitivity. Theoretical and experimental investigations have shown a very high sensitivity of hollow shell structures to imperfections [79]. These can include material defects, geometric imperfections or asymmetric axial loads. An alternative to using hollow shell structures is to manufacture very thin hollow core cylinders (or microtrusses with hollow core struts) through 3D printing methods. This will provide a surface for the electrodeposition of nanocrystalline metal while keeping the mass of the structure at a minimum. However, in many cases, it is very difficult to completely remove the core. Because of this and the innaccuracy of the hollow shell model in predicting filled-shell loads, the filled shell models are crucial.

The optimization results provide a comparison of the mass efficiencies for various cylinder configurations using known materials and standard optimization procedures. The algorithms and derived expressions can be used to develop practical cylinder geometries for compression members or for the struts of microtrusses.

10.2 Contributions of Research

There are several novel contributions that have resulted from this thesis project; these are highlighted and summarized below.

1. **Accurate core modelling:** A new and accurate core model was developed using the Southwell stress model. For a metal-coated polymer cylinder subject to radial buckling deformations, this model provides an accurate calculation of the strain energy in a polymer core subject to sinusoidal radial deformations. This model was used to develop a new buckling prediction for a filled shell under an axial load, and the performance of this new model exceeded that of the best-available model for filled-shell buckling.
2. **Non-adhesion behaviour:** A lower bound for the buckling behaviour of a non-adhered filled shell was determined. The core model developed for this case only accounts for the core behaviour under radial deformations which push the core inwards (i.e. towards the cylinder centerline). This investigation revealed the implications of assuming perfect adhesion for filled shell buckling predictions, an assumption used in the majority of filled-shell buckling models.

3. **Hollow core geometries:** Hollowing out the core along its axis changes the buckling behaviour of a filled shell, and this can also lead to simultaneous buckling when the core hollowness factor is very high. The hollow core model is a more general form of the full-adhesion model, and can be used for optimization studies.
4. **Inelastic Buckling:** A prediction for the inelastic buckling load of a filled shell was derived by using the tangent modulus in place of the elastic modulus in the previously-derived full-adhesion model. The resulting model was shown to be accurate through non-linear finite element analysis. In the literature, inelastic buckling is a less-explored topic for filled shells.
5. **Experiments on metal-coated polymer cylinders:** The existing body of work on experimental treatment of shells have thus far been focused on hollow shells or foam-filled shells. The experimental program undertaken for this research revealed some limitations of creating high-quality metal-coated polymer specimens for validation purposes, while also illustrating methods for alleviating some of these limitations.
6. **Optimized cylinders:** An algorithm was developed for determining the minimum mass of hollow shell, filled shell or hollow core cylinders. Though hollow shells provide the most mass-efficient solutions, the design of compression members for practical purposes may require filled or partially hollow cylinders; in these cases, these optimization procedures are useful for optimum cylinder design.

10.3 Recommendations for Future Research Directions

The objectives of this thesis project were met, and novel contributions were made to the area of filled-shell buckling and structural mechanics. However, for future research efforts that may stem from this thesis project, some recommendations are provided here.

The Southwell model is an accurate representation of the stress state of the core. While it was implemented in MATLAB, it could also be written in other programming languages as well. This would aid in later optimization studies, which could be carried out using more efficient algorithms written in other programming environments. In addition, this could also allow for higher mesh densities at a lower computational cost.

In developing the various core models, the behaviours of the models for two values of the core Young's moduli were investigated, while the Poisson's ratio was kept fixed. It is warranted to account for changing values of the Poisson's ratio in future investigations, while also examining a larger range of Young's moduli for the core. In addition, a function for the core parameters (i.e. K) could be fit to various values of the core Poisson ratio and Young's modulus, thereby generating more general core models for each case.

The thin-shell assumption is used for the hollow shell buckling model, and is consistently used in all the approaches for deriving hollow-shell buckling loads (i.e. by Timoshenko, von Karam and Tsien, Southwell and Lorenz); the same assumption was used when deriving the present filled-shell models. Another

recommendation, then, would be to eliminate the thin-shell assumption for these filled-shell predictions. The resulting new predictions created in this way would be more general than the present models, as they would be valid for a wider range of shell thickness values.

For the hollow core model, a 5th-order two-variable polynomial was fit to the strain energy data generated by the Southwell model. A less complicated fit could be used for this model, such that an analytical solution to the buckle wavelength can be derived for hollow-core geometries. This would allow for analytical expressions to be derived for the minimum mass trajectories, instead of relying on the numerical procedures as performed for the present optimization studies. The geometries for minimum mass cylinders could then be determined using the analytical formulas generated as a result of these new, simpler core models.

The development of the non-adhesion model assumed the extreme case where a metal shell and polymer core are not adhered. In reality, a shell and core would be partially adhered, in between the best case of full adhesion and the least desirable case of no adhesion. It is warranted to explore the development of a partial adhesion model which would account for varying degrees of adhesion, and therefore be more complex than the present non-adhesion model. This resulting model would be of interest to manufacturers of the metal coatings, such as the suppliers used for the manufacture of the experiment samples.

An approach often used in determining inelastic buckling predictions is to use the reduced modulus. As the present implementation for inelastic buckling uses the tangent modulus, it is of interest to determine the inelastic buckling load using the reduced modulus method, and compare these results to both experimental and finite element results.

Finally, in the area of experiments many facets require improvement. More specimens would need to be tested for a complete experimental program, while more careful specimen design and manufacturing is necessary. Trial specimens will need to be created to ensure that the electrodeposition process produces uniform coatings. If using core materials other than ABS, coating processes may need adjusting to account for new surface chemistries as this is known to cause adhesion issues.

References

[1] A. Lausic, "Manufacturing Optimal Nanocrystalline Microtruss Materials," Ph.D. dissertation, University of Toronto, 2016.

[2] R. Smith, "Just Press Print," 2014. [Online]. Available: http://ngm.nationalgeographic.com/2014/12/3d-printer/methods-graphic

[3] J. Won, "Wave Propagation Behaviour in Symmetric and Non-symmetric Three-dimensional Lattice Structures for Tailoring the Band Gap," Ph.D. dissertation, University of Toronto, 2016.

[4] A. Lausic, C. Steeves, and G. Hibbard, "Effect of grain size on the optimal architecture of electrodeposited metal/polymer microtrusses," *Journal of Sandwich Structures and Materials*, vol. 16, no. 3, pp. 251–271, 2014.

[5] G. N. Karam and L. J. Gibson, "Elastic Buckling of Cylindrical Shells with Elastic Cores - Part 2: Experiments," *International Journal of Solids and Structures*, vol. 32, no. 8/9, pp. 1285–1306, 1995.

[6] D. d. G. Allen, *Relaxation Methods in Engineering and Science*. New York: McGraw-Hill, 1954.

[7] RePliForm, "RepPliKote Technical Elements." [Online]. Available: http://www.repliforminc.com/RePliKoteTechnical.htm

[8] "GARDN Annual Report 2016-2017," Tech. Rep., 2017. [Online]. Available: https://gardn.org/wp-content/uploads/2018/01/GARDN-rapport-annuel-EN-WEB-2017-08-01.pdf

[9] D. M. Pitera, M. Dehaan, D. Brown, R. T. Kawai, S. Hollowell, D. Bruns, and B. K. Rawden, "Blended Wing Body Concept Development with Open Rotor Engine Integration," Tech. Rep., 2011.

[10] D. P. Wells, "Cruise Speed Sensitivity Study for Transonic Truss Braced Wing," in *55th AIAA Aerospace Sciences Meeting*, 2017, pp. 1–11.

[11] Y. R. Hicks, S. A. Tedder, and R. C. Anderson, "Alternative Bio-Derived JP-8 Class Fuel and JP-8 Fuel: Flame Tube Combustor Test Results Compared using a GE TAPS Injector Configuration," in *52nd AIAA/SAE/ASEE Joint Propulsion Conference*, 2016, pp. 1–16.

[12] J. Morris, "Falcon 20 First Civil Jet To Fly On 100% Biofuel," *Aviation Week and Space Technology*, 2012. [Online]. Available: http://aviationweek.com/business-aviation/falcon-20-first-civil-jet-fly-100-biofuel

[13] SAFRAN, "Electric taxiing," 2017. [Online]. Available: https://www.safran-landing-systems.com/systems-equipment/electric-taxiing-0

[14] D. P. Raymer, *Aircraft Design: A Conceptual Approach*, 5th ed. Reston: AIAA Education Series, 2012.

[15] The Boeing 737 Technical Site, "Boeing 737 Production." [Online]. Available: http://www.b737.org.uk/production.htm

[16] J. Hale, "Boeing 787: From the Ground Up," *Boeing AERO*, pp. 17–23, 2008. [Online]. Available: http://www.boeing.com/commercial/aeromagazine/articles/qtr{_}4{_}06/AERO{_}Q406{_}article4.pdf

[17] G. Marsh, "Airbus A350 XWB update," 2010. [Online]. Available: https://www.materialstoday.com/composite-applications/features/airbus-a350-xwb-update/

[18] W. D. Callister, *Materials Science and Engineering: An Introduction*, 7th ed. York: John Wiley & Sons, 2007.

[19] A. P. Mouritz, *Introduction to Aerospace Materials*. Elsevier Ltd, 2012.

[20] G. Patfroot, *Polymers: An Introduction to their Physical and Rehological Behaviour*. Belgium: E. Story Scientific Publishers, 1974.

[21] L. Gordon, B. Bouwhuis, M. Suralvo, J. Mccrea, G. Palumbo, and G. Hibbard, "Micro-truss nanocrystalline Ni hybrids," *Acta Materialia*, vol. 57, no. 3, pp. 932–939, Feb. 2009.

[22] G. Mallory and J. Hajdu, *Electroless Plating: Fundamentals and Applications*. Cambridge University Press, 1990.

[23] L. J. Gibson and M. F. Ashby, *Cellular Solids: Structure and Properties*. New York: Pergamon Press, 1988.

[24] H. G. Allen, *Analysis and Design of Structural Sandwich Panels*. Hungary: Pergamon Press, 1969.

[25] V. S. Deshpande, M. F. Ashby, and N. A. Fleck, "Foam Topology Bending versus Stretching Dominated Architectures," *Acta Materialia*, vol. 49, no. 6, pp. 1035–1040, 2001.

[26] I. Gibson, D. Rosen, and B. Stucker, *Additive Manufacturing Technologies*, 2nd ed. New York: Springer, 2015.

[27] C. Schubert, M. C. van Langeveld, and L. a. Donoso, "Innovations in 3D printing: a 3D overview from optics to organs." *The British Journal of ophthalmology*, vol. 98, no. 2, pp. 159–61, feb 2014.

[28] U. Erb, "Electrodeposited Nanocrystals: Synthesis, Properties and Industrial Applications," *Nanostructured Materials*, vol. 6, no. 5-8, pp. 533–538, 1995.

[29] K. Kumar, H. Van Swygenhoven, and S. Suresh, "Mechanical behavior of nanocrystalline metals and alloys," *Acta Materialia*, vol. 51, no. 19, pp. 5743–5774, Nov. 2003.

[30] D. Clark, D. Wood, and U. Erb, "Industrial Applications of Electrodeposited Nanocrystals," *Acta Metallurgica*, vol. 9, no. 6, pp. 755–758, 1997.

[31] I. Brooks, G. Palumbo, G. D. Hibbard, Z. Wang, and U. Erb, "On the intrinsic ductility of electrodeposited nanocrystalline metals," *Journal of Materials Science*, vol. 46, no. 24, pp. 7713–7724, Jul. 2011.

[32] U. Erb, G. Palumbo, B. Szpunar, and K. Aust, "Electrodeposited vs. Consolidated Nanocrystals: Differences and Similarities," *Acta Metallurgica*, vol. 9, pp. 261–270, 1997.

[33] A. Lausic, B. Bouwhuis, J. McCrea, G. Palumbo, and G. Hibbard, "Mechanical anisotropy in electrodeposited nanocrystalline metal/metal composite foams," *Materials Science and Engineering: A*, vol. 552, pp. 157–163, aug 2012.

[34] S. P. Timoshenko and J. M. Gere, *Theory of Elastic Stability*. New York: McGraw-Hill, 1961.

[35] T. von Karman and H.-S. Tsien, "The Buckling of Thin Cylindrical Shells under Axial Compression," *Journal of the Aeronautical Sciences*, vol. 8, no. 8, pp. 303–312, 1941.

[36] R. Southwell, "On the General Theory of Elastic Stability," *Proceedings of the Royal Society A: Mathematical, Physical and Engineering Sciences*, vol. 213, no. 497-508, pp. 187–244, 1981.

[37] R. Lorenz, "Achsensymmetrische verzerrungen in dunnwandingen hohlzzylindern," *Zeitschrift des Vereines Deutscher Ingenieure*, vol. 52, no. 43, pp. 1706–1713, 1908.

[38] R. Southwell, *Relaxation Methods in Theoretical Physics: Volume II*. Oxford: Clarendon Press, 1956.

[39] R. Southwell, "Some practically important stress-systems in solids of revolution," *Proceedings of the Royal Society A: Mathematical, Physical and Engineering Sciences*, vol. 180, no. 983, p. 387, 1942.

[40] A. L. Lu, M. L. Sui, and K. Lu, "Superplastic Extensibility Nanocrystalline Copper at Room Temperature," *Science*, vol. 287, no. 5457, pp. 1463–1466, 2012.

[41] J. Giallonardo, U. Erb, K. Aust, and G. Palumbo, "The influence of grain size and texture on the Young's modulus of nanocrystalline nickel and nickel iron alloys," *Philosophical Magazine*, vol. 91, no. 36, pp. 4594–4605, Dec. 2011.

[42] A. Molladavoudi, S. Amirkhanlou, M. Shamanian, and F. Ashrafizadeh, "The Production of Nanocrystalline Cobalt Titanide Intermetallic Compound via Mechanical Alloying," *Intermetallics*, vol. 29, pp. 104–109, Oct. 2012.

[43] N. A. Fleck, V. S. Deshpande, and M. F. Ashby, "Micro-architectured materials: past, present and future," *Proceedings of the Royal Society A: Mathematical, Physical and Engineering Sciences*, vol. 466, no. 2121, pp. 2495–2516, jun 2010.

[44] J. C. Maxwell, "On the calculation of the equilibrium and stiffness of frames," *Philosophical Magazine Series 4*, vol. 27, no. 182, pp. 294–299, 1864.

[45] B. Budiansky, "On the minimum weights of compression structures," *International Journal of Solids and Structures*, vol. 36, no. 24, pp. 3677–3708, Aug. 1999.

[46] J. Wallach and L. Gibson, "Mechanical behavior of a three-dimensional truss material," *International Journal of Solids and Structures*, vol. 38, no. 40-41, pp. 7181–7196, oct 2001.

[47] A. Bellini and S. Gucceri, "Mechanical characterization of parts fabricated using fused deposition modeling," *Rapid Prototyping Journal*, vol. 9, no. 4, pp. 252–264, 2003.

[48] H. K. Rafi, T. L. Starr, and B. E. Stucker, "A comparison of the tensile, fatigue, and fracture behavior of Ti-6Al-4V and 15-5 PH stainless steel parts made by selective laser melting," *International Journal of Advanced Manufacturing Technology*, vol. 69, no. 5-8, pp. 1299–1309, 2013.

[49] T. Kellner, "GE Is Building The World's Largest 'Additive' Machine For 3D Printing Metals," *GE Reports*, jun 2017. [Online]. Available: https://www.ge.com/reports/ge-building-worlds-largest-additive-machine-3d-printing-metals/

[50] 3D Systems, "Stereolithography," 2017. [Online]. Available: https://www.3dsystems.com/on-demand-manufacturing/stereolithography-sla

[51] C. W. Hull, "Apparatus for production of three-dimensional objects by stereolithography [patent]," 1986. [Online]. Available: https://www.google.com/patents/US4575330%7D

[52] Z. Zhou, D. Li, J. Zeng, and Z. Zhang, "Rapid fabrication of metal-coated composite stereolithography parts," *Proceedings of the Institution of Mechanical Engineers, Part B: Journal of Engineering Manufacture*, vol. 221, no. 9, pp. 1431–1440, jan 2007.

[53] A. G. Evans, J. W. Hutchinson, N. A. Fleck, M. F. Ashby, and H. N. Wadley, "The topological design of multifunctional cellular metals," *Progress in Materials Science*, vol. 46, no. 3-4, pp. 309–327, 2001.

[54] K. W. Whitten, R. E. Davis, M. L. Peck, and G. G. Stanley, *Chemistry*, 8th ed. Brooks Cole, 2007.

[55] M. Charbonnier and M. Romand, "Polymer pretreatments for enhanced adhesion of metals deposited by the electroless process," *International Journal of Adhesion and Adhesives*, vol. 23, no. 4, pp. 277–285, jan 2003.

[56] D. Schroer, R. J. Nichols, and H. Meyer, "Pretreatment of Polymer Surfaces - The Crucial Step Prior to Metal Deposition.pdf," *Electrochimica Acta*, vol. 40, no. 10, pp. 1487–1494, 1995.

[57] J. E. McCaskie, N. Merrick, and C. Tsiamis, "Metal plating on plastics [patent]," 1985.

[58] A. Garcia, T. Berthelot, P. Viel, A. Mesnage, P. Jégou, F. Nekelson, S. Roussel, and S. Palacin, "ABS polymer electroless plating through a one-step poly(acrylic acid) covalent grafting," *ACS Applied Materials and Interfaces*, vol. 2, no. 4, pp. 1177–1183, 2010.

[59] K. L. Mittal, "Adhesion aspects of metallization of organic polymer surfaces," *Journal of Vacuum Science and Technology*, vol. 13, no. 1, pp. 19–25, 1976.

[60] C.-L. Lee, Y.-C. Huang, and L.-C. Kuo, "Catalytic effect of Pd nanoparticles on electroless copper deposition," *Journal of Solid State Electrochemistry*, vol. 11, no. 5, pp. 639–646, 2007.

[61] G. N. Patel, D. Bolikal, and H. H. Patel, "Chromic Acid Free Etching of Polymers for Electroless Plating [patent]," 1992.

[62] J. W. Hutchinson, "Delamination of compressed films on curved substrates," *Journal of the Mechanics and Physics of Solids*, vol. 49, no. 9, pp. 1847–1864, 2001.

[63] H.-h. Yu and J. W. Hutchinson, "Influence of substrate compliance on buckling delamination of thin films," *International Journal of Fracture*, vol. 113, pp. 39–55, 2002.

[64] J. Lian, D. Jang, L. Valdevit, T. A. Schaedler, A. J. Jacobsen, W. B. Carter, and J. R. Greer, "Catastrophic vs Gradual Collapse of Thin-Walled Nanocrystalline Ni," *Nano Letters*, vol. 11, no. 10, pp. 4118–4125, 2011.

[65] P. Benham, R. Crawford, and C. Armstrong, *Mechanics of Engineering Materials*, 2nd ed. Harlow: Pearson Prentice Hall, 1996.

[66] K. R. F. Andrews, G. L. England, and E. Ghani, "Classification of the Axial Collapse of Cylindrical Tubes under Quasi-Static Loading," *International Journal of Mechanical Sciences*, vol. 25, no. 9, pp. 687–696, 1983.

[67] R. Hibbeler, *Mechanics of Materials*. New York: Macmillan Publishing Company, 1991.

[68] T. Allan, "Experimental and Analytical Investigation of the Behaviour of Cylindrical Tubes Subject to Axial Compressive Forces," *Journal of Mechanical Engineering Science*, vol. 10, no. 2, pp. 182–197, 1968.

[69] W. Yang, C. Chao, and J. McKittrick, "Axial compression of a hollow cylinder filled with foam: a study of porcupine quills," *Acta Biomaterialia*, vol. 9, no. 2, pp. 5297–304, Feb. 2013.

[70] W. Yang and J. McKittrick, "Separating the influence of the cortex and foam on the mechanical properties of porcupine quills," *Acta biomaterialia*, vol. 9, no. 11, pp. 9065–74, Nov. 2013.

[71] J. Teng and J. Rotter, *Buckling of Thin Metal Shells*. London: CRC Press, 2004.

[72] NASA, "Buckling of Thin-Walled Circular Cylinders," Tech. Rep., 1968.

[73] D. Bushnell, "Buckling of Shells - Pitfall for Designers," *AIAA Journal*, vol. 19, no. 9, pp. 1183–1226, Sep. 1981.

[74] L. Donnell, "A New Theory for the Buckling of Thin Cylinders Under Axial Com pression and Bending," *Transactions of the ASME, Aeronautical Engineering*, vol. AER-56-12, pp. 795–806, 1935.

[75] S. B. Batdorf, "A Simplified Method of Elastic Stability Analysis for Thin Cylindrical Shells: Part I - Donnell's Equation," *NACA TN 1341*, 1947.

[76] W. T. Koiter, "On the Stability of Elastic Equilibrium (translated from Dutch)," Ph.D. dissertation, Delft University of Technology, 1945.

[77] H. Langhaar, "General Theory of Buckling," *Applied Mechanics Reviews*, vol. 11, no. 11, pp. 585–588, 1958.

[78] R. Tennyson, "An Experimental Investigation of the Buckling of Circular Cylindrical Shells in Axial Compression using the Photoelastic Technique," *UTIAS Report No. 102*, 1964.

[79] V. Weingarten, E. Morgan, and P. Seide, "Elastic Stability of Thin-Walled Cylindrical and Conical Shells under Axial Compression," *AIAA Journal*, vol. 3, no. 3, pp. 500–505, 1965.

[80] J. W. Hutchinson, R. Tennyson, and D. Muggeridge, "The effect of a local axisymmetric imperfection on the buckling behaviour of a circular cylindrical shell under axial compression," *AIAA Journal*, vol. 9, no. 1, pp. 48–52, 1971.

[81] R. Tennyson, "A Note on the Classical Buckling Load of Circular Cylindrical Shells Under Axial Compression," *AIAA Journal*, vol. 1, no. 2, pp. 475–475, 1963.

[82] G. Gough, C. Elam, and N. de Bruyne, "The Stabilization of a Thin Sheet by a Continuous Supporting Medium," *Journal of the Royal Aeronautical Society*, vol. 44, pp. 12–43, 1940.

[83] Dassault Systemes, "Eigenvalue buckling prediction," 2011. [Online]. Available: http://abaqusdoc.ucalgary.ca/books/usb/default.htm?startat=pt03ch06s02at02.html

[84] C. C. Fu and W. Shuqing, *Computational Analysis and Design of Bridge Structures*. CRC Press, 2014.

[85] T. Chen, "On Introducing Imperfection in the Non-Linear Analysis of Buckling of Thin Shell Structures," Ph.D. dissertation, Delft University of Technology, 2014.

[86] M. P. Nemeth and J. H. Starnes, "The NASA Monographs on Shell Stability Design Recommendations: A Review and Suggested Improvements," *NASA TP-1998-206290*, 1998.

[87] R. Tennyson, "Buckling of circular cylindrical shells in axial compression," *AIAA Journal*, vol. 2, no. 7, pp. 489–520, 1964.

[88] R. Tennyson, "Buckling Modes of Circular Cylindrical Shells under Axial Compression," *AIAA Journal*, vol. 7, no. 8, pp. 1481–1487, 1969.

[89] M. Frocht, *Photoelasticity*. London: J. Wiley and Sons, 1941.

[90] M. Hetenyi, *Beams on Elastic Foundations*. Ann Arbor: University of Michigan Press, 1946.

[91] A. D. Kerr, "Elastic and Viscoelastic Foundation Models," *Journal of Applied Mechanics*, vol. 31, no. 3, pp. 491–498, 1964.

[92] D. Dinev, "Analytical Solution of a Beam on Elastic Foundation by Singularity Functions," *Engineering Mechanics*, vol. 19, no. 6, pp. 381–392, 2012.

[93] E. Winkler, *Die Lehre von der Elastizitat und Festigkeit*, Prague, 1867.

[94] C. A. Steeves and N. A. Fleck, "Collapse mechanisms of sandwich beams with composite faces and a foam core, loaded in three-point bending - Part I: analytical models and minimum weight design," *International Journal of Mechanical Sciences*, vol. 46, no. 4, pp. 561–583, apr 2004.

[95] J. Zhang, "Elastic/Plastic Buckling of Cylindrical Shells with Elastic Core under Axial Compression," Ph.D. dissertation, McGill University, 2009.

[96] P. Seide, "The Stability Under Axial Compression and Lateral Pressure of Circuluar-Cylindrical Shells with a Soft Elastic Core," *Journal of the Aeronautical Sciences*, vol. 29, no. 7, pp. 851–862, 1962.

[97] T. Myint-U, "Stability of Axially Compressed Core-Filled Cylinders," *AIAA Journal*, vol. 4, no. 3, pp. 552–553, 1965.

[98] G. N. Karam and L. J. Gibson, "Elastic Buckling of Cylindrical Shells with Elastic Cores - Part I: Analysis," *International Journal of Solids and Structures*, vol. 32, no. 8/9, pp. 1259–1283, 1995.

[99] D. O. Brush and B. O. Almroth, "Buckling of Core-Stabilized Cylinders under Axisymmetric External Loads," *Journal of the Aerospace Sciences*, vol. 29, no. 10, pp. 1164–1170, 1962.

[100] V. I. Weingarten and Y. S. Wang, "Stability of Shells Attached to Elastic Core," *Journal of the Engineering Mechanics Division*, vol. 102, no. 5, pp. 839–848, 2014.

[101] Y. Zhao, Y. Cao, X.-Q. Feng, and K. Ma, "Axial compression-induced wrinkles on a core–shell soft cylinder: Theoretical analysis, simulations and experiments," *Journal of the Mechanics and Physics of Solids*, vol. 73, pp. 212–227, 2014.

[102] A. Kounadis and X. Lignos, "Buckling of tube-like shells filled with other material under uniform axial compression," *Engineering Structures*, vol. 22, no. 8, pp. 961–967, Jun. 2000.

[103] T. Y. Reddy and R. J. Wall, "Axial Compression of Foam-Filled Thin-Walled Circular Tubs," *International Journal of Impact Engineering*, vol. 7, no. 2, pp. 151–166, 1988.

[104] I. Malyutin, P. Pilipenko, V. Georgievskii, and V. Smykov, "Experimetnal and Theoretical Study of the Stability, in Axial Compression, of Cylindrical Shells Reinforced with an Elastic Filler," *Soviet Applied Mechanics*, vol. 16, no. 2, pp. 1057–1060, 1980.

[105] T. Ozbakkaloglu and T. Vincent, "Axial Compressive Behavior of Circular High-Strength Concrete-Filled FRP Tubes," *Journal of Composites for Construction*, vol. 18, no. 2, 2014.

[106] S. Guler, M. Aydogan, and A. Çopur, "Axial capacity and ductility of circular UHPC-filled steel tube columns," *Magazine of Concrete Research*, vol. 65, no. 15, pp. 898–905, Aug. 2013.

[107] W. S. Goree and W. A. Nash, "Elastic Stability of Circular Cylindrical Shells Stabilized by a Soft Elastic Core," *Experimental Mechanics*, vol. 2, no. 5, pp. 142–149, 1962.

[108] I. Hall, O. Ebil, M. Guden, and C.-J. Yu, "Quasi-static and dynamic crushing of empty and foam-filled tubes," *Journal of Materials Science*, vol. 36, no. 24, pp. 5853–5860, 2001.

[109] D. Kachman, "Test report on buckling of propellant cylinders under compressive loads," *Space Technology Laboratories, Inc*, vol. GM 59-7520, pp. 6–24, 1959.

[110] J. Yao, "Buckling of Axially Compressed Long Cylindrical Shell with Elastic Core," *Journal of Applied Mechanics*, vol. 29, no. 2, pp. 329–334, 1962.

[111] F. Shanley, "The Column Paradox," *Journal of the Aeronautical Sciences*, vol. 13, no. 5, p. 678, 1946.

[112] F. Shanley, "Inelastic Column Theory," *Journal of the Aeronautical Sciences*, vol. 14, no. 5, pp. 261–268, 1947.

[113] W. Ramberg and W. R. Osgood, "Description of stress-strain curves by three parameters," *National Advisory Committee For Aeronautics*, vol. NACA TN 90, 1943.

[114] E. Voce, "A Practical Strain-hardening Function," *Metallurgica*, vol. 51, pp. 219–226, 1955.

[115] J. T. Hwang and C. A. Steeves, "Optimisation of 3-D Lattice Cores in Composite Sandwich Structures," *Journal*

of Composite Materials.

[116] M. A. Dawson and L. J. Gibson, "Optimization of cylindrical shells with compliant cores," *International Journal of Solids and Structures*, vol. 44, no. 3-4, pp. 1145–1160, 2007.

[117] L. Valdevit, J. W. Hutchinson, and A. G. Evans, "Structurally optimized sandwich panels with prismatic cores," *International Journal of Solids and Structures*, vol. 41, no. 18-19, pp. 5105–5124, 2004.

[118] T. N. Sullivan, B. Wang, H. D. Espinosa, and M. A. Meyers, "Extreme lightweight structures: avian feathers and bones," *Materials Today*, vol. 20, no. 7, pp. 377–391, 2017.

[119] L. J. Gibson and M. F. Ashby, *Cellular Materials in Nature and Medicine*. Cambridge: Cambridge University Press, 2010.

[120] L. R. Herrmann, "Stress Functions for the Axisymmetric, Orthotropic, Elasticity Equations," *AIAA Journal*, vol. 2, no. 10, pp. 1822–1824, 1964.

[121] D. d. G. Allen, L. Fox, and R. Southwell, "Relaxation Methods Applied to Engineering Problems. VIID: Stress Distributions in Elastic Solids of Revolution," *Philosophical Transactions of the Royal Society of London A: Mathematical and Physical Sciences*, vol. 239, no. 810, pp. 501–537, 1942.

[122] 3D Systems, "VisiJet M3 Crystal (MJP)," 2018. [Online]. Available: https://www.3dsystems.com/materials/visijet-m3-crystal

[123] S. P. Timoshenko and J. Goodier, *Theory of Elasticity*, 3rd ed. Blacklick: McGraw-Hill, 1970.

[124] C. Calladine, "Inelastic buckling of columns: the effect of imperfections," *International Journal of Mechanical Sciences*, vol. 15, no. 7, pp. 593–604, 1973.

[125] H. March, "Elastic Stability of the Facings of Sandwich Columns," in *Proceedings - Symposia in Applied Mathematics [Vol 3 - Elasticity]*, 1950, pp. 85–106.

[126] J. Fish and T. Belytschko, *A First Course in Finite Elements*, 1st ed. Wiley, 2007.

[127] F. C. Bardi and S. Kyriakides, "Plastic buckling of circular tubes under axial compression - Part I: Experiments," *International Journal of Mechanical Sciences*, vol. 48, no. 8, pp. 830–841, 2006.

[128] E. Bele, B. Bouwhuis, and G. Hibbard, "Failure mechanisms in metal/metal hybrid nanocrystalline microtruss materials," *Acta Materialia*, vol. 57, no. 19, pp. 5927–5935, Nov. 2009.

[129] S. Batterman, "Plastic Buckling of Axially Compressed Cylindrical Shells," *AIAA Journal*, vol. 3, no. 2, pp. 316–325, 1965.

[130] T. W. Cook, "Buckling of Cylindrical Shells with a Granular Core Under Global Bending," Ph.D. dissertation, Delft University of Technology, 2014.

[131] S. Waley and J. Field, "Strain Rate Sensitivity of Polymers in Compression from Low to High Rates," *DYMAT Journal*, vol. 1, no. 3, pp. 211–227, 1994.

[132] Y. Zhou, U. Erb, K. T. Aust, and G. Palumbo, "Young's modulus in nanostructured metals," *Zeitschrift fur Metallkunde*, vol. 94, no. 10, pp. 1157–1161, 2003.

[133] J. Stewart, *Multivariable Calculus*, 6th ed. Belmont: Brooks Cole, 2008.

[134] Diab Group, "Divinycell H200: Technical Data." [Online]. Available: http://www.diabgroup.com/{~}/media/Files/Products/Core-material-products-English/HJuly2017rev17SI.pdf

[135] Plastics International, "LDPE (Low Density Polyethylene." [Online]. Available: https://www.plasticsintl.com/datasheets/LDPE.pdf

[136] Plastics International, "LDPE (Low Density Polyethylene." [Online]. Available: https://www.plasticsintl.com/datasheets/LDPE.pdf